

UNDERSTANDING THE RADIATION EFFECTS ON FIBER OPTIC SENSORS

by

Sohel Rana



A dissertation

submitted in partial fulfillment

of the requirements for the degree of

Doctor of Philosophy in Electrical and Computer Engineering

Boise State University

May 2022

© 2022

Sohel Rana

ALL RIGHTS RESERVED

BOISE STATE UNIVERSITY GRADUATE COLLEGE

**DEFENSE COMMITTEE AND FINAL READING APPROVALS**

of the dissertation submitted by

Sohel Rana

Dissertation Title: Understanding the Radiation Effects on Fiber Optic Sensors

Date of Final Oral Examination: 02 March 2022

The following individuals read and discussed the dissertation submitted by student Sohel Rana, and they evaluated the student's presentation and response to questions during the final oral examination. They found that the student passed the final oral examination.

Harish Subbaraman, Ph.D. Chair, Supervisory Committee

Nirmala Kandadai, Ph.D. Co-Supervisor, Supervisory Committee

Maria Mitkova, Ph.D. Member, Supervisory Committee

Austin D. Fleming, Ph.D. Member, Supervisory Committee

Colby Jensen, Ph.D. Member, External Examiner

The final reading approval of the dissertation was granted by Harish Subbaraman, Ph.D., Chair of the Supervisory Committee. The dissertation was approved by the Graduate College.

## DEDICATION

I would like to dedicate my dissertation to my beloved and beautiful daughter

Samayra Rana Farisha

## ACKNOWLEDGMENTS

I would like to extend my sincerest gratitude to Dr. Harish Subbaraman for being my technical advisor and his continuous support, patience, and encouragement over the past five years. It is impossible to express enough thanks to him for not only providing me the opportunity to work in the Fiber-Optics Laser and Integrated-photonics (FLAIR) lab and perform cutting-edge research, but also for being a counselor, friend and especially a good human being. Indeed, words are not enough to express his contribution to my personal growth.

From the beginning of my Ph.D. journey, I was lucky enough to have Dr. Nirmala Kandadai as my joint technical advisor. I would like to thank her for her guidance, in-depth knowledge, innovative insight, and providing me the scope to work on radiation hardened optical fibers.

This dissertation and work hold a great amount of gratitude to Dr. Austin Fleming. I had the opportunity to work under his mentorship at the Idaho National Laboratory (INL) for the last two years of my Ph.D. He is a great mentor who kept me optimistic and helped me achieve my goals. I really thank him for being a friend and for helping me mature professionally. His guidance and inspiration helped me to think critically.

I would like to thank Dr. Maria Mitkova for being my committee member. Her inspiration and smiling face always encouraged me to work with double speed. I would also like to thank Dr. Samia Islam for being my graduate faculty representative. I am also grateful to Dr. Colby Jensen for agreeing to serve as my external examiner.

I am grateful to all FLAIR and ANML lab members at Boise State for their help and suggestions. I am indebted to the staff members at the Idaho Microfabrication Laboratory (IML) and Boise State Center for Materials Characterization for their support. I would like to thank Pete Miranda, Travis Gabel, and Dr. Nick Bulloss for their patience and training me on several instruments. I also thank Kelly McCary and Dr. Patrick Calderoni at INL for their help and fruitful discussions. I am thankful to Prof. Thomas Blue and Dr. Brandon Wilson from The Ohio State University for their collaboration and suggestions.

I would like to thank my parents, brothers and sisters for their continuous support and encouragement. What I say about my beautiful and lovely wife is not enough, and I could not have moved forward without her support. She has always been caring, patient and has tolerated me in my every situation over the past few years.

This research was supported in part through the Department of Energy Advanced Sensors and Instrumentation program under DOE Idaho Operations Office Contract DE-AC07-05ID14517.

## ABSTRACT

In this dissertation, the effects of radiation (gamma, neutron or mixed gamma and neutron) on optical fiber sensors are studied and new techniques for real-time measurement of radiation-induced macroscopic changes in optical fibers are presented. It is crucial among the research and development efforts in the nuclear energy field to conduct experiments in Advanced Test Reactor (ATR) to support lifetime extension, novel fuels and materials development, better fuel management, and enhanced safety of existing as well as future nuclear power plants (NPP). Due to their unparalleled and unique advantages over traditional sensors, optical fiber sensors are deemed potential candidates for their use in nuclear environments. However, optical fibers are susceptible to high levels of ionizing radiation emitted by fission reactors which are characterized by the highest levels of gamma dose, high flux of neutrons and potentially high temperatures depending on location in a reactor core. It is essential to accurately determine the information related to physical parameters such as temperature, pressure, and strain in nuclear environments for the safety of the existing and future NPPs.

This dissertation starts with inverting a transmission mode long period grating (LPG) to reflection mode using a novel and cost-effective metal coating method since transmission mode LPG limits its applications in tight spaces or in nuclear fields. To understand the metal coating and metal coverage effects on the reflection spectrum of LPG, modeling work was performed, and it was validated by experimental work. We have shown

that the sensitivity of LPGs to physical parameters in both transmission and reflection modes are almost the same.

Next, we have modeled the radiation effects on different fiber optic sensors, proposed empirical models, and performed numerical analysis to understand the effects of nuclear environments on fiber optic sensors. We analyzed the real-time data from fiber Bragg gratings (FBGs) exposed to high neutron fluence and high temperature environments within the ATR at Idaho National Laboratory (INL). We have found that incoming radiation significantly drifts the characteristic signal of FBGs, leading to a temperature measurement error when FBGs are dedicated to temperature sensing. It is well known that neutron and gamma irradiation compacts silica optical fibers, resulting in a macroscopic change in the refractive index (RI) and geometric structure. The change in RI and linear compaction in a radiation environment is caused by three well-known mechanisms: (1) radiation induced attenuation (RIA), (2) radiation induced compaction (RIC), and (3) radiation induced emission (RIE). While RIA degrades the signal strength by creating different types of color centers in the silica fiber, RIC alters the density, and hence RI by displacing the host material atoms. However, Kramers-Kronig relation states that absorption, and hence the RIA, also modifies the RI of the silica fiber. Apart from RIA and RIC, other phenomena such as temperature, dose rate, stress relaxation, and dopant compositions exchange may change the RI. To overcome these problems, we have proposed an effective technique to measure the change in RI and compaction of optical fiber due to any specific phenomena the fiber is subjected to, including RIC, RIA, dopant diffusion, temperatures, dose, dose rate, etc. By knowing the individual contribution of RI and fiber length to the signal drift, it is possible to reduce the radiation induced signal drift

in optical fiber sensors and provide accurate information regarding the temperature inside a radiation environment.

Fission gas detection in nuclear environments is another important aspect that needs to be focused on. Pressure induced by fission gases during irradiation may lead to loss of coolant accident (LOCA), which can cause severe damage to the NPPs. We have modeled and fabricated optical fiber-based sensors to enable real-time monitoring of fission gases, which allows understanding the implications of fission gas release during an accident, important for safe and high performance.

## TABLE OF CONTENTS

DEDICATION.....	iv
ACKNOWLEDGMENTS.....	v
ABSTRACT .....	vii
LIST OF TABLES.....	xv
LIST OF FIGURES .....	xvi
LIST OF ABBREVIATIONS.....	xxiii
SUMMARY OF CONTRIBUTION.....	xxvi
LIST OF PUBLICATIONS.....	xxix
CHAPTER ONE: OPTICAL FIBER AND FIBER OPTIC SENSORS.....	1
1.1 Optical Fiber.....	1
1.1.1 Important Parameters of Optical Fiber.....	2
1.2 Building Block of Silica (SiO <sub>2</sub> ) Structure.....	7
1.3 Optical Fiber Sensors.....	8
1.3.1 Grating Based Sensors.....	9
1.3.2 Distributed Sensors.....	11
1.3.3 Single Point Sensors.....	14
CHAPTER TWO: RADIATION EFFECTS ON OPTICAL FIBER TECHNOLOGY ...	15
2.1 Types of Radiation.....	15
2.2 Radiation Induced Defects in Silica .....	16

2.2.1 Frenkel Defects.....	18
2.2.2 Dangling Defects .....	20
2.3 Radiation Induced Mechanisms .....	25
2.3.1 Radiation Induced Attenuation.....	25
2.3.2 Radiation Induced Compaction .....	28
2.3.3 Radiation Induced Emission.....	29
CHAPTER THREE: LONG PERIOD GRATING AND ITS APPLICATIONS.....	31
3.1. Transmission LPGs and Their Drawbacks .....	31
3.2. Geometric Structure of a Distributed Reflective LPG .....	33
3.3. Simulation Results and Discussions.....	34
3.3.1. Single Reflective LPG .....	34
3.3.2. Distributed Reflective LPG.....	39
3.4. Metal Coating.....	43
3.4.1. Metal Coating Process .....	45
3.5. Metal Coated Reflective LPG.....	47
3.6. Coating Length on LPG Spectrum.....	49
3.7. Reflection LPG Based Sensors .....	52
3.7.1. Temperature Sensing .....	52
3.7.2. Refractive Index Sensing .....	54
CHAPTER FOUR: RADIATION EFFECTS ON OPTICAL FIBER SENSORS: MODELING AND EXPERIMENT.....	58
4.1 Models for OFSs .....	59
4.1.1 Model for Fiber Bragg Grating.....	59
4.1.2 Model for Long Period Grating.....	61

4.1.3 Model for Fabry-Perot (F-P).....	63
4.2 Numerical Analysis of How RIC Affects OFS at Low Doses .....	65
4.2.1 RIC Effects on FBG .....	66
4.2.2 RIC Effects on FBG Considering Length Change.....	67
4.2.3 RIC Effects on LPG .....	70
4.2.4 RIC Effects on LPG Considering Length Change.....	71
4.2.5 RIC Effects on F-P .....	72
4.2.6 RIC Effects on F-P Considering Length Change.....	73
4.3 RIC Effects on OFS at High Doses .....	74
4.3.1 RIC Effects on FBG at High Doses .....	76
4.3.2 RIC Effects on LPG at High Doses.....	77
4.3.3 RIC Effects on F-P at High Doses .....	78
4.3.4 RIC Induced Temperature Error .....	79
4. 4 RIA Effects on OFSs .....	80
4. 5 Radiation Exposure of FBGs.....	82
4. 6 Irradiated FBGs .....	84
4. 7 Results and Discussion.....	86
4. 7.1 Effects of RIA on Irradiated FBGs .....	88
4.7.2 Effects of RIC on Irradiated FBGs.....	89
4.7.3 Calculation of Compaction and Refractive Index.....	90
4.7.4 FBG Modeling Based on Experimental Data .....	94
<b>CHAPTER FIVE: REAL-TIME MEASUREMENT OF MACROSCOPIC CHANGES IN OPTICAL FIBERS .....</b>	<b>101</b>
5.1 Objective.....	102

5.2 Geometric Structure and Principles .....	103
5.3 Compaction Analysis .....	107
5.4 Radiation Effects on Cavities .....	108
5.5 Thermal Effects on Cavities .....	113
5.6 Fabrication and Experiment of Cascaded FPI .....	115
5.6.1 Fabrication Procedures of Cascaded FPI .....	117
5.6.2 Temperature Effects on Cascaded Cavities .....	120
5.6.3 Thermal Expansion Coefficient Measurement .....	121
5.6.4 Thermo-Optic Coefficient Measurement .....	124
5.7 Discussions and Applications .....	126
CHAPTER SIX: FIBER OPTIC GAS PRESSURE SENSORS .....	129
6.1. Plenum Pressure .....	129
6.2. Fiber Optic Pressure Sensors .....	130
6.3. Fabrication Procedures .....	132
6.4. Working Principle and Results .....	134
6.5. Argon Gas Sensing Using SMF-CAP-PCF .....	139
6.6. Argon Gas Sensing Using SMF-CAP-CAP .....	141
CHAPTER SEVEN: FUTURE PLANNING ON RESEARCH .....	143
7.1. Reduction of Radiation Induced Drift for Temperature Sensing .....	143
7.2. Pressure Sensing in Nuclear Reactor .....	143
7.3. Long Term Annealing of Optical Fiber .....	144
CHAPTER EIGHT: CONCLUSIONS .....	145
BIBLIOGRAPHY .....	148

APPENDIX ..... 173

## LIST OF TABLES

Table 4.1	Radiation-induced RI changes in a B/Ge codoped fiber reported by Kher et al. [123]. .....	65
Table 4.2	Calculated values of density and length compaction (based on the RI values) using Eqs. 4.2,4.3, and 4.4.....	69
Table 4.3	Gamma radiation induced RI change in different compositional fibers at MGy dose.....	75
Table 4.4	Calculated values for higher doses, as obtained by inputting the fitting constant values from Fig. 4.10 into Eq. (4.5).....	76
Table 4.5	Radiation-induced temperature errors in FBG, LPG, and F-P sensors at higher doses.....	80
Table 4.6	RIA values obtained from [180].....	81
Table 5.1	Original and retrieved length of cavities of the cascaded FPI. ....	107
Table 5.2	Reconstructed cavity length before and after irradiation to a fast fluence of <b><math>2.4 \times 10^{21} \text{ n/cm}^2</math></b> at a temperature of $95^\circ\text{C}$ .....	110
Table 6.1	Fusion splicing parameters for all structures .....	133
Table A.1	Commercially purchased fibers along with the radiation response.....	175
Table A.2.	Dopant concentration of different fibers at core .....	178

## LIST OF FIGURES

Figure 1.1	Optical fiber schematic[1].....	2
Figure 1.2	Schematic of single mode and multi-mode fiber[3] .....	3
Figure 1.3	Loss spectrum of a silica based optical fiber[4] .....	5
Figure 1.4	Dispersion in optical fiber[6].....	7
Figure 1.5	General structure of optical fiber sensor. ....	8
Figure 1.6	Basic scattering mechanism of light in an optical fiber[43].....	11
Figure 2.1	Intrinsic point defects in silica glass structure[71]. (a) No defects. (b) ODC(I). (c) ODC(II). (d) Peroxy linkage. (e) Interstitial O <sub>2</sub> . (f) Interstitial O <sub>3</sub> . (g) Transition metals. (h) Hydroxyl ions. (i) Silicon hydride. (j) E'-centre. (k) NBOHC. (l) Peroxy radical. ....	17
Figure 2.2.	The attenuation band of Si-related defects[72].....	18
Figure 2.3	Change in density in vitreous silica on irradiation in nuclear reactors (taken from[134]).....	29
Figure 3.1	Schematic of a distributed reflective LPG sensor design comprising of $n$ number of LPGs within a single fiber and all the designing parameters. .	33
Figure 3.2	Spectrum of the designed LPG as a function of wavelength for different grating period numbers ( $N$ ) for $n=1$ and grating period of $390 \mu\text{m}$ : (a) transmitted spectrum and (b-f) reflected spectrum for $Lc = Lend = 1450\Lambda$ .....	35
Figure 3.3	Effects of metal coating length on the reflected spectrum of the LPG for $n=1$ , $N=45$ and grating period is of $\Lambda = 390 \mu\text{m}$ : (a) transmitted spectrum and (b-f) reflected spectrum. ....	37
Figure 3.4	Effects of metal coating length on the reflected spectrum of the LPG for $n=1$ , $N=45$ and grating period is of $\Lambda = 390 \mu\text{m}$ while keeping the $Lend = 1450\Lambda$ fixed: (a) transmitted spectrum and (b-d) reflected spectrum. ....	37

Figure 3.5	Effects of coating coverage on the spectrum of the designed LPG for $n = 1$ , $N = 45$ : (a) transmitted spectrum before inclusion of the metal coating, (c-f) reflected spectrum.....	38
Figure 3.6	Effect of coating length on the reflected spectrum of the designed two LPGs ( $n=2$ ) added in series and $L_{end} = 1450\Lambda_1$ (a) transmitted spectrum before inclusion of the metal coating, (b-d) reflected spectrum. ....	40
Figure 3.7	Effects of coating coverage on the spectrum of the designed LPG for $n = 2$ and $N = 45$ : (a) transmitted spectrum before inclusion of the metal coating, (b-d) reflected spectrum.....	40
Figure 3.8	Spectrum of the cascaded two LPGs for different configurations for $n = 2$ and $N = 45$ : (a) transmitted spectrum before inclusion of the metal coating, (b-e) reflected spectrum. ....	41
Figure 3.9	Spectrum of the cascaded three LPGs when $L_c=L_{end} = 1450\Lambda_3$ for $n = 3$ and $N = 45$ and grating period of $\Lambda_1 = 390 \mu\text{m}$ , $\Lambda_2 = 374\mu\text{m}$ , and $\Lambda_3 = 346 \mu\text{m}$ . ....	43
Figure 3.10.	A schematic of metal coated LPG with all associated parameters. Metal is coated over length L and the end facet. ....	45
Figure 3.11	Step by step metal coating process by brush coating technique. ....	46
Figure 3.12	Scanning electron microscope (SEM) image of a coated fiber near the LPG section.....	47
Figure 3.13	Experimental setup to record reflected spectrum from the metal coated LPG (1, 2, and 3 indicate the port of the circulator).....	48
Figure 3.14	Measured transmitted spectrum (dotted blue) and reflected spectrum (red) for a coating length of 60 cm. ....	48
Figure 3.15	Measured transmitted spectrum (dotted blue) and reflected spectrum (solid red) for coating length of 1 cm.....	49
Figure 3.16	Measured transmitted spectrum (dotted pink) and reflected spectra after 1 day (solid red), and after 3 weeks (solid blue) for a coating length of 60 cm. ....	50
Figure 3.17	Schematic of different coating length on LPG contained fiber. ....	51
Figure. 3.18	Effect of coating length on the reflection spectrum of the LPG: (a) simulation results and (b) experimental results.....	52

Figure. 3.19	The measured relative wavelength shifts of LPG as a function of temperature: (a) transmission mode LPG and (b) reflection mode LPG. . 53
Figure. 3.20	The measured relative wavelength shifts of LPG as a function of RI: (a) transmission mode LPG and (b) reflection mode LPG..... 55
Figure 4.1	(a) FBG schematic, where $n_{core}$ , $n_{clad}$ , and $\Lambda_{FBG}$ are the RIs of the core, cladding, and grating period, respectively; (b) the reflection spectrum of the designed FBG for $\Lambda_{FBG}= 0.5353 \mu\text{m}$ and grating strength $(\Delta n) = 10^{-4}$ ..... 61
Figure 4.2	(a) LPG schematic, where $n_{core}$ , $n_{clad}$ , and $\Lambda_{LPG}$ are the RIs of the core, cladding, and grating period, respectively; (b) transmission spectrum of the designed LPG for $\Lambda_{LPG}= 348 \mu\text{m}$ and grating strength $(\Delta n) = 6 \times 10^{-4}$ ..... 62
Figure 4.3	(a) Schematic of an EFPI, where $IO$ , $IR$ , and $LC$ are the incoming light, reflected light, and cavity length, respectively; (b) interferometric fringes obtained due to interference within the cavity length $LC = 200 \mu\text{m}$ ..... 64
Figure 4.4	RIC effects on FBG: redshift in the Bragg wavelength from 1550 to 1550.16 nm as the dose is increased from 0 to 1540 kGy, where $\Delta\lambda_B$ denotes the Bragg wavelength shift. .... 67
Figure 4.5	RIC effects on FBG considering length change: blueshift in the Bragg wavelength from 1550 to 1549.98 nm as the dose is increased from 0 to 1540 kGy, where $\Delta\lambda_B$ denotes the Bragg wavelength shift..... 69
Figure 4.6	RIC effects on the transmission spectrum of the designed LPG along with the resonance wavelength shift ( $\Delta\lambda_R$ ) for the $LP_{0,11}$ cladding mode when dose is increased from 0 to 1540 kGy..... 71
Figure 4.7	RIC effects on the transmission spectrum of the designed LPG considering length change along with the resonance wavelength shift ( $\Delta\lambda_R$ ) for the $LP_{0,11}$ cladding mode when the dose is increased from 0 to 1540 kGy.. 72
Figure 4.8	RIC effects on the interferometric fringes of the designed F-P when the dose is increased from 0 to 1540 kGy, where FSR is the spectral distance between two adjacent fringe peaks for a given radiation. .... 73
Figure 4.9	RIC effects on the interferometric fringes of the designed F-P considering length length when the dose is increased from 0 to 1540 kGy, where FSR is the spectral distance between two adjacent fringe peaks for a given radiation..... 74

Figure 4.10	Curve fitting for relative density as a function of dose using the values from Table 4.2.....	75
Figure 4.11	Calculated RI with the experimental values at MGy dose.....	76
Figure 4.12	RIC effects on FBG at high doses: blueshift of 0.039 nm in the Bragg wavelength when the dose is increased from 0 to 7 MGy and radiation-induced changes in length and RI are considered. ....	77
Figure 4.13	RIC effects on the transmission spectrum of the designed LPG at high doses. ....	78
Figure 4.14	RIC effects on the interferometric fringes of the designed F-P sensor at high doses.....	79
Figure 4.15	Effect of RIA on the spectra of (a) FBG and (b) LPG, using the same design parameters applied earlier.....	81
Figure 4.16	Effect of RIA on F-P at various doses, using the same design parameters applied earlier.....	82
Figure. 4.17	The Bragg grating sensors are spaced 3 cm apart from the end of the optical fiber. ....	85
Figure 4.18	Thermal modeling of temperature in the experiment capsule.....	85
Figure 4.19	Spectra of five FBGs prior irradiation. ....	86
Figure 4.20	Spectra of all survival FBGs with irradiation hours.....	87
Figure 4.21	Neutron fluence (left) and thermocouple temperature (right) as a function of irradiation time.....	87
Figure 4.22	RIA and irradiation temperature as a function of irradiation time.....	88
Figure 4.23	RI-BWS of survival FBGs as a function of irradiation time. ....	90
Figure 4.24	Neutron induced volumetric compaction at five different irradiation temperatures. ....	92
Figure 4.25	Neutron induced refractive index variation at five different irradiation temperatures.....	93
Figure 4.26	Neutron-induced RI variation at five different irradiation temperatures, using two different approaches. Each color reflects the indicated temperature, irrespective of whether the line is solid or dashed. ....	94

Figure 4.27	Spectrum of FBG using equations (4.11) and (4.12). .....	96
Figure 4.28	Effect of radiation induced RI ( $n$ ) and grating period ( $\Lambda$ ) on the Bragg wavelength of the designed FBG. The legend colors indicate the same temperature irrespective of solid or dotted line. ....	96
Figure 4.29	RI-BWS at different irradiation temperatures. ....	97
Figure 4.30	The effects of refractive index ( $n$ ), grating period ( $\Lambda$ ), and both ( $n + \Lambda$ ) on the Bragg wavelength of the FBG modeled in MATLAB. ....	98
Figure 5.1	Schematic of the designed cascaded Fabry-Perot interferometer. ....	104
Figure 5.2	(a) total spectrum of the cascaded FPI and (b) the spatial frequency distribution of the total spectrum using FFT. ....	105
Figure 5.3	Retrieved signals using bandpass filters and inverse FFT for (a) air cavity and (b) silica cavity. ....	106
Figure 5.4	Reconstructed signals for (a) air cavity before irradiation, (b) air cavity after irradiation, (c) silica cavity before irradiation, (d) silica cavity after irradiation. ....	109
Figure 5.5	Spectra of FBG in different conditions: before irradiation (black curve), radiation induced RI effect (blue curve), radiation induced grating period effect (green curve), and radiation induced combined effect of RI and grating period (red curve) on the Bragg wavelength. ....	112
Figure 5.6	Fabrication steps of cascaded FPI by using only cleaving and splicing and the complete cascaded FPI structure. ....	118
Fig. 5.7	Spectral response of fabricated cascaded FPI: (a) total reflection spectrum, (b) optical frequency domain distribution of the total reflection spectrum, (c) reconstructed cavity length of EFPI, and (d) reconstructed cavity length of IFPI. ....	119
Figure 5.8	Experimental setup to record signal at different temperatures. ....	121
Figure 5.9	Measured spectra of the air cavity at different temperatures .....	123
Figure 5.10	Measured air cavity length as a function of applied temperature. ....	124
Figure 5.11	Retrieve spectra of the silica cavity at different temperatures. ....	125
Figure 5.12	Measured refractive index of silica as a function of applied temperature. ....	126

Figure 6.1	Microscopic images of sensors based on differently structured FPIs: (a) SMF-CAP-PCF, (b) SMF-CAP-CAP, and (c) SMF-CAP-SMF.....	132
Figure 6.2	Experimental setup to test the gas response of different sensors.....	136
Figure 6.3	Reflection spectra of the differently structured Fabry-Perot sensors at different gas pressures: (a) SMF-CAP-PCF, (b) SMF-CAP-CAP, and (c) SMF-CAP-SMF. ....	136
Figure 6.4	Relative resonant dip wavelength shift of all the sensors when under gas pressure, along with their sensitivity ( $S$ ) and linearity ( $R^2$ ). The discrete points (marked in blue and red) indicate the experimental data when the cavity is pressurized and depressurized, respectively. The black line shows the linear fitting of the experimental data, and the green line indicates where the simulated data overlap the experimental data: (a) SMF-CAP-PCF: $S = 0.5$ nm/MPa and $R^2 = 0.998$ ; (b) SMF-CAP-CAP: $S = 0.5$ nm/MPa and $R^2 = 0.9978$ ; and (c) SMF-CAP-SMF: $S = 0.49$ nm/MPa and $R^2 = 0.9996$ . ....	137
Figure 6.5	Reflection spectra of SMF-CAP-PCF based FPI at different argon gas pressure. ....	140
Figure 6.6	Wavelength shift as a function applied argon gas pressure. ....	140
Figure 6.7	Reflection spectra of SMF-CAP-CAP based FPI at different argon gas pressure .....	141
Figure 6.8	Wavelength shift as a function applied argon gas pressure .....	142
Figure A.1	EMPA for finding doping concentrations of fibers.....	177
Figure A.2	Experimental setup for temperature testing of fibers. ....	179
Figure A.3	Temperature effects on different compositional germanium doped fibers at 1550 nm .....	180
Figure A.4	Temperature effects on different compositional germanium doped fibers at 1310 nm .....	181
Figure A.5	Temperature effects on different compositional germanium doped fibers at 1064 nm .....	182
Figure A.6	Temperature effects on different compositional PSC fibers at 1550 nm.	183
Figure A.7	Temperature effects on different compositional PSC fibers at 1310 nm.	184

Figure A.8	Temperature effects on different compositional PSC fibers at 1064 nm.	184
Figure A.9	Temperature effects on Boron-Germanium codoped fiber at different wavelengths. ....	185
Figure A.10	Temperature effects on Erbium doped fiber at different wavelengths....	186
Figure A.11	Temperature effects on Neodymium doped fiber at different wavelengths. ....	187
Figure A.12	Temperature effects on Ytterbium doped fiber at different wavelengths. ....	188

## LIST OF ABBREVIATIONS

NPP	Nuclear power plant
OFS	Optical fiber sensor
FBG	Fiber Bragg grating
LPG	Long period grating
F-P	Fabry-Perot
FPI	Fabry-Perot interferometer
RIC	Radiation induced compaction
RIA	Radiation induced attenuation
RIE	Radiation induced emission
RI	Refractive index
MTIR	Modified total internal reflection
LOCA	Loss of coolant accident
ATR	Advanced testing reactor
MGy	Mega Gray
GGy	Gigga Gray
PBG	Photonic bandgap
SMF	Single mode fiber
SM	Single mode
MM	Multimode
NA	Numerical aperature

NIR	Near infrared
UV	Ultra-violet
VIS	Visible
dB	Decibel
LED	Light emitting diode
OSA	Optical spectrum analyzer
fs	Femtosecond
OTDR	Optical time domain reflectometry
SNR	Signal to noise ratio
LVDT	Linear variable differential transformer
OA	Optical absorption
PL	Photoluminescence
EPR	Electron paramagnetic resonance
NBOHC	Non-bridging oxygen hole center
ODC	Oxygen deficiency center
FWHM	Full width half maximum
POL	Peroxy linkage
CL	Cathod luminescence
OH	Hydroxyl radical
PSC	Pure silica core
EMPA	Electron microprobe analyzer
BWS	Bragg wavelength shift
SLD	Superluminescent diode

IR	Infrared radiation
VIS	Visible
RIU	Refractive index unit
BBS	Broadband source

## SUMMARY OF CONTRIBUTION

Optical fiber technologies within the nuclear industry have shown growing interest for both data communication and sensing applications. Rigorous research and development programs are implemented in an attempt to improve the safety of the currently existing as well as future plants. It is essential to monitor better fuel management, support lifetime extension and develop new reactor concepts to provide an uninterrupted emission free energy supply in a safe way for the next generation. Optical fiber technologies can contribute to this aspect compared to their counterparts owing to their plethora of advantages which include but are not limited to small size, immunity to electromagnetic interference (EMI), robust structure, chemically passive, light weight, remote sensing and multiplexing capabilities. However, their performance is greatly affected under high levels of radiation, for example, in a fission reactor. The high-level of gamma ( $\gamma$ ) dose in the order of  $\sim$  GGy and high flux of neutrons along with the high temperatures in a fission reactor alter the optical as well as mechanical properties of optical fibers. The most probable effect is the RIA, which degrades the signal strength significantly. However, RIA does not drift the signal that causes measurement error as much as occurred by RIC, which changes the density of the fiber material through the knock-on process. Since density is related to RI and length of the fiber, it can be said that RIC causes signal drift by altering these two governing parameters of optical fiber. However, signal drift as well as attenuation of optical fiber in a nuclear environment greatly depends on the fiber compositions and can be greatly improved.

This work started by modeling the reflective LPG and understanding the coating length and coating coverage effects on the reflection spectrum of LPG. We introduce a simple and cost-effective brush coating method to realize the reflective LPG. Since silver paste was used as the coating material and it was cured, it is expected that this coating can survive at high temperatures. The modeling work on reflective LPG is verified by experimental work.

Next, we numerically analyze the radiation effects on different types of resonance-based fiber optic sensors such as fiber Bragg grating (FBG), long period grating (LPG), and Fabry-Perot (F-P). Based on the given radiation-induced compaction in literature, we have shown through our modeling work how these sensors behave at high levels of gamma dose. Since this work has been carried out in collaboration with Idaho National Laboratory (INL), USA, we tested regenerated FBGs in the ATR at INL in high radiation and high temperature ( $\sim 800^{\circ}\text{C}$ ) fields. The RIA and the RIC of these sensors have been investigated to understand their effects on the signal drift. We have found that high temperature significantly counteracts the radiation effects. The macroscopic changes in FBGs caused by radiation have been calculated using well established numerical equations. Then, the values of macroscopic changes have been inserted into our modeled FBG to observe the radiation-induced signal drift. It has been observed that the signal drift in FBGs obtained by experiment is different from that of the modeled FBG. It is because in modeling work only compaction-induced RI and length changes obtained by numerical equations have been used. However, RI and length may change due to RIA, stress relaxation, compositional exchange, dose, dose rate, etc. To predict the correct signal drift, it is necessary to consider the RI and the length change caused by the specific phenomena to

which the fiber is subjected, including RIC, RIA, dopant diffusion, temperatures, dose, and dose rate, etc. An on-line measurement of the radiation-induced RI and length changes can be a potential way for understanding the structural changes of optical fiber and measuring the signal drift in fiber sensors in a nuclear environment. With an aim to achieve this, we have introduced an effective technique which will provide real-time variation of RI and length of fiber in a radiation environment no matter what (RIA, RIC, temperature, dopant diffusion, stress relaxation, or any combination of them) causes it.

We have also focused on fission gas sensing using simple optical fiber sensors so as to understand the implications of fission gas release during an accident, important for safe, high performance.

We have organized this dissertation as follows: Chapter 1 discusses the silica based optical fiber, its structure, and different types of fiber optic sensors. Chapter 2 reports on background on radiation effects on optical fiber and fiber optic sensors. Chapter 3 thoroughly discusses about the novel metal coating method and the applications of reflection mode LPGs. Chapter 4 reports radiation effects on fiber optic sensors both numerically and experimentally. Chapter 5 discusses a technique for real-time measurement RI and length change. Chapter 6 presents the fission gas sensing based on fiber optic sensors. Chapter 7 presents some future perspectives. Chapter 8 presents the conclusion of this dissertation.

## LIST OF PUBLICATIONS

### Submitted Manuscripts

1. **S. Rana**, A. Fleming, N. Kandadai, H. Subbaraman, “Regenerated type I fiber Bragg grating exposed to high temperature and high neutron fluence” *Optics Express* (will be submitted)
2. **S. Rana**, A. Fleming, N. Kandadai, H. Subbaraman, “Differently structured Fabry-Perot interferometers for gas pressure sensing” *IEEE Sensors Journal* (under review)

### US Patents

1. H. Subbaraman, **S. Rana**, N. Kandadai, “Reflective long period grating,” U.S. Patent 11280642, March 22, 2022.

### Journals

1. **S. Rana**, A. Fleming, H. Subbaraman, N. Kandadai, “Real-time measurement of parametric influences on the refractive index and length changes in silica optical fibers” *Opt. Express*, vol. 30, no. 9, pp. 15659-15668, 2022.
2. **S. Rana**, N. Kandadai, H. Subbaraman, “Experimental validation of a true reflective long period grating design methodology” *Results in Optics*, vol. 7, 2022.
3. **S. Rana**, A. Fleming, N. Kandadai, H. Subbaraman, “Active compensation of radiation effects on optical fibers for sensing applications”, *Sensors*, vol. 21, no. 24, 2021.

4. **S. Rana**, H. Subbaraman, A. Fleming, N. Kandadai, “Numerical analysis of radiation effects on fiber optic sensors,” *Sensors*, vol. 21, no. 12, 2021.
5. **S. Rana**, N. Kandadai, H. Subbaraman, “Towards the Design of a Wideband Reflective Long Period Grating Distributed Sensor,” *J. Phys. Commun.*, vol. 4, no. 6, 2020.
6. M. A. Mollah, **S. Rana**, H. Subbaraman, “Polarization filter realization using low-loss hollow-core anti-resonant fiber in THz regime,” *Results in Physics*, vol. 17, 2020.
7. B. Wilson, **S. Rana**, H. Subbaraman, N. Kandadai, T. Blue, “Modeling of the Creation of an Internal Cladding in Sapphire Optical Fiber Using the  $6\text{Li}(n,\alpha)3\text{H}$  Reaction,” *J. Lightw. Technol.*, vol. 36, no. 23, pp. 5381-5387, 2018.
8. **S. Rana**, N. Kandadai, H. Subbaraman, “A Highly Sensitive, Polarization Maintaining Photonic Crystal Fiber Sensor Operating in the THz Regime,” *Photonics*, vol. 5, no. 4, pp. 1-9, 2018.
9. **S. Rana**, A. S. Rakin, M. R. Hasan, M. S. Reza, R. Leonhardt, D. Abbott, H. Subbaraman, “Low loss and flat dispersion Kagome photonic crystal fiber in the terahertz regime,” *Opt. Commun.*, vol., 410, Nov. 2017.
10. M. R. Islam, S. Akter, A. A. Rifat, **S. Rana**, K. Ahamed, R. Ahmed, H. Subbaraman, D. Abbott, “Spiral photonic crystal fiber based dual-polarized surface Plasmon resonance biosensor” *IEEE Sens. J.*, vol., no. 99, Nov. 2017.
11. **S. Rana**, A. S. Rakin, H. Subbaraman, R. Leonhardt, D. Abbott, “Low loss and low dispersion fiber for transmission applications in the terahertz regime,” *IEEE Photon. Technol. Lett.*, vol. 29, no. 10, pp. 830-833, May 2017.

## **Conferences/Presentations**

1. **S. Rana**, N. Kandadai, H. Subbaraman, “Reflective long period grating based refractive index sensor,” *In 2021 IEEE Photonics Conference (IPC)*, 2021.
2. **S. Rana**, N. Kandadai, H. Subbaraman, “Reflective long period grating based temperature sensors,” in *Optical Components and Materials XVIII*, Mar. 2021, vol. 11682, p. 1168219.
3. **S. Rana**, H. Subbaraman, N. Kandadai, “A simple and cost-effective metal coating method for reflective long period grating sensors,” in *Infrared Sensors, Devices, and Applications X*, Aug. 2020, vol. 11503, p. 115030K
4. **S. Rana**, H. Subbaraman, N. Kandadai, “Role of Metal Coating Parameters on the Reflective Long Period Grating Spectrum,” *OSA Optical Sensor and Sensing Congress (ES, FTS, HISE sensors)* p. EThA.5. 2019.
5. **S. Rana**, B. Badamchi, B. Joshi, H. Subbaraman, N, Kandadai, “Towards Time Stable Fiber Optic Sensors for Harsh Environment,” *NPIC&HMIT*, 2019, Florida, USA



## CHAPTER ONE: OPTICAL FIBER AND FIBER OPTIC SENSORS

It is necessary to deal with the optical fibers and fiber optic sensors before introducing the radiation effects on them. This chapter discusses a general description of optical fibers and some of their optical properties. This section also covers the building block of silica fiber and some of the most important parameters of optical fibers, and fiber optic sensors.

### 1.1 Optical Fiber

Optical fiber is a cylindrical dielectric waveguide that transmits light at the expense of very low loss at a large distance. The optical fiber works on principles similar to other waveguides with the important inclusion of cylindrical axis of symmetry. Generally, optical fibers most commonly use silica (silicon dioxide:  $\alpha$ -SiO<sub>2</sub>) either in pure form or with some dopants. Silica is chosen for its extremely low propagation loss and amazing mechanical strength against pulling and bending. A polymer coating is applied over the optical fiber to protect the fibers as glass is very fragile.

Optical fiber consists of a core and a cladding to guide light. The core has a refractive index (RI) slightly higher than the radially surrounded cladding. The diameter of the core can vary from 5-10  $\mu\text{m}$  for single mode fiber and 50-200  $\mu\text{m}$  for multimode fiber whereas cladding is of 125  $\mu\text{m}$  for most of the cases. A schematic of optical fiber is shown in Fig. 1.1. The RI (measures the degree of light slow down when going from vacuum

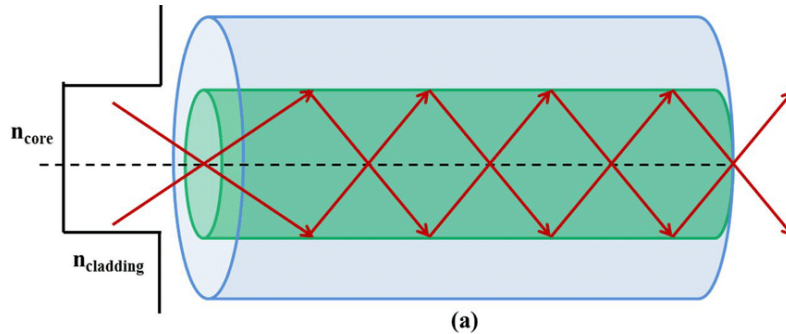


**Figure 1.1 Optical fiber schematic[1]**

to any other media) profile of an optical fiber can have step index or graded index depending on the application[2]. Whereas the RI in a step index fiber changes sharply from core to cladding, it is a radial change of RI in a graded index fiber[2]. The light guides in an optical fiber on the mechanism of either modified total internal reflection (MTIR) or photonic bandgap (PBG). Please note that we discuss the MTIR mechanism in a step index fiber throughout the report unless otherwise stated. For a step index fiber, the core has a slightly higher RI than that of the cladding. As a result, light follows the total internal reflection at the core/cladding interface.

### 1.1.1 Important Parameters of Optical Fiber

**Numerical aperture (NA):** It is an important parameter that defines the light gathering capacity of an optical fiber and it depends on the refractive indices of core and cladding and can be expressed as[2]

$$NA = \sqrt{n_{core}^2 - n_{clad}^2} \quad (1.1)$$

where  $n_{core}$  and  $n_{clad}$  are the refractive indices of the core and the cladding respectively.

**Modes of optical fiber:** Depending on the number of modes propagating through the core, the fiber can be divided into two types:

- *Single mode (SM) fiber*: If only the fundamental mode is guided in the core. The diameter of SM fiber is of about 8-12  $\mu\text{m}$  for fiber operating in the infrared (IR) range.
- *Multi-mode (MM) fiber*: if more than one mode propagates in the core. This type of fiber has a core diameter of about 50-200  $\mu\text{m}$ .

The schematic of a SM and a MM fiber is shown in Fig. 1.2. It is seen from the figure that the core of the SM fiber is too small to support only one mode whereas for MM fiber, it supports a number of modes.

**V-number**: It is an important parameter that determines the single mode nature of an optical fiber. It is also commonly used as normalized frequency. Many fiber parameters can be expressed in terms of V-number like number of modes, cutoff condition of fiber etc.

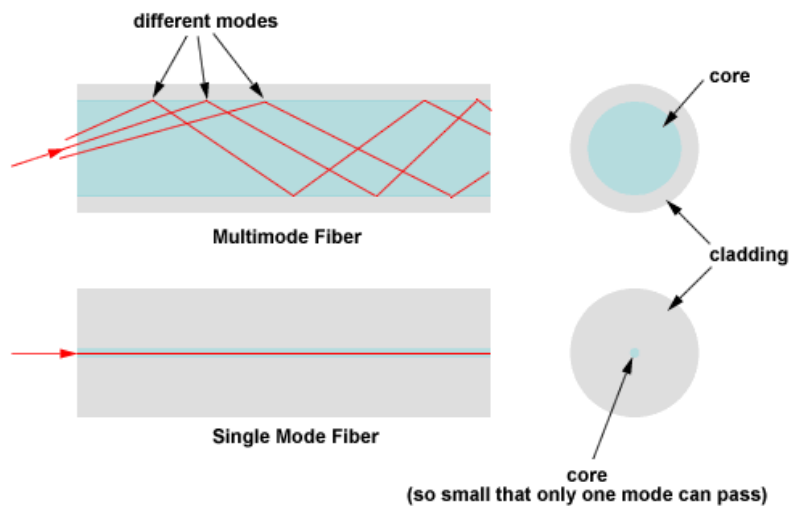


**Figure 1.2 Schematic of single mode and multi-mode fiber[3]**

Mathematically, V-number can be represented by the following expression

$$V = \frac{2\pi r_{core}}{\lambda} \sqrt{n_{core}^2 - n_{clad}^2} \quad (1.2)$$

where  $r_{core}$  is core radius. A step index fiber becomes single mode for a given wavelength when  $V \leq 2.405$ .

**Cutoff wavelength:** An optical fiber supports only one mode for specific wavelengths longer than a value known as cutoff wavelength[2]

$$\lambda_{cutoff} = \frac{2\pi r_{core}}{V} NA \quad (1.3)$$

**Fiber modes:** Modes are the solution of electromagnetic wave equations. Since light follows the MTIR at the core/cladding boundary in order to propagate through the core, the geometry and the compositions determine the modes in the optical fiber. There are primarily two different types of modes that exist in an optical fiber. One is radiation mode, in which light energy propagates out of the core. Another one is the guided mode, in which light energy is confined into the core and propagates along the fiber.

**Mode field diameter:** In a SM fiber, a fair amount of light is contained in the cladding outside of the core, which means that the mode field diameter of the fundamental mode is larger than the core of the fiber. Typically, mode field diameter is defined as the radial position where light falls  $e^{-2}$  of the peak intensity.

**Attenuation:** One of the attractive features of optical fibers is the low loss in the near infrared (NIR) region of wavelength. Loss in an optical fiber is the reduction of optical power as light propagates through the fiber. It is defined as the ratio of optical output power ( $P_{out}$ ) from a fiber length of  $L$  to the optical input power ( $P_{in}$ ) with a unit of dB/km and is expressed as

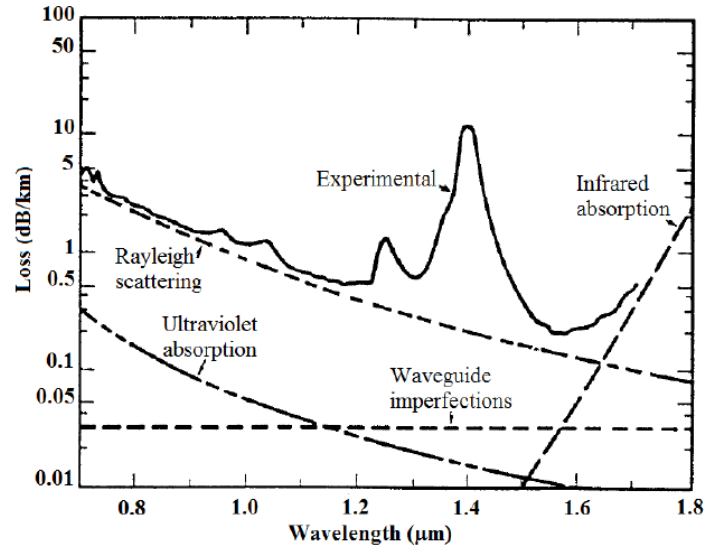


**Figure 1.3 Loss spectrum of a silica based optical fiber[4]**

$$\alpha(dB/km) = \frac{1}{L} \frac{P_{out}}{P_{in}} \quad (1.3)$$

A typical attenuation spectrum of silica optical fiber is shown in Fig. 1.3. There are different mechanisms that induce attenuation in an optical fiber and some of them are discussed below[5].

- *Scattering loss*: Macroscopic variations in the RI due to the inhomogeneous density causes this type of loss. Scattering loss depends on the wavelength of light.
- *Absorption loss*: It is due to the material compositions and vibration modes of the molecules.
- *Bending loss*: It is due to the bending of fiber. When a fiber undergoes a bend with a radius larger than the fiber diameter, it causes a macrobending loss. On the other hand, a bend of the fiber axis due to the drawing fabrication step causes microbending loss.

**Dispersion:** Dispersion is another key phenomenon that broadens the propagating signal through optical fiber for a long distance. It describes the process of how an input

signal broadens/spreads out as it propagates/travels down the fiber. Dispersion mainly occurs due to the dependence of phase velocity of light on the wavelength. There are different types of dispersion that limit the propagation of signal over a long distance.

- *Chromatic dispersion*: It is a phenomenon which spreads the signal over time resulting from the different speeds of light. Chromatic dispersion is the combination of both material and waveguide dispersion. In material dispersion, the signal broadens due to the RI dependence on the wavelength. Waveguide dispersion occurs due to dependence of the mode propagation constant on the fiber parameters (core radius, and core-cladding RI difference) and light wavelength. These two effects in a proper condition can cancel each other out giving a wavelength with approximately zero chromatic dispersion.
- *Modal dispersion*: It occurs mainly in a multimode fiber where different modes propagate at different speeds of light. It is known that different incidence angles create different modes or path of light to propagate. Some of the modes propagate in straight while others follow a zigzag path. As a result, these modes reach at different times and broaden the signal. Figure 1.4 shows the typical dispersion in an optical fiber.
- *Polarization mode dispersion*: It represents the polarization dependence of the propagation characteristics of light waves in optical fibers. There always exists a slight difference in two orthogonal polarizations of light in optical fibers. When light propagates inside a fiber, these two orthogonal modes continuously exchange

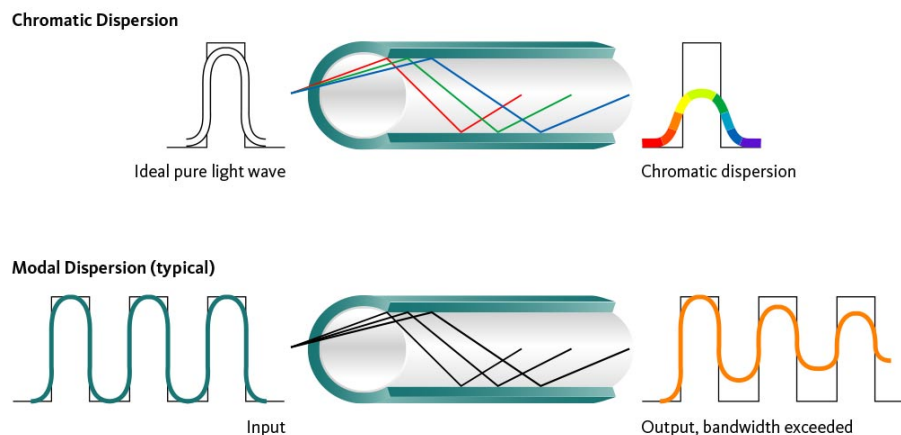


**Figure 1.4 Dispersion in optical fiber[6]**

light energies between them. The moment the energy inside these two modes transfers at different speeds in a fiber, polarization mode dispersion occurs.

## 1.2 Building Block of Silica ( $\text{SiO}_2$ ) Structure

The building block of silica based optical fiber is a continuous random network of  $\text{SiO}_4$  tetrahedra joined by bridging oxygen atoms[7]. The  $\text{SiO}_4$  tetrahedra unit consists of a silicon atom surrounded by four oxygen atoms with the Si-O bond length of 1.62 Å and the O-Si-O angle of  $109.5^\circ$  as for the quartz that is its crystalline form[8]. The disorder of the glass state generally arises from the Si-O-Si angle which varies between  $120^\circ$  and  $180^\circ$  with a maximum value of  $144^\circ$ - $150^\circ$ . The silica structure is constituted by (Si-O) $k$  rings where  $k$  is distributed between 3 and 10, with most of the rings having 6-7 size[8]. It has been reported that the 3-rings are planar with Si-O-Si angle of  $130.5^\circ$  and strained Si-O bonds. On the other hand, the 4-rings cannot be planar but slightly folded up with Si-O-Si angle of  $160.5^\circ$ [9], [10].

### 1.3 Optical Fiber Sensors

Over the last decade, there has been a significant development of optical fiber sensors (OFS) performing in the telecommunication ranges 1.31  $\mu\text{m}$  and 1.55  $\mu\text{m}$  due to its enormous applications in many fields such as biomedical analysis, chemical industries and environment monitoring[11]–[14]. They have been developed to work on a wide variety of physical properties like temperature, chemical changes, electric and magnetic fields, vibrations, strain, displacement (position), flow, pressure, rotation, radiation, liquid level, and light intensity. In harsh environments, OFS proves reliable and are rigid sensing devices over their counterpart electrical sensors. Optical fiber sensors have the advantages over electrically based sensors which includes immunity to electromagnetic interference, remote sensing capability, low loss, small size and light weight[15]. Moreover, sensors based on optical fiber technology do not need any electrical input at the sensing point and related to its isolation. This technology offers quick response and can be easily multiplexed. Several thermocouples can be replaced by a single fiber to measure temperature which thus reduces the waste material.

The basic building block of an OFS system is shown in Fig.1.5 which mainly consists of optical source (LED, laser, laser diode etc), optical fiber (single-mode or multimode), sensing or modulation (intensity, phase, polarization etc), and receiver

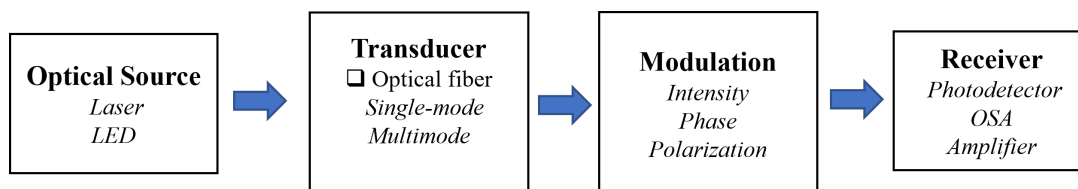


**Figure 1.5** General structure of optical fiber sensor.

(photodetector, amplifier, optical spectrum analyzer (OSA)). Based on the sensing region in optical fiber, OFSs can be categorized into the following types.

### 1.3.1 Grating Based Sensors

Intensive study on fiber gratings began after the introduction of effective and advanced fabrication methods in 1989[16]. Fiber gratings have found applications in add/drop filters, amplifier gain flattening filters, fiber lasers, dispersion compensators and so on for optical communication[17]. Following these, significant research has been performed on sensors based on fiber gratings, some of which are now available commercially. Based on the grating period, fiber gratings sensors are two types: fiber Bragg grating (FBG) or small period grating and long period grating (LPG). The grating period of FBG is generally less than 1  $\mu\text{m}$  whereas for LPG it is between 100-1000  $\mu\text{m}$ . These two types of grating based sensors are discussed in the subsequent subsections.

#### 1.3.1.1 Fiber Bragg Grating

Among fiber optic sensors, FBG is the most mature and commonly used sensor. FBG is a periodic RI modulation in the optical fiber core. Most commonly, FBG is created by periodically altering the core RI, but another type of manufacturing method, physically deforms the fiber to create the required optical modulation[18]. However, the most common and popular technique to write the grating is by UV-irradiation. Besides the illumination of the fiber by UV light, there are several ways to manufacture FBGs by altering the RI. These include the followings: irradiation from a carbon-dioxide laser, radiation with femtosecond pulses, writing by electric discharge, ion implantation, and dopant diffusion into the fiber core[18], [19]. Recently, femtosecond (fs) laser-etched FBG

sensors have shown outstanding performance in a harsh environment like material testing reactor (MTR)[20].

In an FBG, the fundamental guided mode couples to a counterpropagating guided mode if the following phase-matching condition is satisfied[18]

$$\lambda_B = 2n_{eff}\Lambda_{FBG} \quad (1.4)$$

where  $\lambda_B$  is the Bragg wavelength,  $n_{eff}$  is the effective RI of the core and  $\Lambda_{FBG}$  is the grating period (distance between two adjacent high and low RI). This  $\lambda_B$  is very sensitive to any external changes in physical parameters. FBG based sensors have been applied to monitor temperature[21], [22], pressure[23], strain[22], displacement[24], humidity[25], acceleration[26], high magnetic field[27], force[28], and acoustic[29]. Recently, FBGs have been applied in nuclear environments to monitor different parameters[30]–[32].

### 1.3.1.2 Long Period Grating

LPG is similar to FBG but has a larger grating period (100-1000  $\mu\text{m}$ ) compared to FBG's period (0.1-1  $\mu\text{m}$ ). As a result, light coupling occurs between the fundamental core mode and numbers of co-propagating cladding modes, and therefore the transmission spectrum shows a number of discrete attenuation bands depending on the phase-matching condition[33], [34]. The wavelength at which light coupling takes place in an LPG is called the resonance wavelength and it is given by[34]

$$\lambda_R = (n_{eff,co} - n_{eff,cl}^m)\Lambda_{LPG} \quad (1.5)$$

where  $\lambda_R$  is the resonance wavelength,  $n_{eff,co}$  is the effective RI of the guided core mode, and  $n_{eff,cl}^m$  is the effective RI of the mth order cladding mode. The resonance wavelengths are dependent on the grating period and the refractive indices of the fiber core and the

cladding. A small change of physical parameters can cause a large shift of resonance wavelength, and therefore increase the sensitivity of LPG based sensors. The simultaneous multi-parameter sensing capabilities of LPG have found a plethora of applications over FBGs[35]–[39]. Owing to their high sensitivity, LPG sensors were also tested against radiation[35], [40], [41]. However, for being in transmission mode in nature, LPGs are not suitable candidate in nuclear environment.

### 1.3.2 Distributed Sensors

Distributed optical sensors enable continuous, real-time measurements of different physical parameters along the entire length of the optical fiber. The basic principle of a distributed optical fiber sensor is optical time domain reflectometry (OTDR) which was first introduced to monitor signal attenuation[42]. The beauty of optical fiber sensors are the distributed sensing capabilities over other sensor technologies. Distributed sensors provide a wealth of information along the length of the fiber with reduced cost. Based on the optical medium interaction with light, distributed sensing can be classified into three types:

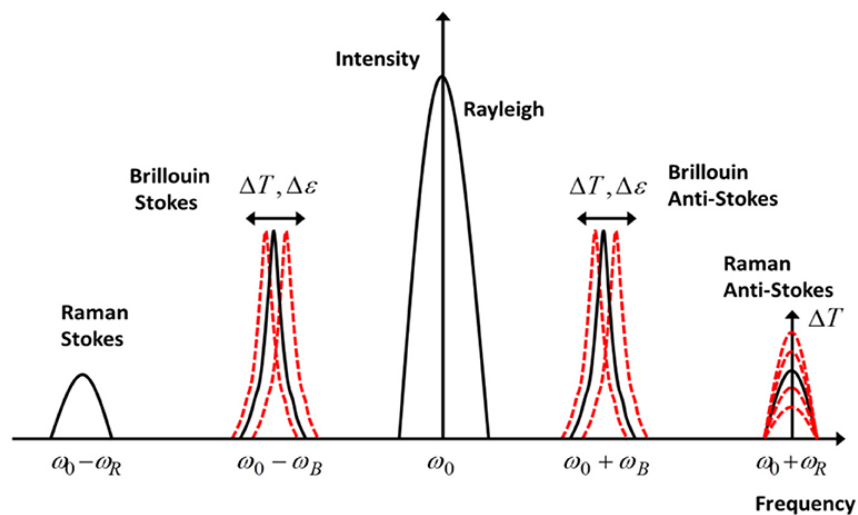


Figure 1.6 Basic scattering mechanism of light in an optical fiber[43].

(1) Rayleigh scattering, (2) Brillouin scattering, and (3) Raman scattering. A brief description of these scattering is given below. A basic light scattering phenomenon is shown in Fig. 1.6.

#### 1.3.2.1 Rayleigh Scattering Based Distributed Sensing

Among the light scattering phenomenon, Rayleigh scattering is the elastic scattering caused by the random variation of the optical medium. The variation of the medium occurs maybe due to the change in density or dopants concentration. Rayleigh scattering is also the strongest scattering the occurs in a fiber. External parameters like temperature strain, pressure, radiation etc. alter the scattered amplitude of Rayleigh scattering. By knowing the scattered amplitude at a reference point, it is possible to extract the external parameters that cause the change in amplitude.

Although different effective techniques exist, the most common and reliable method to collect the Rayleigh backscattering signal is OTDR. In an OTDR, a narrow pulse signal is transmitted through the fiber and a back scattered signal is received at the same end as a function of position along the optical fiber length. Since the light velocity and the propagation time are known, it is easy to calculate the distance based on  $Distance = velocity \times time$ . A Rayleigh sensor is commonly used for temperature monitoring[44], [45]. However, nowadays it has been applied to nuclear environments also[46].

#### 1.3.2.2 Brillouin Scattering Based Distributed Sensing

Brillouin scattering is an inelastic scattering in which the wavelength of incident light is modified by the energy levels of sound waves or phonons. Photons scattered to higher frequencies are termed anti-stokes components and those scattered to lower frequencies are called stokes components. In optical fibers, Brillouin scattering occurs

essentially only in backward direction. However, rather weak forward Brillouin scattering is also possible due to effects of the acoustic waveguide. As a result, the frequency of the scattered light is slightly less than the incident one. The Brillouin scattering can be spontaneous or stimulated depending on the fluctuation of density of the optical fiber. If the amount of light scattered by the thermal fluctuation is small enough to initiate further change in density, then spontaneous scattering happens. However, when the incident light interacts with the counter-propagating wave in order to create a beat pattern that causes the periodic fluctuation of density to generate an acoustic wave. The frequency difference between the incident and the counter-propagating is called the Brillouin shift. This Brillouin shift depends on the composition of the fiber and the external parameters. Distributed sensors based on Brillouin scattering have found potential applications in temperature[47], and pressure[48], and also structural health monitoring[49] sensing. Like other fiber optic sensors, Brillouin distributed sensors have been applied in radiation environments[50].

### 1.3.2.3 Raman Scattering Based Distributed Sensing

Raman scattering is also an inelastic scattering which is caused by thermally induced molecular vibration of glass fiber. Like Brillouin scattering, it is characterized by a frequency shift of scattered light. The frequency shift is adequate with the characteristic vibration frequencies of the molecules. Among the frequencies shifted intensity, only the intensity of an anti-Stokes frequency component is an indicator of temperature environment. So, by calculating the ratio between anti-Stokes and Stokes component intensity, temperature information at the scattering point can be extracted. OTDR is used to map location information in Raman scattering. But the low Raman scattering coefficient,

which is about three orders of magnitude weaker than that of Rayleigh scattering, low signal to noise ratio (SNR), makes the interrogation process complicated. Raman distributed sensors have been widely used to monitor different physical parameters such as temperature[51], strain[52], and displacement[53]. Sensors based on Raman scattering were also reported in nuclear environments to monitor temperature[54].

### 1.3.3 Single Point Sensors

In a single point sensor, a small portion of optical fiber works as a sensing element. Single point sensors are generally applied when the interested parameters are at only one location, or several point sensors are not possible to install. These sensors are drawing attention due to their small size and strong immunity against harsh environments. In a single point sensor, the sensor head is utilized to monitor the external measurands. A very common example of a point sensor is Fabry-Perot. Point sensors have found applications almost everywhere to monitor external parameters such as temperature[55], pressure[56], strain[57], humidity[58], and chemicals[59]. Besides these applications, single point sensors based on Fabry-Perot have been widely used in nuclear environments for monitoring high temperature[31] and displacement[60], [61].

In summary of this chapter, optical fibers are showing growing interest among the technologies due to their unique characteristics. OFS made from optical fibers are being deployed in almost everywhere due to their unique characteristics. In recent years, OFSs have turned into a potential candidate in nuclear environments for monitoring high temperatures, thanks to their high melting point and radiation hardness.

## CHAPTER TWO: RADIATION EFFECTS ON OPTICAL FIBER TECHNOLOGY

Various types of materials are considered and being used for nuclear fuel, cladding and structures for advanced nuclear reactors. However, these materials undergo significant changes during the irradiation cycle. In-pile detection of fuel, clad, and structures are needed to understand the real-time behavior during irradiation testing of fuels and materials in MTRs. As an alternative to existing instruments, such as linear variable differential transducers (LVDT) and electrical sensors, optical fiber technology has been deemed a competitive candidate in monitoring physical parameters within nuclear environments. Like all other materials, silica based optical fiber alters its optical, mechanical, and chemical properties under intense radiation. It is necessary to understand the radiation effects on optical fiber and OFS for the deployment and sensing various parameters using them. This chapter discusses the effects of radiation on optical fibers and OFS.

### **2.1 Types of Radiation**

Radiation is a process by which energy is emitted as either waves or particles. Generally, radiation is classified as ionizing and non-ionizing. If the energy of incoming radiation is enough to knock off atoms, then it is called non-ionizing radiation. The example of non-ionizing radiation includes neutrons,  $\text{He}^+$ ,  $\text{D}^+$ , etc.[62]. On the other hand, if the incoming radiation is able to cause damage to the host material it interacts with by breaking chemical bonds is called ionizing radiation such as gamma rays, X-rays, UV rays, etc.[62]–[69] are the common ionizing radiation. When ionizing radiation interacts with silica optical fiber, it deposits sufficient amounts of energy on the silica and as a result, it

induces color centers in the host fiber material. These color center induced defects have absorption bands in the transmission window of electromagnetic waves. These changes may involve the breaking of basic building blocks of the silica glass structures and producing new bonds. Radiation can also produce ions or radicals that do not further react to form formal bonds but are partially stabilized by bypassing excess energy to the nearby atoms. When ionizing radiation induces electron-hole pairs, the free charges move to the low-energy defects centers or traps within the silica glass matrix. The stability of these defect centers or traps depends on the nature of the defects or the lifetime of the trap's holes or electrons. At room temperature, these defects or traps may exist for a long time. Unlike ionizing irradiation, particle irradiation or non-ionizing radiation displaces the host atoms in the silica glass matrix and varies the local density or volume.

## **2.2 Radiation Induced Defects in Silica**

There are various factors which create different types of defects in silica glass matrix which includes the presence of impurities or dopants in glass, radiation, temperatures, and the fiber drawing process. The defects provide rise to electronic states within the bandgap, and therefore increases the absorption bands in the ultraviolet (UV) and visible (VIS) part of the spectrum and the tail extends into the IR regime. Irradiating silica networks produces ionization and correlated radiolytic processes. These lead to the emission of photons or forces atomic displacement in silica structure which causes point defects in  $\text{SiO}_2$ . The nature of defects in  $\text{SiO}_2$  can be affected by external parameters, such as fabrication process, nature of irradiation, stress, change of temperature, impurities in silica network (H, Ge, P, etc), and by intrinsic parameters of optical fibers, such as core, cladding or specific dopants. The defects add new energy bands in the dielectric, which

change the absorption spectrum of the fiber. The defects affecting the optical spectrum can be divided into Frenkel defects and Dangling bonds (silicon dangling bond or the "generic" E'-center)[70]. The optical absorption (OA) and luminescence bands caused by both of these defect types are detected by OA, and Raman or photoluminescence (PL) spectroscopies across different optical wavelength bands. Electron paramagnetic resonance spectroscopy (EPR) is utilized to identify molecular-scale structures of paramagnetic defects possessing an unpaired electron. Frenkel defects and dangling bonds are discussed in greater detail in the following subsections. Please note that symbols ( $\equiv$ ) and ( $=$ ) denote the bonds of a Si with three and two oxygen atoms respectively and ( $\cdot$ ) and ( $\cdot\cdot$ ) indicate an unpaired

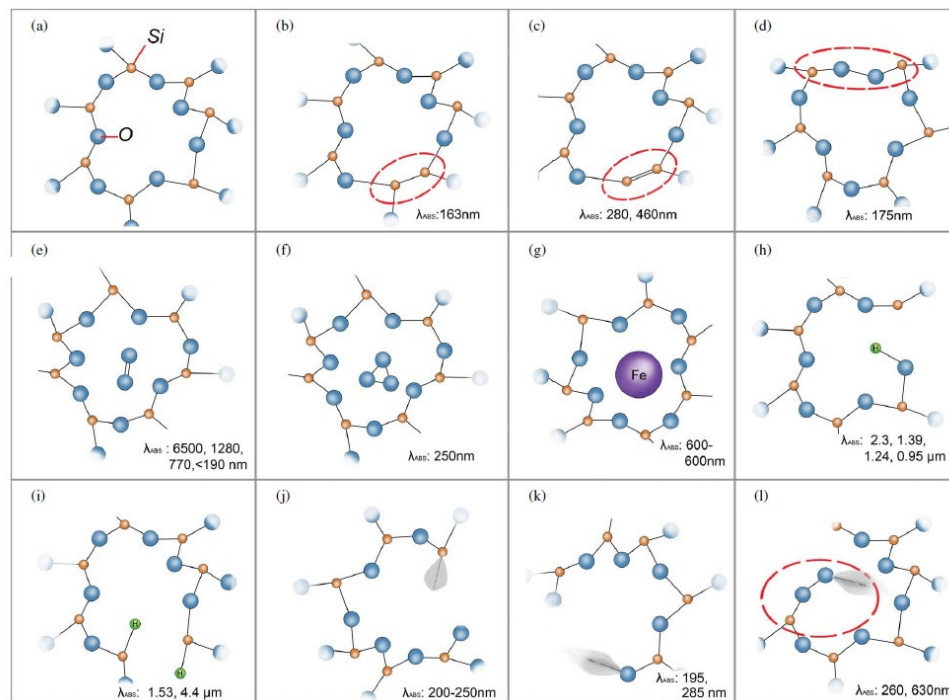


**Figure 2.1 Intrinsic point defects in silica glass structure[71]. (a) No defects. (b) ODC(I). (c) ODC(II). (d) Peroxy linkage. (e) Interstitial O<sub>2</sub>. (f) Interstitial O<sub>3</sub>. (g) Transition metals. (h) Hydroxyl ions. (i) Silicon hydride. (j) E'-centre. (k) NBOHC. (l) Peroxy radical.**

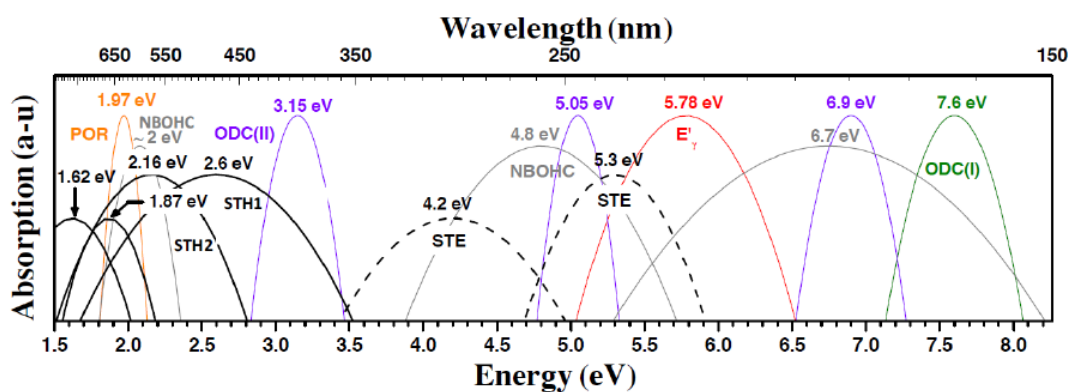


**Figure 2.2.** The attenuation band of Si-related defects[72].

electron and two paired electrons in the same orbital, respectively. The most common types of intrinsic defects and optical attenuation bands of the Si-related defects are shown in Figs. 2.1 and 2.2, respectively.

### 2.2.1 Frenkel Defects

Frenkel defect is a type of defect wherein an atom is displaced from its position in a lattice to an interstitial site, creating a vacancy. In silica, there are four types of Frenkel defects: (1) neutral oxygen vacancy, (2) interstitial oxygen molecules, (3) peroxy linkages and (4) interstitial ozone molecules, which are discussed below.

*Neutral oxygen vacancy ("Si-Si bond")*: Neutral oxygen vacancy is created in silica glass and  $\alpha$ -quartz when irradiated under gamma radiation with a dose greater than 1 MGy. It is diamagnetic and has a characteristic absorption spectrum at 7.6 eV[73]. This defect is also created by ArF or F<sub>2</sub> excimer laser interaction with fibers having interstitial H<sub>2</sub>. There is ongoing research focused on trying to find the relationship between neutral oxygen vacancy and divalent silicon centers in silica, understanding the process of charge trapping in oxygen vacancy, and conversion of silica structure to paramagnetic trapped hole E'-centers.

*Interstitial oxygen molecule  $O_2$* : Interstitial oxygen molecules occur in fibers drawn in oxygen-rich (concentration  $>10^{17} \text{ cm}^3$ ) environments. They are also created when fibers are irradiated at high temperatures or through the diffusion of oxygen in silica[74]. Oxygen embedded in  $\text{SiO}_2$  up to a concentration of  $10^{14} \text{ cm}^3$ [75] is detected by laser excitation at 765 nm wavelength. The excitation leads to a Raman band at  $1549 \text{ cm}^{-1}$ [76] and a very narrow band photoluminescence at 1272 nm at room temperature.

*Interstitial Oxygen or peroxy linkage (POL)  $\equiv \text{Si-O-O-Si}$* : Some of the oxygen in oxygen-excess silica forms an incorrect oxygen-oxygen band called peroxy linkages ( $\equiv \text{Si-O-O-Si}$ , POL). Excimer  $\text{F}_2$  laser (7.9 eV), creates this defect in the process of photolysis of super stoichiometric interstitial  $\text{O}_2$  molecules in oxygen-rich silica fiber[77]. The transition energy is insensitive to glassy disorder because of O-O interaction [76]. Also, POL has the lowest energy configuration among all oxygen interstitial defects[78]. The energy of the POL absorption band is around 6.4-6.8 eV with a small oscillator strength, 200 Hz frequency, and such absorption would be hard to detect against the background of other bands in deep UV[73].

*Interstitial ozone molecule ( $\text{O}_3$ )*: This defect is typically created in irradiated oxygen-rich silica fiber. The characteristic absorption peak of this defect is around 258 nm wavelength (4.8 eV)[79], [80]. However, other researchers have shown that this absorption is caused by non-bridging oxygen hole centers (NBOHC) (will be discussed later) making it difficult to predict the existence of this defect[81]. The 4.8 eV absorption band of ozone molecules can be distinguished from that of NBOHCs by full-width-half-maximum (FWHM)[79].

### 2.2.2 Dangling Defects

Dangling bonds are created due to the absence of atoms that terminate the dissociated bonds, resulting in unpaired electrons in an atom in a molecular network.

The dangling bonds are divided into the following categories:

*Oxygen deficient centers (ODC)*: Neutral ODC is created by relaxing the silica structure upon removing bridging oxygen. Several researchers created the models for ODCs. ODC is diamagnetic and is detected using photoluminescence (PL) or cathode luminescence (CL) spectroscopy[82]. There are two types of ODCs: neutral oxygen vacancy ODC (I) and two-fold coordinated silicon ODC (II). Arnold in[83] reported the first model hypothesis for ODC (II) as a neutral diamagnetic oxygen vacancy. Neutral oxygen vacancy ODC (I) consists of a bond between two Si atoms without an oxygen bond. It represents one of the most common defects in silica fibers in the form of simple bridging oxygen vacancies. Two Si atoms could either relax and create a stable silicon-silicon bond (relaxed oxygen vacancy) or create an unrelaxed silicon bond (unrelaxed oxygen vacancy). Under some undeclared condition, each one of them can be a precursor for the other. It has a strong optical absorption bands around 7.6 eV[82]–[84]. In a thermal reaction, ODC(I) is converted to =Si-H with hydrogen molecules. Oxidation is used to remove this defect. Imai et al. created a model for unrelaxed oxygen for ODC (I). Two-fold coordinated silicon ODC (II) consists of Si coordinated with two O atoms =Si••. ODC (II) is a diamagnetic center that has weak optical absorption band, called B<sub>2</sub> band, with a peak at 5.03 eV with two emission bands peaked at 4.4 eV and 2.7 eV. This defect is created under MGy doses of gamma irradiation, neutron knock-on of bridging oxygen atoms, or in oxygen-deficient fabrication conditions. During the growth process, the

concentration of ODC (II) depends upon the oxygen deficiency conditions. Skuja et al. determined the two-fold coordinated silicon models for ODC (II)[84].

*Silicon dangling bond or the "generic" E'-center:* Silicon dangling bond or the E'-center is one of the most studied defects in the silica network. E'-center defects were observed for the first time in 1956 by R. A. Weeks in neutron-irradiated  $\alpha$ -quartz (E'). It can be detected in silica using EPR spectroscopy [85]. The defect consists of a silicon-dangling bond with six paired electrons and one unpaired electron. The defect either can be a neutral defect or can be part of a positively charged oxygen vacancy in an even more complex defect. The complex defect could be either a trapped-hole center in neutral oxygen vacancies in pure-silica glass networks under high temperature or a trapped-electron center at a low temperature. Predominantly, it results from hole-trapped in neutral oxygen vacancies in pure silica network[86]. The hydroxyl radicals (OH) in the glass and irradiation energy are effective parameters that aid the formation of E' defects. E' defect concentration growth in optical fiber is influenced by drawing conditions of the fiber (temperature, tension, and speed)[87]. There are several atomistic types for E'-centers in amorphous silica due to different annealing kinetics which depend on the type of irradiation and water content. These types are detected by EPR are labeled with subscript  $\alpha, \beta, \gamma, \delta$  ( $E'\alpha, E'\beta, E'\gamma, E'\delta$ ) in bulk materials[88], [89]. The most common and extensively studied E'-center defect is  $E'\gamma$  in irradiated  $\text{SiO}_2$  which has absorption band at 5.8 eV ( $\sim 213.8$  nm) with FWHM=0.8 eV[90]. The existence of three E'-center ( $E'\alpha, E'\beta, E'\gamma$ ) is studied in two high-OH ( $\sim 100$  ppm) and low-OH ( $<5$  ppm) optical fiber under 100 keV X-rays at 77 K or  $^{60}\text{Co}$   $\gamma$ -rays ( $\sim 1$  MeV) near

300 K for wide range of annealing temperature[89]. In this study, E'-center induced by  $\gamma$ -rays bleaches at higher annealing temperature compare to E'-center induced by X-rays. It confirms the thermal instability of X-ray-induced centers independent of irradiation temperature between 77 and 300 K.

*Oxygen dangling oxygen bond:* The non-bridging oxygen hole center (NBOHC) defect consists of two oxygen atoms linked to silicon atoms, instead of the usual one oxygen atom. The silicon atoms are each linked to three oxygen atoms. This defect is created by breaking strained Si-O bonds or often by breaking network-bound hydroxyl groups[80]. NBOHC defect acts as a precursor of the ionizing-radiation-induced peroxy radical,  $\equiv\text{SiO-O}$ . Alternatively, the breaking of the O-O bond is possible weak[91], which can result in two non-bridging oxygen hole centers ( $\equiv\text{Si-O}\cdot$ ). The oxygen related defect is electrically neutral and paramagnetic in the silica network. Glass network with NBOHC defect subjected to different radiation doses changes its color due to the emergence of color centers. Griscom et al. found that irradiation of silica fiber with 1-1200 kGy leads to the creation of two absorption bands at 410 nm and 600 nm wavelength, changing the color of the glass to dark brown[92]. In[93], it is shown that the cross-section of absorption spectra increases as the dose is increased from 1 to 1200 kGy, and the sensitivity of the absorption peak at 600 nm is less than that at 410 nm wavelength. The absorption band of silicate glass under gamma irradiation is due to the creation of two NBOHC: HC1 at 410 nm and HC2 at 600 nm[92]. HC1 and HC2 are oxygen-dangling bonds associated with alkaline ions and formed in alkaline silicate glasses. The HC1 center is a hole trapped in the 2p orbital of one NBOHC. The HC2 center is a hole trapped in two or three

NBOHC[94]. They exist on silica surfaces and can be interconverted with surface E'-centers. Then emerging color center due to E'-center causes color changes in glass network under different radiation dose[72]. Low temperature (77 K) EPR, photoluminescence can detect NBOHC[95].

*Peroxy radicals (POR):* Peroxy radicals (POR) is depicted as  $\equiv\text{Si-O-O}\cdot$ . The POR is best characterized as an oxygen excess defect in silica[80], [96]. POR in silica is a paramagnetic defect that consists of a Si atom linked to a O<sub>2</sub> molecule with an unpaired electron that is delocalized over anti bonding  $\pi$ -type orbital of the O-O bond. This defect is formed by the reaction of interstitial O<sub>2</sub> with silicon dangling bond and is isolated by EPR measurement at low temperature (77 K)[97]. POR and NBOHC typically convert into each other by adding or removing oxygen atoms[98]. As a result, the closeness of the optical absorption band of POR and NBOHC parameters in silica creates complex changes in absorption spectra, such as "pseudo bands" due to the difference spectrum of two close Gaussians[70]. Furthermore, NBOHC, POR, and interstitial ozone molecule defects are responsible for the creation of a peak at 258 nm (4.8 eV) wavelength in UV range in any irradiated silica. Detection of POR and interstitial defects is difficult due to overlap with NBOHC band[99]. In other words, in this spectral range, attribution of an absorption band to POR is still challenging[70].

*Self-trapped hole center (STH):* Self-Trapped Hole Centers (STH) are generated by the combination of electronic excitation energy of electron-hole pairs and electron-phonon interactions in optical fibers[100]. Color center is one of the defects that is created by self-trapped carriers, where electrons or holes are trapped

at perfect sites in the glass network. Silica glass can be said to be free of defects if it comprises an ideal continuous random network of apex-connected  $\text{SiO}_4$  tetrahedral and is free of impurities, broken bonds, vacancies, or abnormal coordination numbers. Thus, self-trapping of carriers by small polaron formation can be seen in silica glass comprises an ideal continuous random network, free of impurities, broken bonds, and vacancies[101]. In high-OH silica, STH has never been identified because hydrogen atom released by radiolysis of OH groups reacts with STH to form ESR protons[102]. VIS to the IR part of the spectrum, low-OH/low-Cl pure silica fiber under lower dose ( $< 1$  MGy) irradiation show different absorption band peaks at a wavelength greater than 450 nm due to STH defects. Specific peaks include those at 2.6 eV, 2.16 eV, 1.88 eV and 1.62 eV[72]. Griscom[103] first identified STH by ESR studies and deduced the existence of two types of STHs:(1) STH1 [Self Trapped Hole Center (1)] where a hole is trapped on single bridging oxygen and is generally not considered to be a defect[103]. In this structure, two silicon atoms linked together with an oxygen atom bridge and each of these silicon atoms are linked to three other oxygen atoms. (2) STH2 [Self Trapped Hole Center (2)], where a delocalized hole (over two equivalent bridging oxygen of the same  $\text{SiO}_4$  tetrahedron) is trapped on two bridging oxygen species across a silicon atom to which both are bonded[101], [104]. STH is only stable at cryogenic temperatures[101]. This center occurs at low temperatures and anneals out at temperatures above 200 K[103]. Some variants of STHs are stable even at room temperature[101]. For example, in densified silica, the thermal stability of STHs is higher than that in normal silica[105].

*SiOH groups:* Hydroxyl Radical (OH) defect is when a silicon atom, bonded

to four oxygen atoms has a hydrogen attached to one of the oxygen atoms. Radiolysis can break the O-H bonds in high-OH fibers (high concentration of O-H bonds) when exposed to gamma irradiation. In these fibers, displaced oxygen atoms make water molecules, and a large concentration of H can passivate NBOHC and  $E'\gamma$ -centers causes in increasing the OH absorption. Therefore, hydroxyl defects exhibit OH vibrational resonance with various harmonics. The recombination rate of defect centers with hydrogen and/or water molecules increases with temperature. In high OH fibers, water peak has a strong harmonic or absorption band at 1385 nm. In contrast, in low-OH fibers, due to limited OH absorption, there is higher transmission in the infrared spectrum, but there is a potential to the form  $E'\gamma$  and NBOHC[106]. Thus, in commercial applications, "dry" fiber (low OH) is often preferred where an alkali ion may be present, which, after the generation of radiolytic charge carriers, dissociates and leads to the formation of NBOHC[107], [108].

### **2.3 Radiation Induced Mechanisms**

Neutron and gamma irradiation is known to compact silica, resulting in macroscopic changes in RI and geometric structure. The change in RI and linear compaction in a radiation environment is caused by three well-known mechanisms: (1) radiation induced attenuation (RIA), (2) radiation induced compaction (RIC), and (3) radiation induced emission (RIE). These three dominant mechanisms will be discussed in detail in the following subsections.

#### **2.3.1 Radiation Induced Attenuation**

RIA increases the linear attenuation in silica based fibers when fibers are exposed to radiation because radiation creates different types of defects which alter the absorption

band[72], [109]. RIA reduces the amplitude of the spectral response and is caused by radiation-induced defects in silica material, resulting in modification of the fiber absorption band. Different parameters govern the RIA levels and kinetics, which include chemical compositions of fibers[110], [111], manufacturing process[112]–[114], light guiding properties of fibers, the nature of irradiation (X-ray, gamma ray, neutron etc.)[115], the dose rate[115]–[117], wavelength of light being used[118], [119], injected light power[120], irradiation temperature [121], [122], etc. RIA leads to RI change through the Kramers-Kronig relation[123], [124]. The RIA contributed RI calculation using Kramers-Kronig relation is complex, and one needs to consider the spectrum in a wide frequency range. Although radiation exposure creates defects in silica ( $\alpha$ -SiO<sub>2</sub>) in the UV-VIS range, its tails extend into the IR region. While most of the previous research agrees that pure silica core (PSC) and fluorine doped fibers show high radiation resistant, loading of these fibers by suitable amount of H<sub>2</sub> and O<sub>2</sub> further improve their performance in radiation environment[109], [125], [126]. It has been reported that O<sub>2</sub> loading suppresses RIA by reducing the self-trapped hole(STH1)[126], [127] and H<sub>2</sub> loading passivates the optically-active defects, improving radiation resistance in the fiber in visible-near infrared frequency range[126]. However, most of the works dedicated to the H<sub>2</sub> loading technique to improve the radiation resistant performed either in gamma radiation or at a low neutron fluence. However, fibers exposed to mixed high gamma and neutron fluence may behave completely different.

Although substantial investigation work has been conducted to observe the effects of RIA on optical fibers and sensors, such effects at extremely high neutron fluence and high temperatures have yet to be researched. Little research has been performed

on the influence of high neutron fluence on RIA[30], [31], [128]. Among the research that has been done, Cheymol et al.[129], tested a number of a-SiO<sub>2</sub> based fibers and measured their corresponding RIA at a neutron fluence of  $1.3 \times 10^{20}$  n/cm<sup>2</sup>. Though they observed a high RIA in the visible range, the RIA degraded significantly in the IR region. The minimum RIA they reported was less than 10 dB in the 800-1100 nm wavelength range. They also tested the hollow core fibers under extreme neutron fluence and monitored their RIAs. Hollow core fibers showed very low RIA (< 1dB) before failing upon reaching a fluence of  $9 \times 10^{20}$  n/cm<sup>2</sup>. They also reported RIA at different cycles of irradiation times. While the RIA increased of regular solid fibers during irradiation, some recoveries were observed due to thermal annealing when the irradiation was turned off. However, during the next irradiation period, the RIA instantly returned to the same exact level seen just prior to irradiation shutdown and the possible reason for this could be the prompt re-activation of all annealing defects. It was suggested that thermal annealing (close to room temperature) only releases the charge carriers from the defect sites, but does not actually change defect sites, which fill up again during irradiation. The recovery of RIA was approximately (visual inspection) ~2 dB (1310 nm), ~0.5 dB (1064 and 980 nm) for STU1 fiber and ~1 dB (1064) for Forc3 fiber. Remy et al[31]., then tried to show the reflectivity of three FBGs after exposing them to a fast neutron fluence between  $3 - 5 \times 10^{19}$  n<sub>fast</sub>/cm<sup>2</sup>. The reflectivity of these FBGs reduced from 8.8 to 1.3% (HC-1), 62.8 to 7.9% (HC-2), and 18.7 to 0.4% (HC-4). The effect of a high neutron fluence of  $2.4 \times 10^{21}$  n<sub>fast</sub>/cm<sup>2</sup> on a-SiO<sub>2</sub> at three different temperatures was reported in[128]. The RIA was predicted to be between ~ 3 dB -70 dB, based on an empirical model. They also

reported temperature-dependent RIA and suggested that RIA decreased at high temperatures due to untrapping of charge carriers from defect sites.

### 2.3.2 Radiation Induced Compaction

RIC alters the fiber density through Knock-on process, leading to a compaction in the overall fiber structure. While RIA change the RI of fiber Kramers-Kronig's relationship, RIC does it via Lorentz-Lorenz[130], [131] and point dipole theory[132]. It has been reported that silica under fast neutron irradiations ( $\sim 10^{19} \text{ n/cm}^2$ ) reach to a state in which further neutron fluence does not alter the density anymore, and this state is termed as metamict phase for silica. It was also reported that silica tends to metamict phase with about a 3% density increase that results in a change of RI by 0.5%[62], [133]. This was first reported by Primak et al.[134] in experimenting on vitreous silica, which is shown in Fig. 2.3. They considered the isotropic change of the sample, but real fiber loses its homogeneity during the drawing process. As a result, the amount of compaction seen in real fiber is somewhat different from the  $\text{SiO}_2$  sample, which was later demonstrated by Remy et al.[31]. In[31], the authors measured the RIC of different fiber samples at a temperature of  $291^\circ\text{C}$  under at fast neutron fluence of  $3$  to  $5 \times 10^{19} \text{ n/cm}^2$  and found the linear compaction between 0.24-0.34%. The change in density/compaction due to RIC results in a significant spectral shift in a resonance-based sensor's response[135]. While it is believed that RIC rather than RIA dominates in changing the density of silica, and thus introduces radiation induced signal drift in resonance based OFSSs, other phenomena like dopant diffusion, temperatures, dose, dose rate, stress relaxation and so on may also contribute to the density change [30], [31], [122], [128]. The effect of temperature on different compositional the fibers can be seen in Appendix A.

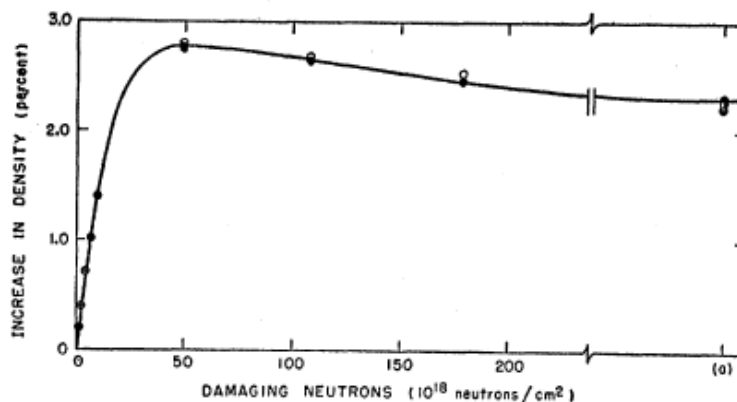


**Figure 2.3** Change in density in vitreous silica on irradiation in nuclear reactors (taken from[134])

### 2.3.3 Radiation Induced Emission

Radiation-induced emission (RIE) adds noise to the useful signal through emitted radiation[72] from defects excited by radiation or Cherenkov emissions[136]. RIE is generated when pre-existing or radiation-induced point defects are excited by incoming particles, causing a parasitic signal (radiation-induced luminescence or Cherenkov emissions)[122]. This parasitic signal superimposes onto the transmitted data and decreases the signal-to-noise ratio of the fiber system. At room temperature, thermal bleaching of radiation-induced point defects during or after irradiation partially recovers the transmission. It was suggested that thermal annealing (close to room temperature) only untraps the charge carriers from the defect sites, but defect sites remain unchanged which filled up again during the irradiation[129]. For applications in which the sensor operates in the infrared domain, the effect of RIE is neglected. RIE is generally considered in the ultra-violet (UV)-visible wavelength spectrum [72].

Based on the discussion of this chapter, it can be said that radiation degrades the signal strength as well as alters the density of the fiber material. While RIA is primarily responsible for the signal distortion, RIC drifts the signal by altering the density. In

sensing applications, RIC is more important than the RIA since RIC causes measurement errors by drifting the signal. There are several ways to minimize the RIA, thanks to the radiation hardened fibers. Please note that radiation hardened fibers mean lower RIA. It has no relation with the RIC.

## CHAPTER THREE: LONG PERIOD GRATING AND ITS APPLICATIONS

Long period gratings (LPGs) offer a plethora of applications in significant fields, such as sensing, imaging, spectroscopy, communications, and biotechnology,[137] due to their high sensitivity and ease of fabrication. However, LPGs are a transmissive mode in nature which limit their applications in different area. In this chapter, we discuss the possible solutions to overcome the problems associated with transmission mode LPGs and propose a cost-effective method to invert transmission mode LPG to reflection mode LPG.

### 3.1. Transmission LPGs and Their Drawbacks

A quick recap from Chapter 1, a long period grating (LPG) works on the principle of light coupling between the fundamental core mode and a number of co-propagating cladding modes[34], [138], [139]. Such coupling results in an LPG transmission spectrum with a number of discrete attenuation bands depending on the phase matching condition for a resonance wavelength ( $\lambda_m$ ) given by[34] :

$$\lambda_m = (n_{eff,co} - n_{eff,cl}^m)\Lambda \quad (3.1)$$

where  $n_{eff,co}$  is the effective RI of the guided core mode,  $n_{eff,cl}^m$  is the effective RI of the m-th order cladding mode and  $\Lambda$  is the grating period. It can be seen from equation (3.1) that the resonance wavelengths are dependent on the grating period and the effective refractive indices of the core and the cladding modes. Since external parameters, such as temperature, pressure, or a secondary medium in close proximity with the cladding can directly influence the effective indices of the cladding modes, the resonance wavelengths also respond to these changes. Thus, LPG sensors have found several potential

applications in monitoring temperature, strain, and refractive index[35]–[39]. However, an LPG is limited in applications in that it can only be used as a transmission sensor, compared to a fiber Bragg grating (FBG) sensor which is convenient as a reflection mode sensor. From a packaging viewpoint, it is preferable to use the same facet for coupling light into and out of the fiber to maximize their applications[140].

To overcome the abovementioned limitation of a conventional LPG design, several LPG designs have recently been reported in literature that can operate in the reflection mode[141]–[145]. For example, in [142], an LPG based on the Michelson interferometer was investigated to collect light reflected from the end facet of fiber at the input facet. However, interferometric fringes containing reflected spectrum made data interpretation cumbersome. Then in[143], a reflective LPG containing a polymer microtip at the end facet that reflects select cladding modes was proposed. Although this reflective LPG was able to measure the refractive indices of water/glycerol solution, a complex fabrication process for polymer microtip using photo polymerization was utilized. In[145], a very compact reflective LPG that reflects light without interferometric fringes was reported. In this design, both the fiber end facet and the side of the fiber was coated with silver metal in order to obtain a reflected spectrum that mimicked the transmitted spectrum. The design and operation of the reflective LPG was limited to within a narrow bandwidth around one of the resonance wavelengths, thus limiting the understanding of the use of the sensor across a wide bandwidth, specifically for distributed sensing applications. Additionally, the reflective LPG design used a very short length of end coating which was not optimized to completely mimic the transmission spectrum shape.

In this work, we show that – (1) the coating length, defined as length of the metal coating from the end facet of the fiber, and (2) the coating coverage, defined as the ratio of metal coating length over the LPG to the total length of the LPG, have a significant impact on the reflected spectrum over a wide bandwidth. Using these results, we present an optimized design for reflective distributed LPG structure comprising of  $n$  number of LPGs with different periods in a single fiber that entirely mimics the transmission spectrum over a wide bandwidth for the first time.

### 3.2. Geometric Structure of a Distributed Reflective LPG

A schematic diagram of the proposed distributed sensor design comprising of cascaded reflective LPGs is shown in Fig. 3.1. The grating period of the  $n$ -th LPG is denoted by  $\Lambda_n$ .  $L_c$  denotes the coating length,  $L_{gn}$  is the length of  $n$ -th LPG,  $L_{end}$  is the length of the tail end of the fiber measured from the end facet to the end of the  $n$ -th LPG,  $d_i$  is the distance between two adjacent LPGs. In this design, we used gold as the metal coating the fiber. Please note that in all of the cases considered in this paper for reflective LPG, the fiber end facet is always coated with metal. We used commercially available FIMMWAVE Photon Design software, a fully vectorial mode solver, to simulate

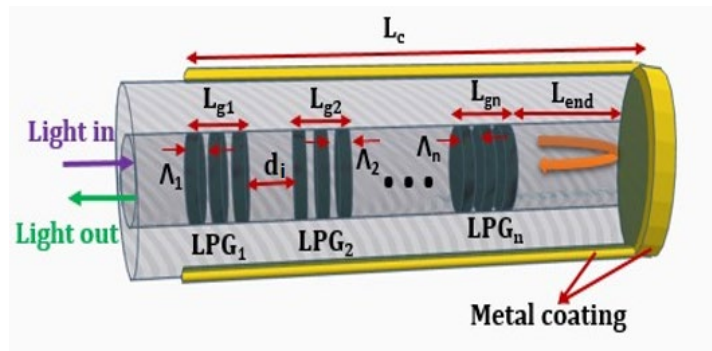


**Figure 3.1** Schematic of a distributed reflective LPG sensor design comprising of  $n$  number of LPGs within a single fiber and all the designing parameters.

the reflective LPG design. We considered the fiber parameters of commercially available SMF-28 fiber in our FIMMWAVE models and used the grating strength value of the proposed LPG of  $3 \times 10^{-4}$ [146].

### 3.3. Simulation Results and Discussions

The simulation results and associated discussions are organized in the following way. First, in Section 3.3.1, based on our recent work[147], we discuss the effects of design parameters on the spectrum of a single reflective LPG. Next, in Section 3.4, we present the simulation results for a distributed reflective LPG design and present the optimized design of a distributed reflective LPG structure that completely mimics the transmission spectrum shape over a 400nm wide bandwidth.

#### 3.3.1. Single Reflective LPG

The effect of coating length and coating coverage on the reflected spectrum of a single LPG is discussed thoroughly and then the same principle is used to demonstrate the distributed reflected LPGs.

##### 3.3.1.1. Effects of Grating Length on the Reflected Spectrum of LPG

We first studied the effect of the grating length (number of grating periods,  $N$ ) on the reflected spectrum. For our chosen design parameters ( $\Lambda = 390 \mu\text{m}$  and grating strength of  $3 \times 10^{-4}$ ), the core mode couples to  $LP_{05}$ ,  $LP_{07}$ ,  $LP_{09}$  cladding modes. This results in three discrete resonances at 1382 nm, 1406 nm, and 1558 nm, respectively, as shown in Fig. 3.2. The higher the order of the coupled cladding mode, the higher is the sensitivity of the corresponding resonance wavelength to external parameters since higher order cladding modes are in close proximity to the interface between cladding and

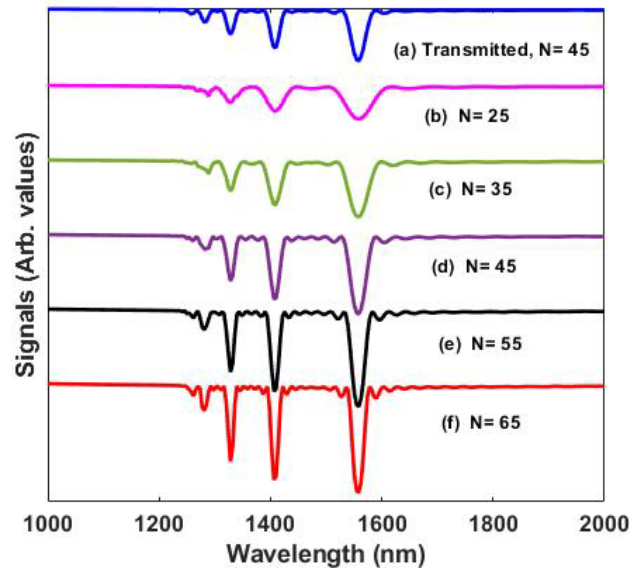


**Figure 3.2** Spectrum of the designed LPG as a function of wavelength for different grating period numbers ( $N$ ) for  $n=1$  and grating period of  $390 \mu\text{m}$ : (a) transmitted spectrum and (b-f) reflected spectrum for  $L_c = L_{end} = 1450\lambda$ .

surrounding medium. We increased the value of  $N$  from 25 to 65 in steps of 10. It is known from the coupled mode theory that the coupling strength depends on the RI contrast, and the local variation of mode fields over a specific fiber length [148]. This can be seen from the simulated reflected spectra in Figs. 3.2 (b-f) for  $N = 25-65$ , that with an increasing  $N$ , the resonance dips get narrower and deeper due to an increase in the coupling strength. However, the positions of the resonant dips remain unaltered. A reference transmission spectrum for  $N=45$  is shown in Fig. 3.2(a), and it can be seen that the transmission and the reflected spectra for  $N=45$  completely resemble each other in shape. Hence, for our studies throughout the paper, we choose a value of  $N=45$ .

### 3.3.1.2. Effects of Coating Length on the Reflected Spectrum of LPG

For  $N=45$ , we studied the effect of the metal coating length ( $L_c$ ) on the reflected spectrum. To do this, we set  $L_c=L_{end}$  and varied the coating length from  $25\lambda - 2550\lambda$  in steps of  $25\lambda$ . Only spectra for,  $25\lambda$ ,  $725\lambda$ ,  $1450\lambda$ ,  $1800\lambda$  and  $2550\lambda$  are shown Figs.

3.3(b-f). The simulated results indicate splitting in some of the resonant dips for a critical length  $L_c < 1450\lambda$ . On the other hand, when  $L_c \geq 1450\lambda$ , the reflected spectrum follows the transmission spectrum without any splitting. We hypothesize that the side coating effectively absorbs the coupled cladding modes beyond the critical length of the coating while it propagates at the cladding/metal interface. Since the coupled cladding modes are absorbed by the metal coating, the LPG reflected spectrum does not show any interferometric fringes. However, a suitable coating length is highly required to absorb all the coupled cladding modes. It can be said that coating length less than  $1450\lambda$  is not sufficient to absorb all the coupled cladding modes, especially for operating over a wide bandwidth. The threshold value of the coating length beyond which the transmitted and reflected spectra mimic substantially was determined by calculating the correlation coefficient between these two spectra. We determined the coating length by setting a threshold correlation factor of 99.5% over which the reflected spectrum follows the transmitted spectrum completely. Therefore, we choose a value of  $L_c = 1450\lambda$  for our design. Setting the value of  $L_{end} = 1450\lambda$ , we further looked at the effect of varying the coating length from  $L_c = 0$  to  $L_c = L_{end} = 1450\lambda$  on the reflected spectrum. It can be seen from the Figs. 3.4(b-d) that as the coating length is changed from 0 [Fig. 3.4(b)] to  $L_{end}/2$  [Fig. 3.4(c)] to  $L_{end}$  [Fig. 3.4(d)], the reflected spectrum increasingly mimics the transmitted spectrum [Fig. 3.4(a)], where at 100%, the reflected and transmitted spectrum are identical over a 400 nm bandwidth. In all cases in Fig. 3.4, the reflected spectra show reduced intensity but increased resonance depth compared to transmission spectrum.

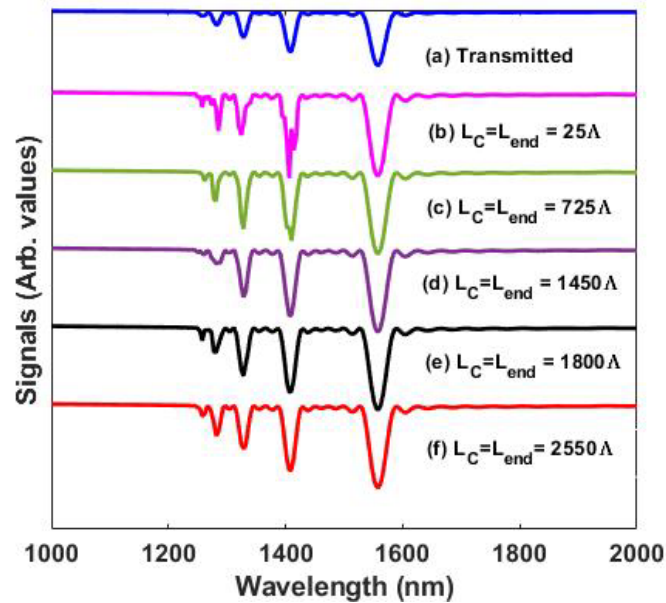


**Figure 3.3** Effects of metal coating length on the reflected spectrum of the LPG for  $n=1$ ,  $N=45$  and grating period is of  $\Lambda = 390 \mu\text{m}$ : (a) transmitted spectrum and (b-f) reflected spectrum.

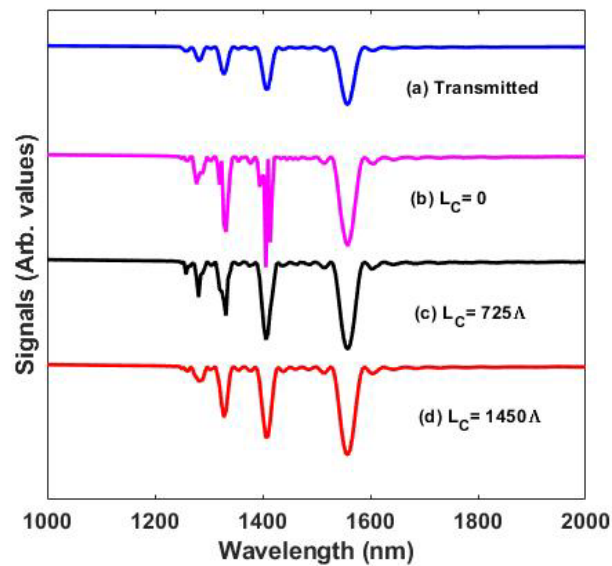


**Figure 3.4** Effects of metal coating length on the reflected spectrum of the LPG for  $n=1$ ,  $N=45$  and grating period is of  $\Lambda = 390 \mu\text{m}$  while keeping the  $L_{\text{end}} = 1450\Lambda$  fixed: (a) transmitted spectrum and (b-d) reflected spectrum.

### 3.3.1.3. Effects of Coating Coverage on the Reflected Spectrum of LPG

Finally, we studied the effects of coating coverage on the reflected spectrum for LPG with a grating period of  $\Lambda = 390 \text{ } \mu\text{m}$ . Figures 3.5(c-e) shows how the coating coverage changes the spectra from the optimized reflected spectrum ( $L_c = L_{end} = 1450\Lambda$ ) [Fig. 3.5 (b)] . It can be seen that for 25% coverage [Fig. 3.5(c)], the shape of the dip centered around 1558 nm starts to change and continues for 50% coverage [Fig. 3.5(d)] and completely vanishes for 75% and 100% coverage [Figs.3.5 (e-f)]. This happens because the metal coated directly over the grating influences the cladding modes, which in turn alters the coupling condition. From the single reflective LPG simulations, we conclude that in order for the reflected spectrum to completely mimic the transmission spectrum shape over a large bandwidth, a coating length greater than  $1450\Lambda$  and a coating coverage of 0% are the optimal parameters.

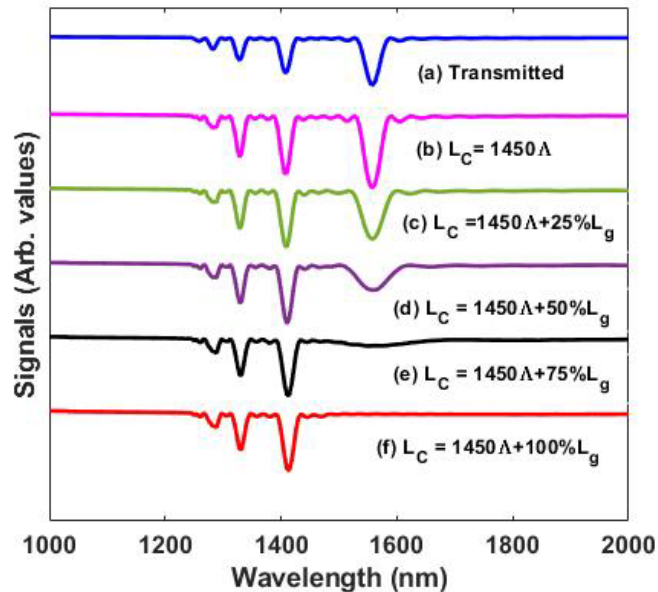


**Figure 3.5** Effects of coating coverage on the spectrum of the designed LPG for  $n = 1, N = 45$ : (a) transmitted spectrum before inclusion of the metal coating, (c-f) reflected spectrum.

### 3.3.2. Distributed Reflective LPG

Next, we looked at the effect of including multiple LPGs within the same fiber on the reflected spectrum. For these simulations, we chose three LPGs with periods equal to  $\Lambda_1 = \Lambda = 390 \text{ } \mu\text{m}$  (LPG1),  $\Lambda_2 = 374 \mu\text{m}$  (LPG2), and  $\Lambda_3 = 346 \text{ } \mu\text{m}$  (LPG3) for designing a distributed reflective LPG with up to 3 different LPGs in a single fiber. Please note that LPGs are added from the end facet coating side and  $L_{end}$  is fixed at  $1450\Lambda_1$ . Just like for an LPG grating period of  $\Lambda_1 = 390 \text{ } \mu\text{m}$ , we also performed simulations described in Section 3.3 for grating periods of  $\Lambda_2 = 374 \text{ } \mu\text{m}$  and  $\Lambda_3 = 346 \text{ } \mu\text{m}$ . These simulations provided the same trends as those observed for the case of  $\Lambda_1 = 390 \text{ } \mu\text{m}$  period reflective LPG. Please note that the most higher order dips for grating periods of  $\Lambda_1 = 390 \text{ } \mu\text{m}$ ,  $\Lambda_2 = 374 \text{ } \mu\text{m}$ , and  $\Lambda_3 = 346 \text{ } \mu\text{m}$  are centered around the wavelengths of 1558 nm, 1500 nm, and 1400 nm, respectively

#### 3.3.2.1. Effects of Coating Coverage and Coating Length for $n = 2$

We consider a simple case of a distributed reflective LPG design with two LPGs ( $n=2$ ). Figure 3.6(a) shows the simulated transmission spectrum when two LPGs with grating periods of  $\Lambda_1 = \Lambda = 390 \mu\text{m}$  (LPG1), and  $\Lambda_2 = 374 \text{ } \mu\text{m}$  (LPG3) are included within the same fiber.  $L_{end}$  is fixed at  $1450\Lambda_1$ . Figures 6.6(b-d) show the effect of coating length on the LPG closest to the fiber facet ( $\Lambda_1 = 390 \text{ } \mu\text{m}$ ) on the reflected spectrum. Similar to the effects observed in a single LPG case, when  $L_c = L_{end} = 1450\Lambda_1$ , the reflected spectrum mimics the transmitted spectrum completely. It can also be observed that dips for the higher order cladding modes are at wavelengths of 1558 nm and 1500 nm,

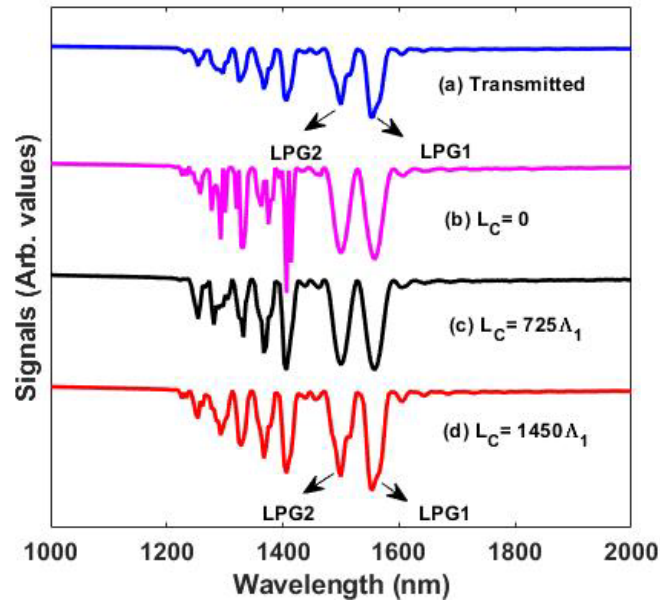


**Figure 3.6** Effect of coating length on the reflected spectrum of the designed two LPGs ( $n=2$ ) added in series and  $L_{end} = 1450\Lambda_1$  (a) transmitted spectrum before inclusion of the metal coating, (b-d) reflected spectrum.

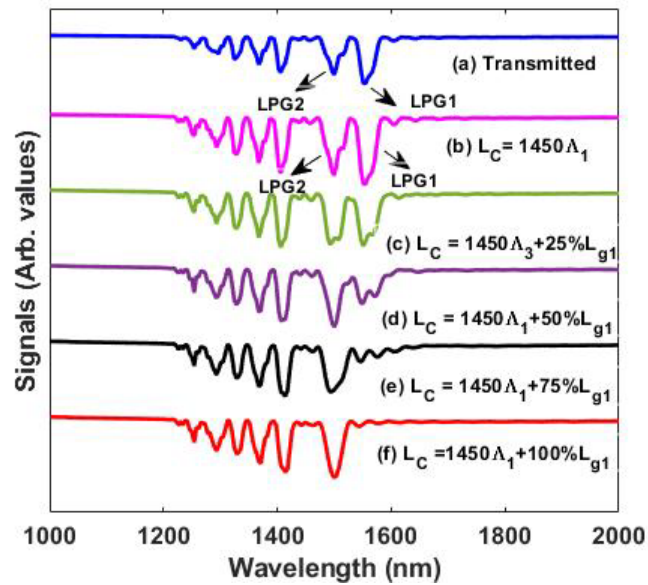


**Figure 3.7** Effects of coating coverage on the spectrum of the designed LPG for  $n=2$  and  $N=45$ : (a) transmitted spectrum before inclusion of the metal coating, (b-d) reflected spectrum.

which are also the dips for individual LPGs with grating period of  $\Lambda_1 = 390\mu\text{m}$  (LPG1) and  $\Lambda_2 = 374\mu\text{m}$  (LPG3), respectively. Figure 3.7 shows the effect of coating coverage on the LPG spectrum. It can be seen from Figs. 3.7(c-f) that similar to the single LPG case, coating coverage leads to splitting or disappearance of dips.

We also considered the effect of coating the metal over the length of the fiber between the two LPGs. Figs. 3.8(c-e) show the effect of coating metal over different areas of the fiber for  $L_{\text{end}} = 0$ .  $L_c = d$  [Fig. 3.8(c)],  $L_c = L_{g1} + d$  [Fig. 3.8(d)], and  $L_c = L_{g1} + d + L_{g2}$  [Fig. 3.8(e)], are the cases for when the metal is coated over the length between the gratings, the length between the gratings and over the last grating, and the length between the grating and both gratings, respectively. Please note that  $L_{g1}$  is the grating length of the LPG ( $\Lambda_1 = 390\mu\text{m}$ ) closest to the end facet and  $L_{g2}$  is for  $\Lambda_2 = 374\mu\text{m}$ .

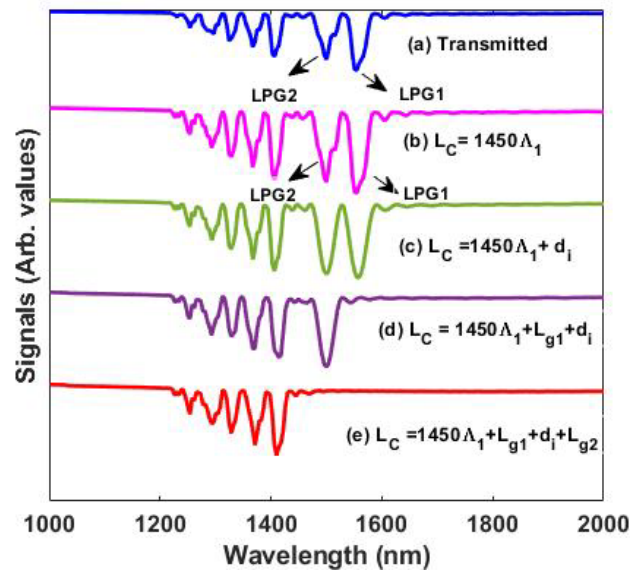


**Figure 3.8** Spectrum of the cascaded two LPGs for different configurations for  $n = 2$  and  $N = 45$ : (a) transmitted spectrum before inclusion of the metal coating, (b-e) reflected spectrum.

Fig. 3.8(b) shows the reflected spectrum for our optimized design parameters. It can be observed from Fig. 3.8(c) that while the dips for reflected spectrum are at the same wavelength as those for transmission spectrum on Fig. 3.8(a), the coating significantly affects the shape of the reflected spectrum. For these cases of Figs. 3.8(d-e), disappearance, and shifting of the dips can be observed, and the reflected spectra do not mimic the transmitted spectrum for any configuration. Thus, it can be concluded that the reflected spectrum follows the transmitted spectrum only when the metal coating is over the coating length  $L_c = L_{end} \geq 1450\Lambda_1$  and is absent elsewhere.

### 3.3.2.2. Effects of Coating Coverage and Coating Length for $n = 3$

Simulation results from the single LPG and the dual cascaded LPGs indicate that  $L_c = L_{end} \geq 1450\Lambda_1$  provides reflected spectrum that mimics the transmitted spectrum. Following this, a three cascaded reflection mode LPG is designed and simulated only for  $L_c = L_{end} = 1450\Lambda_1$ . Three LPGs with grating periods of  $\Lambda_1 = 390 \mu\text{m}$  (LPG1),  $\Lambda_2 = 374 \mu\text{m}$  (LPG2), and  $\Lambda_3 = 346 \mu\text{m}$  (LPG3) are added in a series, and the simulation results are shown in Fig. 3.9. It can be seen that the reflected spectrum completely mimics the transmitted spectrum when  $L_c = L_{end} = 1450\Lambda_1$  and no metal is coated anywhere else. Thus, we have generated an optimized design solution for a distributed reflective LPG comprising of multiple LPGs. Since the designed triple cascaded LPGs consists of these three grating periods, it is expected that it will couple light at wavelengths of 1558 nm, 1500 nm and 1400 nm. It can be seen from Fig. 3.9 that dips for the higher order cladding modes are at wavelengths of 1558 nm, 1500 nm and 1400 nm as expected. The effects of metal coating parameters on the spectrum of reflective LPGs for  $n = 1, 2,$  and 3 number of gratings in a single fiber have been presented. Coating metal over the grating or over

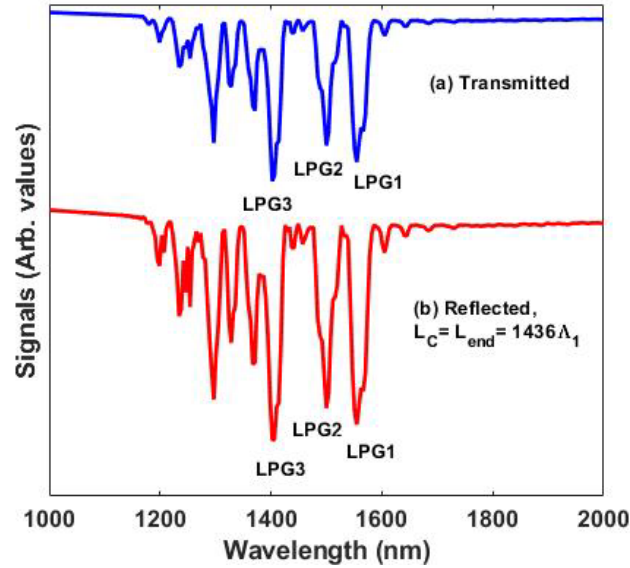


**Figure 3.9** Spectrum of the cascaded three LPGs when  $L_c=L_{end} = 1450\Lambda_3$  for  $n=3$  and  $N=45$  and grating period of  $\Lambda_1 = 390\ \mu\text{m}$ ,  $\Lambda_2 = 374\ \mu\text{m}$ , and  $\Lambda_3 = 346\ \mu\text{m}$ .

any region between the LPGs either splits or leads to disappearance of some of the dips since it influences the cladding modes directly, and therefore, changes the coupling conditions. On the other hand, coating the tail end after the last LPG alone with metal provides a reflected spectrum that completely mimics the transmitted spectrum. The design methodology presented in this paper can be applied to a distributed sensor design comprising of  $n$  number of cascaded LPGs.

### 3.4. Metal Coating

To verify the modeling work, we then applied metal coating on the commercially available LPGs to work in reflection mode and monitored their spectra. We introduced a novel and cost-effective technique to coat an LPG sensor with silver paste to realize a reflection mode operation. While successful demonstrations of reflective-mode operation were demonstrated, the previous works involved the use of expensive or complicated

processes, such as sputtering, thermal evaporation or mirroring for fabrication, and the maximum coating length was limited to 2 cm.

For the first time (to the best of our knowledge), we coat 60 cm of an LPG from the grating end to the end facet of the fiber using a simple coating method. The coating length was chosen based on our previous numerical analysis[147], [149] in which we showed that a coating length greater than  $1450\lambda$  is sufficient to provide reflected spectrum that closely mimics the transmitted spectrum. We used commercially available silver paste as the coating material. The reflective LPG provides spectrum that follows the transmitted spectrum over a wide bandwidth. The proposed technique to coat the fiber is simple and cost effective compared to sputtering or thermal evaporation methods. What is more, long lengths of fibers can easily be coated without breaking it. It is anticipated that this novel way of coating the fiber can pave the way for widespread use of reflective LPG sensors as well as metal embedded fiber optic sensors.

The schematic of a reflective LPG is shown in Fig. 3.10 where  $L$  is the coating length measured from the fiber end facet to the grating end,  $\Lambda$  is the grating period and  $t$  is the thickness of the metal coating. The metal coating is applied both at the fiber end facet as well as the tail length. While the end facet coating reflects the guided core mode light, side coating effectively absorbs the coupled cladding modes. When a broadband light is launched into the fiber, the core mode interacts with the grating and couples to the co-propagating many cladding modes. Since the coupled cladding modes interact with the metal coating, they can be absorbed completely by choosing a suitable coating length. On the other hand, the core mode is reflected at the end facet coating. This reflected mode interacts with the grating again to couple to cladding modes. Thus, the obtained reflected

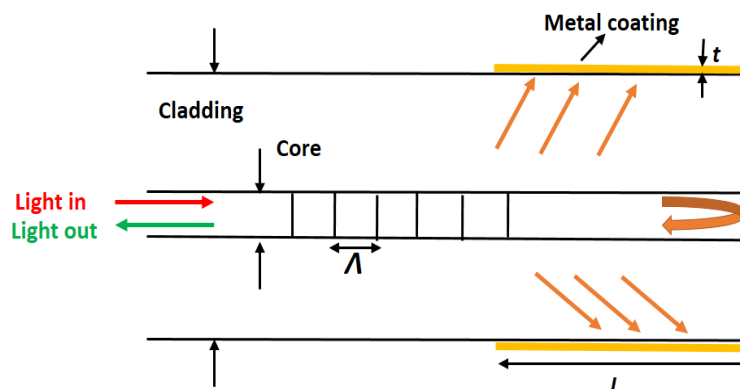


**Figure 3.10.** A schematic of metal coated LPG with all associated parameters. Metal is coated over length  $L$  and the end facet.

light shows reduced intensity compared to transmission mode operation. Complete absorption of cladding modes by the metal coating later prevents the operation of the device as a Michelson Interferometer (MI), thus providing a clean reflected spectrum free of interferometric fringes.

#### 3.4.1. Metal Coating Process

A commercially available silver paste (DuPont 5000) was used to coat 60 cm long fiber segment from the LPG grating end to the end facet of fiber in order to get the reflected spectrum that completely mimics the transmitted spectrum. We used LPGs from TECHNICA with a grating period of  $450 \mu\text{m}$ . The metal coating steps are schematically shown in Figs. 3.11(a-f). As the first step, we cleaned the uncoated fiber and dried the fiber with a heat gun. The fiber tip was then cleaved at a distance of 60 cm from the grating end using a fiber cleaving tool. A Kapton sheet with a length of 1m was cleaned and dried [Fig. 3.11(a)]. The Kapton sheet was then fixed on a flat table. We then brush-coated the silver paste on the cleaned Kapton paper to a length of about 60 cm. We carefully placed the 60 cm long fiber segment beyond the grating into the paste to coat the lower half of the fiber [Fig. 3.11(b)]. We ensured that the grating portion of the fiber did not touch silver paste.

Then, we used a brush to coat the upper half of the fiber [Fig. 3.11(c)]. We left the fiber in the paste for 5-10 minutes to allow for voids to be filled with silver paste [Fig. 3.11(d)]. Then, we lifted the fiber carefully and used a heat gun to dry the coating for 3-5 seconds [Fig. 3.11(e)]. Next, we inserted the coated fiber into a muffle furnace and thermally treated the coating for 5 minutes at 120°C [Fig. 3.11(f)] to complete the coating process. A scanning electron microscope (SEM) image of the metal coated fiber is shown in Fig. 3.11(g). It can be seen that the edge of the coating is not straight, and it is due to the inherent nature of the brush coating method. However, this did not affect the spectrum of the reflective LPG since we intentionally maintained a 1 mm gap between the coated portion and gratings to prevent any accidental coating over the LPG section. The measured average coating thickness along the fiber was found to be  $6\pm 0.1\ \mu\text{m}$ . As the metal coating portion is not the part of sensing element, the non-uniformity of the coating thickness did not disturb the measurands to be measured in the operating environment.

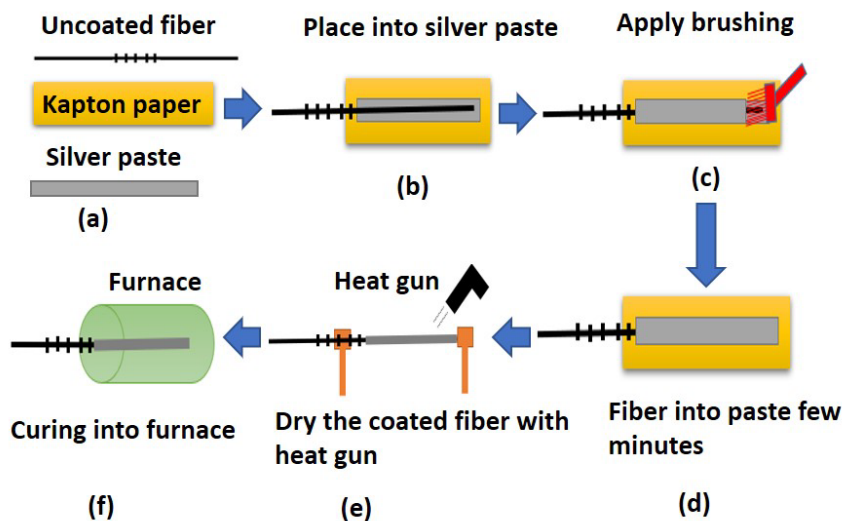


**Figure 3.11** Step by step metal coating process by brush coating technique.

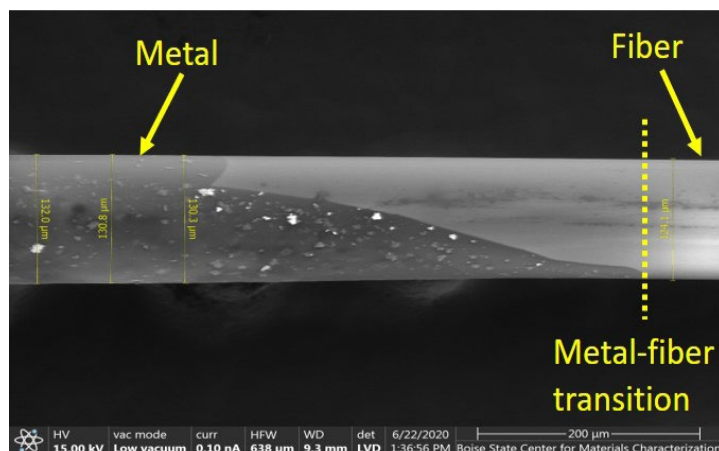


**Figure 3.12** Scanning electron microscope (SEM) image of a coated fiber near the LPG section.

### 3.5. Metal Coated Reflective LPG

Prior to coating the LPG fiber with metal, we recorded the transmission spectrum from the LPG using a superluminescent diode (SM Benchtop SLD from Thorlabs) and an optical spectrum analyzer (OSA, MS9740A, Anritsu). Figure 3.13 shows our experimental setup to measure the reflected spectrum of the metal coated LPG. Light is launched through the fiber from the superluminescent diode with a center wavelength of 1527 nm. A circulator (6015-3-FC - Fiber Optic Circulator, Thorlabs) was used along with the OSA to obtain spectrum from the reflective LPG. Light from the SLD was launched into Port 1 of a circulator. Port 2 of the circulator was connected to the fabricated reflective LPG device. We analyzed the reflected light collected in Port 3 using the OSA. The obtained reflected spectrum from the metal coated LPG is shown in Fig. 3.14. The measured transmission spectrum is also plotted on the same graph for comparison. The core mode couples to three distinct cladding modes within the wavelength range 1430-1630 nm. It can be seen from the figure that the reflected spectrum follows the transmitted spectrum with reduced

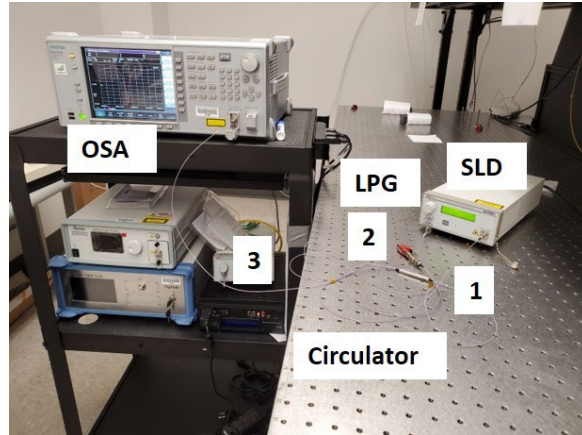


**Figure 3.13** Experimental setup to record reflected spectrum from the metal coated LPG (1, 2, and 3 indicate the port of the circulator).

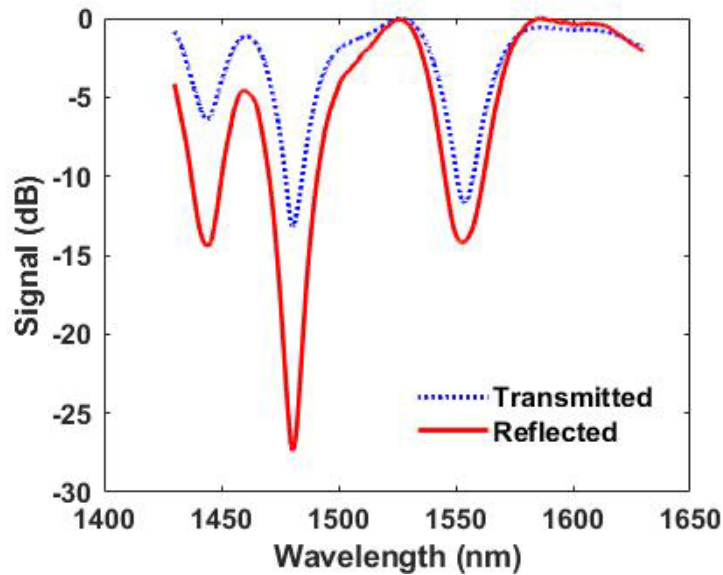


**Figure 3.14** Measured transmitted spectrum (dotted blue) and reflected spectrum (red) for a coating length of 60 cm.

intensity with a calculated correlation factor of 0.91. Furthermore, the reflected spectrum contains no interferometric fringe which may ease the data interrogation technique. It can be said that 60 cm of metal coating length was sufficient to obtain three dips within a wavelength span of 200 nm. As our reflective LPG provides three dips and the spectral dependence of each dip is different from the other to the external parameters like

temperature, strain and refractive index, this sensor can be used to sense multi-parameters simultaneously.

### 3.6. Coating Length on LPG Spectrum

To investigate the effects of coating length on the reflected spectrum of the LPG, we coated another similar LPG with a coating length of 1 cm and the transmitted and the reflected spectra for this LPG are shown in Fig. 3.15. It can be clearly seen from Fig. 3.15 that a 1 cm coating length is not sufficient to absorb all coupled cladding modes, and therefore, splitting of the dips can be observed. What is more, the calculated correlation factor was found to be 0.5585 between the transmitted and the reflected spectrum. A rigorous explanation of coating length effect on the reflected spectrum of an LPG can be found in ref[149].

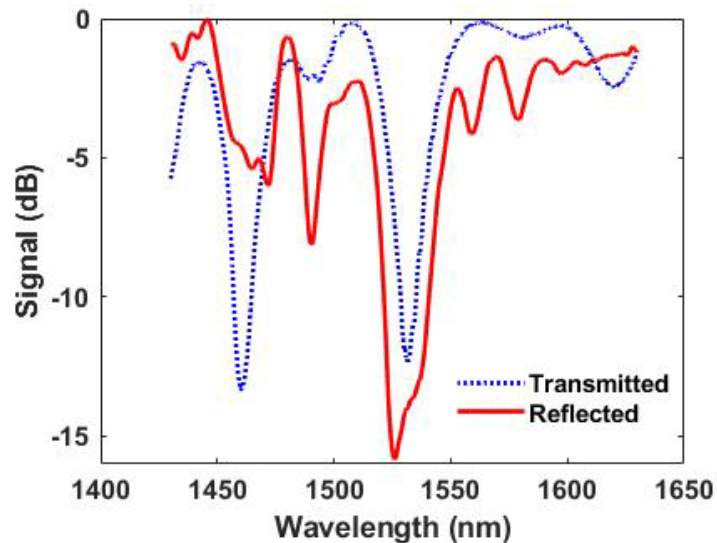


**Figure 3.15** Measured transmitted spectrum (dotted blue) and reflected spectrum (solid red) for coating length of 1 cm.

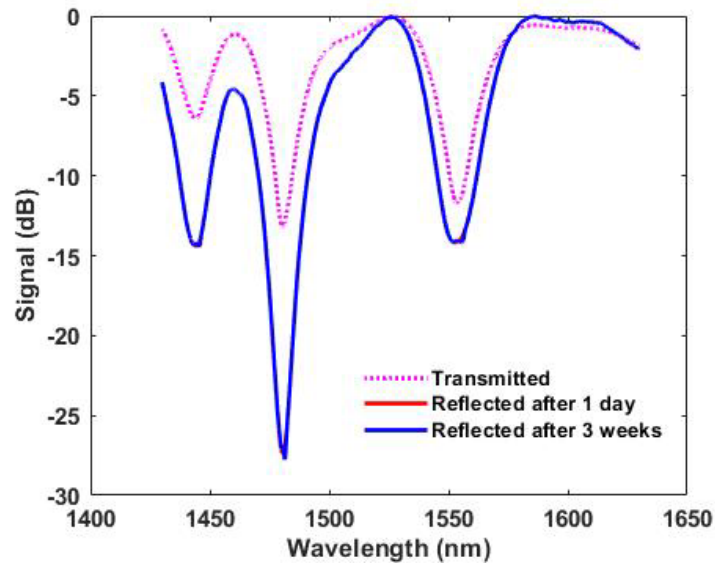


**Figure 3.16** Measured transmitted spectrum (dotted pink) and reflected spectra after 1 day (solid red), and after 3 weeks (solid blue) for a coating length of 60 cm.

To test the robustness of the fabricated metal coated LPG, we recorded the spectrum of the LPG with a coating length of 60 cm after three weeks. It can be seen from Fig. 3.16 that there is no obvious change in the spectrum.

Next, we fabricated couples of reflection LPGs using the coating method discussed above. This time the effect of coating length on the reflection spectrum of LPG is analyzed both analytically and experimentally. Different length of fiber beyond the grating was coated. Figure. 3.17 shows a schematic of a reflective LPG showcasing three scenarios- 100% (full coating length), 50% coating length and end facet coating or tip coating (0% coating length) (represented by arrows). The effect of coating length on the reflection spectrum is shown in Fig. 3.18(a) numerically and Fig. 3.18(b) experimentally. For our modeling work[149], we used commercially available FIMMWAVE software, a fully vectorial mode solver. We considered a grating period of 280  $\mu\text{m}$  and SMF-28 fiber's

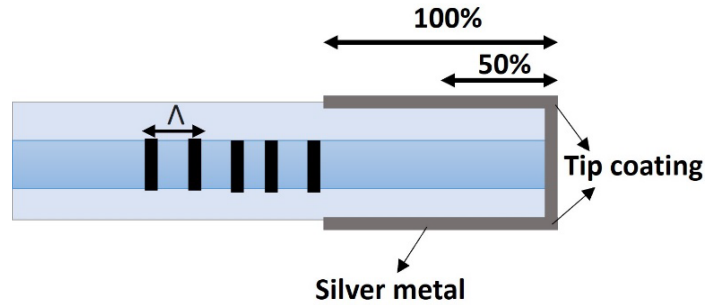


**Figure 3.17 Schematic of different coating length on LPG contained fiber.**

parameters. It was found from the simulation results that the core mode couples to the  $LP_{0,7}$  cladding mode within the wavelength range 1460-1580 nm. It can be seen from both simulation and experimental results in Fig. 3.18 that when the coating was applied only at the tip of the 60 cm length fiber beyond the grating, the reflection spectrum (red color) looks like an interferometric fringe. However, when the coating length was increased to 50% (30 cm), the depth of the dip around 1500 nm in the reflection spectrum (yellow color) started to increase. However, one can see from the experimental result that the spectrum for 50% coating length also demonstrate interferometric fringes similar to tip coating although a small dip can be seen around 1500 nm. The possible reason might be the insufficient absorption of all the modes within the coated metal providing additional interferometric fringes at other wavelengths. The reflection spectrum (purple color) followed the transmitted spectrum (blue color) only when the coating was applied to the full 60cm length of the fiber. Since the core mode travels twice into the grating and the metal coating itself absorbs light, the reflection light for 100% coating length shows reduced intensity compared to the transmission light. Based on these results, it can be said that the coating effect on the reflection spectrum follow the same trend observed through

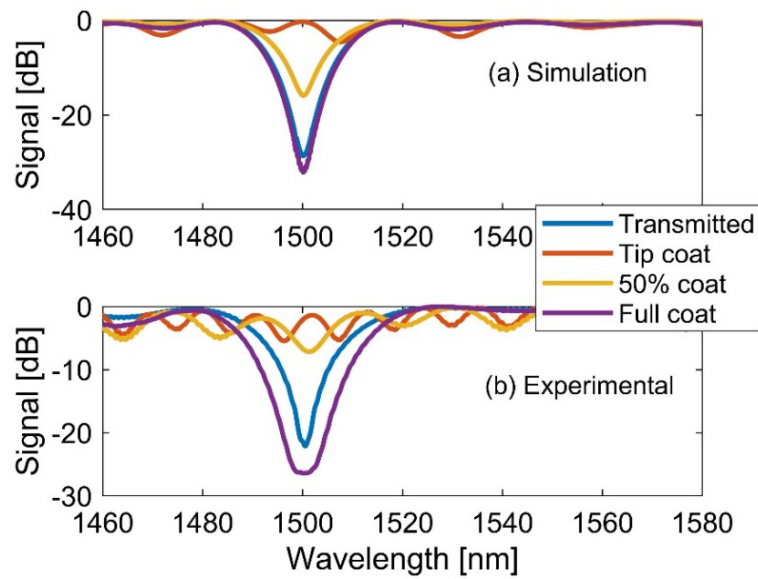


**Figure. 3.18** Effect of coating length on the reflection spectrum of the LPG: (a) simulation results and (b) experimental results.

simulations. This effect of coating length on the reflection spectra supports our modeling work in [149].

### 3.7. Reflection LPG Based Sensors

To demonstrate how good a fully reflective LPG compares to its transmissive LPG counterpart, we also used our coated LPG as a sensor to measure temperature between 21 to 191°C and for RI sensing of a water/glycerol solution. We compared the results from our reflected LPG against uncoated transmitted LPG.

#### 3.7.1. Temperature Sensing

The effect of temperature on LPG can be found by partially differentiating the Eq. (3.1) with respect to temperature and can be expressed as[39]

$$\frac{d\lambda_m}{dT} = \frac{d\lambda_m}{d(\partial n_{eff})} \frac{d(\partial n_{eff})}{dT} + \frac{d\lambda_m}{d\Lambda} \frac{d\Lambda}{dT} \quad (3.2)$$

where  $T$  is the temperature and  $\partial n_{eff} = n_{eff,co} - n_{eff,cl}^m$  is the differential effective RI.

Equation (3.2) consists of two parts: the first term on the right-hand side denotes the

material contribution and the second term indicates the waveguide contribution to the thermally induced shift. To realize the temperature sensitivity of the transmission mode and reflection mode LPG sensors, we used a controllable hot plate to heat the LPG section from 21° to 191°C with a step of 2°C/min. We also placed a k-type thermocouple at the interface of gratings and hotplate for measurement accuracy. We saved the data at every 20°C interval. Figure 3.19 shows the relative shift in the resonance wavelength of the LPG. The red circles in Fig. 3.19 represent the experimental data and blue line is a linear fit to these data point. It can be seen that the resonance wavelength shows a redshift with increasing temperature since the effective refractive indices of the core and the cladding

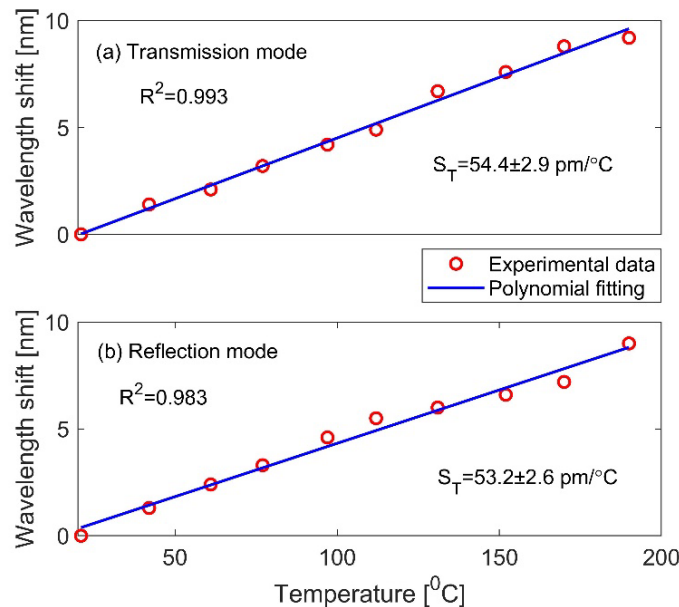


**Figure. 3.19** The measured relative wavelength shifts of LPG as a function of temperature: (a) transmission mode LPG and (b) reflection mode LPG.

increase with temperature. However, the core refractive index changes more compared to the cladding one due to the presence of germanium dopants in the core. We found that for the transmission mode LPG results shown in Fig. 3.19(a), the resonance wavelength shift was 9.25 nm, leading to a temperature sensitivity coefficient ( $S_T$ ) of 54.4 pm/°C. The

obtained sensitivity coefficient for the reflection mode LPG data in Fig. 3.19(b) is 53.2 pm/°C which is very close to the transmission mode LPG case. For both cases, the sensitivities are larger than short period gratings[33], [39], [138], [150]. Since we used the coating on a commercially available LPG from TECHNICA, there was no room for modifying structural parameters except coating the fiber and measuring the parameters. However, the temperature sensitivity can be increased in several ways reported in[33], [138], [146], [150]. It can also be seen in Fig. 3.19 that the resonance wavelength change with temperature is not linear, and this non-linearity can be attributed to temperature dependent thermo-optic coefficient of the core and the cladding[151]. This non-linearity is insignificant for several practical applications since the wavelength shift versus temperature curve can follow a second or a higher order polynomial relationship. However, this non-linear behavior may limit the performance of LPG sensor when simultaneous strain and temperature measurements are performed.

### 3.7.2. Refractive Index Sensing

Next, we used the metal coated LPG to sense the RI of water/glycerol solution. The solution was prepared by mixing glycerol with de-ionized water with various concentration ratios and their corresponding RIs taken from[143]. We carried out the RI measurement at a constant room temperature. Equation (3.1) suggests that the increment of cladding RI reduces the RI difference between the core and the cladding which in turns provides a blueshift of resonance wavelength. When the LPG was placed in a water/glycerol solution, the RI of the surrounding medium around the cladding increases, which ultimately increases the RI of the cladding modes. It is expected that the resonance wavelength would give a blueshift when the LPG is immersed into the solution. We increased the

concentration of glycerol from 0% to 70% and recorded the spectrum. The relative wavelength shift as a function of RI (glycerol concentration) is shown in Fig. 3.20. The red circles indicate experimental data and blue line shows the higher order polynomial fitting for these data points. It can be seen that the resonance wavelength provides blueshift with increasing RI. In both transmission mode and reflection mode LPG, the resonance wavelength provides a blueshift of  $370 \pm 2.2$  nm when the refractive index changed from 1.33333 (10% solution concentration) to 1.42789 (70% solution concentration), leading to a sensitivity of 3.7 nm/0.1 RIU. It is known that when the RI of the surrounding medium becomes comparable to the cladding RI, the resonance wavelength shows a significant

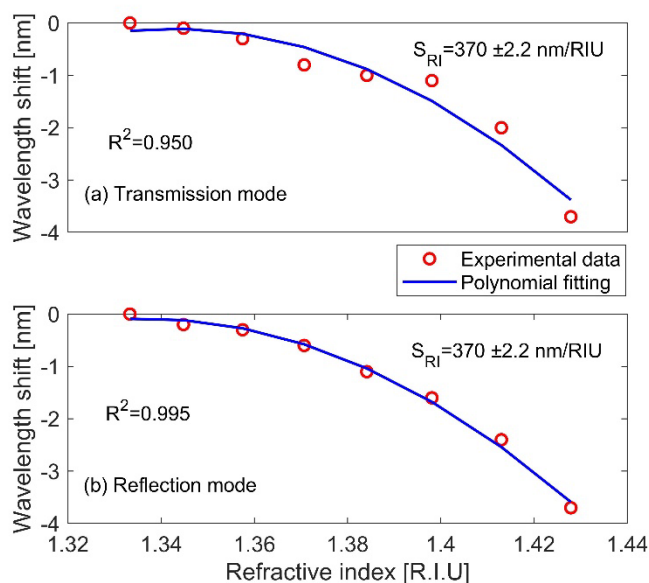


**Figure. 3.20 The measured relative wavelength shifts of LPG as a function of RI: (a) transmission mode LPG and (b) reflection mode LPG.**

shift[152] which is seen for the 70% glycerol concentration in the solution. The reason is that at 70% concentration of glycerol, the RI of the solution (1.42789) becomes comparable to the RI of the cladding (1.444). Since we carried out the RI experiment on a commercial LPG sensor, with no room for modifying any structural parameters, the reported RI

sensitivity of our sensor is smaller compared to [143], [145]. However, like temperature sensitivity, several methods can be employed to enhance the RI sensitivity which includes introducing sensitive doping material [143], coupling to higher order or TAP modes [146], [153] and thinning the cladding diameter [153], [154].

As the spectral dependence of each coupled mode to the external parameters is different, multi-parameters can be sensed using a single LPG. Although the temperature sensitivity coefficient of the LPG sensor is one order magnitude higher than the FBG sensor [39], [138], [150], it has several limitations. As LPG contains a broad dip compared to the Bragg peak of FBG, it makes it difficult to detect the dip. Moreover, LPGs are very sensitive to bends and refractive index changes that may induce an error in temperature measurement. Additionally, multiple resonance dips along with a wide spectrum can limit their multiplexing capabilities.

In conclusion, in this chapter we have shown numerically how coating length and coating coverage affect the spectrum of reflective LPG. Then we have shown experimentally the effect of coating length on the reflection spectrum of LPG to validate our modeling work. While short coating length is more practical and expected, we tried to show the coating effect to validate our modeling work which can aid designers in choosing appropriate coating lengths for their structures. In addition, we measured the temperature and RI using the same LPG but in both transmission mode and reflection mode and compared their corresponding sensitivity coefficients. We found similar sensitivity coefficients both in the transmission mode and the reflection mode LPG. This is the first demonstration of an experimental comparison between the transmission and the reflection mode LPG. It is expected that the LPG coated with simple brush coating method can find

applications in tight space or remote sensing of different parameters with sensitivity.

## CHAPTER FOUR: RADIATION EFFECTS ON OPTICAL FIBER SENSORS: MODELING AND EXPERIMENT

Nuclear power is a potential clean energy solution to the world's ever-increasing energy demand[155], [156]. Power-producing reactors require little in-core instrumentation; however, accurate in-pile measurements are required to qualify new nuclear fuels or extend the burnup of existing fuel designs. Typical commercial electronic sensors often fail under radiation environments such as those encountered in nuclear reactors, so an alternative approach is needed to monitor physical parameters such as temperature, strain, and pressure[72], [109], [157]–[159]. OFS technology has gradually penetrated into the nuclear environment due its enormous intrinsic advantages which includes immune to electromagnetic interference (EMI), wide bandwidth, compact size, fast measurement rate, passive operation, multipoint or distributed sensing etc.,[72], [158], [160]. However, an in-depth understanding of how radiation affects optical fibers and optical fiber sensors (OFS) is required to ensure their reliability and survivability. Early work has shown that three types of resonance-based OFS—fiber Bragg grating (FBG), long-period grating (LPG), and Fabry-Perot (F-P)—have been widely tested in nuclear environments[32], [35], [40], [41], [60], [136], [161], [162]. It is crucial to predict the radiation effects by modeling OFSs numerically and then apply it for real time experiments. In chapter 2, we discussed the radiation mechanisms namely RIA and RIC. In this chapter, first we numerically analyze the macroscopic effects of RIC on three resonance-based types of sensors: FBG, LPG, and F-P. We started our simulation by looking the effects of

variation of RI on these sensors caused by gamma radiation. As the radiation causes the change in the structure of optical sensors which result in macroscopic changes for, example RI change, in the fiber material, the simulation indirectly also analyses the radiation effects on optical structure. Secondly, we analyze the FBGs' performance exposed to a high temperature and high neutron fluence environment.

#### **4.1 Models for OFSs**

To numerically investigate how radiation affects optical performance, we modeled three types of resonance-based sensors (FBG, LPG, and F-P) using a robust and fully vectorial mode solver (FIMMWAVE from PhotonDesign)[163]. This simulation software can solve a large variety of waveguides made of almost any material and any geometry as it supports a rich number of complementary algorithms. FIMMPROP, the integrated part of FIMMWAVE, is a tool for simulating propagation in optical waveguides. For modelling grating based sensors, FIMMPROP uses either Eigenmode Expansion (EME) method or Rigorous Coupled Mode Theory (RCMT). SMF-28 optical fiber parameters used for simulation purposes throughout the paper are: cladding RI = 1.444[164], core diameter = 8.2  $\mu\text{m}$ , cladding diameter = 125  $\mu\text{m}$ , mode field diameter = 10.4 $\pm$ 0.5  $\mu\text{m}$ , and numerical aperture = 0.14. The following sections describe the base model for the three types of OFS in this paper.

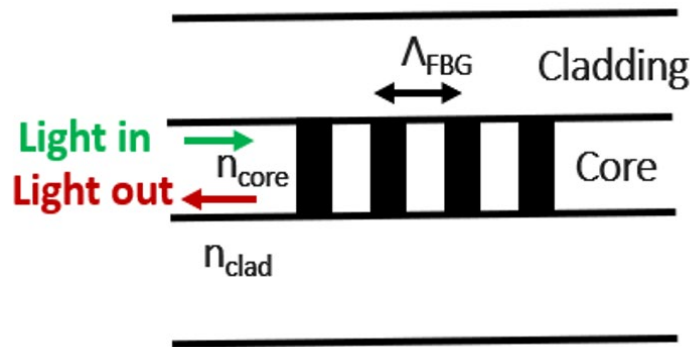
##### **4.1.1 Model for Fiber Bragg Grating**

Among the OFSs, FBG sensors are the most mature and commonly used. Substantial research has concluded that FBG sensors are very insensitive to temperatures and therefore used in nuclear reactors for monitoring real time temperatures[30], [31], [136], [165]–[167]. Considerable progress has been made to understand how radiation affects the

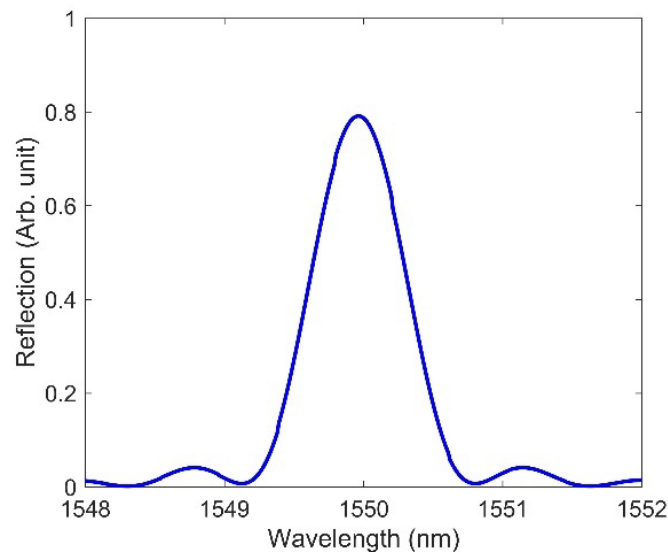
transmission characteristics of optical fiber[72], [159]. However, an in-depth understanding of radiation effects on optical fiber and fiber optic sensors are required for their reliability and survivability. A quick recap from chapter 1: An FBG is created by generating a periodic RI modulation in the fiber core. In an FBG, the fundamental guided mode couples to the counterpropagating guided mode when the following phase-matching condition is satisfied [18]:

$$\lambda_B = 2n_{eff}\Lambda_{FBG} \quad (4.1)$$

where  $\lambda_B$  is the Bragg wavelength,  $n_{eff}$  is the effective RI of the core, and  $\Lambda_{FBG}$  is the grating period. The Bragg wavelength is very sensitive to any external changes in physical parameters such as temperature and pressure. A schematic of the FBG is shown in Fig. 4.1(a), where  $n_{core}$  and  $n_{clad}$  are the RIs of the core and cladding, respectively. To design an FBG in FIMMWAVE, we used a grating period of 0.5353  $\mu\text{m}$  to obtain a Bragg peak near 1550 nm. The effective RI we obtained for the designed FBG is 1.447714. The reflection spectrum of the designed FBG is shown in Figs. 4.1(b) with a distinct peak at 1550 nm observed.



(a)



(b)

**Figure 4.1** (a) FBG schematic, where  $n_{core}$ ,  $n_{clad}$ , and  $\Lambda_{FBG}$  are the RIs of the core, cladding, and grating period, respectively; (b) the reflection spectrum of the designed FBG for  $\Lambda_{FBG} = 0.5353 \mu\text{m}$  and grating strength  $(\Delta n) = 10^{-4}$ .

#### 4.1.2 Model for Long Period Grating

LPGs have also been tested in nuclear environments[40], [41], [168]. An LPG is similar to an FBG except that it has a larger grating period (100–1000  $\mu\text{m}$  as opposed to 0.1–1  $\mu\text{m}$  which has been discussed in chapters 1 and 3. The LPGs are very sensitive devices (even compared to FBG), i.e., a small change in the physical parameters can cause a large shift in the resonance wavelength. LPGs are typically used to sense temperature,

pressure, and external RIs[37], [39]. We chose an LPG with a grating period of  $348 \mu\text{m}$  in order to achieve at least one resonance dip close to the  $1550 \text{ nm}$  wavelength, for which several sources and detectors are commercially available. The schematic and transmission spectrum of the designed LPG are shown in Figs.4.2 (a) and 4.2(b), respectively. For a

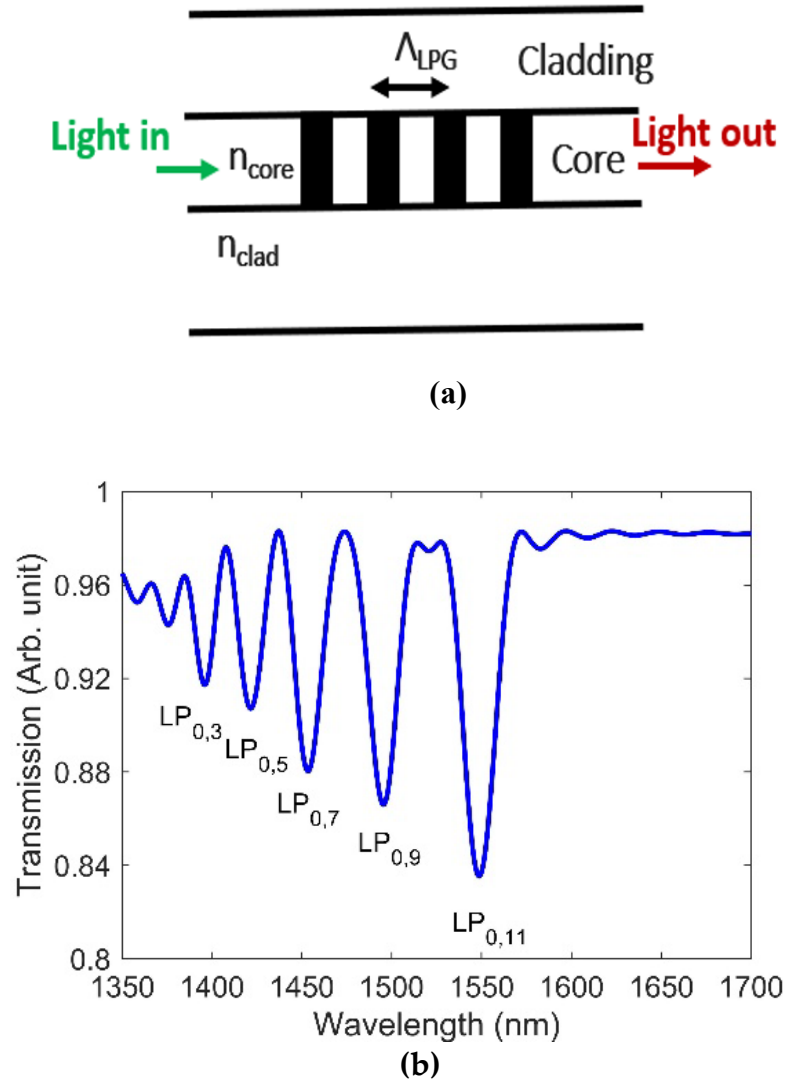


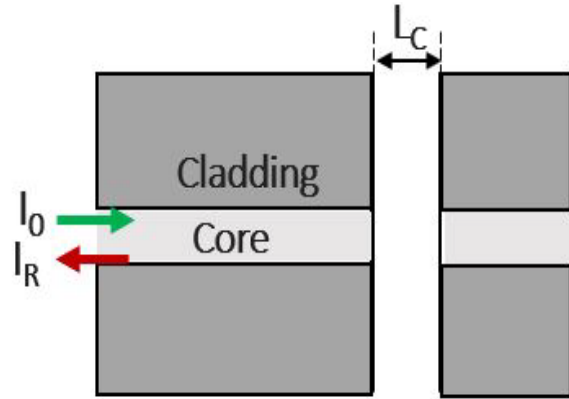
**Figure 4.2** (a) LPG schematic, where  $n_{core}$ ,  $n_{clad}$ , and  $\Lambda_{LPG}$  are the RIs of the core, cladding, and grating period, respectively; (b) transmission spectrum of the designed LPG for  $\Lambda_{LPG} = 348 \mu\text{m}$  and grating strength  $(\Delta n) = 6 \times 10^{-4}$ .

uniform grating, the cladding modes featuring only circularly symmetric field couples to the core mode. Analysis of cladding mode resonance and coupling coefficients shows that

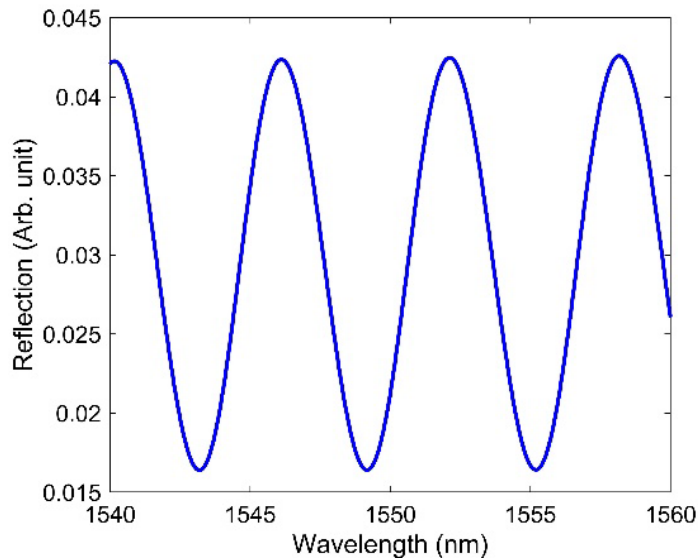
low-order even modes (e.g., 2, 4, 6) contain very little power in the fiber core, whereas low-order odd modes (e.g., 1, 3, 5) have a peak localized in the core[169]. As a result, the coupling between the low-order even modes and the fundamental core mode of the fiber is expected to be very weak. In our designed LPG, the core mode couples to five odd-number cladding modes ( $LP_{0,3}$ ,  $LP_{0,5}$ ,  $LP_{0,7}$ ,  $LP_{0,9}$ , and  $LP_{0,11}$ ), thus supporting the cladding mode analysis discussed in[169]. Please note that the resonance wavelength for coupling to the  $LP_{0,11}$  cladding mode is situated at 1550 nm.

#### 4.1.3 Model for Fabry-Perot (F-P)

F-P sensors feature several potential applications for nuclear environments, due to their insensitivity to radiation [60], [61], [162]. An F-P interferometer consists of two reflective surfaces surrounding a cavity. In an intrinsic F-P interferometer, the fiber, mirrors, and cavity are made within a single fiber. In contrast, in extrinsic F-P interferometer (EFPI)



(a)



(b)

**Figure 4.3** (a) Schematic of an EFPI, where  $I_0$ ,  $I_R$ , and  $L_C$  are the incoming light, reflected light, and cavity length, respectively; (b) interferometric fringes obtained due to interference within the cavity length  $L_C = 200 \mu\text{m}$ .

sensors, the cavity (containing either a different medium or air) is situated between a fiber tip and an external reflecting mirror. A schematic of an EFPI is shown in Fig. 4.3(a). The interferometric fringes of the simulated F- P sensor with a cavity length of  $200 \mu\text{m}$  are shown in Fig. 4.3 (b). Please note in all the designs of FBG, LPG, and F-P simulated in the paper, the same fiber parameters values as described in the beginning of this Chapter were used.

## 4.2 Numerical Analysis of How RIC Affects OFS at Low Doses

To study how RIC affects OFS at low doses, we applied the change in RI values that resulted from the RIC observed by Kher et al.[123] (see Table 4.1) to our simulation models. Kher et al. derived the gamma-ray-induced RI change of a single-mode fiber by observing the resonance wavelength shift in an LPG. They used CO<sub>2</sub> lasers to inscribe the LPG. However, please note that inscription techniques of gratings play a crucial role in sensing different physical parameters in radiation environment. It is well known that radiation significantly affects the basic characteristics of FBG sensors such as peak wavelength, spectral width, and amplitude and the magnitudes of these changes largely depend on the grating type and fabrication technique[136]. Similar to FBG, radiation also changes the structural parameters of LPG and again it depends on the inscription technique, grating type, and composition of fibers[41], [168], [170]. It has been reported that fs-etched compared to conventional UV irradiated gratings can survive a long time in radiation environments without significant degradation of gratings parameters[32], [136], [161]. In this section, we present our simulation results regarding how RIC affects the aforementioned sensors, based on these observed changes in the RI.

**Table 4.1 Radiation-induced RI changes in a B/Ge codoped fiber reported by Kher et al. [123].**

Dose (kGy)	Refractive index change ( $\Delta n_{core}$ )
6.5	$0.21 \times 10^{-4}$
10.4	$0.25 \times 10^{-4}$
102	$0.60 \times 10^{-4}$
1049	$1.60 \times 10^{-4}$
1540	$1.85 \times 10^{-4}$

#### 4.2.1 RIC Effects on FBG

The radiation-induced RI changes shown in Table 4.1 are applied in the FBG model to observe their effects on the FBG spectra. Please note that we added the RI change values to the grating portion (in both high and low RIs). Figure 4.4 plots the Bragg wavelength changes due to RIC at various doses. We observed that increasing the dose resulted in a redshift in the Bragg peak, since increased RI shifts the Bragg wavelength to the longer wavelength side, as per Eq. (4.1). A high dose (1540 kGy) provides the largest Bragg peak amplitude in comparison with a no-dose condition—something unusual for an FBG under a radiation field. It was reported that increasing the radiation dose degrades the amplitude of the Bragg peak, due to the significant attenuation caused by radiation-induced color-center generation[31], [72], [109]. If the attenuation effects are not considered, Fig. 4.4 would indicate that an increasing RI change resulting from the radiation dose is accompanied by an increase in the amplitude of the Bragg peak, since we are independently analyzing the RIC effect. While our preliminary simulation results showed a redshift of the

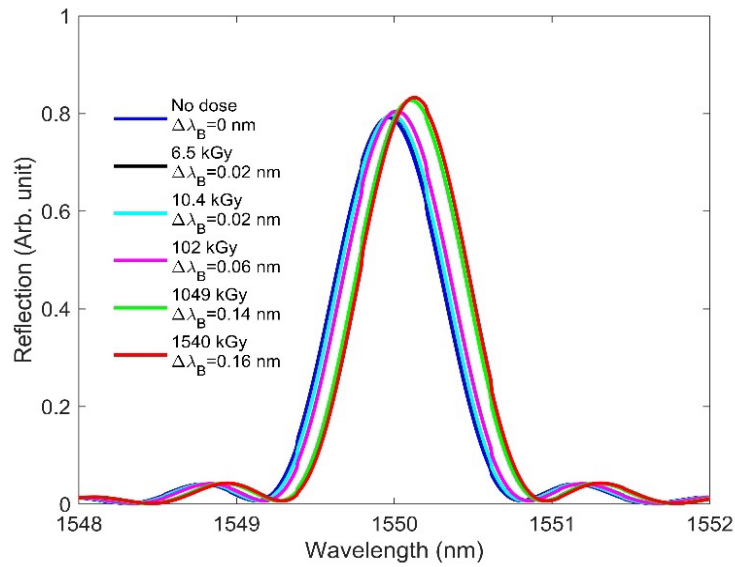


**Figure 4.4 RIC effects on FBG: redshift in the Bragg wavelength from 1550 to 1550.16 nm as the dose is increased from 0 to 1540 kGy, where  $\Delta\lambda_B$  denotes the Bragg wavelength shift.**

Bragg wavelength as a function of increasing doses, this contradicted the experimental findings reported in[30], [31], [128]. In the next section, we discuss another key aspect—one that involves RIC effects and considers the length change—for accurately predicting the resonance shift behavior in FBG.

#### 4.2.2 RIC Effects on FBG Considering Length Change

While our simulation results for FBG demonstrate a redshift of the Bragg wavelength ( $\lambda_B$ ) due to the radiation-induced RI change, experimental results reported in[30], [31], [128] showed a radiation-induced blueshift of  $\lambda_B$ . Comparing the simulation results to the experimental work reported in[30], [31], [128] suggests that additional parameters must be considered for simulating our designs.

In our earlier simulation, we did not consider material density variations due to changes in the RI, as described by the Lorentz-Lorenz relation[135] given by:

$$\frac{n^2-1}{n^2+2} = \frac{4\pi}{3} N\alpha = \frac{4\pi}{3} \left(\frac{\rho N_A}{M}\right)\alpha \quad (4.2)$$

where  $n$ ,  $\rho$ ,  $N_A$ ,  $M$ , and  $\alpha$  are the RI, density of the material, Avogadro number, molecular weight, and electronic polarizability of silica glass, respectively.

A change in density modifies the volume of the fiber material and, hence, the FBG/LPG grating period as well as the cavity length for the F-P interferometer. The density change relates to the volumetric change and can be represented by the following expression:

$$\frac{\rho_2 - \rho_1}{\rho_2} = \frac{v_1 - v_2}{v_1} = C_v \quad (4.3)$$

where  $\rho_1$ ,  $v_1$ ,  $\rho_2$ ,  $v_2$ , and  $C_v$  are the initial density, initial volume, final density, final volume, and volumetric compaction, respectively. Considering the isotropic change in volume, the relationship between volumetric compaction ( $C_v$ ) and linear compaction ( $C_l$ ) can be expressed by the following equation:

$$C_l = 1 - (1 - C_v)^{1/3} \quad (4.4)$$

A linear compaction is required to observe the effect of the length (or grating period) change caused by radiation on the resonance-based sensors. The changes in density and length due to radiation-induced RI change values were calculated using Eqs. 4.2, 4.3, and 4.4, and the calculated results are shown in Table 4.2. Along with the radiation-induced RI change, we added the grating period change (linear compaction) to our FBG model in order to see their overall effect on the FBG spectra. Figure 4.5 shows the Bragg wavelength shift as a function of dose when both the radiation-induced RI and length changes were considered for simulation. It is observed that, this time, the Bragg wavelength sees

**Table 4.2** Calculated values of density and length compaction (based on the RI values) using Eqs. 4.2,4.3, and 4.4.

Dose (kGy)	$\Delta n_{core}$	$\frac{\Delta \rho}{\rho_1}$ (%)	$C_v$ (%)	$C_l$ (%)
0	0	0	0	0
6.5	$0.21 \times 10^{-4}$	0.00403	0.00403	0.00134
10.4	$0.25 \times 10^{-4}$	0.00479	0.00479	0.00159
102	$0.60 \times 10^{-4}$	0.01152	0.01152	0.00384
1049	$1.60 \times 10^{-4}$	0.03071	0.03069	0.01023
1540	$1.85 \times 10^{-4}$	0.03551	0.03549	0.01183

a blueshift with increasing doses. While the increase in the RI produces a redshift of the Bragg wavelength, the compaction of length (reduced grating period) provides a competing blueshift. As the FBG grating period is generally very small ( $0.5353 \mu\text{m}$  in our design), even a small change in length caused by radiation induces a significant blueshift in the Bragg wavelength. Figure 4.5 reveals that the length-change effect on the Bragg

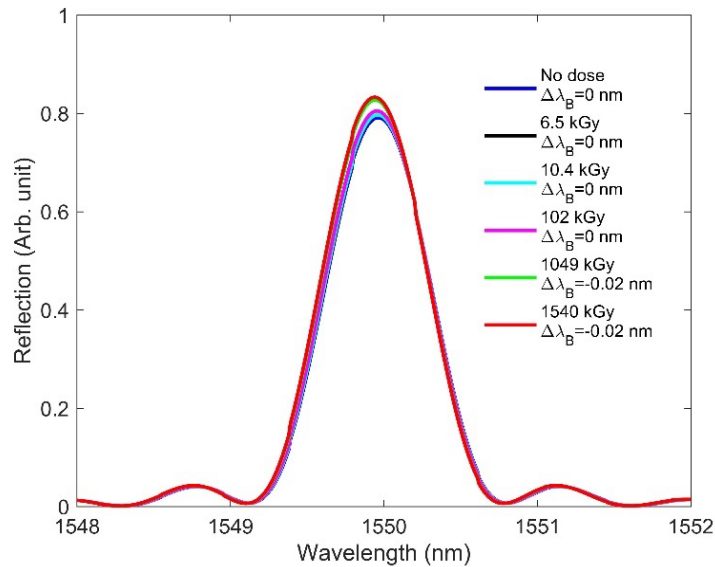


**Figure 4.5** RIC effects on FBG considering length change: blueshift in the Bragg wavelength from 1550 to 1549.98 nm as the dose is increased from 0 to 1540 kGy, where  $\Delta\lambda_B$  denotes the Bragg wavelength shift.

wavelength counteracts the RI effect, producing a zero Bragg wavelength shift up to 102 kGy. At higher doses (1049–1540 kGy), the compaction effect on the Bragg wavelength dominates; as a result, the Bragg wavelength shifts towards the shorter wavelengths, thus supporting the experimental results reported in [30], [31], [128]. Please note that in [30], [31], [128], Neutron irradiation induced shift was reported. However, both gamma and neutron irradiation alter the RI of the host fiber although their mechanism to change the RI are different [171].

#### 4.2.3 RIC Effects on LPG

Here, we analyze how RIC affects the spectra of LPG. This is accomplished by inserting the radiation-induced RI values from Table 4.1 into our design. We assume no radiation-induced change in the pure silica-based cladding RI. It has been reported that pure silica based cladding composition has been shown to be resistant to gamma up-to 1 MGy due to the absence of precursors of radiation induced color centers like NBOHC and E'-centers [91]. Since no radiation-induced change in the cladding RI is considered, the resonance wavelength is expected to shift significantly due to the large effective RI difference between the core and cladding ( $n_{eff,co} - n_{eff,cl}^m$ ). As with FBG, the RI change values due to radiation were added to the grating portion. Figure 3.6 shows the transmission spectrum for the designed LPG when only the RI change due to radiation was considered in the simulation. Please note that, throughout the paper, we only considered the resonance wavelength shift of the LP<sub>0,11</sub> cladding mode. The resonance wavelength is seen to shift from 1550 to 1588.08 nm when the accumulated dose is increased from a no-dose condition to 1540 kGy. This is due to the dependency of the resonance wavelength on the differential

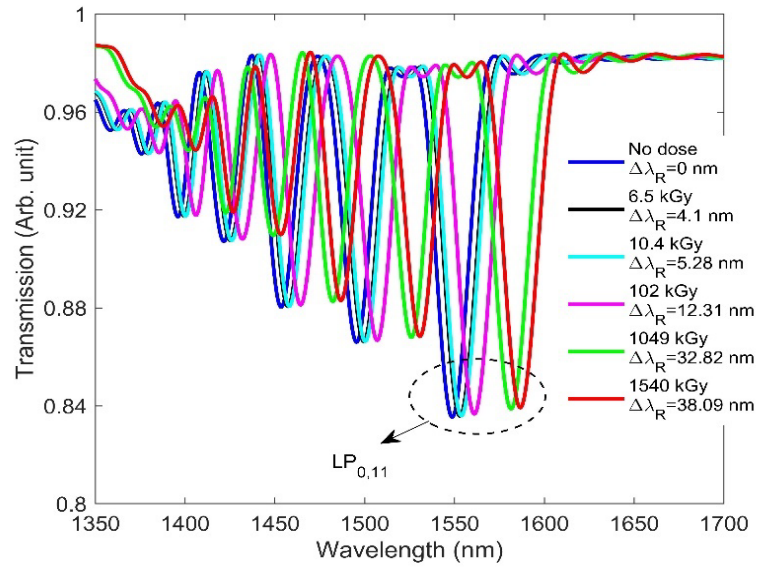


**Figure 4.6** RIC effects on the transmission spectrum of the designed LPG along with the resonance wavelength shift ( $\Delta\lambda_R$ ) for the  $LP_{0,11}$  cladding mode when dose is increased from 0 to 1540 kGy.

RI between the core and cladding. The simulation results show good agreement with the experimental results reported in [123], where the researchers demonstrated a redshift of the resonance wavelength with increasing doses.

#### 4.2.4 RIC Effects on LPG Considering Length Change

Figure 4.7 shows the combined effect of the radiation-caused RI and length changes on the spectra of the designed LPG. It is seen from Fig. 4.7 that the resonance wavelength shift is slightly smaller than when the length change was not considered (Fig. 4.6), due to the competing blueshift effect induced by the length change effect. Since the grating period of the designed LPG is  $348 \mu\text{m}$ , a small change in the grating period due to the radiation, does not significantly affect the resonance wavelength. Furthermore, the resonance wavelength shift of LPG under gamma radiation was observed which cannot be attributed to changes in grating period [123]. As a result, the effect of the RI on the LPG spectra

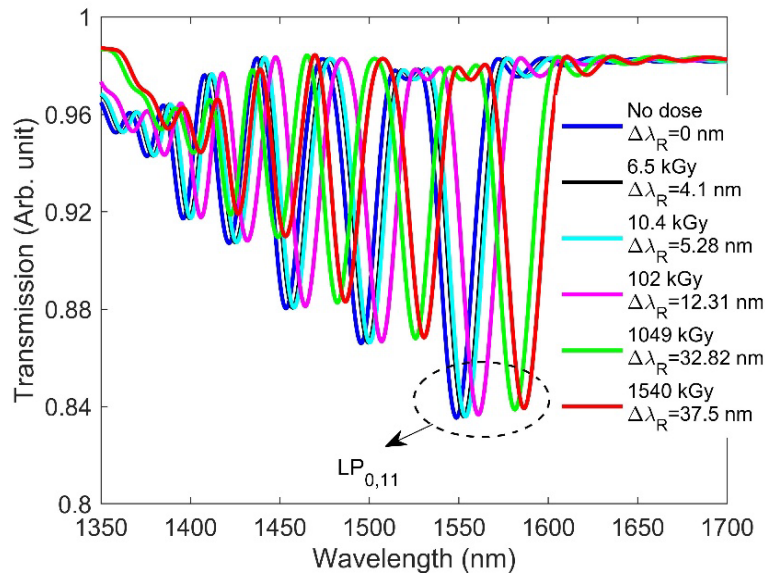


**Figure 4.7 RIC effects on the transmission spectrum of the designed LPG considering length change along with the resonance wavelength shift ( $\Delta\lambda_R$ ) for the LP<sub>0,11</sub> cladding mode when the dose is increased from 0 to 1540 kGy.**

dominates the length compaction effect, and the resonance wavelength shifts towards the longer wavelength for increasing doses.

#### 4.2.5 RIC Effects on F-P

Here, we focus on how RIC affects F-P sensor performance. We designed an EFPI in which the cavity is comprised of an air medium. We considered one end surface of the cavity to be metal and the other to be the fiber facet. Because of the air cavity, the radiation-induced RI change to the fiber did not affect the wavelength characteristics of the fringes. As a result, the free spectral range (FSR)—namely, the spectral distance between two adjacent fringe peaks—remained constant with increasing doses (Fig. 4.8).

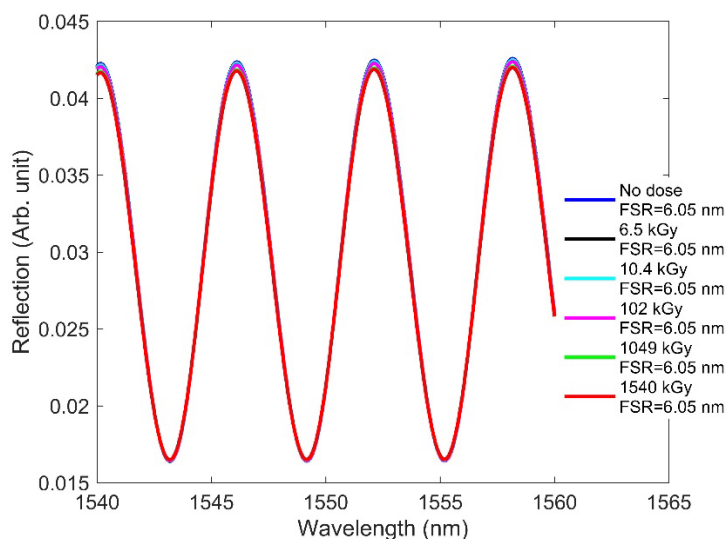


**Figure 4.8 RIC effects on the interferometric fringes of the designed F-P when the dose is increased from 0 to 1540 kGy, where FSR is the spectral distance between two adjacent fringe peaks for a given radiation.**

#### 4.2.6 RIC Effects on F-P Considering Length Change

It is necessary to consider the radiation-induced length change to observe how RIC affects the designed F-P sensor, even though the cavity medium is air. For simulation purposes, we considered a roughly 50- $\mu\text{m}$ -long fiber segment exposed to radiation beyond the fixing point for examples like in [60], and compaction was calculated for that length. The responses of the sensor can differ, depending on the choice of cavity length as well as the fiber length exposed to a radiation field. For example, F-P sensors with different lengths of lead-in fibers were intentionally exposed to radiation, and compaction was assessed on the fiber tips in [60]. The calculated length change taken from Table 4.2 was used to simulate the F-P sensor. Fig. 4.9 shows the fringe pattern and FSR of the designed F-P sensor at different doses. We observed no change in the fringe position, owing to a similarly negligible change in the effective cavity length. Of the three types of sensors studied in regard to low-dose effects, the F-P sensor was found to be the most robust to radiation.

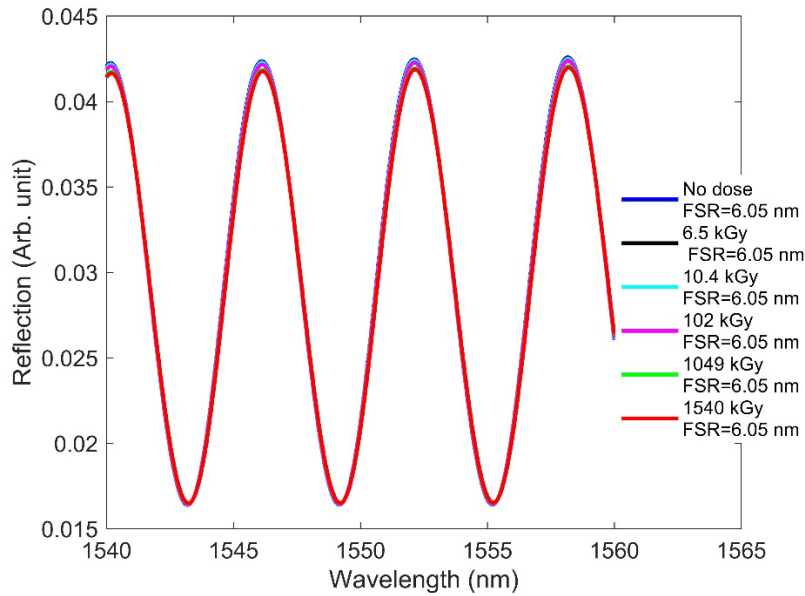


**Figure 4.9 RIC effects on the interferometric fringes of the designed F-P considering length length when the dose is increased from 0 to 1540 kGy, where FSR is the spectral distance between two adjacent fringe peaks for a given radiation.**

Thus, F-P sensors can be considered a potential candidate for measuring physical parameters in nuclear environments when the accumulated dose reaches 1540 kGy.

### 4.3 RIC Effects on OFS at High Doses

As discussed earlier, radiation alters the RI by means of compactions and creating diferent types of defects in the host fiber. Several works have been reported to observe the gamma radiation induced change in RI values in MGy doses[172]–[174] which are shown in Table 4.3. It is seen that the change in RI is not consistent with the accumulated doses since several factors, such as dose rate, composition of fibers, and irradiation temperature can affect the RI change. So far, we have considered radiation effects at lower doses. To study the effects on OFS at high doses, we used the radiation-induced density values from

**Table 4.3** Gamma radiation induced RI change in different compositional fibers at MGy dose.

Type of fiber	Dose rate	Total dose	$\Delta n_{core}$	Refs.
Telecom grade	N/A	1.6 MGy	$\sim 10^{-4}$	Gusarov et al.[172]
SMF-28	23 kGy/h	5 MGy	$1.7 \times 10^{-3}$	Kniazewski et al.[174]
Ge, N doped	20 kGy/h	7 MGy	$3 \times 10^{-4}$	Brichard et al.[173]

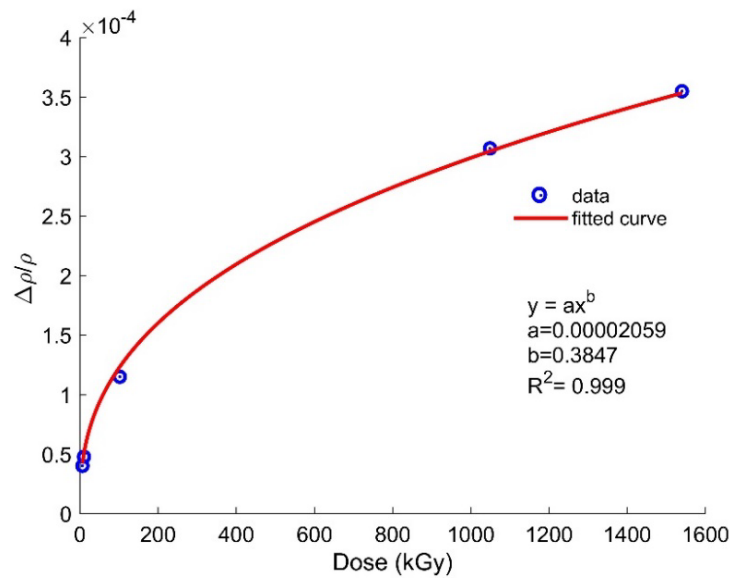


**Figure 4.10** Curve fitting for relative density as a function of dose using the values from Table 4.2.

Table 4.2 and fitted the relative density vs. dose plot using a power law fit [see Fig. 4.10]. Using the fitting constant values, we calculated the density, RI, and length changes for the sensors at higher doses of up to 7 MGy via the following power law equation[171]:

$$\frac{\Delta \rho}{\rho_1} = AD^c \quad (4.5)$$

where  $A$  is the material-dependent constant and  $c$  is another constant[171]. Based on fitting parameters, we determined the values of  $A$  and  $C$  to be 0.00002059 and 0.3847, respectively. By inserting the values of the fitting constants into Eq. (4.5), the RI and length

compaction were calculated for doses of 1.6, 5, and 7 MGy. The extrapolated data calculated by our approach is shown in Table 4.4. To validate our extrapolation, we found three experimental works within MGy regime with their modified change in RI[172]–[174] within the core shown in Fig. 4.11 along with our extrapolated data (star marker). The details of the three experimental works are given in Table 4.3.

**Table 4.4** Calculated values for higher doses, as obtained by inputting the fitting constant values from Fig. 4.10 into Eq. (4.5).

Dose	$\Delta n_{core}$	$\frac{\Delta\rho}{\rho_1}$ (%)	$C_v$ (%)	$C_l$ (%)
1.6 MGy	$1.87 \times 10^{-4}$	0.03589	0.03587	0.01196
5 MGy	$2.91 \times 10^{-4}$	0.05580	0.05577	0.01859
7 MGy	$3.31 \times 10^{-4}$	0.06357	0.06353	0.02118

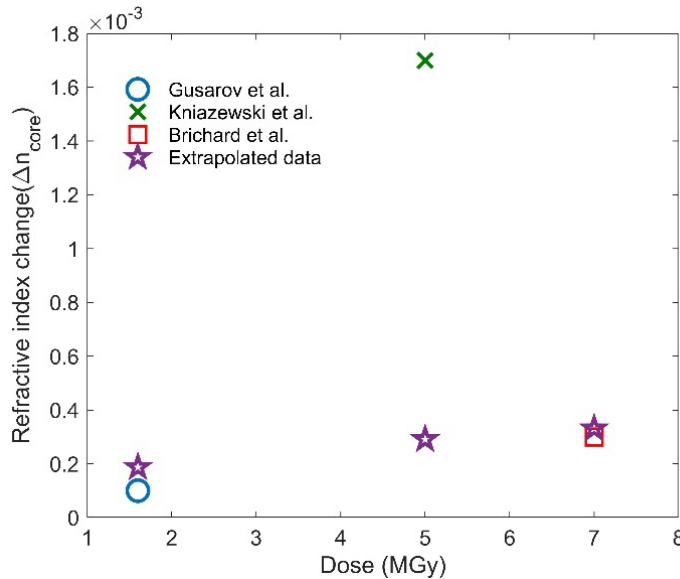


**Figure 4.11** Calculated RI with the experimental values at MGy dose.

#### 4.3.1 RIC Effects on FBG at High Doses

The effects of RIC on the FBG spectra at high doses which are similar to those observed at low doses are shown in Fig. 4.12, wherein, as is consistent with earlier

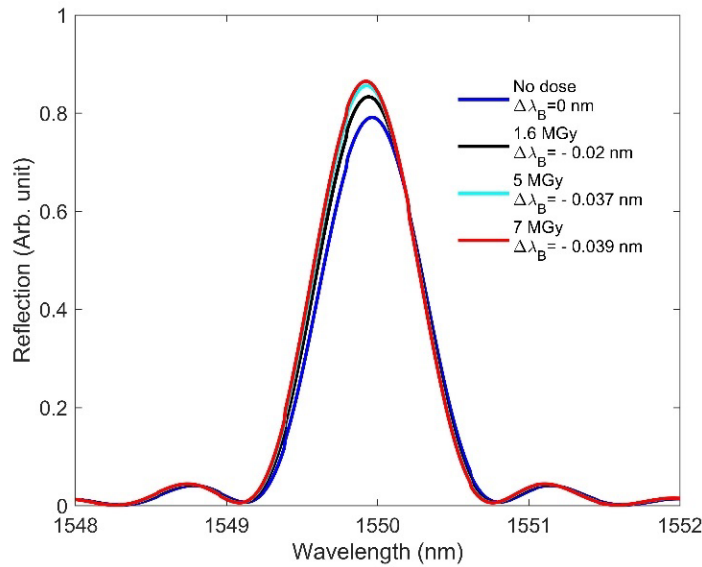


**Figure 4.12 RIC effects on FBG at high doses: blueshift of 0.039 nm in the Bragg wavelength when the dose is increased from 0 to 7 MGy and radiation-induced changes in length and RI are considered.**

observation, we see a significant blueshift in the Bragg wavelength when increasing the dose from 0 to 7MGy. As the radiation-induced changes in length compaction and RI are significant at high doses, the Bragg wavelength shows a large blueshift of 0.039 nm. At high doses, the length compaction effects on the Bragg wavelength completely dominate the RI effect by producing a blueshift.

#### 4.3.2 RIC Effects on LPG at High Doses

The effect of RIC on LPG at high doses is shown in Fig. 4.13. It is seen that, as the dose increases from 0 to 7 MGy, the resonance wavelength shifts significantly towards longer wavelengths. As mentioned in Section 4.1.2, a small radiation-induced RI change creates a large effective RI difference ( $n_{eff,co} - n_{eff,cl}^m$ ) between the core and cladding modes. Table 4 shows that the radiation-induced RI change is large enough to produce a 86.14 nm redshift of the resonance wavelength at a dose of 7 MGy. Although the radiation-induced length compaction is large at high doses, it has little effect on the resonance

wavelength shift. This is because, compared to the grating period of the designed LPG, it is still very small. For a better understanding of how radiation affects LPG, it is important to consider the RI change in the coupled cladding modes from the phase matching curve in order to correct the excessive shift of the resonance wavelength[175].

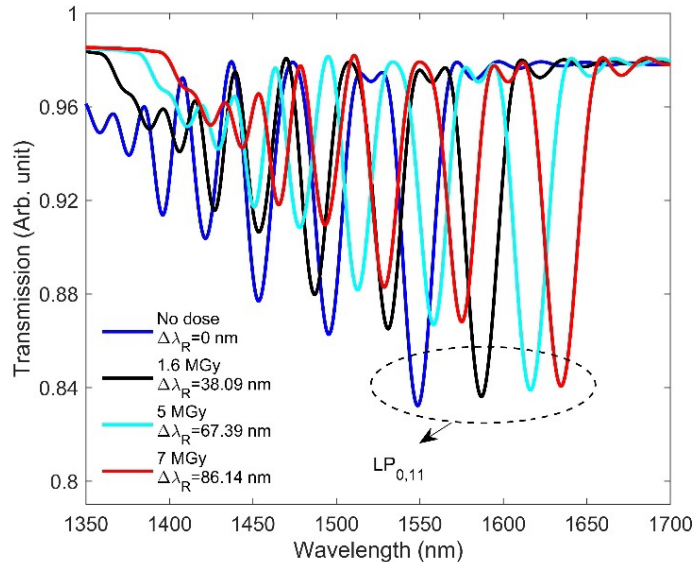


**Figure 4.13** RIC effects on the transmission spectrum of the designed LPG at high doses.

#### 4.3.3 RIC Effects on F-P at High Doses

The effect of RIC on the spectrum of the F-P interferometer at high doses is shown in Fig. 4.14. Even at high doses, no change of fringe spacing can be observed. As the exposed length utilized to observe the compaction effect was only 50  $\mu\text{m}$  in our designed F-P sensor, the radiation-induced length compaction remains very small compared to the cavity length of 200  $\mu\text{m}$ . The cavity length will change significantly—and hence the FSR as well—if the length exposed to the radiation is large and the compaction is assessed using that large length.

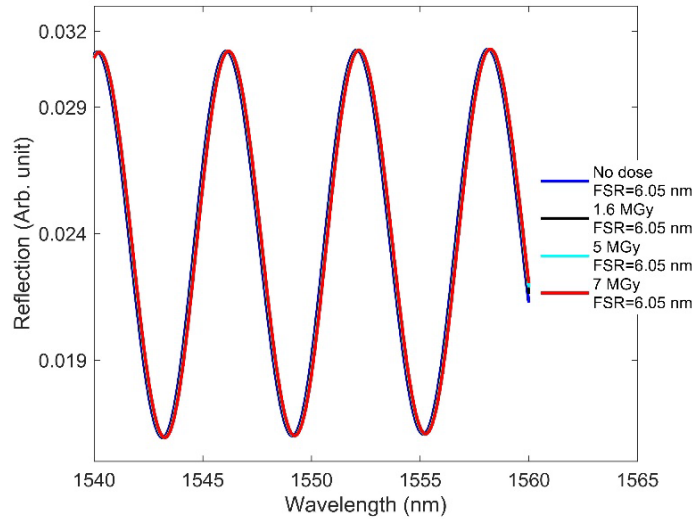


**Figure 4.14 RIC effects on the interferometric fringes of the designed F-P sensor at high doses.**

#### 4.3.4 RIC Induced Temperature Error

The temperature sensitivities of SMF-28-based FBG and LPG sensors are 10 and 92 pm/°C, respectively [32], [33], [39], [135]. For F-P sensors, depending on their structure, the sensitivity can differ: 13.6 pm/°C [55], 1.56 and 1.87 nm/°C [176], 5.2 nm/°C [177], and 11.86 and 19.55 nm/°C [178]. Radiation-induced shift in wavelength of fiber sensors causes temperature measurement error if these sensors are used for temperature sensing. Table 4.5 shows the temperature errors of these three types of sensors at different doses. Please note that the temperature error for the F-P sensor was calculated by considering the lowest sensitivity of 13.6 pm/°C. We observe that, in LPG, a small change in core RI due to radiation induces a significant wavelength shift and hence the radiation-induced temperature measurement error, most probably as a result of not considering the radiation-induced RI change of the coupled cladding modes. For FBG and F-P, even at high doses the radiation-induced temperature error is quite small, as is acceptable in nuclear environments. We calculated errors based on the wavelength shift for all sensors. While

the maximum error in temperature measurement for FBG is 3.9°C, it is only 0°C for F-P. Based on the wavelength shifts of the three types of sensors, the F-P sensor seems to show the most radiation-resistant response under high-radiation environments, both at low and high doses.

**Table 4.5 Radiation-induced temperature errors in FBG, LPG, and F-P sensors at higher doses.**

Dose	Temperature error		
	FBG	LPG	F-P
1.6 MGy	2°C	414°C	0
5 MGy	3.7°C	732°C	0
7 MGy	3.9°C	936°C	0

#### 4. 4 RIA Effects on OFSs

In this section, we present the independent effect of RIA on the three types of OFSs. RIA darkens fibers under radiation environments, and is heavily dependent upon dopants and defects[30], [72], [135]. Each different fiber composition will produce a different RIA effect. However, the overall trends remain consistent for any type of fiber. The RIA values obtained in[179], [180] are shown in Table 4.6, and these were used when designing sensors in FIMMWAVE. To compute the effect of RIA, we inserted into our sample FBG, LPG, and F-P models (discussed in Section 4.1) the loss values from Table 4.6, as obtained from[179], [180]. To observe how RIA affects FBG and F-P, we assumed that a 5-m length of fiber was exposed to radiation. The intensity was then calculated using different radiation values for these sensors. The RIA effects on the three types of sensors are shown in Figs. 4.15 and 4.16. The amplitude of the reflected light in FBG (Fig. 4.15[a]) and F-P

**Table 4.6 RIA values obtained from [180].**

Dose (kGy)	Dose rate (rad/min)	Loss (dB/km)	Loss (cm <sup>-1</sup> )
0	0	0	0
1	0.01	2.1	0.00009
1	0.1	2.96	0.00012
66	333	48	0.00208
85	167	50	0.00217

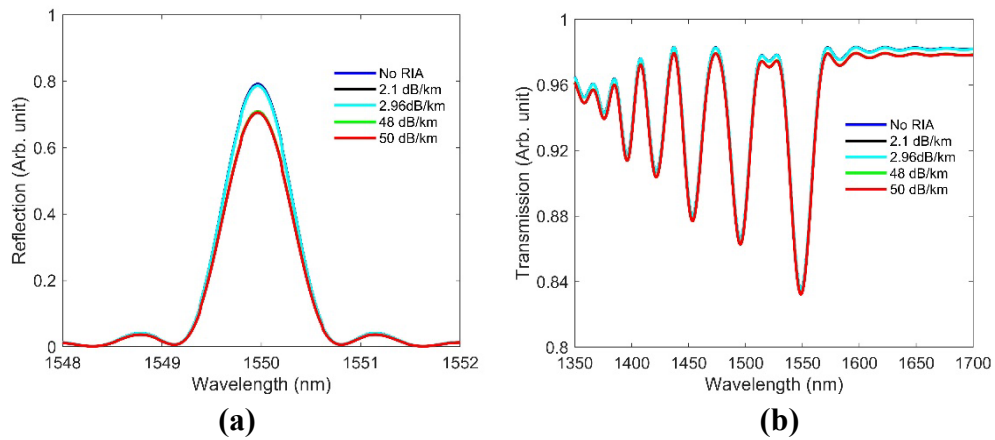


**Figure 4.15 Effect of RIA on the spectra of (a) FBG and (b) LPG, using the same design parameters applied earlier.**

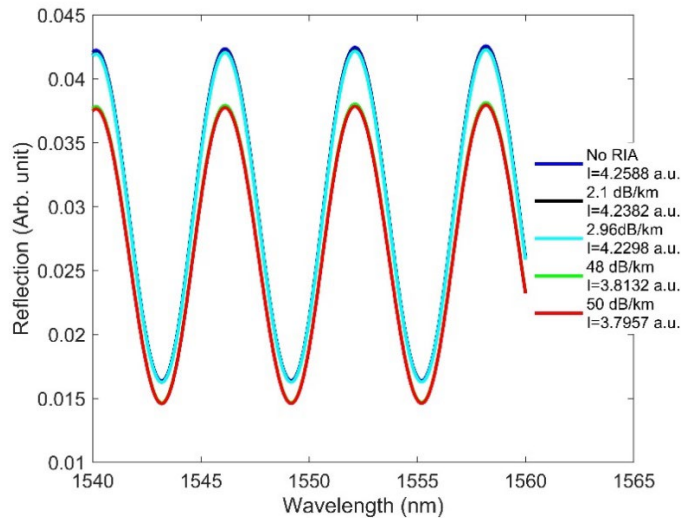


**Figure 4.16 Effect of RIA on F-P at various doses, using the same design parameters applied earlier.**

[Fig. 4.16] is seen to reduce with increasing RIA, as expected. The LPG sensor responded to increasing RIA with a larger dip in its transmitted spectrum (improved contrast), whereas no change in contrast occurred for FBG and F-P as a result of RIA. We believe this is because the sensor lengths for FBG and F-P are very small compared to that of LPG. In the case of FBG, there was no contrast variation, since RIA affects the Bragg peak and sidelobe peaks equally. It is also apparent from Figs. 4.15 and 4.16 that RIA only reduces the signal strength, without affecting the resonance wavelength position. Future work is needed to include the effects of both RIC and RIA and compare them against experimental results.

#### 4.5 Radiation Exposure of FBGs

So far the radiation effects on OFSs have been discussed numerically and it has been shown that FBG and F-P are the two potential candidates for monitoring temperature in a radiation environment. In the next few subsections, we will discuss about the high neutron and high temperature effects on FBGs. As discussed earlier, FBGs are the most

matured and commonly used OFSs. However, the stability of the grating and performance of FBGs largely depends on the grating inscription techniques. FBGs are classified as Type I, Type II, Type IA, Type IIA based on the grating writing techniques, and the effect of radiation on these different types of FBGs were thoroughly discussed in[136]. In the radiation experiment, we exposed Type I regenerated FBGs for their excellent temperature and radiation stability[181]. In order to fabricate regenerated FBGs, the type I gratings were inscribed in photosensitive SMF-28 fiber by CEA, France. The regeneration occurred when these “seeds” gratings were heated above a certain temperature until its erasure. The details of the type I regeneration gratings can be found in[181]. The irradiation test was carried out in the Advanced Test Reactor (ATR) at Idaho National Laboratory for approximately 500 effective full-power days over a temperatures range of 750°C–1350°C, depending on the specific capsule. In studying the response of FBGs, we found that at the end of irradiation cycles, only one of 10 FBGs had a visible peak, while radiation-induced Bragg wavelength shifts (RI-BWS) for that FBG varied from few a picometers to ~ 2.5 nm. This high RI-BWS can be attributed to the significant changes in the grating period and refractive index (RI), as caused by material compaction due to high neutron fluence. Using various approaches, we calculated the RI change due to temperature dependent radiation induced compaction, then compared their corresponding values. A better understanding of compaction—and hence the changes in the grating period and RI of FBGs exposed to nuclear environments may unlock many possibilities for fiber optic sensors applications in harsh conditions.

#### 4. 6 Irradiated FBGs

As part of the Advanced Gas Reactor (AGR)-5/6/7 irradiation experiment, two optical fibers, each containing five Bragg gratings were irradiated. The type I gratings were written in photosensitive SMF-28 fiber by CEA (France). Regeneration occurred when these “seed” gratings were heated above a certain temperature until its erasure. Details on the regenerated type I regeneration gratings can be found in [181]. AGR 5/6/7 was conducted as part of the U.S. Department of Energy AGR Fuel Development and Qualification Program. Capsule 5 contained the OFS and was located on the top of the test train to enable easier access for the instrumentation lead-out tube. The irradiation was planned for approximately 500 effective full-power days (corresponding to about two and a half calendar years), with peak fuel temperatures of 750 and 1350°C, depending on the specific AGR capsule. The two optical fibers containing the Bragg sensors and the thermocouples (TC) were inserted from the top of the capsule. The gratings, which were essentially identical, were labeled #1–5 with grating #5 being the one closest to the distal end of the probe and furthest into the ATR core as shown in Fig. 4.17. Gratings #1 and #2 were above the ATR driver fuel (“out of core”). During installation, the optical fiber probes were initially connected incorrectly. The first opportunity to correct this error was after 1200 hours of reactor operation. After correcting the connections, it was determined that one probe had been broken during installation, and that the other was working properly. Each grating was 3 mm long, and they were spaced 30 mm apart, center-to-center, for a total of 5 temperature measurements within 120 mm. The optical fiber sensors were encased within a metallic capillary tube 300 mm in length, thus constituting the probe. The Figure 4.18 shows the thermal modeling of temperature in extreme capsule as a function

of length for the entire irradiation cycle. Figure 4.19 shows the spectra of the five FBGs prior to their being irradiated. Among these FBGs, FBG1(Grating#1) and FBG2(Grating#2) survived for a long time.

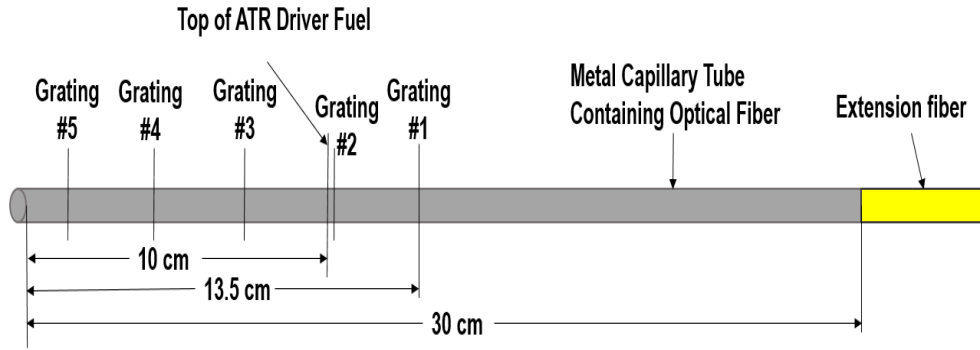


**Figure. 4.17** The Bragg grating sensors are spaced 3 cm apart from the end of the optical fiber.

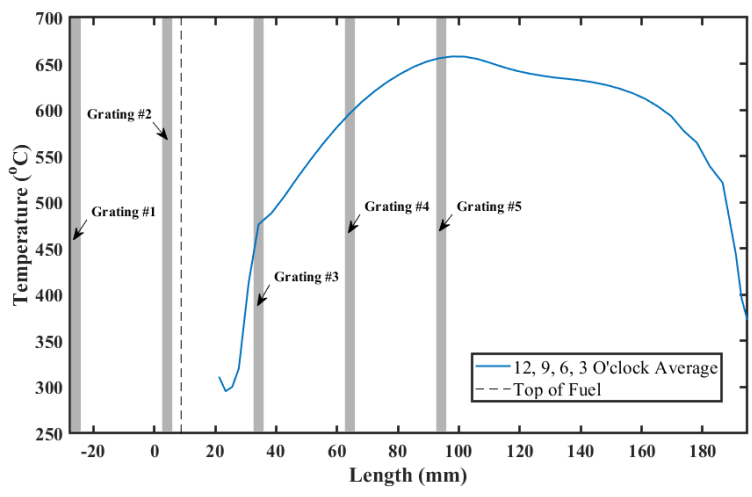


**Figure 4.18** Thermal modeling of temperature in the experiment capsule.

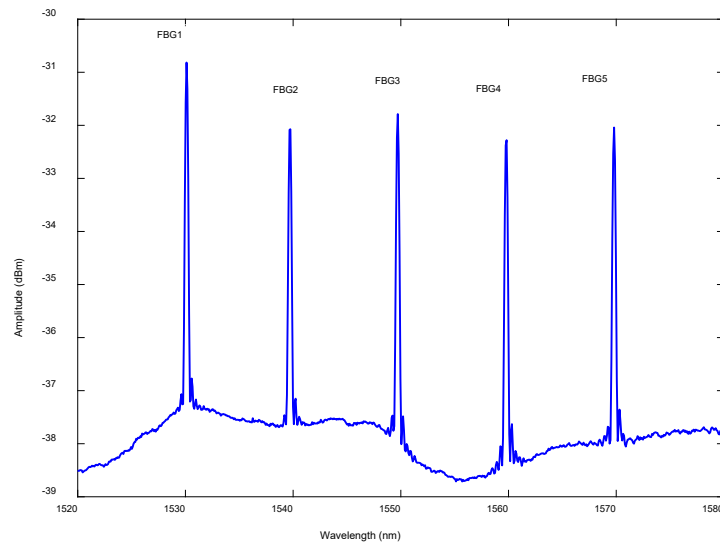


**Figure 4.19 Spectra of five FBGs prior irradiation.**

#### 4.7 Results and Discussion

The spectral response of FBGs throughout the irradiation time is shown in Fig. 4.20. No visible peaks were seen prior to 1200 irradiation hours, and the reason was improper installation and then corrections as described. Of five FBGs irradiated, only three (FBG1, FBG2, and FBG3) survived after 1200 hours, and their corresponding peaks are situated at wavelengths of 1530 nm, 1540 nm, and 1550 nm, respectively. Depending on the location and the accumulated fluence experience, FBG1 survived for a long time compared to the FBG2 and FBG2. It is also seen from Fig. 4.20 that the peak of FBG2 disappeared between 5000 and 6000 irradiation hours whereas FBG3 disappeared between 3500 and 4500 hours. Irradiation temperature measured by thermocouple (right y-axis) and accumulated neutron fluence (left y-axis) as a function of irradiation time is shown in Fig 4.21 for FBG1(solid line), FBG2 (dashed line), and FBG3 (dotted line). It can be seen from Fig. 4.21 that while the reactor was turned off, the temperature dropped and the neutron fluence remained at a constant value. The accumulated neutron fluence experienced by FBG1, FBG2, and FBG3

at the end of irradiation cycle were  $\sim 2.02 \times 10^{21} \text{ n/cm}^2$ ,  $\sim 5.7 \times 10^{21} \text{ n/cm}^2$ , and  $\sim 1.04 \times 10^{22} \text{ n/cm}^2$  respectively. At the end of the irradiation cycle [Fig. 4.20], we found that the peak of FBG1 was visible while all others disappeared. Such disappearance of the

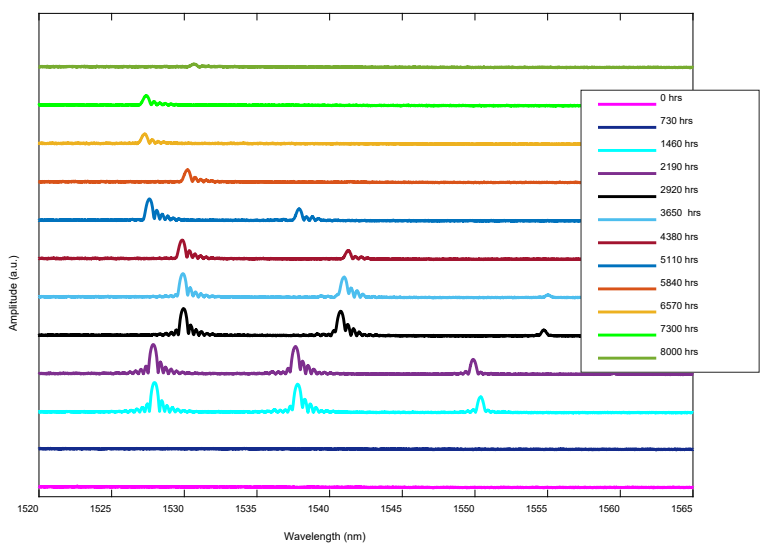


**Figure 4.20** Spectra of all survival FBGs with irradiation hours.

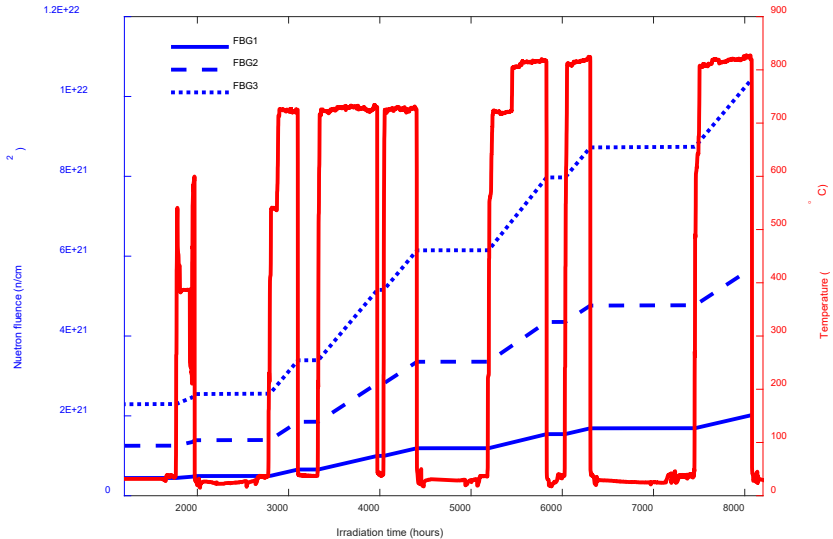


**Figure 4.21** Neutron fluence (left) and thermocouple temperature (right) as a function of irradiation time.

FBG can be attributed to the high neutron fluence and high temperatures which degrade the FBG's peak significantly. It is logical to predict that FBG3 will disappear first, followed by FBG2 and then FBG1 for experiencing high neutron fluence as well as high temperature.

#### 4. 7.1 Effects of RIA on Irradiated FBGs

We analyzed the RIA of all three FBGs, based on the peak amplitude value. Please note that while we analyzed the RIA of FBG1 for entire irradiation cycle, it was up to 3615 and 5480 irradiation hours due to the complete erasure of Bragg peaks for FBG2 and FBG3, respectively. The difference between the peak amplitudes prior to and during the irradiation of the FBG of interest provides the RIA. It can be seen from Fig. 4.22 that the RIA increases in FBGs during irradiation and recovers during the reactor off condition. An unexpectedly large RIA can be observed at the start of the irradiation since no peak was visible before 1200 hours of irradiation time and it was due to the incorrect installation of FBGs. It is

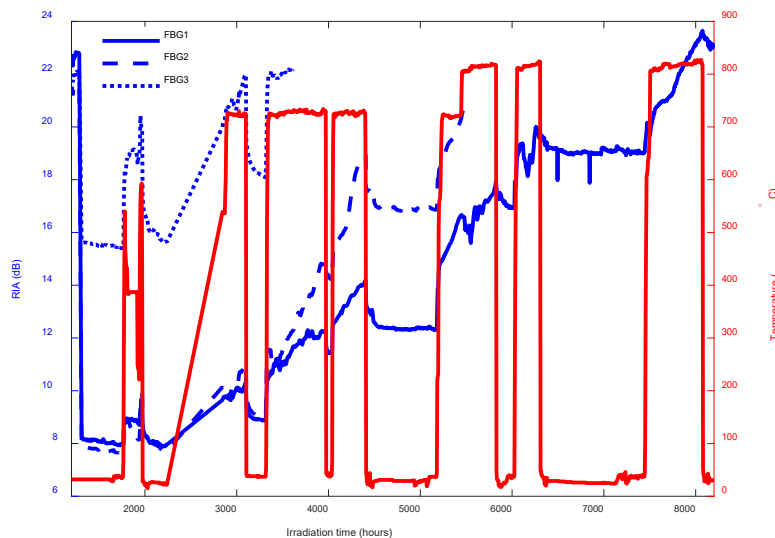


**Figure 4.22 RIA and irradiation temperature as a function of irradiation time.**

seen that the RIA starts from some values greater than 0 dB and the reason is that there was a fiber installation problem that affected the first 1200 hours, meaning that data was

analyzed after that time period. Since the FBGs had already experienced high neutron fluence prior to 1200 hours, the RIA started greater than 0 dB. The RIA of FBG2 and FBG3 are high compared to that of FBG1. There are two possible reasons for this: (1) they experienced higher neutron fluence than did FBG1, and (2) they experienced higher irradiation temperature. While the first statement is true as validated by the accumulated neutron fluence [see Fig. 4.21], the second statement is mere hypothesis, which will be discussed later. The amount of recovery for the FBGs during the reactor off condition was ~2 dB, as is consistent with the Ref.[129].

#### 4.7.2 Effects of RIC on Irradiated FBGs

Compaction changes the RI as well as the length (grating period) of the FBG, thus shifting the Bragg wavelength. The effect of neutron fluence on the Bragg wavelength is shown in Fig. 4.23, revealing that that the Bragg wavelength provides a large blue shift at low temperature, but a smaller one at high temperatures. It makes sense because blueshift in Bragg wavelength by neutron induced compaction is partially compensated for by thermally induced redshift. It can also be noticed from Fig. 4.23 that, while FBG1 shows a large blue shift for almost an entire irradiation cycle, FBG3 shows a redshift before it's disappearance. The FBG2 shows both a blueshift and a redshift of Bragg wavelength. This behavior can be explained on the basis of the temperature effect and the position of the FBGs. Although FBG2 experienced a higher fluence than did the FBG1, it shows redshift also. This may be because FBG2 experienced higher temperature than the FBG1, significantly compensating for the compaction effects. In the case of FBG3, the temperature effects dominated the irradiation effects throughout the irradiation cycle by providing a significant redshift. Therefore, it can be said both the high neutron fluence and

the high temperature caused the quick erasure of grating of FBG2 and FBG3. As FBG2 and FBG3 did not survive up to the end of irradiation cycle, all subsequent discussion on compaction will be based on FBG1. It can also be noticed from Fig. 4.23 that temperature

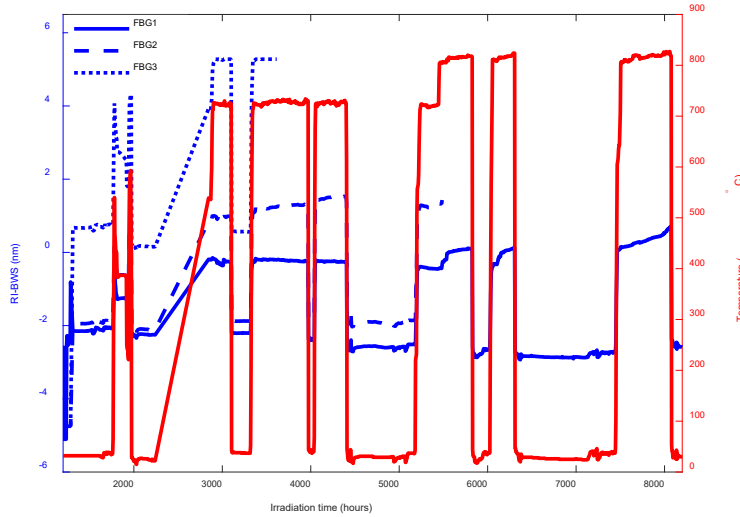


**Figure 4.23 RI-BWS of survival FBGs as a function of irradiation time.**

reduced the blueshift for FBG1. A redshift is observed between 5560 and 8200 hours during the irradiation at very high temperatures. We believe that, at very high temperatures ( $\sim 800^{\circ}\text{C}$ ), compaction of the grating period is completely compensated for by the thermal expansion of the fiber. As a result, the increased RI, resulting from both compaction and temperature causes a redshift of the Bragg wavelength.

#### 4.7.3 Calculation of Compaction and Refractive Index

The volumetric compaction under high fast neutron fluence was proposed by authors in[62] and is given by the following equation:

$$C(\varphi) = C_{\infty} \left(1 - \exp\left(-\frac{\varphi}{\varphi_S}\right)\right) \quad (4.6)$$

where  $C(\varphi)$  is the amount of compaction dependent on neutron fluence  $\varphi$ ,  $C_{\infty}$  is the equilibrium compaction, and  $\varphi_S$  is the fluence at which the fiber material gets saturated.

This equation does not consider the slight recovery of the compaction prior to reaching equilibrium compaction. They hypothesized that this small recovery of compaction is related to the ionization process rather than the knock-on process[62]. Although a fair amount of work has been performed regarding the compaction of quartz, vitreous silica, and fiber samples, the effect of high irradiation temperature has yet to be investigated[30], [31], [62], [134], [182], [183]. Recently, Petrie et al.[128], reported the effects of high neutron fluence and high temperature (688°C) on a-SiO<sub>2</sub> sample. They found compaction to be highly temperature-dependent and reported that the compaction value goes from 2.2+0.13% to 0.52+0.11% when irradiation temperature was increased from 95°C to 688°C for the same fast neutron fluence of  $2.4 \times 10^{21} n_{fast}/cm^2$ . Such change in compaction suggests that for the same amount of compaction, more neutron fluence is required at high temperatures than that at low temperature. Please note that high temperature counteracts the compaction rather than to say that compaction decreases with increasing temperature.

We for the first time, irradiated FBGs at a very high neutron fluence of  $\sim 10^{22} n/cm^2$  and at a very high irradiation temperature of  $\sim 800^\circ C$ . The temperature-dependent compaction is calculated in a fashion similar that proposed by Petrie et al.[128]

$$C(\varphi, T) = C_\infty(T) \left(1 - \exp\left(-\frac{\varphi}{\varphi_S(T)}\right)\right) \quad (4.7)$$

$$C_\infty(T) = 0.023 + 6.30 \times 10^{-6} T - 2.60 \times 10^{-6} T^2 \quad (4.8)$$

$$\varphi_S(T) = \varphi_0 \left(\exp\left(-\frac{E_a}{kT}\right)\right) = 3.42 \times 10^{19} n/cm^2 \exp\left(-\frac{0.036 eV}{kT}\right) \quad (4.9)$$

The parameters  $\varphi_0$  and  $E_a$  were calculated from the two sets of data available in the literature: (1)  $\varphi < 10^{19} n/cm^2$  and  $T = 60^\circ C$ [134]; and (2)  $10^{19} n/cm^2 < \varphi <$

$3 \times 10^{19} \text{ n/cm}^2$  and  $T = 250^\circ\text{C}$ [30]. We used the same values for  $E_a$  and  $\varphi_0$  as reported in[128].

The volumetric compaction calculated by using Eq. (4.7) is shown in Fig. 4.24 as a function of accumulated neutron fluence for different irradiation temperatures. Note that the compaction is always measured at room temperature when the fiber cools down. As the irradiation temperatures in this experiment varied between room temperature and  $\sim 800^\circ\text{C}$ , we calculated the compaction —and hence the RI for five averaged irradiation temperatures (i.e., 300, 400, 500, 600, and  $700^\circ\text{C}$ ). Figure 4.24 reveals compaction becomes saturated to a value of between 1.8% ( $300^\circ\text{C}$ ) and 0.45% ( $700^\circ\text{C}$ ) instead of 3% (which was predicted by Primak et al.[134]). The vertical dotted line shows the start of the data collection in our experiment considering the installation problem that occurred over

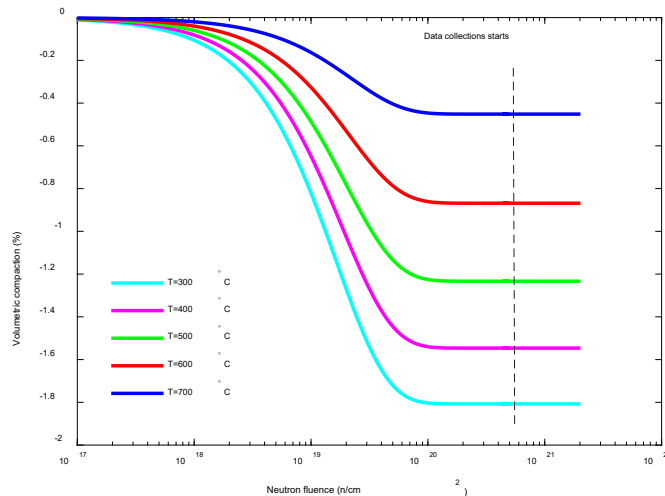


**Figure 4.24 Neutron induced volumetric compaction at five different irradiation temperatures.**

the first 1200 hours of irradiation. At the beginning of the data collection, the FBGs experienced a high fluence of  $\sim 4.4 \times 10^{20} \text{ n/cm}^2$  and amount of compaction at this fluence becomes saturated. As a result, we also calculated the amount of compaction that occurs

between fluences  $10^{17}$  n/cm<sup>2</sup> and  $10^{19}$  n/cm<sup>2</sup> (not measured fluence) to show how compaction varies with fluence before they get saturated. It can also be seen that the compaction gets counteracted by the increased irradiation temperature for the same neutron fluence which was reported in [128].

The compaction (density) change relates to the RI of the fiber via the extended point dipole theory [132]

$$\frac{n^2-1}{4\pi+b(n^2-1)} = \frac{\alpha}{M} \rho \quad (4.10)$$

where  $n$ ,  $\rho$ ,  $M$ ,  $\alpha$ , and  $b$ , are, respectively the RI of silica, the density of silica, molecular weight of silica, electronic polarizability of silica, and electronic overlap between adjacent dipoles in the silica glass. The optimized parameters reported in [132] were used to calculate the change in RI from the density. The change in RI using Eq. (4.10) due to the neutron induced compaction at different temperatures is shown in Fig. 4.25. The change in the RI increases by up to 0.56% at an irradiation temperature of 300°C. As the temperature

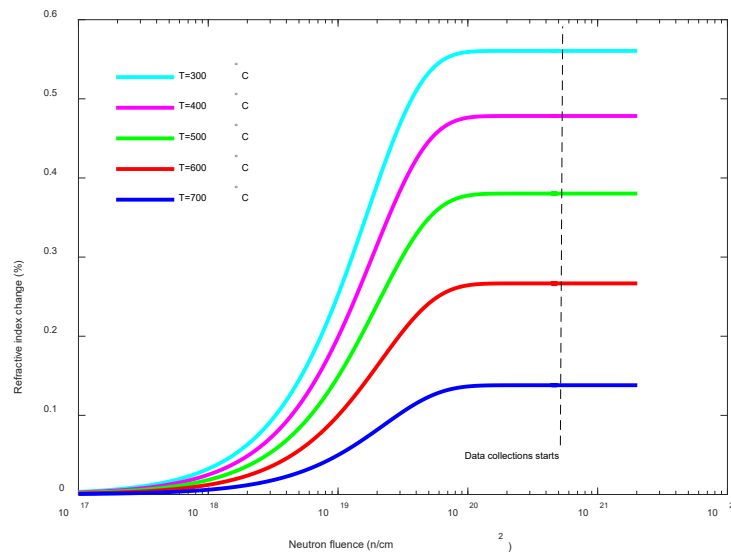


**Figure 4.25 Neutron induced refractive index variation at five different irradiation temperatures.**

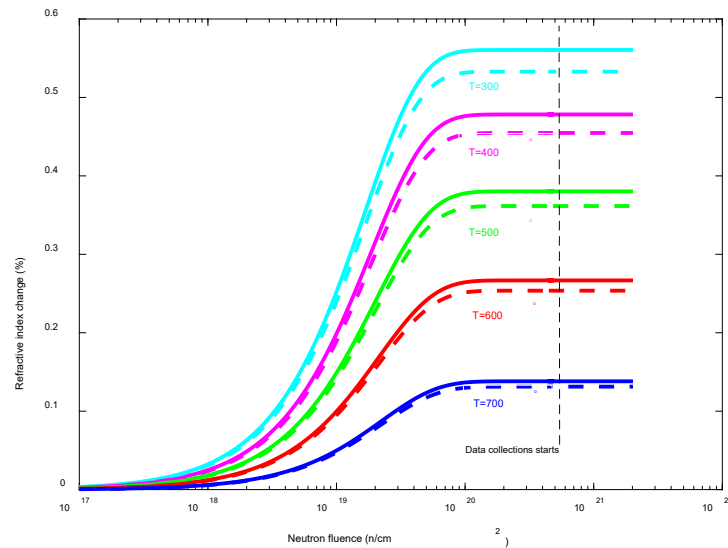


**Figure 4.26 Neutron-induced RI variation at five different irradiation temperatures, using two different approaches. Each color reflects the indicated temperature, irrespective of whether the line is solid or dashed.**

increases, it counteracts the compaction and as a result, the compaction induced RI of fiber decreases. Although temperature increases the RI silica optical fiber due to the positive thermo-optic coefficient of silica, it counteracts the neutron induced compaction significantly. As a result, at temperature of 700°C, only a small change in the RI can be observed.

We also calculated the radiation-induced refractive index change using the sensitivity factor ( $\frac{\text{change in refractive index}}{\text{change in density}} = \frac{dn}{d\rho} = 0.19$ ) reported by Devine[184]. Using the extended point dipole theory (solid line) and a sensitivity factor of 0.19 (dashed line), Fig. 4.26 shows the compaction-caused change in the RI.

#### 4.7.4 FBG Modeling Based on Experimental Data

Since compaction alters the RI as well as the grating period of the FBG, a shift in the Bragg wavelength can be expected according to Eq. (4.1). Considering the isotropic changes of volume, the linear compaction can be calculated from the volumetric

compaction using Eq. (4.4). To evaluate the effects of radiation-induced change in RI and grating period, we modeled an FBG in the MATLAB software by following the theoretical approach described in [135]. It is well known from couple mode theory (CMT) that the reflectivity ( $R$ ) of a uniform grating can be represented as follows [185], [186]

$$R = \frac{\sinh^2\left(\kappa L \sqrt{1 - \left(\frac{\delta}{\kappa}\right)^2}\right)}{\left(1 - \left(\frac{\delta}{\kappa}\right)^2\right) \cosh^2\left(\kappa L \sqrt{1 - \left(\frac{\delta}{\kappa}\right)^2}\right) + \left(\frac{\delta}{\kappa}\right)^2 \sinh^2\left(\kappa L \sqrt{1 - \left(\frac{\delta}{\kappa}\right)^2}\right)} \quad (4.11)$$

where  $\kappa = \frac{\pi}{\lambda_{Bragg}} \eta \Delta n^{mod}$  is the coupling coefficient,  $\delta = \frac{2\pi n_{eff}}{\lambda} - \frac{\pi}{\Lambda}$  and  $\frac{\delta}{\kappa}$  is the detuning ratio depending on  $\left(\frac{\lambda}{\lambda_{Bragg}}\right)$ ,  $\Delta n^{mod}$  is the grating strength. The modal overlap factor ( $\eta$ ), which defines the core power, can be expressed as [187]

$$\eta = \frac{\pi^2 \emptyset_{core}^2 NA^2}{\lambda^2 + \pi^2 \emptyset_{core}^2 NA^2} \quad (4.12)$$

where  $\emptyset_{core}$  and  $NA$  are the core diameter and the numerical aperture of the fiber respectively. The spectrum of the designed FBG using this approach is shown in Fig. 4.27. The parameters were chosen such that the Bragg peak is very close to 1530 nm. Depending on the change in the RI and the grating period (linear compaction), the Bragg wavelength undergoes either a redshift or a blueshift.

Next, we inserted the compaction-induced RI and grating period values into our FBG model to monitor the RI-BWS. Note that, in the rest of the paper, compaction-induced grating period always denotes a reduced grating period. The independent effect of the calculated RI and linear compaction (grating period) on the Bragg wavelength of the FBG is shown in Fig. 4.28. Please note that we did not insert the change in grating period into our FBG model when simulated RI effect or vice-versa. While the radiation-induced length compaction (grating period,  $\Lambda$ ) provides a blueshift in the Bragg wavelength (dashed line),

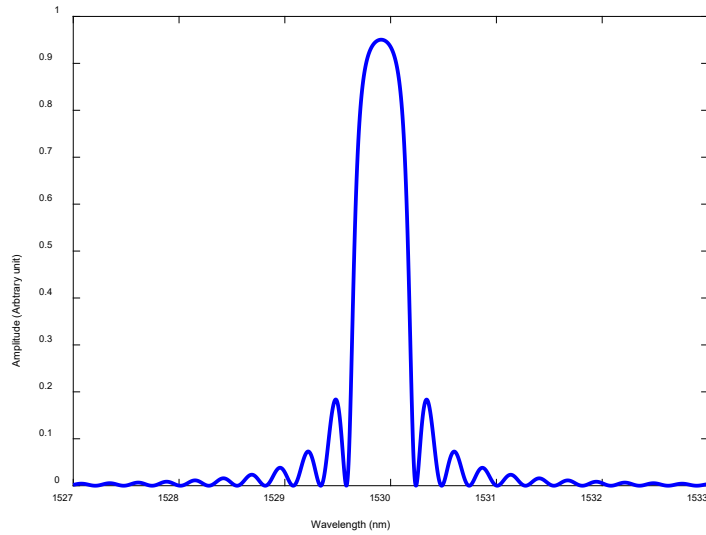


**Figure 4.27** Spectrum of FBG using equations (4.11) and (4.12).

the RI change ( $n$ ) gives a redshift (solid line), and both shifts are expected. As the fluence increases (and thus the compaction), the corresponding RI and linear compaction increases. As a result, the RI-BWS is small at low fluence and large at high fluence. The combined

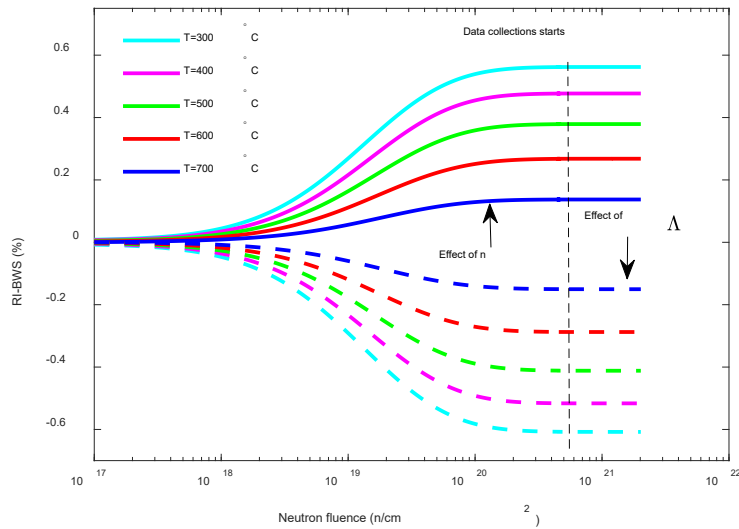


**Figure 4.28** Effect of radiation induced RI ( $n$ ) and grating period ( $\Lambda$ ) on the Bragg wavelength of the designed FBG. The legend colors indicate the same temperature irrespective of solid or dotted line.

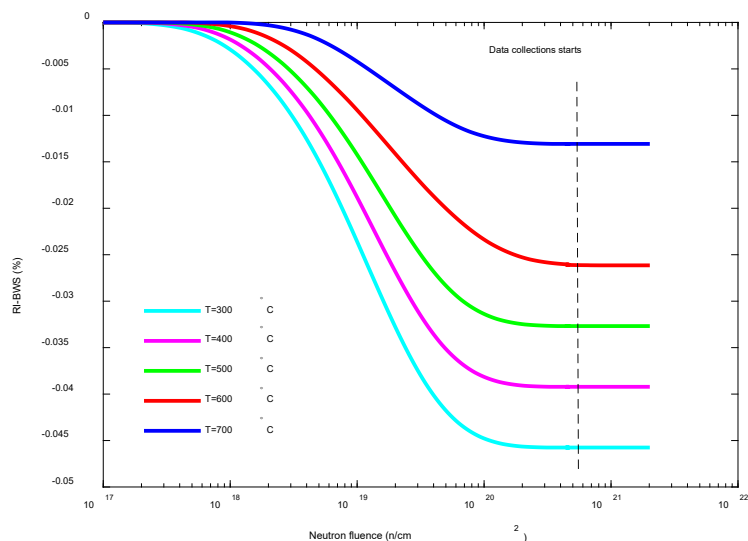


**Figure 4.29 RI-BWS at different irradiation temperatures.**

effect of radiation-induced grating period and RI changes on the Bragg wavelength is shown in Fig. 4.29. It can be seen that at the beginning (at low fluence) the RI-BWS due to grating period change almost counteracts RI-BWS caused by RI change. As the fluence increases, the effect of grating period change on the RI-BWS dominates the RI effects by providing a blueshift of the Bragg wavelength. It can also be seen that the RI-BWS decreases as the irradiation temperature increases for a given neutron fluence. It is because the temperatures partially counteract the grating period change effects on the Bragg wavelength. The maximum RI-BWS was observed to be 0.046% at a temperature at 300°C whereas the minimum RI-BWS was 0.013% for a temperature of 700°C with a saturated compaction condition. The RI-BWS in Fig. 4.23 (experimental results) at temperatures close to 300°, 400°, 500°, 600°, and 700°C, are totally different from the RI-BWS based on the modeling work.

As a final attempt, we tried to calculate the changes in the RI and the grating period by considering an arbitrary volumetric compaction of 0-3% and then observing their effect on the Bragg wavelength. The effects of RI and grating period individually as well as their

combined effect on the Bragg wavelength is shown in Fig. 4.30. It is observed that the effect of RI (solid blue line) and grating period (solid red line) on the Bragg wavelength is very close when compaction is small (0-0.1%). However, the effect of grating period dominates the effect of RI on the Bragg wavelength when compaction becomes greater, and this can be seen from the combined effect of RI and grating period (solid green line), which always lies below the zero line (dashed black line), indicating a blueshift. This modeling work also supports that it is the grating period effect over the RI, which dominates in Bragg wavelength shifting.

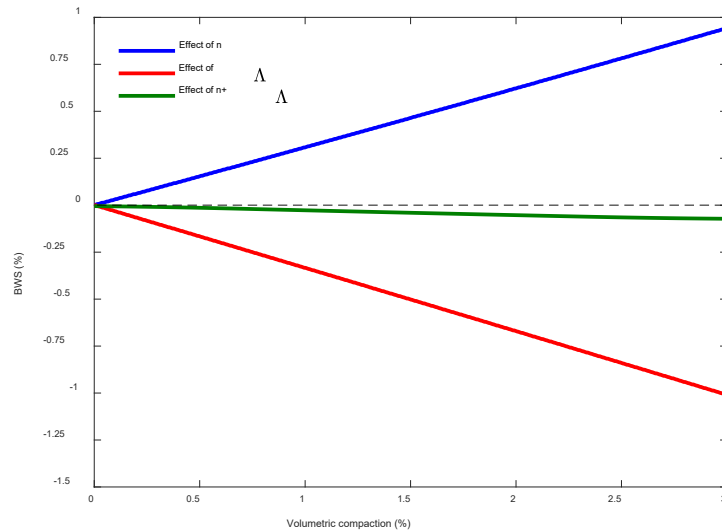


**Figure 4.30** The effects of refractive index ( $n$ ), grating period ( $\Lambda$ ), and both ( $n+\Lambda$ ) on the Bragg wavelength of the FBG modeled in MATLAB.

It is seen that the RI-BWS [see Fig. 4.29] from the modeled FBG due to the calculated values of RI and grating period from the experimental neutron fluence by using different numerical Eqs. (4.7)-(4.10) are different from the experimentally observed RI-BWS (see Fig. 4.23). It is because only compaction-induced RI variation was considered. However, RI may change due to RIA, stress relaxation, compositional exchange, dose,

dose rate, etc. To predict the correct RI-BWS, it is necessary to consider the RI change caused by the specific phenomena to which the fiber is subjected, including RIC, RIA, dopant diffusion, temperatures, dose, and dose rate, etc. An on-line measurement of the radiation-induced RI and length changes can be a potential way for understanding the structural changes of optical fiber and measuring the RI-BWS in an FBG in a nuclear environment.

In summary, in this chapter, first the RIC effects on the three types of OFS have been explored numerically at both low and high doses. We modeled the base design for the three types of OFS and plotted their corresponding spectra under no-dose conditions. Next, we showed numerically how a radiation-induced change in RI and length affect the spectra of sensors at doses of up to 1540 kGy. Upon observation of wavelength shift due to radiation, FBG, LPG, and F-P show a wavelength shift of 0.02, 37.5, and 0 nm at a dose of 1540 kGy, which correspond to temperature measurement errors of 2°, 407°, and 0°C, respectively. Next, we calculated the change in density, RI, and linear compaction at high doses based on the values at low doses using power law equation. Then, the calculated values were used in our model to study the effects of RIC at up to 7 MGy.

Secondly, we irradiated type I regenerated FBG samples to high neutron fluence and high temperatures in order to understand how radiation affects them. As both irradiation temperatures and neutron fluence degrade the FBG amplitude only one out of five FBGs survived at the end of entire irradiation cycle. It has been shown that high neutron fluence compacts the fiber significantly and therefore causes a large RI-BWS. However, high temperatures counteract the compaction effect because it expands the material. The change in RI and grating period of a FBG due to radiation has been calculated

using different numerical equations. The calculated values of RI and grating periods then has been inserted into a modeled FBG and assessed the RI-BWS. It has been found that the RI-BWS obtained from the irradiation experiment is larger than the RI-BWS obtained from the modeling work. The possible reasons can be not to consider all phenomena the FBG is subjected to, including RIC, RIA, dopant diffusion, temperatures, stress relaxation, dose, and dose rate. It is expected that an online measurement of RI and length (grating period) change in a radiation environment will help to understand the difference in RI-BWS between the experimental and modeling works.

## CHAPTER FIVE: REAL-TIME MEASUREMENT OF MACROSCOPIC CHANGES IN OPTICAL FIBERS

As discussed in earlier chapters that two primary contributions are usually considered that lead to the sensor's drift in a radiation environment: the first one is related to the absorption bands of point defects, and the second one is related to the densification of fibers. So far, RIC has been calculated using power law[171] and exponential function[62]. Then Lorentz-Lorenz relationship, Point dipole theory, sensitivity factor, and a few empirical equations have been utilized to find out the change in RI and linear compaction[128]–[130], [132], [171], [188]. The RIA contributed RI calculation using Kramers-Kronig relation is complex and needs to consider the spectrum in a wide frequency range[124]. The immediate question arises whether these methods (Lorentz-Lorenz, point dipole theory) consider the combined RIC, RIA, and dopant diffusion effects on the RI change or only consider the RIC effects on the RI change. In that sense, these methods do not represent the whole picture regarding RI change due to radiation. An online measurement for RI and length changes due to radiation can be a potential way to understanding the structural change of optical fiber in a nuclear environment. Online measurement may provide the change in RI of optical fiber due to any specific phenomena the fiber is subjected to, including RIC, RIA, dopant diffusion, temperatures, etc. The online measurement of these properties would help to better understand the structural changes silica experiences in a radiation environment, which is already known to be temperature, dose, and dose rate dependent[30], [31], [122], [128]. Once macroscopic

properties are measured, it is comparatively easy to understand how they would impact the sensor performance; therefore, in real-time correct the sensors drift. Although there are several ways to observe the macroscopic changes, we are proposing one method that has high potential. As RI and length compaction are the input parameters for the resonance-based OFS, accurate calculation of these parameters is of great importance to predict the actual radiation effects on OFS and correct the sensor drift.

### **5.1 Objective**

In this chapter, we discuss a simple cascaded Fabry-Perot interferometer (FPI) to measure the radiation induced change in RI along with length compaction. An online measurement of RI with the help of simple cascaded FPI may provide in-depth information about the change in RI due to radiation no matter whether compaction, RIA, dopant diffusion, temperature, or a combination of them cause it. The cascaded FPI consists of a hollow cavity (air/gas cavity) and a solid cavity (silica cavity). The air cavity can be used to measure the radiation induced linear compaction from the spectral response since RI shows no or little change. However, radiation alters both the length and the RI in the silica cavity. Considering the same amount of linear compaction of both cavities, change in RI can be measured from the spectral response of the silica cavity. Separation of the signal for each cavity is required to calculate the change in RI of the silica cavity with the help of the air cavity. We use the fast Fourier transform (FFT) algorithm to convert the wavelength domain signal into frequency domain. Then two bandpass filters are applied to separate the signals of each cavity. Finally, inverse FFT is used to convert the filtered signals into wavelength domain.

First, modeling work on FPI has been performed based on the numerical equations. Since radiation experiment is expensive and time consuming, we tried to give the validation of our modelling work by performing a temperature experiment with the cascaded FPI to measure the RI and the length in real-time. In a similar way discussed for radiation effect, the thermal expansion from the air cavity can be used to calculate the change in RI in the silica cavity. However, we are planning to put our cascaded FPI into the ATR at INL to monitor *in situ* the RI and the length variation in nuclear environment. This simple way of finding the radiation induced change in RI and linear compaction simultaneously may help improve understanding of the radiation effects on OFS.

## 5.2 Geometric Structure and Principles

The cascaded FPI, shown in Figure 5.1, consists of a hollow silica capillary fiber (HCF) of length  $L_1$  spliced between a coreless silica fiber (CLF) of length  $L_2$  and a lead single mode fiber (SMF) of arbitrary length. The air cavity has a cavity length ( $L_1$ ) of 117  $\mu\text{m}$  and RI ( $n_1$ ) of 1. The silica cavity has a cavity length ( $L_2$ ) of 211  $\mu\text{m}$  and RI ( $n_2$ ) of 1.44402. The value of RI  $n_2$  has been calculated by using the three-term Sellmeier Equation [189] at 1550 nm of wavelength. The cavity lengths were chosen in such a way so that the signal peak of each cavity does not overlap each other in spatial frequency domain. There is one more cavity that consists of  $L_1 + L_2$  and is sometimes referred to as a hybrid cavity (air-silica cavity). The main components of this cascaded FPI are three reflective interfaces,  $M_1$  (between the interface of lead SMF and HCF),  $M_2$  (between the interface of end facet HCF and CLF), and  $M_3$  (between the interface of end facet CLF and air). The total interference spectrum from the cascaded FPI is a three-beam interference and can be expressed by [190]

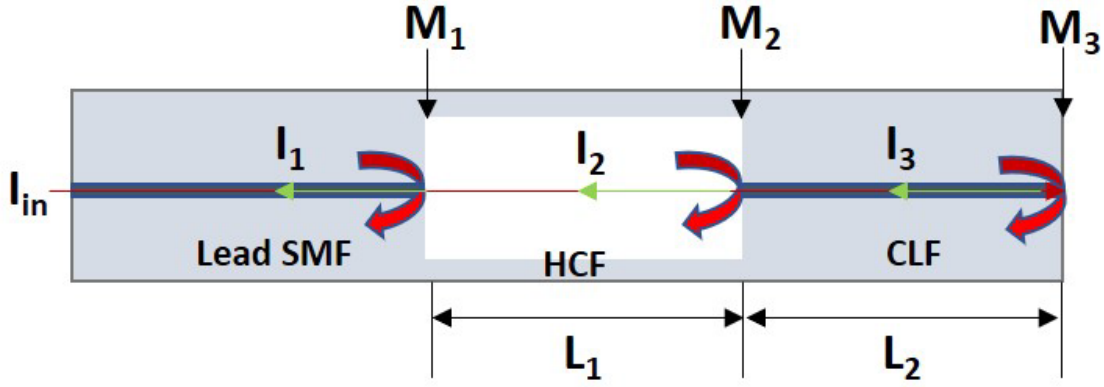
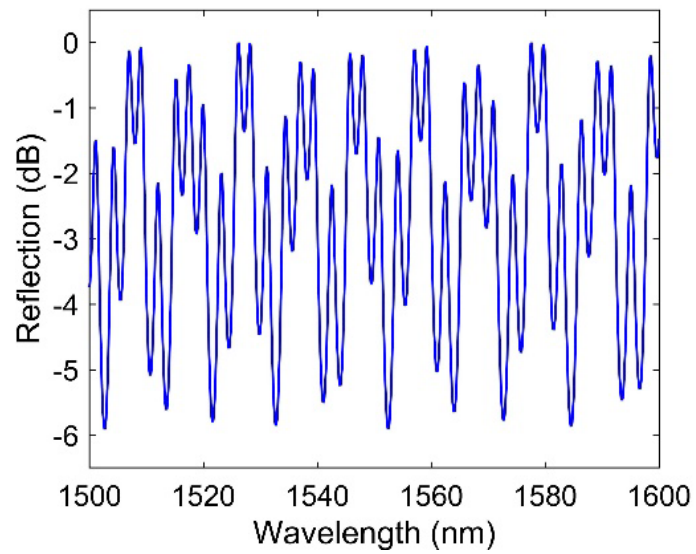


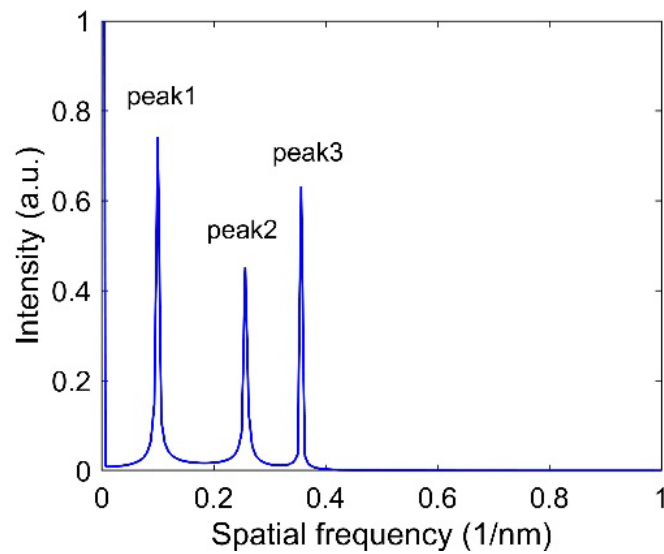
**Figure 5.1** Schematic of the designed cascaded Fabry-Perot interferometer.

$$I = I_1 + I_2 + I_3 + 2\sqrt{I_1 I_2} \cos(\varphi_{air}) + 2\sqrt{I_2 I_3} \cos(\varphi_{silica}) + 2\sqrt{I_1 I_3} \cos(\varphi_{air-silica}) \quad (5.1)$$

where  $\varphi_{air} = \frac{4\pi n_1 L_1}{\lambda}$ ,  $\varphi_{silica} = \frac{4\pi n_2 L_2}{\lambda}$ , and  $\varphi_{air-silica} = \frac{4\pi}{\lambda} (n_1 L_1 + n_2 L_2)$  are the phase of the air cavity (first cavity), silica cavity (second cavity), and hybrid cavity, respectively. The total spectrum from the cascaded FPI is shown in Fig. 5.2(a). To separate the reflection spectrum of each cavity, optical frequency domain signal processing was used to retrieve the air cavity and the silica cavity. The fast Fourier transform (FFT) algorithm is applied to the total spectrum, and the corresponding spatial frequency domain distribution is shown in Fig. 5.2 (b). It is seen that three peaks are available in the frequency domain. These three peaks are situated at  $0.1 \text{ nm}^{-1}$  (peak 1),  $0.2562 \text{ nm}^{-1}$  (peak 2), and  $0.3562 \text{ nm}^{-1}$  (peak 3). The spatial frequency values of the air cavity, silica cavity, and hybrid cavity are calculated as  $f_1 = \frac{2n_1 L_1}{\lambda_1 \lambda_2}$ ,  $f_2 = \frac{2n_2 L_2}{\lambda_1 \lambda_2}$ , and  $f_1 + f_2$ , respectively, where  $\lambda_1$  and  $\lambda_2$  are the wavelengths of adjacent peaks or dips in the reflection spectrum of each cavity. Calculation of the spatial frequency for each cavity indicates that peak 1, peak 2, and peak 3 correspond to the peaks of air cavity, silica cavity, and hybrid cavity, respectively.



(a)



(b)

**Figure 5.2** (a) total spectrum of the cascaded FPI and (b) the spatial frequency distribution of the total spectrum using FFT.

The spatial frequencies of the air cavity ( $f_1$ ) and the silica cavity ( $f_2$ ) are related to the optical path difference (OPD) of these two cavities. The crosstalk between the two cascaded cavities can be reduced by increasing the OPD between the air cavity and the

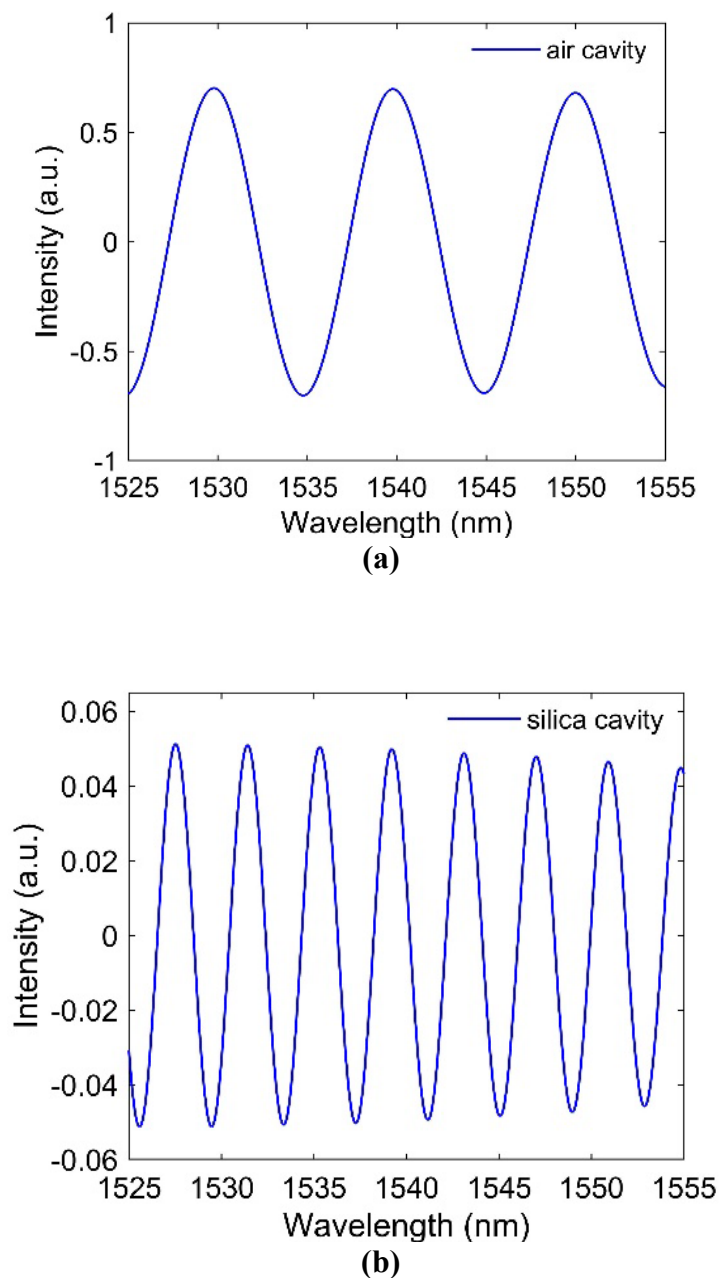


**Figure 5.3 Retrieved signals using bandpass filters and inverse FFT for (a) air cavity and (b) silica cavity.**

silica cavity. To extract the signals for each cavity from the total reflection spectrum, two bandpass filters are used. The interference spectrum of the air cavity is obtained by filtering the total spectrum using a bandpass filter centered on peak1 and for the silica cavity centered on peak 2. Then, the lengths of the air cavity and silica cavity can be obtained by

using  $L_1 = \frac{\lambda_1 \lambda_2}{2n_1(\lambda_1 - \lambda_2)}$  and  $L_2 = \frac{\lambda_1 \lambda_2}{2n_2(\lambda_2 - \lambda_1)}$ , respectively, if  $n_1$  and  $n_2$  are known. The reconstructed spectrum for the air cavity and silica cavity is shown in Figures 5.3(a) and 5.3(b), respectively. Table 5.1 shows the original and reconstructed length of the cavities. It is seen that the retrieved lengths of the cavities are almost same as that of the original length of the cavities. There is one more term called free spectral range (FSR), which is the spectral distance between two adjacent peaks or dips. This is calculated for the air cavity and the silica cavity as  $FSR_{air} = \frac{\lambda_1 \lambda_2}{2n_1 L_1}$  and  $FSR_{silica} = \frac{\lambda_1 \lambda_2}{2n_2 L_2}$ .

**Table 5.1 Original and retrieved length of cavities of the cascaded FPI.**

Cavity	Original cavity length ( $\mu\text{m}$ )	Retrieved cavity length ( $\mu\text{m}$ )
Air cavity	117	117.39
Silica cavity	211	210.69

### 5.3 Compaction Analysis

Since radiation compacts the silica material, it is necessary to analyze compaction for both cavities in a cascaded FPI. As the proposed cascaded FPI consists of an air cavity and a silica cavity, the radiation induced change in RI for both cavities would be different. Furthermore, as the two cavities are very close to each other, we assume the change in length compaction is identical for both cavities since they will experience the same environment. The length compaction information is obtained from the interference spectrum of the air cavity as no change occurs in RI for being hollow cavity. If  $L_{1i}$  is the initial cavity length and  $L_{1f}$  is the compacted length of the air cavity due to the exposure of radiation, the linear compaction ( $C_{l-air}$ ) is

$$C_{l-air} = \frac{L_{1i} - L_{1f}}{L_{1i}} \quad (5.2)$$

As the second cavity is based on silica, both the change in RI and length will occur. If  $L_{2i}$  is the initial cavity length and  $L_{2f}$  is the compacted length of the silica cavity due to the exposure of radiation, the linear compaction ( $C_{l-silica}$ ) is

$$C_{l-silica} = \frac{L_{2i} - L_{2f}}{L_{2i}} = C_{l-air} \quad (5.3)$$

As mentioned, the length compaction of the silica cavity would be same as that of the air cavity ( $C_{l-silica} = C_{l-air}$ ). Based on that consideration, the compacted length of the silica cavity  $L_{2f}$  can be calculated as

$$L_{2f} = L_{2i} - C_{l-air} L_{2i} \quad (5.4)$$

It is known that optical length equals the physical length multiplied by refractive index of the medium. So, the optical length for the silica cavity,  $L_{op} = n_{2f} L_{2f}$  where  $n_{2f}$  is the compacted RI due to radiation. The optical cavity length,  $L_{op}$ , can be obtained directly from the individual interference spectrum of each cavity. As we already know the  $L_{2f}$ , then  $n_{2f}$  can be calculated easily. In this approach, linear compaction and RI can be identified independently, and in real-time.

#### 5.4 Radiation Effects on Cavities

In order to see the radiation effects on the RI and the length of the fiber in real-time, it is necessary to fabricate a cascaded FPI and expose it to radiation. It is simple to calculate  $C_{l-air}$  and  $n_{2f}$  using Eq. (5.2) -(5.4) from the measured fringe spectrum of a fabricated cascaded FPI. Since we did not irradiate the cascaded FPI, we relied on the experimental values reported in [128] to evaluate the feasibility of our designed model. The reported values for linear and volumetric compaction are  $0.73 \pm 0.04\%$  and  $2.20 \pm 0.13\%$ , respectively, in [128]. These values were measured after exposing the silica to a fast neutron

fluence of  $2.4 \times 10^{21} \text{ n/cm}^2$  at a temperature of  $95^\circ\text{C}$ . Point dipole theory is then used in Eq. (5.10) to calculate the final  $n_{2f}$  from the density (volume compaction) based on the values reported in[128]. We input the changes in RI and length due to a fast neutron fluence

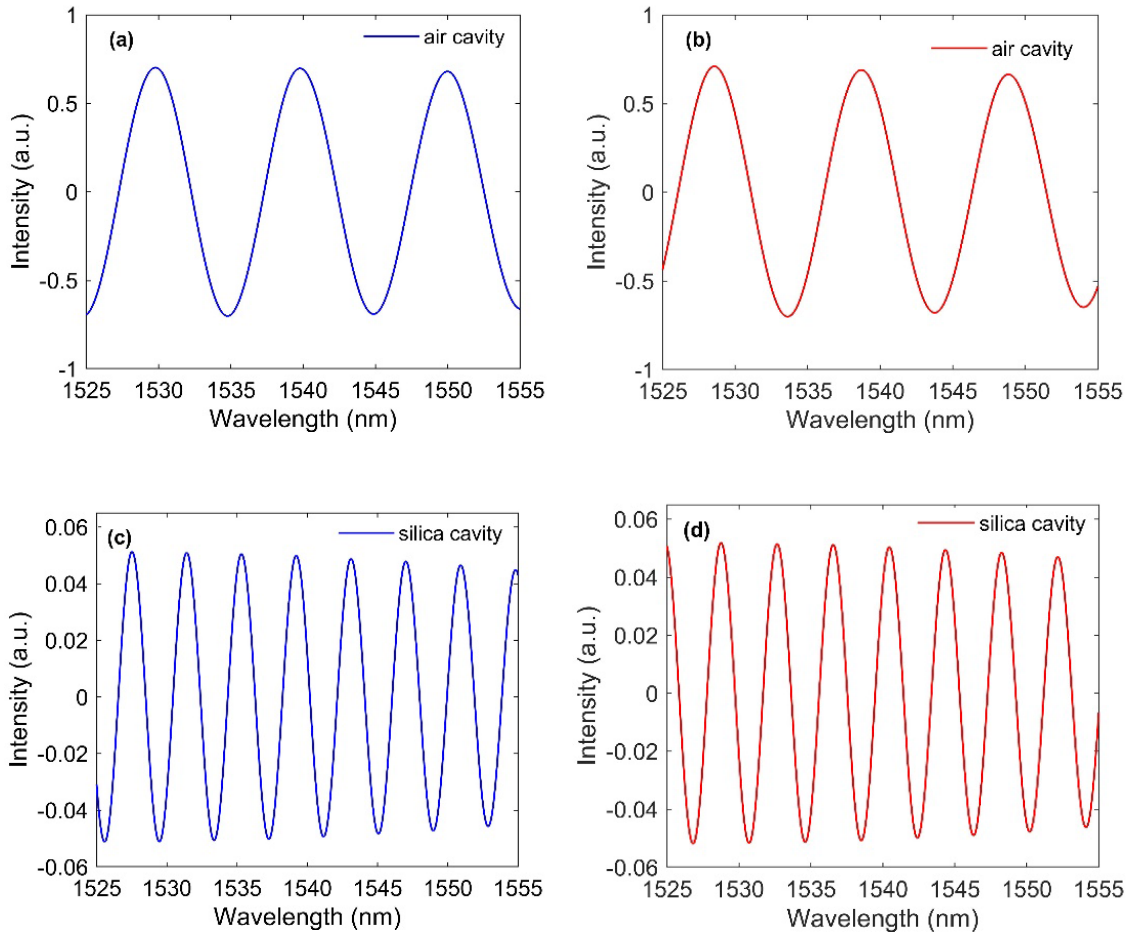


**Figure 5.4** Reconstructed signals for (a) air cavity before irradiation, (b) air cavity after irradiation, (c) silica cavity before irradiation, (d) silica cavity after irradiation.

of  $2.4 \times 10^{21} \text{ n/cm}^2$  at a temperature of  $95^\circ\text{C}$  to our cascaded FPI model and ran a simulation. The individual cavity spectrum from the simulation before and after irradiating to a fluence of  $2.4 \times 10^{21} \text{ n/cm}^2$  is shown in Fig. 5.4. As the fiber is compacted it is expected that the cavity lengths will decrease in comparison to previous reconstructed cavity length. It is seen that there is a spectral change in Figs. 5.4(b) and 5.4(d) due to the

radiation effects from their original spectra Figs 5.4(a) and 5.4(b). Table 5.2 shows the reconstructed length of cavities before and after the irradiation. It is seen that the reconstructed cavity lengths change from 117.39 to 116.56  $\mu\text{m}$  for the air cavity and from 210.69 to 209.20  $\mu\text{m}$  for the silica cavity. Once we conduct an experiment, we can then measure the RI from the silica cavity with the help of the air cavity and can verify our simulation work.

**Table 5.2 Reconstructed cavity length before and after irradiation to a fast fluence of  $2.4 \times 10^{21} \text{ n/cm}^2$  at a temperature of  $95^\circ\text{C}$ .**

Cavity	Before irradiation retrieved original cavity length ( $\mu\text{m}$ )	After irradiation retrieved compacted cavity length ( $\mu\text{m}$ )
Air cavity	117.39	116.56
Silica cavity	210.69	209.20

Since the changes in RI and length due to radiation can be measured using cascaded FPI, it is possible to input these values into FBG sensor to observe the radiation-induced signal drift. As the first step to comprehend the radiation effects on FBG, we modelled a FBG by using the theoretical analysis described in[135]. We used Eq. (4.11) -(4.12) to model the FBG according to the couple mode theory. We choose the parameters of the FBG in such a way to get the Bragg peak close to 1550 nm of wavelength. We inserted the values of RI and length compaction in to our FBG model for a fast neutron fluence of  $2.4 \times 10^{21} \text{ n/cm}^2$  at a temperature of  $95^\circ\text{C}$ . First, we simulated the FBG without any radiation exposure. The spectrum of FBG before irradiation is shown in Fig. 5.5 (black line), and it can be seen that the Bragg wavelength is at 1549.9 nm. Then we considered the radiation effect on the Bragg wavelength by inserting only RI change obtained by Eq. (4.10) due to a fast neutron fluence of  $2.4 \times 10^{21} \text{ n/cm}^2$  at a temperature of  $95^\circ\text{C}$ [128].

Please note that we did not consider the RIA induced RI change as it's quite complex and requires the full spectrum of light. It can be observed that Bragg wavelength gives a redshift of 10.62 nm (blue line) due to the increased RI induced by radiation. In a similar way, we input the radiation induced grating period (linear compaction) change into our model while considered no change in RI. It is seen that compacted length provides a blueshift of 11.31 nm (green line). It is well known that increased RI shifts the Bragg wavelength to the longer wavelength side, whereas a compacted grating period shifts it to the shorter wavelength side according to Eq. (4.1). Then we inserted the radiation induced change both in the RI and the grating period in our FBG model and ran a simulation. An overall shift of 0.77 nm (red line) to the shorter wavelength side can be observed, which indicates the effect of length compaction dominates over the effect of RI. It is interesting to see that there is no reduction of Bragg amplitude due to the radiation which is not the normal case. Experimental results indicate that radiation reduced the amplitude of the Bragg peak[30], [128], and the possible reasons might be the defect generation and eraser of gratings. As we did not consider any RIA in our simulation, the amplitude of the Bragg peak slightly increased due to the increased RI. An overall shift of 0.77 nm led to a temperature error of 77°C by assuming the FBG temperature sensitivity coefficient of 10 pm/°C.

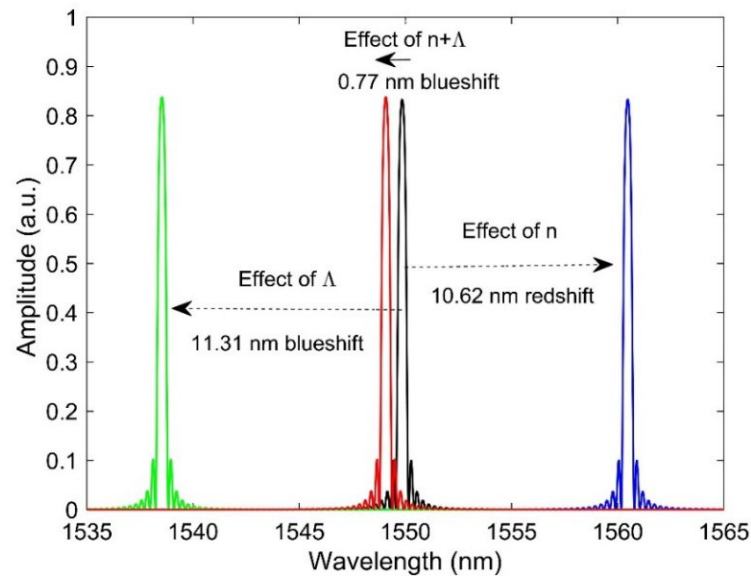


**Figure 5.5 Spectra of FBG in different conditions: before irradiation (black curve), radiation induced RI effect (blue curve), radiation induced grating period effect (green curve), and radiation induced combined effect of RI and grating period (red curve) on the Bragg wavelength.**

It is also possible that RIA induced change in RI may further accelerate the errors. By knowing the macroscopic changes that cause a shift of 0.77 nm for FBG, it is possible to correct the drift.

Here our effective technique based on cascaded FPI may work. The alteration of RI may occur due to RIC, RIA, temperature, and so on in a radiation environment. However, Lorentz-Lorenz or point dipole theory only helps to calculate compaction (or density) induced RI change. To understand the whole picture, it is crucial to know the RI change caused by all possible reasons (RIA, RIC, irradiation temperature, dopant diffusion, etc.) due to radiation. An online measurement of macroscopic changes, no matter what it causes, may provide the actual change in RI and length, which can be then used to correct the sensor drift.

### 5.5 Thermal Effects on Cavities

In this section, the thermal effects on cavities, as well as gas RI is considered, if the air cavity is filled with helium gas. From now on, the air cavity will be called a gas cavity (for simulation works only) for better understanding, since it is filled with helium gas. As the thermo-optic and the thermal expansion coefficients are well defined for a pure silica-based cavity, we mainly investigate the thermal effects on the gas cavity. Temperature relates to the pressure through the ideal gas law expressed by

$$PV = mRT \quad (5.5)$$

where  $P$ ,  $V$ ,  $m$ ,  $R$ , and  $T$  are the pressure, volume, amount of gas, ideal gas constant, and temperature, respectively. If the diameter of the gas cavity is  $40 \mu\text{m}$  (inner diameter of silica capillary tube) and as the cavity length of the gas cavity ( $117 \mu\text{m}$ ) is known,  $V$  and hence,  $m$  can be calculated at normal temperature and pressure (NTP). Then pressure  $P_2$  at temperature  $T_2$  ( $300^\circ\text{C}$  in our case) is calculated. Once pressure is known, strain and hence the change in length can be determined by using

$$\Delta L = \text{strain} \times L = \frac{P}{Y} \times L = \frac{FL}{AY} \quad (5.6)$$

where  $P$ ,  $Y$ ,  $F$ , and  $A$  are the pressure, Young's modulus, applied force to the gas cavity, and cross-sectional area of glass, respectively. Since the overall radius of the capillary tube is  $62.5 \mu\text{m}$  and the radius of the glass in the capillary tube is  $20 \mu\text{m}$ , then  $A = \pi(62.5^2 - 20^2) \times 10^{-12} \text{m}^2$ . The force acting on the glass due to pressure is  $F \cong P \times \pi \times 20^2 \times 10^{-12} \text{m}^2$ . As the Young's modulus for bare silica fiber is  $69.22 \pm 0.42 \text{ GPa}$ [191], strain induced length change,  $\Delta L$ , can be calculated by performing some iterations until the result gets convergence. We obtained strain induced  $\Delta L$  of  $0.038 \text{ nm}$  at  $300^\circ\text{C}$ , which is very small compared to the thermally induced  $\Delta L$  of  $11.43 \text{ nm}$  of pure silica fiber, considering

the thermal expansion coefficient of  $4.1 \times 10^{-7}/^{\circ}\text{C}$ . As a result, pressure induced length change can be neglected compared to the thermally induced one.

Next, we emphasize the temperature effect on the RI of helium gas. The RI of gas can be determined from the Lorentz-Lorenz equation, and it can be written in the form of

$$\frac{n^2-1}{n^2+2} = A_R \rho_m + B_R \rho_m^2 \quad (5.7)$$

where  $\rho_m$  is the density in moles per unit volume,  $A_R$  is the molar polarizability, and  $B_R$  is the second refractivity virial coefficient. To calculate the density  $\rho_m$ , the  $m$  is calculated first at NTP since  $V$  is known. The molar refractivity  $A_R$  for helium gas is calculated using the following expression in[192]

$$A_R = 0.51725407 + \frac{1197.5410}{\lambda^2} + \frac{3.290677 \times 10^6}{\lambda^4} + \frac{9.800874 \times 10^9}{\lambda^6} \quad (5.8)$$

where  $\lambda$  is the wavelength of light used. The refractivity virial coefficient  $B_R$  is calculated using the expression suggested by[192]:

$$B_R = -0.032 - 0.0001T \quad (5.9)$$

Please note that the above expression for  $B_R$  was developed at a wavelength of 633 nm. However, we used this value of  $B_R$  at 1550 nm, since  $B_R$  has only a small effect on the refractive index (modify the result less than  $2 \times 10^{-10}$ )[192]. Then the value of each parameter is inserted into Eq. (5.7), and the refractive index  $n$  is calculated. For high temperature  $T_2$  (300°C in our case), thermally induced  $\Delta L$  and hence the new length is calculated using the thermal expansion coefficient of pure silica. New volume is then determined from the new length assuming other parameters remain unchanged. Based on the new volume, density  $\rho$  and  $n$  are calculated at 300°C. The obtained difference in RIs

between NTP and 300°C is  $7.4 \times 10^{-9}$ , which is very small and can be neglected. We investigated the strain induced length change and temperature induced RI of the gas cavity and found that both are very small and can be neglected. The only parameter remains that dominates on the interferometric fringe of the gas cavity is the thermally induced length expansion.

### **5.6 Fabrication and Experiment of Cascaded FPI**

Until now, we have presented the simulation results on how radiation affects the RI and length of optical fiber. Since radiation experiment is time consuming and expensive, we did a temperature test to see if the cascaded FPI can be used to monitor the changes in RI and length. Similar to radiation, temperature changes both the length and the RI, thermal test of our cascaded FPI may validate our modeling work.

Real-time monitoring of RI and length variation in an optical fiber induced by environmental parameters, such as temperature, strain, pressure, and radiation has been of great importance in characterizing optical devices since the birth of optical fibers[193]–[195]. In practice, the sensors based on optical fibers can be calibrated with the knowledge of parametric influence on the RI and length changes. For a widespread application, namely real-time temperature sensing, fiber optic sensors such as FBGs and FPIs, have been applied to measure the change in RI with temperature[195]–[197]. However, the thermo-optic coefficient (TOC) which is a measure of the RI change as a function of temperature maybe positive or negative, and this depends on two processes which are driven by change in temperature[198]. The density of an optical fiber may decrease with increasing temperature because the material expands. Reduction in density leads to negative RI [199]. However, heating the optical fiber polarizes it significantly and increases RI[198], [200].

Although these two individual mechanisms can lead to positive or negative RI, the net effect has shown to be positive for silica optical fibers[201]. The TEC, which provides the variation of length with temperature at constant pressure, is always positive for silica optical fiber and almost one order of magnitude smaller than the TOC. Several methods have proven to be effective for measuring RI and hence the TOC; these include interferometric[202], [203] and prismatic methods[189], [204]. However, prismatic methods are non-fiber methods, and their direct application for TOC measurement may provide inaccurate results for optical fiber. RI due to temperature and hence the TOC can also be measured by direct techniques such as refracted near-field, multiwavelength interferometry, computerized tomography, differential interference-contrast microscopy, and quantitative phase microscopy[205]. However, some of these measurements require the cut of the fiber (destructive analysis) and may not provide real-time changes of RI due to the post recovery. Recent years FBGs, F-Ps, and combination of them have been used to measure the TOC in real-time of optical fibers; however, fabrication of FBGs, inclusion of femtosecond(fs) laser, etching, and so on make sensor's structure complex and increase the cost[195]–[197]. Moreover, FBG-based techniques may have temperature limitation due to the dependence on temperature for grating stability. So far, the reported values for the TOC of silica-based optical fibers using existing methods are between  $3 \times 10^{-6}/^{\circ}\text{C}$  and  $2.37 \times 10^{-5}/^{\circ}\text{C}$  at different temperatures and wavelengths[195]–[197], [204], [206], [207]. While there are several techniques for real-time monitoring of TEC and TOC of silica optical fibers are currently exist, an optical structure having the following advantages such as ease of fabrication, ability to survive in harsh environments, and cost-effectiveness are yet to be expected.

Here, we propose and use a cascaded Fabry-Perot interferometer (FPI) structure consisting of an extrinsic FPI (EFPI) and an intrinsic FPI (IFPI) as a way to accurately measure the TOC and TEC for silica optical fibers within a temperature range of 21–486°C. The EFPI is used to monitor the cavity length because it is an air cavity, and the RI of air is almost invariant with temperature. On the other hand, temperature alters the RI and the length of the IFPI for a solid cavity made of pure silica. Because the TEC of a silica capillary tube and pure silica fiber is the same, it is possible to extract the RI change from IFPI by using length in the EFPI. Due to differences in the cavities, air versus silica, the Fabry-Perot responses would be different. To separate individual signals for each cavity from the mixed signal of cascaded FPI, we apply a fast Fourier transform (FFT) algorithm to convert the wavelength domain signal to the spatial-frequency domain and then use Butterworth filters. Inverse Fourier transform is applied on the filtered signals to reconstruct the individual signal again in wavelength domain. Since the proposed structure is made of silica capillary and optical fiber, simple cleaving and splicing processes are required for the fabrication. Moreover, for being all silica structure, the cascaded FPI structure can be applied in extreme radiation environment to determine the effect of other parametric influences such as pressure and radiation as these effects are directly coupled to the RI and length changes.

#### 5.6.1 Fabrication Procedures of Cascaded FPI

In order to fabricate the cascaded FPI, we applied simple cleaving and splicing processes. We used SMF-28 single mode fiber as the lead in fiber and capillary tubes with inner diameters of 39.2  $\mu\text{m}$  (TSP040150) from Polymicro Technologies to construct EFPI. As a first step, we cleaved the single mode fiber, the capillary tube, and the coreless (CL)

fiber using cleaving tool (CT101/102, Fujikura) [Fig. 5.6(a)] and then fusion spliced of SMF-28 and capillary tube using fusion splicer (70S+ Fusion Splicer, Fujikura) [Fig. 5.6(b)]. Then a linear stage with precise accuracy in conjunction with cleaving tool was used to cleave the spliced capillary at distance of  $148 \mu\text{m}$  from the splicing point [Fig. 5.6(b)]. A CL fiber from Thorlabs was cleaved and spliced with the capillary tube to complete the air cavity [Fig. 5.6(c)]. The CL fiber was chosen for the silica cavity in order to get the information about pure silica optical fiber. Then we cleaved the CL fiber at a distance of  $323 \mu\text{m}$  from the capillary/CL fiber splicing point to construct the [Fig. 5.6(c)]. The complete structure of cascaded FPI with required parameters is shown in Fig. 5.6(d). The microscopic image of the fabricated cascaded FPI is shown in Fig. 5.6(e) where  $L_1$  and

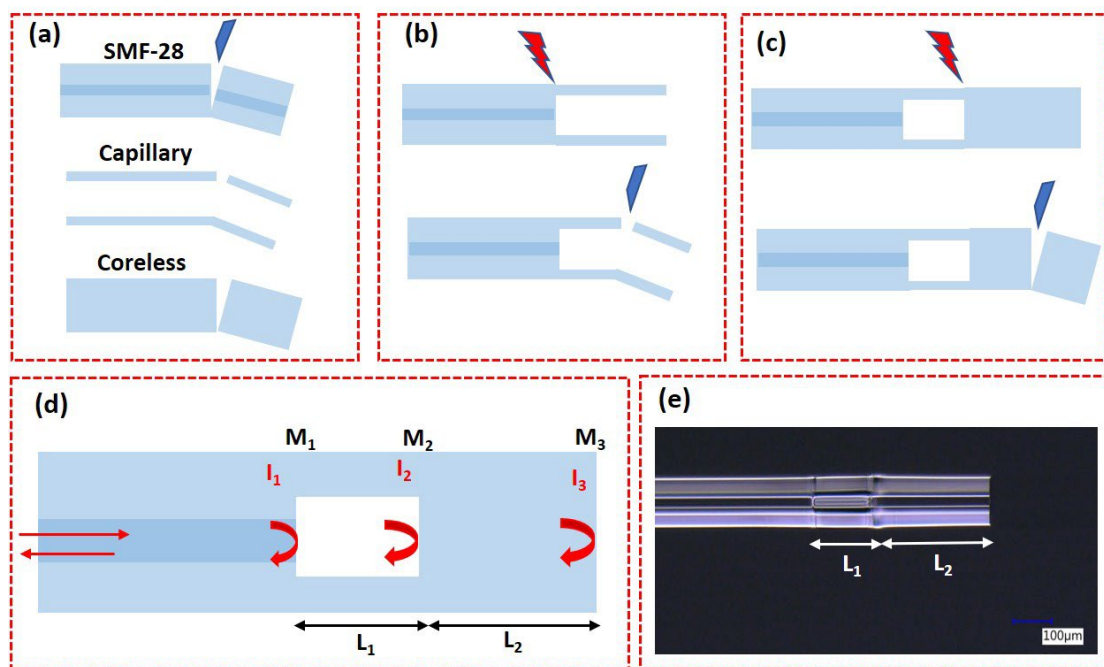


**Figure 5.6** Fabrication steps of cascaded FPI by using only cleaving and splicing and the complete cascaded FPI structure.

$L_2$  denotes the cavity length for the EFPI and the IFPI, respectively. The measured cavity lengths are to be  $L_1=148 \mu\text{m}$  and  $L_2=323 \mu\text{m}$ . The interference spectrum of the cascaded

FPI recorded by Micron Interrogator is shown in Fig. 5.7(a) and the frequency domain this signal is shown in Fig. 5.7(b). It is seen that there are three dominant peaks namely peak1, peak2, and peak3, which corresponds to three cavities. The peak1 corresponds to the air cavity which was confirmed by calculating the spatial frequency  $(\frac{2n_1L_1}{\lambda_1\lambda_2})$  where  $\lambda_1$  and  $\lambda_2$  are the wavelengths of adjacent peaks or dips in the reflection spectrum of each cavity. In a similar way, peak2 and peak3 belong to the silica and hybrid cavity, respectively. The measured spatial frequencies of the air cavity and the silica cavities were found to be  $0.125$

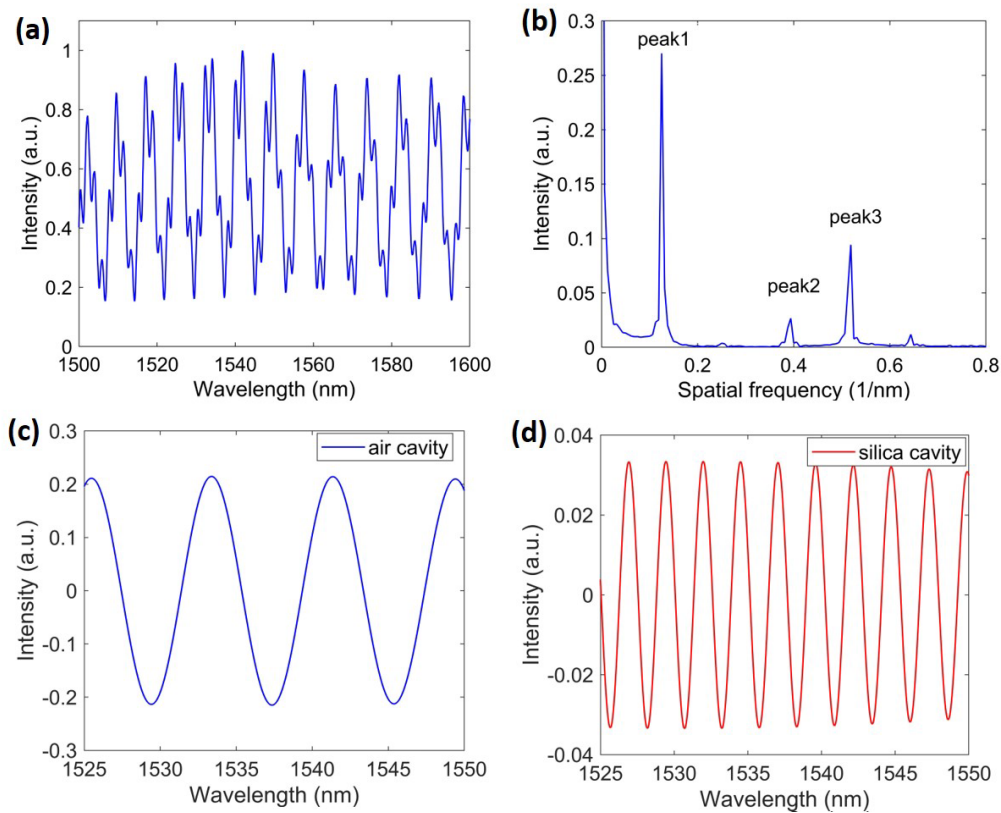


**Fig. 5.7 Spectral response of fabricated cascaded FPI: (a) total reflection spectrum, (b) optical frequency domain distribution of the total reflection spectrum, (c) reconstructed cavity length of EFPI, and (d) reconstructed cavity length of IFPI**

$\text{nm}^{-1}$  (peak1) and  $0.39375 \text{ nm}^{-1}$  (peak2), respectively which corresponds to a cavity length of  $\sim 147$  and  $\sim 321 \mu\text{m}$ . These calculated cavity lengths are close to the actual measured

cavity lengths. The individual cavity length was reconstructed by using filter and inverse FFT discussed earlier. The retrieved spectrum for the air cavity and the silica cavity is shown in Figs. 5.7(c) and 5.7(d), respectively. The free spectrum range (FSR), which is defined as the spectral distance between two adjacent peaks/dips was found to be  $\sim 8$  and  $\sim 2.54$  nm for the air cavity and the silica cavity, respectively, which is consistent with their cavity lengths.

### 5.6.2 Temperature Effects on Cascaded Cavities

With the basic specifications of the two cavities determined and baseline spectrum measured, we next studied the effect of temperature on both cavities. In order to measure the TEC and TOC, the fabricated cascaded FPI was placed inside a tube furnace with endcaps to ensure no air flow. A k-type thermocouple was also placed very close to the FPI to measure the temperature at the location of the FPI in the furnace to improve measurement accuracy. A schematic of the measurement setup is shown in Fig. 5.8. The temperature of the furnace was increased from ambient to  $486^{\circ}\text{C}$  with a ramp rate of  $5^{\circ}\text{C}/\text{min}$ . The total reflection signal was recorded at different temperatures using the Micron Optics Interrogator. For each measurement, a hold time of 30 minutes was used to stabilize the temperature before recording data. The recorded data were then analyzed to reconstruct the signal for each cavity discussed in Section 5.1. The air cavity shows a thermal expansion only with temperature because it is made of silica capillary tubes. On

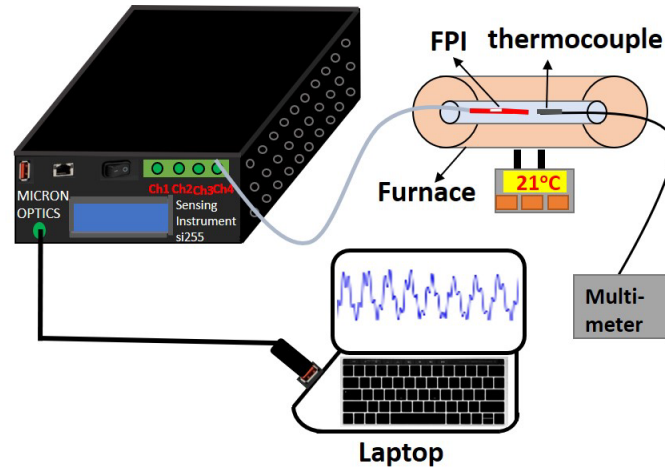


**Figure 5.8** Experimental setup to record signal at different temperatures.

the other hand, the silica cavity is an IFPI, and temperature changes both the RI and the length of the cavity. These properties from both cavities can be used to measure TEC and the TOC in real time.

### 5.6.3 Thermal Expansion Coefficient Measurement

The TEC of an optical fiber plays a key role in optical fiber sensing technology. Although the TEC ( $\sim 5.5 \times 10^{-7}/^{\circ}\text{C}$ ) is well defined for fused silica sample, it changes for optical fiber with temperature[195], [197]. To monitor the TEC in real-time, the designed cascaded FPI was used. Since the EFPI is hollow and the change in air RI with temperature is very small, which calculated by the following expression[208]

$$n_1 = 1 + \frac{2.8793 \times 10^{-9} \times P}{1 + 0.003661 \times T} \quad (5.10)$$

where  $P$  is the absolute pressure and  $T$  is the operating temperature. In this equation, the change in RI of air with temperature is negligible because the second term in the right-hand side remains almost constant by the increased temperature and temperature-induced increased pressure because the air is sealed in a nearly constant-volume cavity. Because the spectrum of an FPI is governed by the optical length of the cavity, and for the air cavity,

the effect of RI is so small as to be neglected. The length expansion of the cavity is the parameter expected to be dominant. The inner diameter of the capillary tube is of 39.2  $\mu\text{m}$ , which leaves a 42.9  $\mu\text{m}$  wall thickness, which experiences a length expansion. The response of air cavity at different temperatures were recorded from the experiment described above. Then the cavity length of the air cavity was calculated from the measured spectrum using the following two peak methods[209]:

$$L_1 = \frac{\lambda_1 \lambda_2}{2n_1(\lambda_2 - \lambda_1)} \quad (5.11)$$

where  $\lambda_1$  and  $\lambda_2$  are the wavelengths of adjacent peaks or dips in the reflection spectrum. Because the spectrum of the air cavity contains many peaks, instead of relying on any specific two peaks, the mean value of  $\lambda_1 \lambda_2$  and  $(\lambda_2 - \lambda_1)$  of all adjacent two peaks were used to retrieve the cavity length. We obtained a cavity length of  $\sim 147 \mu\text{m}$  at room temperature from the measured spectrum using the Eq. (3). The spectra of the air cavity at six temperatures – 21, 100, 197, 291, 388, and 486°C are shown in Fig. 5.9. Because this is an air cavity, the dip/peak wavelength shifts a small amount with temperature. As temperature expands the cavity length, the interference spectra get closer. The cavity length at each temperature was calculated from each spectrum using the Eq. (5.11). Then these cavity lengths at each temperature were plotted against temperature to find the TEC, which is shown in Fig. 5.10. We performed the experiment twice to confirm the repeatability of the cascaded FPI structure. The solid red circles are the mean experimental data at each temperature, and the solid blue line shows the linear fitting of these data. The error bar in

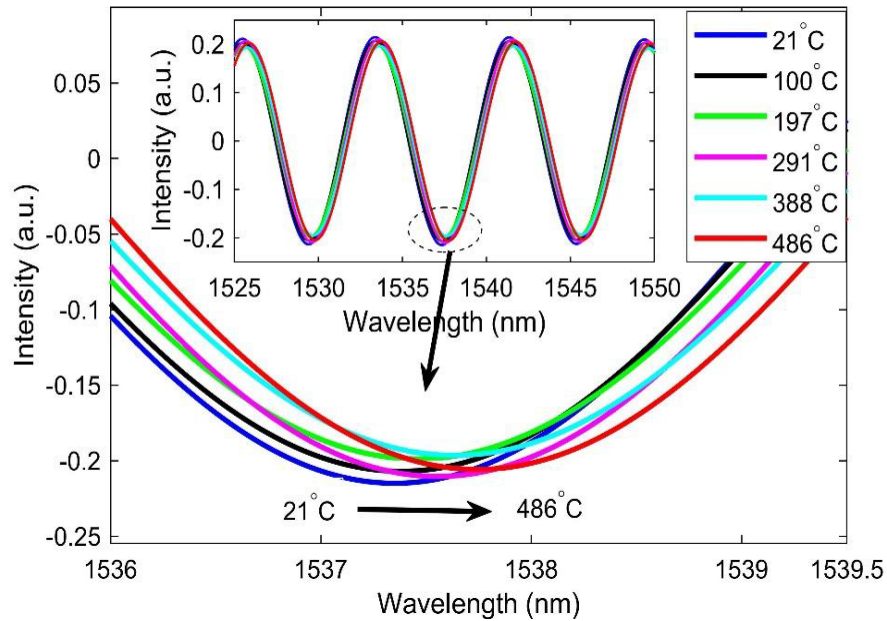


**Figure 5.9** Measured spectra of the air cavity at different temperatures

Fig. 5.10 indicates the standard deviation from the mean values. It is seen that the data follow a linear trend upward to the specified temperature range, and the linearity is high. The obtained TEC from these data was found to be  $5.4 \times 10^{-7}/^{\circ}\text{C}$ , which is in good agreement with literature values. Once the air-cavity length is known for each temperature, then the length expansion air ( $\alpha_L$ ) can be represented as

$$\alpha_L = \frac{L_{a,T} - L_{a,i}}{L_{a,i}} \quad (5.12)$$

where  $L_{a,i}$  is the initial air-cavity length at room temperature, and  $L_{a,T}$  is the final air-cavity length at any temperature. Please note that the optical-cavity length and the physical-cavity length are same for the air cavity because air has an RI of 1.

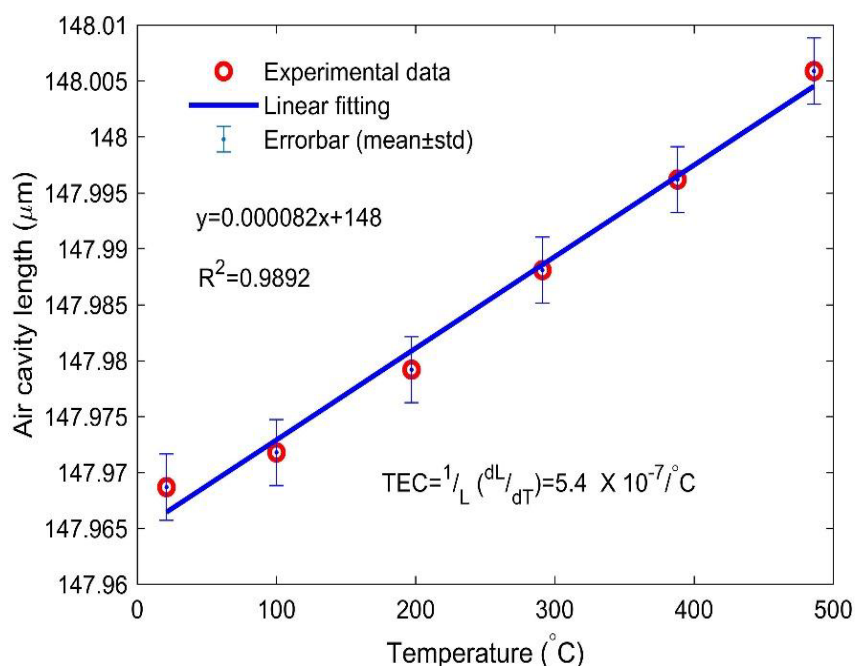


**Figure 5.10** Measured air cavity length as a function of applied temperature.

#### 5.6.4 Thermo-Optic Coefficient Measurement

The TOC is the change in RI with temperature at constant pressure. To measure the TOC real-time, the same experimental setup of Fig. 5.8 was used, and the experiment was repeated twice. Because the IFPI is made of coreless pure silica fiber, temperature alters both the RI and the cavity length. Therefore, the spectrum of the silica cavity contains information about both the RI and the length of the cavity. The spectrum of the silica cavity at different temperatures is shown in Fig. 5.11. It is seen that the spectral position changes continuously with temperature. Since the silica capillary tube and the silica cavity both are made of silica and for being very close proximity of both cavities to each other, it is expected that both the cavities will experience the same length expansion. Please note that length expansion is a relative value and always defined as the change in physical length by using the Eq. (5.13).

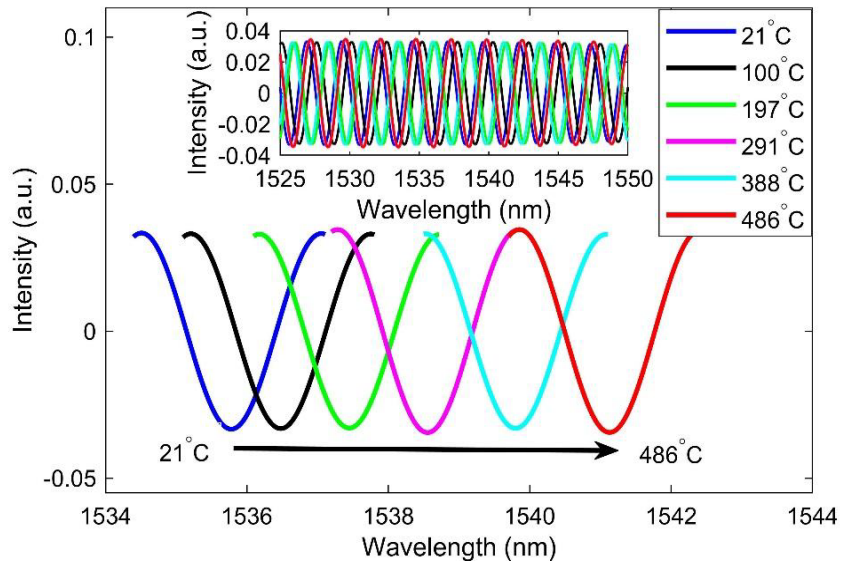


**Figure 5.11** Retrieve spectra of the silica cavity at different temperatures.

$$\frac{L_{Si,T} - L_{Si,i}}{L_{Si,i}} = \alpha_L = \frac{L_{a,T} - L_{a,i}}{L_{a,i}} \quad (5.13)$$

where  $L_{Si,i}$  is the initial cavity length at room temperature and  $L_{Si,T}$  is the final cavity length of the silica cavity at any temperature. Next, the silica-cavity length at any temperature can be calculated by using the below expression

$$L_{Si,T} = L_{Si,i} + L_{Si,i} \times \alpha_L \quad (5.14)$$

Because the silica-cavity length,  $L_{Si,i}$  at room temperature, and  $\alpha$  are known, the cavity length  $L_{Si,T}$  can be calculated from Eq. (5.14). The optical silica-cavity length ( $L_{Si,opt}$ ) is also known from the measured spectrum of the silica cavity. However,  $L_{Si,opt} = n_{2f} \times L_{Si,T}$  where  $n_{2f}$  is the final RI of silica cavity with temperature, which can be easily deduced. The variation of RI of silica optical fiber with temperature is shown in Fig. 5.12. The solid red circles are the mean experimental data, and the solid blue line shows the

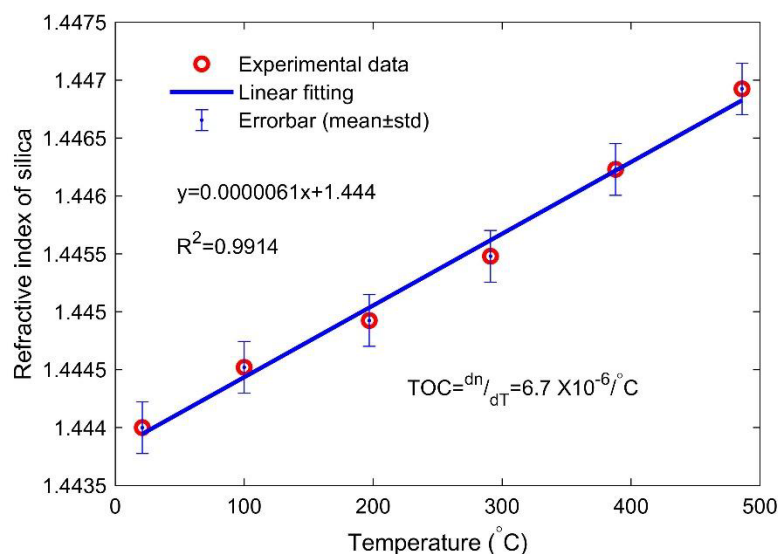


**Figure 5.12 Measured refractive index of silica as a function of applied temperature.**

linear fitting of these data. The error bar in Fig. 5.12 indicates the standard deviation from the mean values. It is seen that the data follow a linear trend up to the specified temperature range, and the linearity is high. The obtained TOC from these data were found to be  $6.7 \times 10^{-6}/^{\circ}\text{C}$ , which is in a good agreement with literature values reported in references[195]–[197], [204], [206], [207].

### 5.7 Discussions and Applications

The change in length and RI of optical fiber has been measured using a simple structure, based on EFPI and IFPI. Because only silica material is used to construct the structure, it is possible to use this structure at high temperatures, unlike FBGs where grating stability depends on the operating temperature. Through this work, we have demonstrated the potential of our simple cascaded FPI structure in accurately determining the RI and length change due to an applied stimulus. *In situ* measurement of RI and length can find a potential application in the nuclear environment. Incoming radiation (gamma ray, neutron fluence, or both) changes the optical as well as the mechanical properties of optical

fibers[30], [31], [122], [128]. Radiation-induced attenuation (RIA) significantly affects the signal strength by creating different types of defects[72], [109] whereas radiation-induced compaction (RIC) causes signal drift by compacting the material[31], [210]. For optical-fiber sensors, it is the RIC over the RIA which causes temperature-measurement errors in the nuclear environment, thanks to radiation-hardened optical fibers. If the RIC is known, it is possible to calculate the RI induced by RIC by using well-established Lorentz-Lorenz relation[130], [131] and point dipole theory[132]. However, these methods only consider the RIC-induced RI change. It has also been shown that RIA, in addition to RIC, causes signal drift [32]. As a result, RIA-induced RI change must also be known to understand radiation-induced signal drift. While Kramers-Kronig relation can be used to assess the change in RI from RIA[123], [124], it requires the full spectrum in a wide frequency range for which dose-dependent data are not available. Besides RIA and RIC, there may be other phenomena, like dopant diffusion, stress relaxation, temperature, and so on, which alter the RI and the length of the optical fiber[211], [212]. Moreover, their individual effects on the RI and the length of the optical fiber may be different from their combined effects. Online measurement may provide the change in RI and length of optical fiber caused by any specific phenomena to which the fiber is subjected, including RIC, RIA, dopant diffusion, and temperatures. Once the individual contribution of RI and length on signal drift are known, it is possible to model an optimized sensor design to correct radiation-induced signal drift while measuring other physical parameters. Because the proposed cascaded FPI can make online measurements of the RI and length changes, it has the potential to be used in high pressure or radiation environments to compensate for signal drift.

In summary, a simple cascaded FPI has been proposed to calculate the RI and length compaction. The air cavity is used to calculate the linear compaction, and then the RI is calculated from the silica cavity by considering the same amount of linear compaction of this cavity to that of the air cavity. However, cavity length separation for each cavity is required to perform this job. The FFT algorithm has been utilized to get the frequency domain signal from the total interference spectrum of the cascaded FPI. Then two bandpass filters have been applied to separate the individual cavity lengths from the total spectrum. First, we performed modeling work and then did the experiment to validate the modeling work. This simple technique by using just cascaded cavities can be used to measure RI and length change due to RIC, RIA, temperature, pressure, dopant diffusion, or any combination of them.

## CHAPTER SIX: FIBER OPTIC GAS PRESSURE SENSORS

Fiber optics sensors are now matured and desirable for many nuclear applications due to their inherent advantages which include small size, robustness, high sensitivity, immunity to electromagnetic interference, and multiplexing capability. In the last couple of years, significant amount of research and development have been conducted on fiber optic sensors, which make them a class of standard instrumentation in many industries. Specifically, for pressure sensing, a wide range of fiber-based sensors have been developed for various pressure ranges and environments. Pressure measurement in fuel rod plenum, coolant pressure during LOCA testing, advanced coolant (helium, sodium, molten salt) pressure for flow loop operation during the fuel burnup is of utmost importance to prevent possible accidents associated with them. Since optical fiber dissolves into water, special designs are required to measure pressure in nuclear reactors. The goal of this chapter is to propose a model to monitor the fission gas pressure into the plenum.

### **6.1. Plenum Pressure**

To create an inert environment and a high thermal conductivity to transfer heat to the fuel cladding, fresh fuel rods are pressured with 2 MPa of helium gas. However, during the fuel burnup, other fission gases like krypton and xenon release, which precipitate into bubbles resulting in fuel swelling. These fission gases propagate to the grain boundary and migrate to the plenum of the fuel rod. The fuel swelling and release of fission gases increase the pressure inside the fuel rod. Releasing of fission gases during the fuel burnup increases the interaction between fuel pallet and cladding, which ultimately damage the fuel quality.

Real-time monitoring of fission gas release is important for fuel performance. Since the space in the plenum region is small, it limits the use of many technologies which can be deployed. Since fiber optic sensors are small and can survive in nuclear environment, they can be deployed to monitor fission gases during the fuel burnup.

## 6.2. Fiber Optic Pressure Sensors

In recent years, gas pressure sensors based on optical fibers have drawn considerable attention, owing to their myriad advantages, which include but are not limited to their compact size, light weight, immunity to electromagnetic interference, high sensitivity, good stability, and multiplexing capabilities. To date, many types of fiber-optic pressure sensors (e.g., FBGs[213], photonic crystal fibers (PCFs)[214], Mach-Zehnder interferometers[215], [216], Sagnac interferometers[217], and FPIs[56], [57], [218]–[229]) have been explored. In particular, FPIs have been widely used for gas pressure sensing, due to their miniature size and high sensitivity. In general, two types of FPI pressure sensors are used: (1) closed cavity and (2) open cavity. In the closed cavity structure, the gas pressure alters the cavity length, and this alteration is used as a basis for sensitivity assessments. However, the change in cavity length of due pressure is negligible because glass fiber has a large Young's modulus (72.9 GPa) and small elasto-optic coefficient (0.17). To enhance the sensitivity of closed cavity structures, a diaphragm with a thickness of tens of micrometers (or even less) as the sensing element is used at the tip of the fiber. However, a thinner diaphragm makes the sensor head fragile. Moreover, under long-term high pressure, the diaphragm may creep. Nevertheless, a number of diaphragm-based FPI pressure sensors have been reported[57], [222]–[224], [227]. On the other hand, in an open cavity extrinsic FPI based pressure sensor, variation in the gas-pressure-induced refractive

index (RI) is utilized to assess sensitivity. This type of structure is more common in gas pressure sensing, and has been widely explored[56], [218]–[221], [225], [226], [228], [229]. Although a femtosecond (fs) laser was used on most fiber-based single-cavity-based FPIs to create the air hole channel that flows the gas in and out of the cavity [56], for a cascaded cavity (i.e., with two or more cavities in series), either an fs laser[219], core-offset structure[220], side open air hole[221], PCFs[226], or thin capillary (CAP)[218], [225] tube is used to flow the gas. Since fs lasers are quite expensive, and signal extraction from cascaded FPIs makes it complex, a simple structure that affords easy signal demodulation is expected. A gas pressure sensor based on a core-offset structure with an angle cleaved end face was reported in[228]. However, the core-offset structure significantly weakens the sensor's mechanical strength. A fiber-tip gas pressure sensor based on dual capillaries, with the diameter of the second capillary being smaller than that of the first capillary and angle cleaved end face was reported in[218]. Due to the angle end face, the Fresnel reflection from the second capillary's fiber-air interface was significantly reduced, and the reflection spectrum looked similar to that of a single-cavity FPI. Apart from the angle end face, which circumvented the unwanted Fresnel reflection and allowed for obtaining a single-cavity- like spectrum from the cascaded FPI, a chemical etching process was also applied in[229] to roughen the end face of the second cavity.

Here, we report on gas pressure sensitivity of open cavity based different structured extrinsic FPIs gas pressure sensors. We fabricate three sensors based on FPI structure: (1) SMF-CAP-PCF, (2) SMF-CAP-CAP, and (3) SMF-CAP-SMF (SMF: single mode fiber; CAP: capillary; PCF: photonic crystal fiber) and among them two (SMF-CAP-CAP and

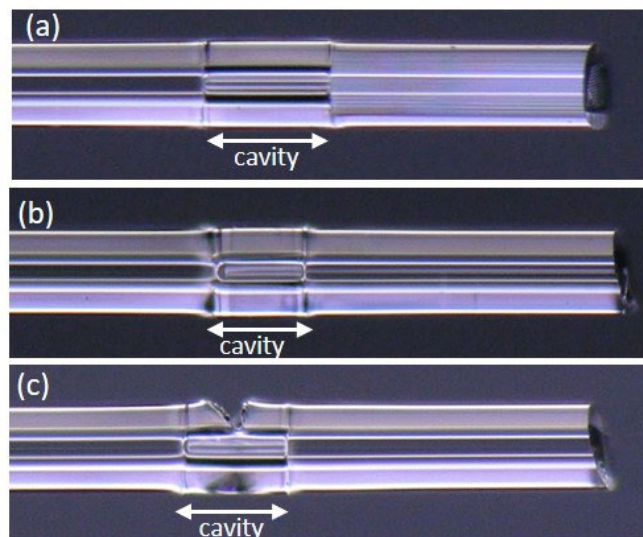


**Figure 6.1** Microscopic images of sensors based on differently structured FPIs: (a) SMF-CAP-PCF, (b) SMF-CAP-CAP, and (c) SMF-CAP-SMF.

SMF-CAP-SMF) are available in literature. We compare these two sensors to our novel SMF-CAP-PCF sensors in terms of sensitivity, fabrication feasibility and cost. For easy signal demodulation, we use an angle cleaved end face for all three structures-based gas sensors. Helium gas pressure was varied from atmospheric to 5 MPa to test the sensitivity of the three different types of structures.

### 6.3. Fabrication Procedures

Figure 6.1 shows microscopic images of the fabricated sensors. For the first two structures (i.e., SMF-CAP-PCF in Fig. 6.1[a] and SMF-CAP-CAP in Fig. 6.1[b]), only cleaving and fusion splicing were required. For the SMF-CAP-SMF structure in Fig. 6.1(c), a glass processor (LZM-120, Fujikura) was used to create an air hole channel, in addition to the cleaving and splicing. We used Polymicro Technologies capillary tubes with inner diameters of 39.2  $\mu\text{m}$  (TSP040150) and 10.8  $\mu\text{m}$  (TSP010150). Note that we only installed the 10.8  $\mu\text{m}$  capillary tube into the SMF-CAP-CAP structure, where it served as the second cavity for flowing the gas in and out the open cavity. Otherwise, we always used the 39.2

$\mu\text{m}$  capillary tube for all three structures. For the PCF, we used an NKT Photonics LMA-8 fiber with a solid core diameter of  $8\ \mu\text{m}$ , an air hole diameter of  $2.22\ \mu\text{m}$ , a pitch of  $5.55\ \mu\text{m}$ , and a total of six air hole rings. To fabricate the SMF-CAP-PCF structure, we first cleaved the SMF and silica capillary tubes using the cleaving tool (CT101/102, Fujikura), then conducted fusion splicing (70S+ Fusion Splicer, Fujikura). We again cleaved the fusion-spliced capillary tube at a specified distance from the spliced position in order to create the open cavity. Finally, we fusion spliced the cleaved PCF to the capillary tube to complete the structure. To reduce the Fresnel reflection, the PCF was cleaved at an angle greater than  $8^\circ$  at a distance from the capillary-PCF fusion point. For the SMF-CAP-CAP structure, we first spliced the SMF to a large-diameter capillary tube ( $39.2\ \mu\text{m}$ ), then cleaved and spliced with a smaller-inner-diameter capillary tube ( $10.8\ \mu\text{m}$ ), and finally cleaved at an angle greater than  $8^\circ$ . We adopted the same procedure to fabricate the SMF-CAP-SMF structure. LZM-120 was used to make an air hole on the capillary tube to enable gas flow. The diameter of the hole was measured to be  $52\ \mu\text{m}$ . Table 6.1 shows the fusion splicing parameters used for fabricating these structures. These parameters were carefully selected to avoid air hole collapse in the PCF and thinner-diameter capillary tube. During fusion splicing of two silica capillaries tubes (TSP040150 and TSP010150) of the SMF-

**Table 6.1 Fusion splicing parameters for all structures**

Structure	Prefuse power	Prefuse time	Arc1 power	Arc1 time
SMF-CAP-PCF SMF-CAP-CAP SMF-CAP-SMF	Std-10 bit	120 ms	Std-70 bit	500 ms

CAP-CAP structure, the large-diameter capillary tube was offset from the electrode arcing points to avoid the unbalanced heating. Note that the same fusion splicing parameters were applied across all splicing points (i.e., SMF-CAP, CAP-CAP, and CAP-PCF).

#### 6.4. Working Principle and Results

Since the Fresnel reflection from the fiber-air interface is low ( $\sim 4\%$ ), the total reflection of individual structure can be considered as the two-beam interference. The intensity of low-finesse two-beam interferences can be expressed as[218]:

$$I = I_1 + I_2 + 2\sqrt{I_1 I_2} \cos\varphi \quad (6.1)$$

where  $I_1$  and  $I_2$  are the reflected intensities from the first and second interfaces of the open cavity, and  $\varphi = \frac{4\pi nL}{\lambda}$  is the phase difference. The symbols  $n$  and  $\lambda$  represent the RI and wavelength of the light, respectively. Since the gas can easily flow in and out of the cavity, the net pressure acting on the cavity is zero. Thus, any wavelength shift due to pressure-induced changes in cavity length is negligible. As discussed earlier, the gas-pressure-induced RI variation dominates the cavity length change, altering the reflection spectrum. While RI variation due to pressure and temperature is rather well documented for air and nitrogen gas, the straightforward relationship between temperature and pressurized helium gas has yet to be researched. As a result, we followed the ideal gas law and Lorentz-Lorenz relation to observe the pressure induced RI, expressible as[230]:

$$\frac{n^2 - 1}{n^2 + 1} \frac{RT}{P} = A \quad (6.2)$$

where  $n$ ,  $R$ ,  $T$ , and  $P$  are the RI of the gas, the universal gas constant, the temperature, and the gas pressure, respectively.  $A$  is the molar refractivity, which is dependent on the mean polarizability and can be expressed as:

$$A = \frac{4\pi}{3} N_A \alpha_p \quad (6.3)$$

where  $N_A$  is the Avogadro's number and  $\alpha_p$  is the mean polarizability, whose value for helium gas is taken from[231].

We calculated an RI difference of 0.00158 for helium gas between atmospheric and 5 MPa pressure. For FPIs, the general sensitivity to any measured physical quantity  $X$  can be expressed as[226]:

$$\frac{\Delta\lambda}{\Delta X} = \lambda \left( \frac{1}{n} \frac{\Delta n}{\Delta X} + \frac{1}{L} \frac{\Delta L}{\Delta X} \right) \quad (6.4)$$

Since gas-pressure-induced changes in cavity length are negligible in an open cavity structure, the gas pressure sensitivity can be written as:

$$S = \frac{\Delta\lambda}{\Delta P} = \frac{\lambda}{n} \times \frac{\Delta n}{\Delta P} \quad (6.5)$$

At room temperature, the calculated helium gas pressure sensitivity is 0.5 nm/MPa.

Next, using ultra-purity helium gas, we focused on the responses of the three differently structured sensors under various gas pressures. A schematic of the experimental setup is shown in Fig. 6.2. We connected the three sensors to the three channels of an optical interrogator (Hyperion interrogator, Micron Optics), and precisely recorded the gas pressure using a high-resolution pressure gauge (Fluke 700G, 1000 PSIG). The gas pressure was increased from atmospheric to 5 MPa—at steps of 0.5 MPa—and the corresponding signal was recorded using the optical sensing interrogator. The reflection spectra of all the sensors under gas pressure are shown in Fig. 6.3. In this figure, the resonant wavelengths are observed to undergo a redshift with increasing gas pressure. As the gas pressure rises, the RI of the gas increases within the cavity, as per Eq. (6.2), which

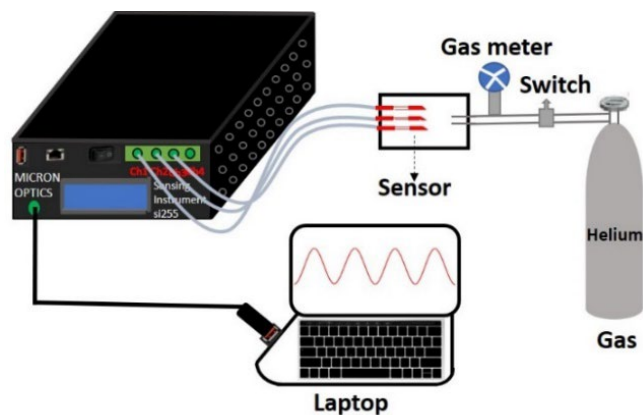


**Figure 6.2** Experimental setup to test the gas response of different sensors.

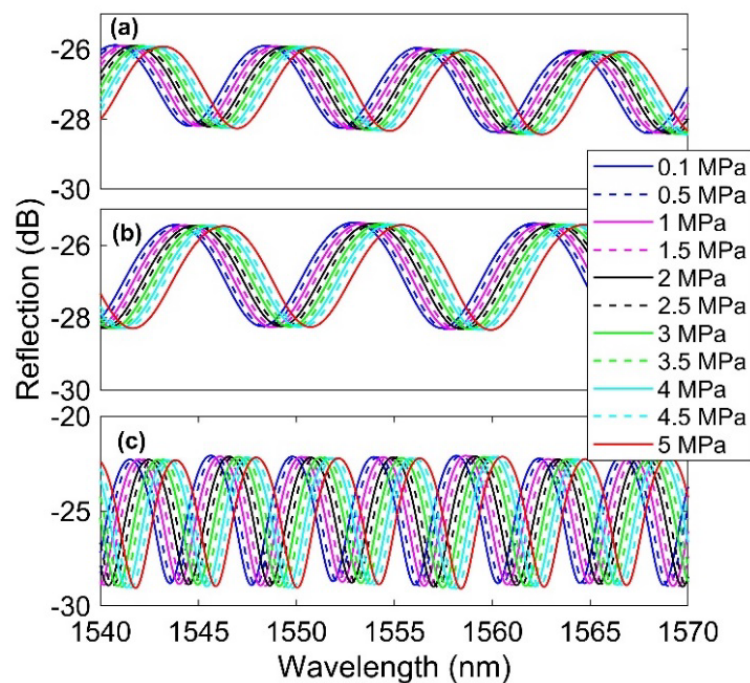


**Figure 6.3** Reflection spectra of the differently structured Fabry-Perot sensors at different gas pressures: (a) SMF-CAP-PCF, (b) SMF-CAP-CAP, and (c) SMF-CAP-SMF.

leads to redshift of wavelength. The relationship between the gas pressure and the wavelength shift is shown in Fig. 6.4. While the experimental data are shown in blue circles (pressurized) and red squares (depressurized), the black line shows the linear fitting of these experimental data. Figure 6.4(a) shows the relative wavelength shift of the SMF-CAP-PCF structure, with a gas pressure sensitivity coefficient of 0.5 nm/MPa, whereas

Figs. 6.5(b) and (c) show sensitivity coefficients of 0.5 nm/MPa and 0.49 nm/MPa for the SMF-CAP-CAP and the SMF-CAP-SMF structures, respectively. The green line in Figs. 6.4(a)–(c) represents where the simulated data overlap the experimental fitting line, thus validating the experimental data. In the simulation, we increased the gas pressure to 5 MPa and calculated the corresponding wavelength shift using Eqs. (6.2)–(6.5). The wavelength shifts almost the same amount whether the cavities are pressured or depressurized, and the linearity is high for all the fabricated sensors' data.

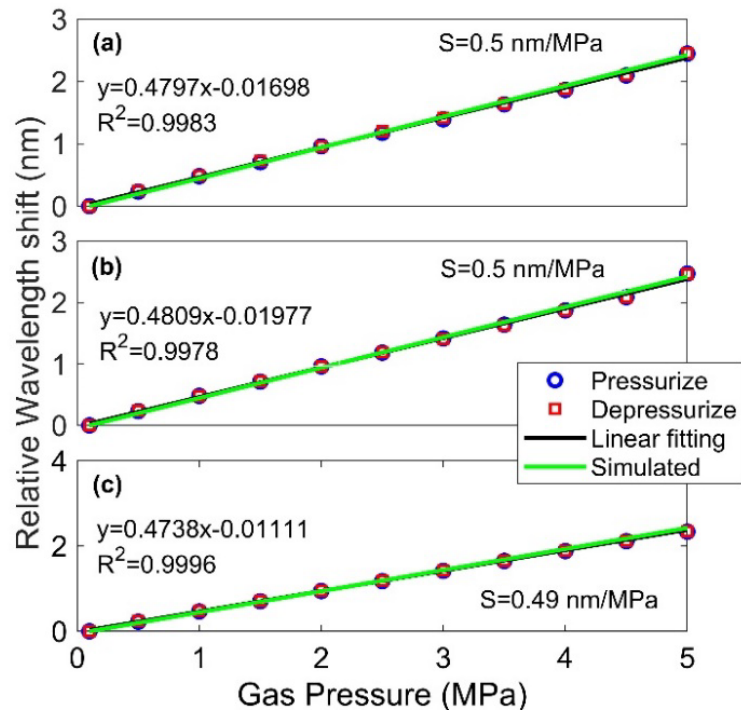


**Figure 6.4** Relative resonant dip wavelength shift of all the sensors when under gas pressure, along with their sensitivity ( $S$ ) and linearity ( $R^2$ ). The discrete points (marked in blue and red) indicate the experimental data when the cavity is pressurized and depressurized, respectively. The black line shows the linear fitting of the experimental data, and the green line indicates where the simulated data overlap the experimental data: (a) SMF-CAP-PCF:  $S = 0.5$  nm/MPa and  $R^2 = 0.998$ ; (b) SMF-CAP-CAP:  $S = 0.5$  nm/MPa and  $R^2 = 0.9978$ ; and (c) SMF-CAP-SMF:  $S = 0.49$  nm/MPa and  $R^2 = 0.9996$ .

Moreover, it is seen that the sensitivity coefficients for three different structured based sensors are within  $0.5 \pm 0.01$  nm/MPa which is very close to the theoretical sensitivity coefficient of 0.5nm/MPa. This validates the experimental results of all the fabricated FPI sensors.

The cavity lengths of SMF-CAP-PCF and SMF-CAP-CAP were close to each other, whereas that of SMF-CAP-SMF was longer. This can be confirmed by looking at the fringe spectra closeness in Fig. 6.3. However, cavity length does not affect gas sensitivity, as demonstrated in Fig. 6.4. Since the SMF-CAP-PCF structure contains a PCF with air holes in the cladding to enable the gas to flow in and out, the intensity of the reflected light is expected to be lower for this structure. The same explanation can be given for SMF-CAP-CAP, as this structure uses a smaller-diameter capillary tube to achieve the same purpose. On the other hand, the reflection intensity is high for SMF-CAP-SMF, since SMF does not have airholes that affects the reflected power. However, to create an air-hole on the capillary tube by laser always weakens the mechanical strength of the sensor. Moreover, extra laser is required to create an air-hole channel on the capillary. As mentioned earlier, it is difficult to separate out an individual signal from the mixed signal of a cascaded FPI (two or more FPIs in series). To overcome this, Xu et al. first reported a dual-capillary-based FPI with an angle cleaved end face[218]. This structure is easy to fabricate and contains the fringe spectrum from a single cavity, thanks to the angle cleaved end face. However, to increase the fringe visibility of interference spectrum, core-offset splicing was conducted. Though we compare the gas sensitivities of all three differently structured FPIs, the SMF-CAP-PCF structure with an angle cleaved end face is especially notable in that it is proposed here for the first time. The beauty of this structure is that it

does not require a laser to create an air hole channel, and there are no issues with the core offset, since the PCF core is solid. The intensity of the reflected light can also be enhanced by using large-diameter solid core PCFs. As the sensitivity of each reported-on structure is almost identical, SMF-CAP-PCF may be the most advantageous, in that it is low-cost. Although various FPI-based gas pressure sensors had been reported on in the literature and compared against each other, we went ahead and fabricated the differently structured FPIs, then tested the resulting sensors by having them all measure the same gas pressure within the exact same environment.

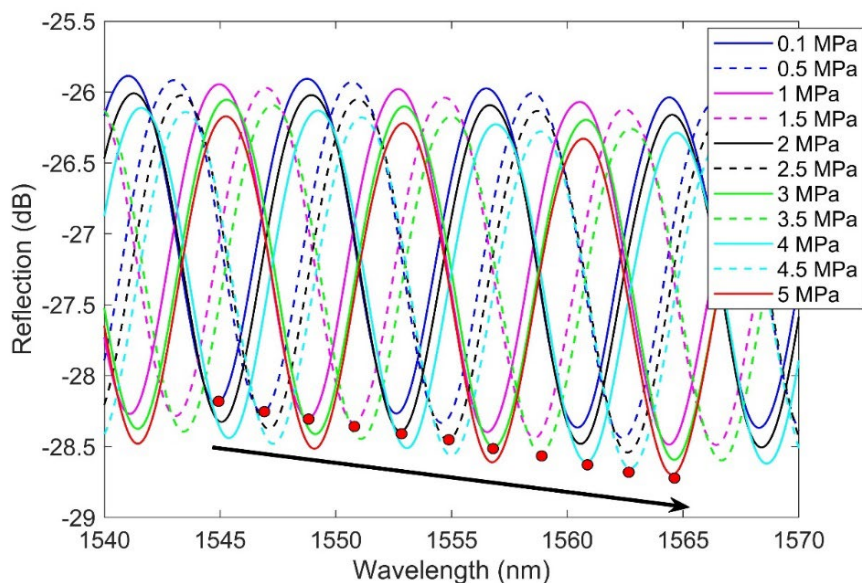
We numerically and experimentally compared the gas pressure sensitivities of three differently structured FPI sensors. It was found that, regardless of cavity length, the sensitivity coefficients of all the sensors were almost identical, as well as in agreement with those of the simulated sensitivity. Here, we reported for the first time on the SMF-CAP-PCF-based FPI sensor with an angle cleaved end face for sensing gas pressure. The advantages and disadvantages of each structure were also discussed.

So far, we have discussed about the helium gas pressure using EFPI. However, during irradiation, different fission gases may accumulate in the plenum region. Next, we focus on gas argon gas pressure sensing using these sensor structures. Two structure-based sensors SMF-CAP-PCF and SMF-CAP-CAP were used to perform this experiment. Since gas pressure sensing using helium gas has already been conducted, we here tested our sensor only with the argon gas.

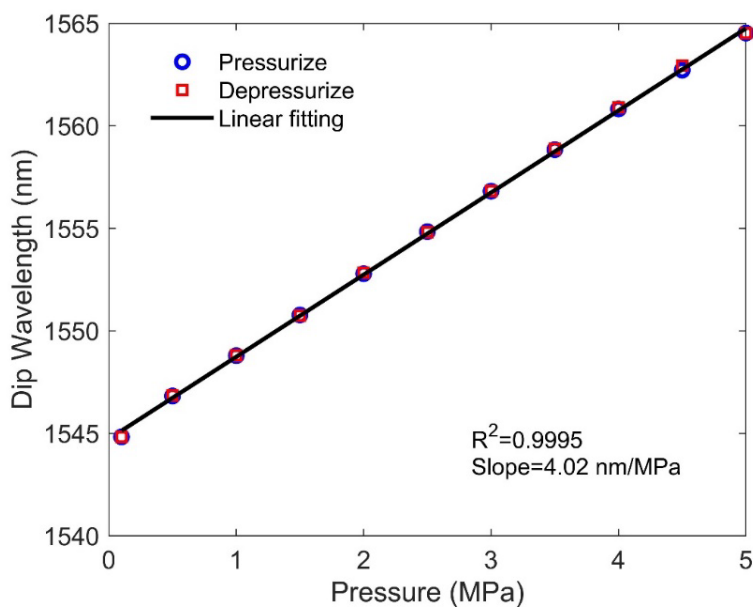
### **6.5. Argon Gas Sensing Using SMF-CAP-PCF**

Figure 6.5 shows the reflection spectra of the SMF-CAP-PCF based FPI sensor when argon gas pressure was increased from atmospheric to 5 MPa. Figure 6.6 shows the

wavelength shift as a function of applied argon gas pressure. It is seen that the wavelength shows a redshift of 20.1 nm when gas pressure was changed from atmospheric to 5 MPa, resulting in a gas pressure sensitivity coefficient of 4.02nm/MPa. It is also observed that



**Figure 6.5** Reflection spectra of SMF-CAP-PCF based FPI at different argon gas pressure.



**Figure 6.6** Wavelength shift as a function applied argon gas pressure.

with pressurize (blue circle) and depressurize (red square) the wavelength shift follow the same trend. The black line denotes the linear fitting of experimental data. We also obtained almost the same sensitivity by using eqs. (6.2)-(6.5) which validates the experimental results.

### 6.6. Argon Gas Sensing Using SMF-CAP-CAP

Figure 6.7 shows the reflection spectra of the SMF-CAP-CAP based FPI sensor when argon gas pressure was increased from atmospheric to 5 MPa. Figure 6.8 shows the wavelength shift as a function of applied argon gas pressure. It is seen that the wavelength shows a redshift of 20.25 nm when gas pressure was changed from atmospheric to 5 MPa, resulting in a gas pressure sensitivity coefficient of 4.05nm/MPa. It is also observed that with pressurize (blue circle) and depressurize (red square) the wavelength shift follow the same trend. The black line denotes the linear fitting of experimental data.

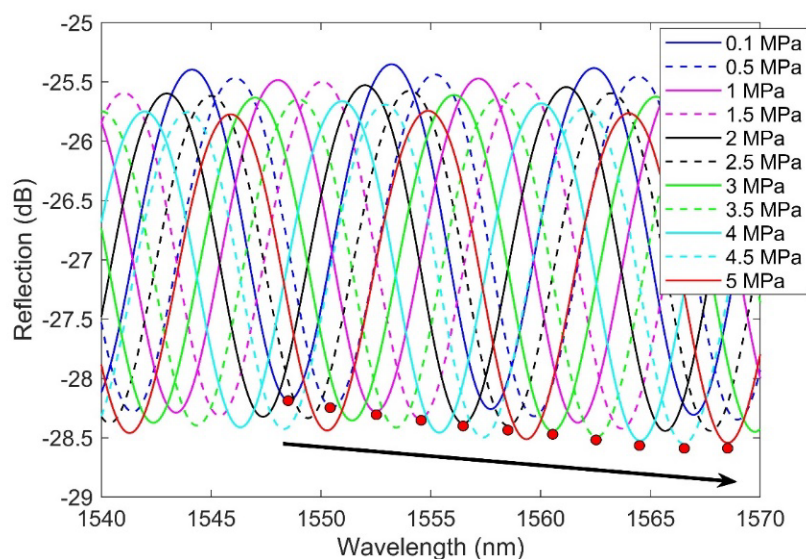


**Figure 6.7** Reflection spectra of SMF-CAP-CAP based FPI at different argon gas pressure

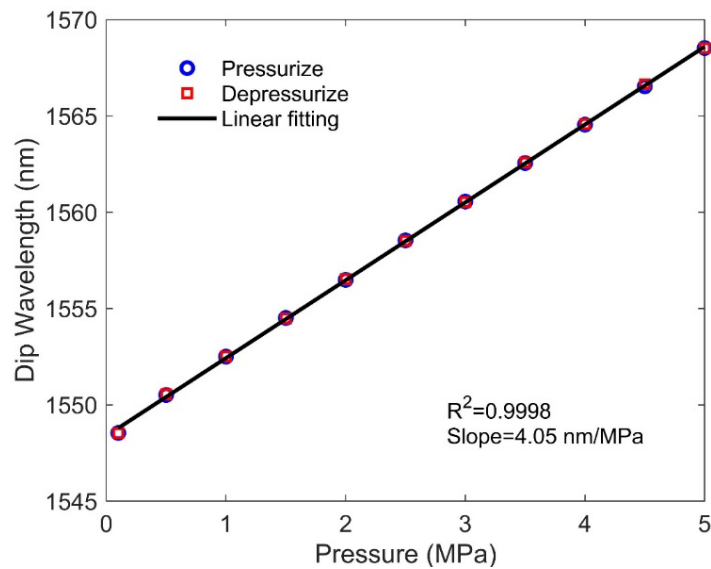


**Figure 6.8 Wavelength shift as a function applied argon gas pressure**

In summary, different structure based FPI sensors have been proposed and experimentally validated for gas pressure sensing. Instead of flat cleaved end facet, we used angle cleaved to ease the signal demodulation. We used helium and argon gas for preliminary test. As different fission gases release during the irradiation, it is important to know which gas is releasing and how for safe and high performance. It is expected that different structure based FPI sensors may be applied to sense fission gas in radiation environment.

## CHAPTER SEVEN: FUTURE PLANNING ON RESEARCH

It is said that research has no ending and always opens doors to improve and extend it. There is a lot of scope to extend the research in this dissertation.

### **7.1. Reduction of Radiation Induced Drift for Temperature Sensing**

Radiation and temperature are the key parameters which drift the characteristic signals of fiber optic sensors significantly in a nuclear environment. However, to separate the radiation-induced drift from the total drift caused by radiation and temperature is quite difficult as both change the length and the RI of the fiber. While we have demonstrated an effective technique to monitor individually length and RI changes of optical fiber in a radiation environment, the next step is to separate the radiation and temperature induced variation of optical fiber in order reduce the temperature measurement error. One way is to use radiation hardened optical fiber and assume the change in optical parameters due to radiation is negligible. However, it has been reported that even radiation hardened fibers have shown significant signal drift in nuclear environment[30]–[32], [129], [161]. Another way is to assume no change in temperature in the reactor full power state and apply machine learning to mitigate the radiation-induced drift[232]. However, there is a big swing in power at the starting of reactor which may induce error in measuring temperature.

### **7.2. Pressure Sensing in Nuclear Reactor**

Fiber optic sensors can be used to monitor fission gases during the irradiation in real-time. However, water pressure, for example in a water-cooled reactor, needs to be measured as well. But fiber optics sensors may not be applied in this case as silica dissolves

in water. A metal diaphragm-based fiber optic sensor can be a potential alternative for measuring water pressure in which optical fiber is protected in a stainless steel to avoid interaction with water.

### **7.3. Long Term Annealing of Optical Fiber**

It is known that thermal treatment up to certain temperature improves the fiber's transmission capacity. However, long-term annealing treatment at high temperature may degrade the fiber performance. As the in-pile condition consists of high radiation and high temperature, sensors used in this environment needs to survive against this extreme condition. The mixed effect of radiation and temperature on optical fibers might be different from the individual effect. Optical fiber thermally treating at different temperatures for long time may be a potential way before deployment of optical fiber sensors in reactor condition to measure real-time temperature.

## CHAPTER EIGHT: CONCLUSIONS

In this dissertation, the effects of radiation on optical fiber sensors have been investigated both numerically and experimentally, and a technique for real-time measurement of RI and length change due to any physical parameters such as radiation, temperature, pressure is proposed to understand how radiation impacts these sensors. The conclusions of this dissertation have been summarized below:

- Since transmission mode sensor, for example LPG, limits its application in tight spaces, we introduced a novel and cost-effective metal coating method which inverts the transmission mode LPG to reflection mode LPG. The modeling work on reflective LPG has been validated by experimental work. Different parameters were measured using the same LPG but in two different modes of operation.
- Different types of resonance-based OFSs were modeled by using commercially available software, and then radiation-induced RI changed values from the literature were inserted into the model design to assess the radiation effects on them. The modeling work stated that radiation induced length compaction needs to be considered along with the radiation induced RI to obtain the RI-BWS. Next, type I regenerated FBGs were exposed to mixed high radiation (gamma and neutron) and high temperature environment in the ATR at INL for 500 effective full power days to observe the radiation effects on the Bragg wavelength experimentally. A significant

blueshift of Bragg wavelength was observed. Since neutron fluence compacts the silica optical fiber, it alters both the RI and the length of optical fiber. The experimental results evident that it was the length compaction over the RI caused by radiation dominated in Bragg wavelength shift. It was also observed that temperature significantly counteracts the neutron induced compaction. It is because temperature thermally expands the silica fiber whereas neutron fluence compacts it. The changes in the RI and the length induced by radiation were calculated by using different numerical equations. Then these values were inserted into a model FBG in order see the RI-BWS. It was seen that the RI-BWS from the modeled FBG due to the calculated values of RI and length change from the experimental neutron fluence by using different numerical equations are different from the experimentally observed RI-BWS. It is because only compaction-induced RI variation was considered. However, RI may change due to RIA, stress relaxation, compositional exchange, dose, dose rate, etc. To predict the correct RI-BWS, it is necessary to consider the RI change caused by the specific phenomena to which the fiber is subjected, including RIC, RIA, dopant diffusion, temperatures, dose, and dose rate, etc. An on-line measurement of the radiation-induced RI and length changes can be a potential way for understanding the structural changes of optical fiber and measuring the RI-BWS in an FBG in a nuclear environment.

- Next, a cascaded F-P structure to measure the macroscopic changes induced in optical fibers by radiation is proposed. Since the cascaded structure

consisted of an air cavity and a silica cavity in series, these cavities were utilized to measure the RI and length change caused by radiation. For being hollow, the air cavity was used to measure the length compaction. Since radiation alters both the RI and the length of the silica cavity, the length compaction from the air cavity was used to monitor the RI in the silica cavity. As the radiation experiment is expensive and time-consuming, a cascaded F-P structure was fabricated and tested against temperature to measure the change in RI and length real-time. Temperature testing was chosen because like radiation, it also alters both the RI and the length of optical fiber. The experimental results stated that the proposed cascaded F-P structure successfully measured the RI and the length in real-time and in accurately. Since this structure can measure the changes in optical fiber caused by physical parameters, it will be tested in ATR at INL to monitor the macroscopic changes in real-time induced by radiation. It is possible to correct the radiation-induced signal drift in OFS, and hence the temperature measurement errors if macroscopic changes are known.

- An extrinsic Fabry-Perot based OFS is demonstrated to measure the fission gas pressure which allows understanding the implications of fission gas release during an accident, important for safe and high performance. Due to lots of intrinsic advantages, OFS can be a potential alternative to monitor fission gases during irradiation.

## BIBLIOGRAPHY

- [1] T. Biswas, "Study of extraordinary light guidance in plasmonic hollow core photonic crystal fiber (PCF) and in specialty PCFs at dirac point for emerging niche applications," Ph.D. dissertation, University of Calcutta, Kolkata, India, 2017.
- [2] J. A. Buck, *Fundamentals of Optical Fibers*, 2nd ed., NJ, USA, John Wiley & Sons, 2004.
- [3] Basic Optics for Optical Fiber, *Fosco Connect*. [Online]. Available: <http://www.fiberoptics4sale.com/wordpress/basic-optics-for-optical-fiber/>
- [4] G. P. Agrawal, *Fiber-Optic Communication Systems*, NJ, USA, John Wiley & Sons, 2012.
- [5] G. Keiser, *Optical Fiber Communications*, New York, NY, USA, McGraw-Hill Science, Engineering & Mathematics, 1983.
- [6] Fiber: The Causes of Limitation on Optical Transmission Distance, *Cablesys*. [Online]. Available: <https://cablesys.com/updates/fiber-the-causes-of-limitation-on-optical-transmission-distance/>
- [7] W. H. Zachariasen, "The atomic arrangement in glass," *J. Am. Chem. Soc.*, vol. 54, no. 10, pp. 3841–3851, Oct. 1932.
- [8] A. C. Wright, "Defect-free vitreous networks: the idealised structure of SiO<sub>2</sub> and related glasses," in *Defects in SiO<sub>2</sub> and related dielectrics: science and technology*, G. Pacchioni, L. Skuja, and D. L. Griscom, Eds. Dordrecht: Springer Netherlands, 2000, pp. 1–35.
- [9] F. L. Galeener, R. A. Barrio, E. Martinez, and R. J. Elliott, "Vibrational Decoupling of Rings in Amorphous Solids," *Phys. Rev. Lett.*, vol. 53, no. 25, pp. 2429–2432, Dec. 1984.

- [10] F. L. Galeener, "Planar rings in glasses," *Solid State Commun.*, vol. 44, no. 7, pp. 1037–1040, Nov. 1982.
- [11] A. D. Kersey and A. Dandridge, "Applications of fiber-optic sensors," *IEEE Trans. Compon. Manuf. Technol.*, vol. 13, no. 1, pp. 137–143, Mar. 1990
- [12] D. A. Jackson, "Fiber Sensor Review," in *Trends in Optical Fibre Metrology and Standards*, O. D. D. Soares, Ed. Dordrecht: Springer Netherlands, 1995, pp. 629–646.
- [13] B. Lee, "Review of the present status of optical fiber sensors," *Opt. Fiber Technol.* vol. 9, no. 2, pp. 57–79, Apr. 2003.
- [14] H.-E. Joe, H. Yun, S.-H. Jo, M. B. G. Jun, and B.-K. Min, "A review on optical fiber sensors for environmental monitoring," *Int. J. of Precis. Eng. and Manuf.-Green Tech.*, vol. 5, no. 1, pp. 173–191, Jan. 2018.
- [15] Y. Li, Z. Hua, F. Yan, and P. Gang, "Metal coating of fiber Bragg grating and the temperature sensing character after metallization," *Opt. Fiber Technol.*, vol. 15, no. 4, pp. 391–397, Aug. 2009.
- [16] G. Meltz, W. W. Morey, and W. H. Glenn, "Formation of Bragg gratings in optical fibers by a transverse holographic method," *Opt. Lett.*, vol. 14, no. 15, pp. 823–825, Aug. 1989.
- [17] Fiber Bragg Gratings: Fundamentals and Applications in Telecommunications and Sensing. *Artech House*. [Online]. Available: <https://us.artechhouse.com/Fiber-Bragg-Gratings-Fundamentals-and-Applications-in-Telecommunications-and-Sensing-P1585.aspx>
- [18] M. M. Werneck, R. C. S. B. Allil, B. A. Ribeiro, and F. V. B. de Nazaré, "A guide to fiber Bragg grating sensors," *Current Trends in Short- and Long-period Fiber Gratings*, Intech: Rijeka, Croatia, 2013.
- [19] A. V. Brakel, "Sensing characteristics of an optical fibre long-period grating Michelson refractometer," Ph.D. dissertation, Rand Afrikaans University, Johannesburg, South Africa, 2017.

- [20] G. Cheymol *et al.*, “Test of fibre Bragg gratings samples under high fast neutrons fluence,” *EPJ Web Conf.*, vol. 170, p. 04004, 2018.
- [21] J. Kou, S. Qiu, F. Xu, and Y. Lu, “Demonstration of a compact temperature sensor based on first-order Bragg grating in a tapered fiber probe,” *Opt. Express*, vol. 19, no. 19, pp. 18452–18457, Sep. 2011.
- [22] N. Liu, Y. Li, Y. Wang, H. Wang, W. Liang, and P. Lu, “Bending insensitive sensors for strain and temperature measurements with Bragg gratings in Bragg fibers,” *Opt. Express*, vol. 19, no. 15, pp. 13880–13891, Jul. 2011.
- [23] F. Urban, J. Kadlec, R. Vlach, and R. Kuchta, “Design of a pressure sensor based on optical fiber Bragg grating lateral deformation,” *Sensors*, vol. 10, no. 12, Art. no. 12, Dec. 2010.
- [24] Q. Jiang and D. Hu, “Microdisplacement sensor based on tilted fiber Bragg grating transversal load effect,” *IEEE Sens. J.*, vol. 11, no. 9, pp. 1776–1779, Sep. 2011.
- [25] B. Gu, M. Yin, A. P. Zhang, J. Qian, and S. He, “Optical fiber relative humidity sensor based on FBG incorporated thin-core fiber modal interferometer,” *Opt. Express*, vol. 19, no. 5, pp. 4140–4146, Feb. 2011.
- [26] A. Stefani, W. Yuan, S. Andresen, and O. Bang, “Polymer optical fiber Bragg grating sensors: Measuring acceleration,” in *35th Australian Conference on Optical Fibre Technology*, Dec. 2010, pp. 1–4.
- [27] C. Ambrosino *et al.*, “Fiber Bragg grating and magnetic shape memory alloy: novel high-sensitivity magnetic sensor,” *IEEE Sens. J.*, vol. 7, no. 2, pp. 228–229, Feb. 2007.
- [28] K. Reck, E. V. Thomsen, and O. Hansen, “MEMS Bragg grating force sensor,” *Opt. Express*, vol. 19, no. 20, pp. 19190–19198, Sep. 2011.
- [29] M. Moccia, M. Pisco, A. Cutolo, V. Galdi, P. Bevilacqua, and A. Cusano, “Opto-acoustic behavior of coated fiber Bragg gratings,” *Opt. Express*, vol. 19, no. 20, pp. 18842–18860, Sep. 2011.

- [30] G. Cheymol *et al.*, “Study of fiber Bragg grating samples exposed to high fast neutron fluences,” *IEEE Trans. Nucl. Sci.*, vol. 65, no. 9, pp. 2494–2501, Sep. 2018.
- [31] L. Remy, G. Cheymol, A. Gusarov, A. Morana, E. Marin, and S. Girard, “Compaction in optical fibres and fibre Bragg gratings under nuclear reactor high neutron and gamma fluence,” *IEEE Trans. Nucl. Sci.*, vol. 63, no. 4, pp. 2317–2322, Aug. 2016.
- [32] A. Morana *et al.*, “Radiation tolerant fiber Bragg gratings for high temperature monitoring at MGy dose levels,” *Opt. Lett.*, vol. 39, no. 18, pp. 5313–5316, Sep. 2014.
- [33] V. Bhatia, “Properties and sensing applications of long-period gratings,” Ph.D. dissertation, Virginia Polytechnic Institute and State University, Blacksburg, Virginia, 1996.
- [34] S. W. James and R. P. Tatam, “Optical fibre long-period grating sensors: characteristics and application,” *Meas. Sci. Technol.*, vol. 14, no. 5, pp. R49–R61, Mar. 2003.
- [35] F. Esposito, A. Srivastava, A. Iadicicco, and S. Campopiano, “Multi-parameter sensor based on single Long Period Grating in Panda fiber for the simultaneous measurement of SRI, temperature and strain,” *Opt. Laser Technol.*, vol. 113, pp. 198–203, May 2019.
- [36] B. A. L. Gwandu *et al.*, “Simultaneous refractive index and temperature measurement using cascaded long-period grating in double-cladding fibre,” *Electron. Lett.*, vol. 38, no. 14, pp. 695–696, Jul. 2002.
- [37] J. Hromadka *et al.*, “Multi-parameter measurements using optical fibre long period gratings for indoor air quality monitoring,” *Sens. Actuators B Chem.*, vol. 244, pp. 217–225, Jun. 2017.
- [38] R. Zawisza, T. Eftimov, P. Mikulic, W. J. Bock, and L. R. Jaroszewicz, “Ambient refractive-index measurement with simultaneous temperature monitoring based on

- a dual-resonance long-period grating inside a fiber loop mirror structure,” *Sensors*, vol. 18, no. 7, Art. no. 7, Jul. 2018.
- [39] V. Bhatia, “Applications of long-period gratings to single and multi-parameter sensing,” *Opt. Express*, vol. 4, no. 11, pp. 457–466, May 1999.
- [40] F. Esposito, A. Stăncălie, D. Neagu, A. Iadicicco, D. Sporea, and S. Campopiano, “Response of long period gratings to gamma and neutron-gamma radiations,” in *Seventh European Workshop on Optical Fibre Sensors*, Aug. 2019, vol. 11199, p. 111990B.
- [41] A. Stancălie *et al.*, “Arc-induced long period gratings in standard and speciality optical fibers under mixed neutron-gamma irradiation,” *Sci. Rep.*, vol. 7, no. 1, Art. no. 1, Nov. 2017.
- [42] M. K. Barnoski and S. M. Jensen, “Fiber waveguides: a novel technique for investigating attenuation characteristics,” *Appl. Opt.*, vol. 15, no. 9, pp. 2112–2115, Sep. 1976.
- [43] Y. Muanenda, C. J. Oton, and F. Di Pasquale, “Application of Raman and Brillouin scattering phenomena in distributed optical fiber sensing,” *Front. Phys.*, vol. 7, p. 155, 2019.
- [44] J. Jin, H. Zhang, J. Liu, and Y. Li, “Distributed Temperature Sensing Based on Rayleigh Scattering in Irradiated Optical Fiber,” *IEEE Sens. J.*, vol. 16, no. 24, pp. 8928–8935, Dec. 2016.
- [45] M. Roman *et al.*, “A spatially distributed fiber-optic temperature sensor for applications in the steel industry,” *Sensors*, vol. 20, no. 14, Art. no. 14, Jan. 2020.
- [46] K. M. McCary, B. A. Wilson, A. Birri, and T. E. Blue, “Response of distributed fiber optic temperature sensors to high-temperature step transients,” *IEEE Sens. J.*, vol. 18, no. 21, pp. 8755–8761, Nov. 2018.
- [47] L. Sheng *et al.*, “Distributed temperature sensing system based on Brillouin scattering effect using a single-photon detector,” *Intl. J. Optics*, vol. 2021, p. e6623987, Apr. 2021.

- [48] A. Méndez and E. Diatzikis, “Fiber optic distributed pressure sensor based on Brillouin scattering,” in *Optical Fiber Sensors (2006)*, paper ThE46, Oct. 2006, p. ThE46.
- [49] J. M. Lopez-Higuera, L. Rodriguez Cobo, A. Quintela Incera, and A. Cobo, “Fiber Optic Sensors in Structural Health Monitoring,” *J. Lightw. Technol.*, vol. 29, no. 4, pp. 587–608, Feb. 2011.
- [50] D. Alasia, A. F. Fernandez, L. Abrardi, B. Brichard, and L. Thévenaz, “The effects of gamma-radiation on the properties of Brillouin scattering in standard Ge-doped optical fibres,” *Meas. Sci. Technol.*, vol. 17, no. 5, pp. 1091–1094, Apr. 2006.
- [51] Y. Liu, L. Ma, C. Yang, W. Tong, and Z. He, “Long-range Raman distributed temperature sensor with high spatial and temperature resolution using graded-index few-mode fiber,” *Opt. Express*, vol. 26, no. 16, pp. 20562–20571, Aug. 2018.
- [52] I. Laarossi *et al.*, “Ultrahigh temperature and strain hybrid integrated sensor system based on Raman and femtosecond FBG inscription in a multimode gold-coated fiber,” *Opt. Express*, vol. 27, no. 26, pp. 37122–37130, Dec. 2019.
- [53] Z. Zhou *et al.*, “Optical fiber displacement sensor based on Stokes Raman backscattering light bending loss,” *Opt. Fiber Technol.*, vol. 66, p. 102667, Oct. 2021.
- [54] F. B. H. Jensen, E. Takada, M. Nakazawa, T. Kakuta, and S. Yamamoto, “Consequences of radiation effects on pure-silica-core optical fibers used for Raman-scattering-based temperature measurements,” *IEEE Trans. Nucl. Sci.*, vol. 45, no. 1, pp. 50–58, Feb. 1998.
- [55] Z. Chen *et al.*, “High-temperature sensor based on Fabry-Perot interferometer in microfiber tip,” *Sensors*, vol. 18, no. 1, Art. no. 1, Jan. 2018.
- [56] L. Zhang *et al.*, “A diaphragm-free fiber Fabry-Perot gas pressure sensor,” *Rev. Sci. Instr.*, vol. 90, no. 2, p. 025005, Feb. 2019.

- [57] H. Bae, D. Yun, H. Liu, D. A. Olson, and M. Yu, “Hybrid miniature Fabry–Perot sensor with dual optical cavities for simultaneous pressure and temperature measurements,” *J. Lightw. Technol.*, vol. 32, no. 8, pp. 1585–1593, Apr. 2014.
- [58] A. M. Shrivastav, D. S. Gunawardena, Z. Liu, and H.-Y. Tam, “Microstructured optical fiber based Fabry–Pérot interferometer as a humidity sensor utilizing chitosan polymeric matrix for breath monitoring,” *Sci Rep*, vol. 10, no. 1, p. 6002, Apr. 2020.
- [59] R. St-Gelais *et al.*, “Gas sensing using polymer-functionalized deformable Fabry–Perot interferometers,” *Sens. Actuators B Chem.*, vol. 182, pp. 45–52, Jun. 2013.
- [60] G. Cheymol, A. Gusarov, S. Gaillot, C. Destouches, and N. Caron, “Dimensional measurements under high radiation with optical fibre sensors based on white light interferometry - report on irradiation tests,” *IEEE Trans. Nucl. Sci.*, vol. 61, no. 4, pp. 2075–2081, Aug. 2014.
- [61] G. Cheymol, B. Brichard, and J. F. Villard, “Fiber optics for metrology in nuclear research reactors—applications to dimensional measurements,” *IEEE Trans. Nucl. Sci.*, vol. 58, no. 4, pp. 1895–1902, Aug. 2011.
- [62] W. Primak and R. Kampwirth, “The radiation compaction of vitreous silica,” *J. Appl. Phys.*, vol. 39, no. 12, pp. 5651–5658, Nov. 1968.
- [63] M. Rothschild, D. J. Ehrlich, and D. C. Shaver, “Effects of excimer laser irradiation on the transmission, index of refraction, and density of ultraviolet grade fused silica,” *Appl. Phys. Lett.*, vol. 55, no. 13, pp. 1276–1278, Sep. 1989.
- [64] W. Primak and R. Kampwirth, “Impurity effect in the ionization dilatation of vitreous silica,” *J. Appl. Phys.*, vol. 39, no. 13, pp. 6010–6017, Dec. 1968.
- [65] J. E. Shelby, “Radiation effects in hydrogen-impregnated vitreous silica,” *J. Appl. Phys.*, vol. 50, no. 5, pp. 3702–3706, May 1979.
- [66] P. L. Higby *et al.*, “Radiation effects on the physical properties of low-expansion-coefficient glasses and ceramics,” *J. Ame. Ceram. Soc.*, vol. 71, no. 9, pp. 796–802, 1988.

- [67] C. B. Norris and E. P. EerNisse, "Ionization dilatation effects in fused silica from 2 to 18-keV electron irradiation," *J. Appl. Phys.*, vol. 45, no. 9, pp. 3876–3882, Sep. 1974.
- [68] C. M. Smith, N. F. Borrelli, D. C. Allan, and T. P. Seward, "Compaction of fused silica under low-fluence/long-term 193-nm irradiation," In Proceedings of the Optical Microlithography X, Santa Clara, CA, USA, 7 July 1997; International Society for Optics and Photonics: Bellingham, WA, USA, 1997; Volume 3051, pp. 116–121.
- [69] R. E. Schenker, F. Piao, and W. G. Oldham, "Material limitations to 193-nm lithographic system lifetimes," In Proceedings of the Optical Microlithography IX, Santa Clara, CA, USA, 7 June 1996; International Society for Optics and Photonics: Bellingham, WA, USA, 1996; Volume 2726, pp. 698–706.
- [70] L. Skuja, M. Hirano, H. Hosono, and K. Kajihara, "Defects in oxide glasses," *phys. status solidi c*, vol. 2, no. 1, pp. 15–24, 2005.
- [71] M. Perry, P. Niewczas, and M. Johnston, "Effects of Neutron-Gamma Radiation on Fiber Bragg Grating Sensors: A Review," *IEEE Sens. J.*, vol. 12, no. 11, pp. 3248–3257, Nov. 2012.
- [72] S. Girard *et al.*, "Radiation Effects on Silica-Based Optical Fibers: Recent Advances and Future Challenges," *IEEE Trans. Nucl. Sci.*, vol. 60, no. 3, pp. 2015–2036, Jun. 2013.
- [73] Y. Ikuta, K. Kajihara, M. Hirano, S. Kikugawa, and H. Hosono, "Effects of H<sub>2</sub> impregnation on excimer-laser-induced oxygen-deficient center formation in synthetic SiO<sub>2</sub> glass," *Appl. Phys. Lett.*, vol. 80, no. 21, pp. 3916–3918, May 2002.
- [74] R. H. Doremus, *Diffusion of Reactive Molecules in Solids and Melts*, NJ, USA, John Wiley & Sons, 2001.
- [75] L. Skuja, B. Güttler, D. Schiel, and A. R. Silin, "Infrared photoluminescence of preexisting or irradiation-induced interstitial oxygen molecules in glassy SiO<sub>2</sub> and  $\alpha$ ," *Phys. Rev. B*, vol. 58, no. 21, pp. 14296–14304, Dec. 1998.

- [76] D. Ricci, G. Pacchioni, M. A. Szymanski, A. L. Shluger, and A. M. Stoneham, "Modeling disorder in amorphous silica with embedded clusters: The peroxy bridge defect center," *Phys. Rev. B*, vol. 64, no. 22, p. 224104, Nov. 2001.
- [77] L. Skuja, K. Kajihara, T. Kinoshita, M. Hirano, and H. Hosono, "The behavior of interstitial oxygen atoms induced by F<sub>2</sub> laser irradiation of oxygen-rich glassy SiO<sub>2</sub>," *Nuclear Instruments and Methods in Physics Research Section B: Beam Interactions with Materials and Atoms*, vol. 191, no. 1, pp. 127–130, May 2002.
- [78] E. P. O'Reilly and J. Robertson, "Theory of defects in vitreous silicon dioxide," *Phys. Rev. B*, vol. 27, no. 6, pp. 3780–3795, Mar. 1983.
- [79] L. Skuja, M. Hirano, and H. Hosono, "Oxygen-Related Intrinsic Defects in Glassy SiO<sub>2</sub>: Interstitial Ozone Molecules," *Phys. Rev. Lett.*, vol. 84, no. 2, pp. 302–305, Jan. 2000.
- [80] D. L. Griscom, "Optical Properties and Structure of Defects in Silica Glass," *J. Ceram. Soc. Jpn.*, vol. 99, no. 1154, pp. 923–942, 1991.
- [81] M. Cannas and F. M. Gelardi, "Vacuum ultraviolet excitation of the 1.9-eV emission band related to nonbridging oxygen hole centers in silica," *Phys. Rev. B*, vol. 69, no. 15, p. 153201, Apr. 2004.
- [82] H. Imai, K. Arai, H. Imagawa, H. Hosono, and Y. Abe, "Two types of oxygen-deficient centers in synthetic silica glass," *Phys. Rev. B*, vol. 38, no. 17, pp. 12772–12775, Dec. 1988.
- [83] G. W. Arnold, "Ion-Implantation Effects in Noncrystalline SiO<sub>2</sub>," *IEEE Trans. Nucl. Sci.*, vol. 20, no. 6, pp. 220–223, Dec. 1973.
- [84] L. N. Skuja, A. N. Streletsky, and A. B. Pakovich, "A new intrinsic defect in amorphous SiO<sub>2</sub>: Twofold coordinated silicon," *Solid State Commun.*, vol. 50, no. 12, pp. 1069–1072, Jun. 1984.
- [85] R. A. Weeks, "Paramagnetic resonance of lattice defects in irradiated quartz," *J. Appl. Phys.*, vol. 27, no. 11, pp. 1376–1381, Nov. 1956.

- [86] D. L. Griscom, "A minireview of the natures of radiation-induced point defects in pure and doped silica glasses and their visible/near-IR absorption bands, with emphasis on self-trapped holes and how they can be controlled," *Phys. Res. Intl.*, vol. 2013, p. e379041, Feb. 2013.
- [87] Y. Hibino and H. Hanafusa, "ESR study on E'-centers induced by optical fiber drawing process," *Jpn. J. Appl. Phys.*, vol. 22, no. 12A, p. L766, Dec. 1983.
- [88] D. L. Griscom and E. J. Friebele, "Fundamental radiation-induced defect centers in synthetic fused silicas: Atomic chlorine, delocalized E' centers, and a triplet state," *Phys. Rev. B*, vol. 34, no. 11, pp. 7524–7533, Dec. 1986, doi: 10.1103/PhysRevB.34.7524.
- [89] D. L. Griscom, "Characterization of three E'-center variants in X- and  $\gamma$ -irradiated high purity  $\alpha$ -SiO<sub>2</sub>," *Nuclear Instruments and Methods in Physics Research Section B: Beam Interactions with Materials and Atoms*, vol. 1, no. 2, pp. 481–488, Feb. 1984, doi: 10.1016/0168-583X(84)90113-7.
- [90] D. L. Griscom, E. J. Friebele, and G. H. Sigel, "Observation and analysis of the primary <sup>29</sup>Si hyperfine structure of the E' center in non-crystalline SiO<sub>2</sub>," *Solid State Commun.*, vol. 15, no. 3, pp. 479–483, Aug. 1974.
- [91] A. L. Tomashuk and M. O. Zabezhailov, "Formation mechanisms of precursors of radiation-induced color centers during fabrication of silica optical fiber preform," *J. App. Phys.*, vol. 109, no. 8, p. 083103, Apr. 2011.
- [92] D. L. Griscom, "Electron spin resonance studies of trapped hole centers in irradiated alkali silicate glasses: A critical comment on current models for HC1 and HC2," *J. Non Cryst. Solids*, vol. 64, no. 1, pp. 229–247, Apr. 1984.
- [93] K. Farah, A. Mejri, F. Hosni, A. H., and B. Boizot, "Formation and decay of colour centres in a silicate glasses exposed to gamma radiation: application to high-dose dosimetry," in *Current Topics in Ionizing Radiation Research*, M. Nenoï, Ed. InTech, 2012.

- [94] M. Suszynska and B. Macalik, "Optical studies in gamma-irradiated commercial soda–lime silicate glasses," *Nuclear Instruments and Methods in Physics Research Section B: Beam Interactions with Materials and Atoms*, vol. 179, no. 3, pp. 383–388, Aug. 2001.
- [95] L. Skuja, K. Kajihara, M. Hirano, and H. Hosono, "Oxygen-excess-related point defects in glassy/amorphous SiO<sub>2</sub> and related materials," *Nuclear Instruments and Methods in Physics Research Section B: Beam Interactions with Materials and Atoms*, vol. 286, pp. 159–168, Sep. 2012.
- [96] E. J. Friebele, D. L. Griscom, M. Stapelbroek, and R. A. Weeks, "Fundamental defect centers in glass: the peroxy radical in irradiated, high-purity, fused silica," *Phys. Rev. Lett.*, vol. 42, no. 20, pp. 1346–1349, May 1979.
- [97] K. Kajihara, M. Hirano, L. Skuja, and H. Hosono, "Role of interstitial voids in oxides on formation and stabilization of reactive radicals: interstitial HO<sub>2</sub> radicals in F<sub>2</sub>-laser-irradiated amorphous SiO<sub>2</sub>," *J. Am. Chem. Soc.*, vol. 128, no. 16, pp. 5371–5374, Apr. 2006.
- [98] K. Kajihara, L. Skuja, M. Hirano, and H. Hosono, "Role of mobile interstitial oxygen atoms in defect processes in oxides: interconversion between oxygen-associated defects in SiO<sub>2</sub> glass," *Phys. Rev. Lett.*, vol. 92, no. 1, p. 015504, Jan. 2004.
- [99] Y. Kim *et al.*, "Magneto-optic characteristics of gamma-ray irradiated Cu-doped optical fiber," in *2013 18th OptoElectronics and Communications Conference held jointly with 2013 International Conference on Photonics in Switching (2013)*, paper WS3\_6, Jun. 2013, p. WS3\_6.
- [100] R. Salh, Defect Related Luminescence in Silicon Dioxide Network: A Review. *Crystalline Silicon-Properties and Uses*, Intech: Rijeka, Croatia, 2013.
- [101] D. L. Griscom, "Self-trapped holes in pure-silica glass: A history of their discovery and characterization and an example of their critical significance to industry," *J. Non Cryst. Solids*, vol. 352, no. 23, pp. 2601–2617, Jul. 2006.

- [102] D. L. Griscom, "Hydrogen model for radiation-induced interface states in SiO<sub>2</sub>-on-Si Structures: A review of the evidence," *J. electron. materials*, vol. 21, no. 7, pp. 763–767, Jul. 1992.
- [103] D. L. Griscom, "Trapped-electron centers in pure and doped glassy silica: A review and synthesis," *Journal of Non-Crystalline Solids*, vol. 357, no. 8, pp. 1945–1962, Apr. 2011, doi: 10.1016/j.jnoncrysol.2010.11.011.
- [104] A. Alessi, S. Girard, C. Marcandella, M. Cannas, A. Boukenter, and Y. Ouerdane, "Raman investigation of the drawing effects on Ge-doped fibers," *J. Non Cryst. Solids*, vol. 357, no. 1, pp. 24–27, Jan. 2011.
- [105] G. Pacchioni, L. Skuja, and D. L. Griscom, *Defects in SiO<sub>2</sub> and Related Dielectrics: Science and Technology*. Springer Science & Business Media, 2012.
- [106] D. P. Hawn, C. M. Petrie, T. E. Blue, and W. Windl, "In-situ gamma radiation induced attenuation in silica optical fibers heated up to 600°C," *J. Non Cryst. Solids*, vol. 379, pp. 192–200, Nov. 2013.
- [107] J. W. H. Schreurs, "Study of some trapped hole centers in X-irradiated alkali silicate glasses," *J. Chem. Phys.*, vol. 47, no. 2, pp. 818–830, Jul. 1967.
- [108] M. J. Weber, *CRC Handbook of Laser Science and Technology Supplement 2: Optical Materials*. CRC Press, 2020.
- [109] S. Girard *et al.*, "Overview of radiation induced point defects in silica-based optical fibers," *Rev. Phys.*, vol. 4, p. 100032, Nov. 2019.
- [110] S. Girard, J. Keurinck, Y. Ouerdane, J.-P. Meunier, and A. Boukenter, "Gamma-rays and pulsed X-ray radiation responses of germanosilicate single-mode optical fibers: influence of cladding codopants," *J. Lightw. Technol.*, vol. 22, no. 8, p. 1915, Aug. 2004.
- [111] E. Regnier, I. Flammer, S. Girard, F. Gooijer, F. Achten, and G. Kuyt, "Low-Dose Radiation-Induced Attenuation at InfraRed Wavelengths for P-Doped, Ge-Doped and Pure Silica-Core Optical Fibres," *IEEE Trans. Nucl. Sci.*, vol. 54, no. 4, pp. 1115–1119, Aug. 2007.

- [112] B. Brichard, S. Agnello, and L. Nuccio, "Comparison between point defect generation by  $\gamma$ -rays in bulk and fibre samples of high purity amorphous SiO<sub>2</sub>," in *2007 9th European Conference on Radiation and Its Effects on Components and Systems*, Sep. 2007, pp. 1–4.
- [113] S. Girard *et al.*, "Transient radiation responses of optical fibers: influence of MCVD process parameters," *IEEE Trans. Nucl. Sci.*, vol. 59, no. 6, pp. 2894–2901, Dec. 2012.
- [114] G. Origlio, M. Cannas, S. Girard, R. Boscaino, A. Boukenter, and Y. Ouerdane, "Influence of the drawing process on the defect generation in multistep-index germanium-doped optical fibers," *Opt. Lett.*, vol. 34, no. 15, pp. 2282–2284, Aug. 2009.
- [115] D. L. Griscom, M. E. Gingerich, and E. J. Friebele, "Model for the dose, dose-rate and temperature dependence of radiation-induced loss in optical fibers," *IEEE Trans. Nucl. Sci.*, vol. 41, no. 3, pp. 523–527, Jun. 1994.
- [116] H. Henschel, O. Koehn, and H. U. Schmidt, "Influence of dose rate on radiation-induced loss in optical fibers," in *Optical Systems in Adverse Environments*, Mar. 1991, vol. 1399, pp. 49–63.
- [117] E. J. Friebele, C. G. Askins, and M. E. Gingerich, "Effect of low dose rate irradiation on doped silica core optical fibers," *Appl. Opt.*, vol. 23, no. 23, pp. 4202–4208, Dec. 1984.
- [118] P. Borgermans, B. Brichard, and M. C. Decreton, "Models for the radiation-induced attenuation in pure silica optical fibers: spectral dependencies and absorption band kinetics," in *Photonics for Space and Radiation Environments II*, Jan. 2002, vol. 4547, pp. 53–60.
- [119] J. Jin, R. Xu, J. Liu, and N. Song, "Experimental investigation of the factors influencing temperature dependence of radiation-induced attenuation in optical fiber," *Opt. Fiber Technol.*, vol. 20, no. 2, pp. 110–115, Mar. 2014.
- [120] H. Henschel and O. Kohn, "Regeneration of irradiated optical fibres by photobleaching," *IEEE Trans. Nucl. Sci.*, vol. 47, no. 3, pp. 699–704, Jun. 2000.

- [121] A. T. Ramsey, W. Tighe, J. Bartolick, and P. D. Morgan, "Radiation effects on heated optical fibers," *Rev. Sci. Instrum.*, vol. 68, no. 1, pp. 632–635, Jan. 1997.
- [122] S. Girard *et al.*, "Combined high dose and temperature radiation effects on multimode silica-based optical fibers," *IEEE Trans. Nucl. Sci.*, vol. 60, no. 6, pp. 4305–4313, Dec. 2013.
- [123] S. Kher, S. Chaubey, S. M. Oak, and A. Gusarov, "Measurement of  $\gamma$ -radiation induced refractive index changes in B/Ge doped fiber using LPGs," *IEEE Photon. Technol. Lett.*, vol. 25, no. 21, pp. 2070–2073, Nov. 2013.
- [124] D. C. Hutchings, M. Sheik-Bahae, D. J. Hagan, and E. W. Van Stryland, "Kramers-Krönig relations in nonlinear optics," *Opt. Quant. Electron.*, vol. 24, no. 1, pp. 1–30, Jan. 1992.
- [125] A. L. Tomashuk *et al.*, "Enhanced radiation resistance of silica optical fibers fabricated in high O<sub>2</sub> excess conditions," *J. Lightw. Technol.*, vol. 32, no. 2, pp. 213–219, Jan. 2014.
- [126] K. Nagasawa, Y. Hoshi, Y. Ohki, and K. Yahagi, "Improvement of radiation resistance of pure silica core fibers by hydrogen treatment," *Jpn. J. Appl. Phys.*, vol. 24, no. 9R, p. 1224, Sep. 1985.
- [127] D. D. Francesca *et al.*, "Influence of O<sub>2</sub> loading pretreatment on the radiation response of pure and fluorine-doped silica-based optical fibers," *IEEE Trans. Nucl. Sci.*, vol. 61, no. 6, pp. 3302–3308, Dec. 2014.
- [128] C. M. Petrie, A. Birri, and T. E. Blue, "High-dose temperature-dependent neutron irradiation effects on the optical transmission and dimensional stability of amorphous fused silica," *J. Non Cryst. Solids*, vol. 525, p. 119668, Dec. 2019.
- [129] G. Cheymol, H. Long, J. F. Villard, and B. Brichard, "High level gamma and neutron irradiation of silica optical fibers in CEA OSIRIS nuclear reactor," *IEEE Trans. Nucl. Sci.*, vol. 55, no. 4, pp. 2252–2258, Aug. 2008.
- [130] H. Kakiuchida, K. Saito, and A. J. Ikushima, "Refractive index, density and polarizability of silica glass with various fictive temperatures," *Jpn. J. Appl. Phys.*, vol. 43, no. 6A, p. L743, May 2004.

- [131] A. Alessi, S. Agnello, S. Grandi, A. Parlato, and F. M. Gelardi, “Refractive index change dependence on Ge(1) defects in  $\gamma$ -irradiated Ge-doped silica,” *Phys. Rev. B*, vol. 80, no. 1, p. 014103, Jul. 2009.
- [132] N. Kitamura, Y. Toguchi, S. Funo, H. Yamashita, and M. Kinoshita, “Refractive index of densified silica glass,” *J. Non Cryst. Solids*, vol. 159, no. 3, pp. 241–245, Jan. 1993.
- [133] E. Lell, N. J. Kreidl, and J. R. Hensler, “Radiation effects in quartz, silica, and glasses.,” *pp 1-93 of Progress in Ceramic Science. Volume 4. Burke, J. E. (ed.). New York, Pergamon Press, Inc., 1966.*, Oct. 1968.
- [134] W. Primak, “Fast-Neutron-Induced Changes in Quartz and Vitreous Silica,” *Phys. Rev.*, vol. 110, no. 6, pp. 1240–1254, Jun. 1958.
- [135] A. Morana, “Gamma-rays and neutrons effects on optical fibers and Bragg gratings for temperature sensors,” Ph.D. dissertation, Université Jean Monnet-Saint-Etienne; Università degli studi, Palerme, Italie, 2013.
- [136] A. Gusarov and S. K. Hoeffgen, “Radiation Effects on Fiber Gratings,” *IEEE Trans. Nucl. Sci.*, vol. 60, no. 3, pp. 2037–2053, Jun. 2013.
- [137] S. Rana, A. S. Rakin, H. Subbaraman, R. Leonhardt, and D. Abbott, “Low loss and low dispersion fiber for transmission applications in the terahertz regime,” *IEEE Photon. Technol. Letters*, vol. 29, no. 10, pp. 830–833, May 2017.
- [138] S. Khaliq, S. W. James, and R. P. Tatam, “Enhanced sensitivity fibre optic long period grating temperature sensor,” *Meas. Sci. Technol.*, vol. 13, no. 5, pp. 792–795, Apr. 2002.
- [139] R. Hou, Z. Ghassemlooy, A. Hassan, C. Lu, and K. P. Dowker, “Modelling of long-period fibre grating response to refractive index higher than that of cladding,” *Meas. Sci. Technol.*, vol. 12, no. 10, pp. 1709–1713, Sep. 2001.
- [140] M. F. S. Ferreira *et al.*, “Roadmap on optical sensors,” *J Opt*, vol. 19, no. 8, Aug. 2017.

- [141] T. Allsop, R. Reeves, D. J. Webb, I. Bennion, and R. Neal, "A high sensitivity refractometer based upon a long period grating Mach-Zehnder interferometer," *Rev. Sci. Instrum.*, vol. 73, no. 4, pp. 1702–1705, Mar. 2002.
- [142] P. L. Swart, "Long-period grating Michelson refractometric sensor," *Meas. Sci. Technol.*, vol. 15, no. 8, p. 1576, 2004.
- [143] M. Jiang, A. P. Zhang, Y.-C. Wang, H.-Y. Tam, and S. He, "Fabrication of a compact reflective long-period grating sensor with a cladding-mode-selective fiber end-face mirror," *Opt. express*, vol. 17, no. 20, pp. 17976–17982, 2009.
- [144] T. V. N. Coelho, J. P. Carvalho, M. J. Pontes, J. L. Santos, and A. Guerreiro, "A remote long-period grating sensor with electrical interrogation assisted by Raman amplification," *Opt. Laser Technol.*, vol. 47, pp. 107–113, Apr. 2013.
- [145] L. Qi *et al.*, "Highly reflective long period fiber grating sensor and its application in refractive index sensing," *Sens. Actuators B Chem.*, vol. 193, pp. 185–189, 2014.
- [146] P. Biswas, N. Basumallick, S. Bandyopadhyay, K. Dasgupta, A. Ghosh, and S. Bandyopadhyay, "Sensitivity enhancement of turn-around-point long period gratings by tuning initial coupling condition," *IEEE Sens. J.*, vol. 15, no. 2, pp. 1240–1245, Feb. 2015.
- [147] S. Rana, H. Subbaraman, and N. Kandadai, "Role of metal coating parameters on the reflective long period grating spectrum," in *Optical Sensors and Sensing Congress (ES, FTS, HISE, Sensors) (2019)*, paper ETh1A.5, Jun. 2019, p. ETh1A.5.
- [148] P. Fan, L.-P. Sun, Z. Yu, J. Li, C. Wu, and B.-O. Guan, "Higher-order diffraction of long-period microfiber gratings realized by arc discharge method," *Opt. Express*, vol. 24, no. 22, pp. 25380–25388, Oct. 2016.
- [149] S. Rana, N. Kandadai, and H. Subbaraman, "Towards the design of a wideband reflective long period grating distributed sensor," *J. Phys. Commun.*, vol. 4, no. 6, p. 065015, Jun. 2020.

- [150] V. Bhatia and A. M. Vengsarkar, "Optical fiber long-period grating sensors," *Opt. Lett.*, vol. 21, no. 9, pp. 692–694, May 1996.
- [151] N. P. Bansal, R. H. Boremus, *Handbook of Glass Properties*. Elsevier, 1986.
- [152] H. Tsuda and K. Urabe, "Characterization of long-period grating refractive index sensors and their applications," *Sensors*, vol. 9, no. 6, Art. no. 6, Jun. 2009.
- [153] Q.-S. Li *et al.*, "An Ultrasensitive long-period fiber grating-based refractive index sensor with long wavelengths," *Sensors*, vol. 16, no. 12, Art. no. 12, Dec. 2016.
- [154] J. Yang, L. Yang, C.-Q. Xu, C. Xu, W. Huang, and Y. Li, "Long-period grating refractive index sensor with a modified cladding structure for large operational range and high sensitivity," *Appl. Opt.*, vol. 45, no. 24, pp. 6142–6147, Aug. 2006.
- [155] I. Piro and R. Duffey, "Nuclear Power as a Basis for Future Electricity Generation," *J. Nucl. Rad/ Sci*, vol. 1, no. 1, Jan. 2015.
- [156] J. A. L. Kotek Ralph G. Bennett, John F., "Next Generation Nuclear Power," *Scientific American*. [Online]. Available: <https://www.scientificamerican.com/article/next-generation-nuclear/>
- [157] M. Bagatin, S. Gerardin, and S. Gerardin, *Ionizing Radiation Effects in Electronics : From Memories to Imagers*. CRC Press, 2018.
- [158] S. Girard *et al.*, "Recent advances in radiation-hardened fiber-based technologies for space applications," *J. Opt.*, vol. 20, no. 9, p. 093001, Aug. 2018.
- [159] F. Berghmans, B. Brichard, A. F. Fernandez, A. Gusarov, M. V. Uffelen, and S. Girard, "An introduction to radiation effects on optical components and fiber optic sensors," in *Optical Waveguide Sensing and Imaging*, Dordrecht, 2008, pp. 127–165.
- [160] A. Birri, B. A. Wilson, and T. E. Blue, "Deduced Refractive Index Profile Changes of Type I and Type II Gratings When Subjected to Ionizing Radiation," *IEEE Sens. J.*, vol. 19, no. 13, pp. 5000–5006, Jul. 2019.

- [161] M. A. S. Zaghoul *et al.*, “Radiation resistant fiber Bragg grating in random air-line fibers for sensing applications in nuclear reactor cores,” *Opt. Express*, vol. 26, no. 9, pp. 11775–11786, Apr. 2018.
- [162] G. Cheymol, J. F. Villard, A. Gusarov, and B. Brichard, “Fibre optic extensometer for high radiation and high temperature nuclear applications,” *IEEE Trans. Nucl. Sci.*, vol. 60, no. 5, pp. 3781–3784, Oct. 2013.
- [163] “Mode Solvers for Optical Waveguides”, *FIMMWAVE*. [Online], Available: [https://www.photond.com/products/fimmwave/fimmwave\\_features\\_20.htm](https://www.photond.com/products/fimmwave/fimmwave_features_20.htm)
- [164] “Optical fiber,” *Wikipedia*. [Online]. Available: [https://en.wikipedia.org/w/index.php?title=Optical\\_fiber&oldid=1025035738](https://en.wikipedia.org/w/index.php?title=Optical_fiber&oldid=1025035738)
- [165] A. I. Gusarov *et al.*, “High total dose radiation effects on temperature sensing fiber Bragg gratings,” *IEEE Photon. Technol. Lett.*, vol. 11, no. 9, pp. 1159–1161, Sep. 1999.
- [166] P. Niay *et al.*, “Behavior of Bragg gratings, written in germanosilicate fibers, against  $\gamma$ -ray exposure at low dose rate,” *IEEE Photon. Technol. Lett.*, vol. 6, no. 11, pp. 1350–1352, Nov. 1994.
- [167] K. Krebber, H. Henschel, and U. Weinand, “Fibre Bragg gratings as high dose radiation sensors,” *Meas. Sci. Technol.*, vol. 17, no. 5, pp. 1095–1102, Apr. 2006.
- [168] F. Esposito, A. Stăncălie, C.-D. Neguț, S. Campopiano, D. Sporea, and A. Iadicicco, “Comparative investigation of gamma radiation effects on long period gratings and optical power in different optical fibers,” *J. Lightw. Technol.*, vol. 37, no. 18, pp. 4560–4566, Sep. 2019,.
- [169] T. Erdogan, “Cladding-mode resonances in short- and long-period fiber grating filters,” *J. Opt. Soc. Am. A*, vol. 14, no. 8, pp. 1760–1773, Aug. 1997.
- [170] G. M. Berruti *et al.*, “Analysis of uncoated LPGs written in B-Ge doped fiber under proton irradiation for sensing applications at CERN,” *Sci Rep*, vol. 10, no. 1, Art. no. 1, Jan. 2020.

- [171] F. Piao, W. G. Oldham, and E. E. Haller, "The mechanism of radiation-induced compaction in vitreous silica," *J. Non Cryst. Solids*, vol. 276, no. 1, pp. 61–71, Oct. 2000.
- [172] A. I. Gusarov *et al.*, "Behavior of fibre Bragg gratings under high total dose gamma radiation," *IEEE Trans. Nucl. Sci.*, vol. 47, no. 3, pp. 688–692, Jun. 2000.
- [173] B. Brichard, O. V. Butov, K. M. Golant, and A. Fernandez Fernandez, "Gamma radiation-induced refractive index change in Ge- and N-doped silica," *J. Appl. Phys.*, vol. 103, no. 5, p. 054905, Mar. 2008.
- [174] P. Kniazewski, M. Kujawinska, F. Berghmans, A. Fernandez, A. Goussarov, and M. V. Uffelen, "Application of the microinterferometric tomography setup to the reliability tests of the fiber sensors exposed to cumulated gamma radiation," in *Nano- and Micro-Metrology*, Aug. 2005, vol. 5858, p. 585805. International Society for Optics and Photonics.
- [175] R. Y.-N. Wong, D. H. J. Juan, M. Ibsen, and P. P. Shum, "Optical Fibre Long-Period Grating Sensors Operating at and around the Phase Matching Turning Point," *Applications of Optical Fibers for Sensing*, Intech: Rijeka, Croatia, 2013.
- [176] L. Li *et al.*, "Ultrahigh sensitive temperature sensor based on Fabry–Pérot interference assisted by a graphene diaphragm," *IEEE Sens. J.*, vol. 15, no. 1, pp. 505–509, Jan. 2015.
- [177] G. Zhang, M. Yang, and M. Wang, "Large temperature sensitivity of fiber-optic extrinsic Fabry–Perot interferometer based on polymer-filled glass capillary," *Opt. Fiber Technol.*, vol. 19, no. 6, Part A, pp. 618–622, Dec. 2013.
- [178] F. Wang *et al.*, "High-sensitivity Fabry-Perot interferometer temperature sensor probe based on liquid crystal and the Vernier effect," *Opt. Lett.*, vol. 43, no. 21, pp. 5355–5358, Nov. 2018.
- [179] M. N. Ott, "Radiation effects data on commercially available optical fiber: database summary," in *IEEE Radiation Effects Data Workshop*, Jul. 2002, pp. 24–31.

- [180] M. Van Uffelen *et al.*, “Long-term prediction of radiation induced losses in single mode optical fibers exposed to gamma rays using a pragmatic approach,” in *2000 IEEE Radiation Effects Data Workshop. Workshop Record. Held in conjunction with IEEE Nuclear and Space Radiation Effects Conference (Cat. No.00TH8527)*, Jul. 2000, pp. 80–84.
- [181] T. Blanchet *et al.*, “Radiation and High Temperature Effects on Regenerated Fiber Bragg Grating,” *J. Lightw. Technol.*, vol. 37, no. 18, pp. 4763–4769, Sep. 2019.
- [182] W. Primak, L. H. Fuchs, and P. Day, “Effects of nuclear reactor exposure on some properties of vitreous silica and quartz,” *J. Ame. Ceram. Soc.*, vol. 38, no. 4, pp. 135–139, 1955.
- [183] J. B. Bates, R. W. Hendricks, and L. B. Shaffer, “Neutron irradiation effects and structure of noncrystalline SiO<sub>2</sub>,” *J. Chem. Phys.*, vol. 61, no. 10, pp. 4163–4176, Nov. 1974.
- [184] “Structure and Imperfections in Amorphous and Crystalline Silicon Dioxide. | Wiley,” NJ, USA, John Wiley-Blackwell, 2000.
- [185] H. Kogelnik, “Coupled wave theory for thick hologram gratings,” *The Bell System Technical Journal*, vol. 48, no. 9, pp. 2909–2947, Nov. 1969.
- [186] D. K. W. Lam and B. K. Garside, “Characterization of single-mode optical fiber filters,” *Appl. Opt.*, vol. 20, no. 3, pp. 440–445, Feb. 1981.
- [187] S. A. Slattery, D. N. Nikogosyan, and G. Brambilla, “Fiber Bragg grating inscription by high-intensity femtosecond UV laser light: comparison with other existing methods of fabrication,” *J. Opt. Soc. Am. B*, vol. 22, no. 2, pp. 354–361, Feb. 2005.
- [188] S. Rana, H. Subbaraman, A. Fleming, and N. Kandadai, “Numerical analysis of radiation effects on fiber optic sensors,” *Sensors*, vol. 21, no. 12, Art. no. 12, Jan. 2021.
- [189] I. H. Malitson, “Interspecimen Comparison of the Refractive Index of Fused Silica\*,†,” *J. Opt. Soc. Am.*, vol. 55, no. 10, pp. 1205–1209, Oct. 1965.

- [190] Y. Wu, Y. Zhang, J. Wu, and P. Yuan, "Fiber-Optic Hybrid-Structured Fabry–Perot Interferometer Based On Large Lateral Offset Splicing for Simultaneous Measurement of Strain and Temperature," *J. Lightw. Technol.*, vol. 35, no. 19, pp. 4311–4315, Oct. 2017.
- [191] P. Antunes, F. Domingues, M. Granada, and P. André, "Mechanical Properties of Optical Fibers," *Selected Topics on Optical Fiber Technology*, Intech: Rijeka, Croatia, 2012.
- [192] J. A. Stone and A. Stejskal, "Using helium as a standard of refractive index: correcting errors in a gas refractometer," *Metrologia*, vol. 41, no. 3, pp. 189–197, Apr. 2004.
- [193] M. Cavillon, P. D. Dragic, and J. Ballato, "Additivity of the coefficient of thermal expansion in silicate optical fibers," *Opt. Lett.*, vol. 42, no. 18, pp. 3650–3653, Sep. 2017.
- [194] E. D. Palik, Thermo-Optic Coefficients, in *Handbook of Optical Constants of Solids*, Burlington: Academic Press, 1997, pp. 115–261.
- [195] H. Gao, Y. Jiang, Y. Cui, L. Zhang, J. Jia, and L. Jiang, "Investigation on the Thermo-Optic Coefficient of Silica Fiber Within a Wide Temperature Range," *J. Lightw. Technol.*, vol. 36, no. 24, pp. 5881–5886, Dec. 2018.
- [196] G. Adamovsky *et al.*, "Peculiarities of thermo-optic coefficient under different temperature regimes in optical fibers containing fiber Bragg gratings," *Opt. Commun.*, vol. 285, no. 5, pp. 766–773, Mar. 2012.
- [197] L. Li, D. Lv, M. Yang, L. Xiong, and J. Luo, "A IR-femtosecond laser hybrid sensor to measure the thermal expansion and thermo-optical coefficient of silica-based FBG at high temperatures," *Sensors*, vol. 18, no. 2, Art. no. 2, Feb. 2018.
- [198] L. Prod'Homme, "A new approach to the thermal change in the refractive index of glasses," *Phys. Chem. Glasses* vol. 1, no. 119, 1960.
- [199] E. Talebian and M. Talebian, "A general review on the derivation of Clausius–Mossotti relation," *Optik*, vol. 124, no. 16, pp. 2324–2326, Aug. 2013.

- [200] T. Bååk, "Thermal Coefficient of Refractive Index of Optical Glasses\*," *J. Opt. Soc. Am.*, vol. 59, no. 7, pp. 851–857, Jul. 1969.
- [201] M. J. O'Dwyer, C.-C. Ye, S. W. James, and R. P. Tatam, "Thermal dependence of the strain response of optical fibre Bragg gratings," *Meas. Sci. Technol.*, vol. 15, no. 8, pp. 1607–1613, Jul. 2004.
- [202] R. M. Waxler and G. W. Cleek, "Refractive indices of fused silica at low temperatures," *J. Res. of NIST-A. Phys. Chem. A*, vol. 75, pp. 279–281, 1971.
- [203] P.-E. Dupouy, M. Büchner, P. Paquier, G. Tréneç, and J. Vigué, "Interferometric measurement of the temperature dependence of an index of refraction: application to fused silica," *Appl. Opt.*, vol. 49, no. 4, pp. 678–682, Feb. 2010.
- [204] J. H. Wray and J. T. Neu, "Refractive index of several glasses as a function of wavelength and temperature," *J. Opt. Soc. Am.*, vol. 59, no. 6, pp. 774–776, Jun. 1969.
- [205] Marcuse, D. Principles of Optical Fiber Measurements, Elsevier Science: Amsterdam, The Netherlands, 2012.
- [206] N. Yang, Q. Qiu, J. Su, and S. Shi, "Research on the temperature characteristics of optical fiber refractive index," *Optik*, vol. 125, no. 19, pp. 5813–5815, Oct. 2014.
- [207] Y. Guo *et al.*, "Theoretical and experimental investigations on the temperature dependence of the refractive index of amorphous silica," *J. Non Cryst. Solids*, vol. 429, pp. 198–201, Dec. 2015.
- [208] M. Deng, C.-P. Tang, T. Zhu, Y.-J. Rao, L.-C. Xu, and M. Han, "Refractive index measurement using photonic crystal fiber-based Fabry-Perot interferometer," *Appl. Opt.*, vol. 49, no. 9, pp. 1593–1598, Mar. 2010.
- [209] Y. Jiang, "High-resolution interrogation technique for fiber optic extrinsic Fabry-Perot interferometric sensors by the peak-to-peak method," *Appl. Opt.*, vol. 47, no. 7, pp. 925–932, Mar. 2008.
- [210] W. Primak, "Mechanism for the radiation compaction of vitreous silica," *J. Appl. Phys.*, vol. 43, no. 6, pp. 2745–2754, Jun. 1972.

- [211] D. Grobnic, C. W. Smelser, S. J. Mihailov, and R. B. Walker, “Long-term thermal stability tests at 1000 °C of silica fibre Bragg gratings made with ultrafast laser radiation,” *Meas. Sci. Technol.*, vol. 17, no. 5, pp. 1009–1013, Apr. 2006..
- [212] D. Grobnic, C. Hnatovsky, S. Dedyulin, R. B. Walker, H. Ding, and S. J. Mihailov, “Fiber Bragg grating wavelength drift in long-term high temperature annealing,” *Sensors*, vol. 21, no. 4, Art. no. 4, Jan. 2021.
- [213] L. Mohanty, L. M. Koh, and S. C. Tjin, “Fiber Bragg grating microphone system,” *Appl. Phys. Lett.*, vol. 89, no. 16, p. 161109, Oct. 2006.
- [214] C. M. Jewart, S. M. Quintero, A. M. B. Braga, and K. P. Chen, “Design of a highly-birefringent microstructured photonic crystal fiber for pressure monitoring,” *Opt. Express*, vol. 18, no. 25, pp. 25657–25664, Dec. 2010.
- [215] Z. Li *et al.*, “Highly-sensitive gas pressure sensor using twin-core fiber based in-line Mach-Zehnder interferometer,” *Opt. Express*, vol. 23, no. 5, pp. 6673–6678, Mar. 2015.
- [216] W. Talataisong, D. N. Wang, R. Chitaree, C. R. Liao, and C. Wang, “Fiber in-line Mach-Zehnder interferometer based on an inner air-cavity for high-pressure sensing,” *Opt. Lett.*, vol. 40, no. 7, pp. 1220–1222, Apr. 2015.
- [217] H. Y. Fu *et al.*, “Pressure sensor realized with polarization-maintaining photonic crystal fiber-based Sagnac interferometer,” *Appl. Opt.*, vol. 47, no. 15, pp. 2835–2839, May 2008.
- [218] B. Xu, C. Wang, D. N. Wang, Y. Liu, and Y. Li, “Fiber-tip gas pressure sensor based on dual capillaries,” *Opt. Express, OE*, vol. 23, no. 18, pp. 23484–23492, Sep. 2015, doi: 10.1364/OE.23.023484.
- [219] B. Xu, Y. Liu, D. Wang, D. Jia, and C. Jiang, “Optical fiber fabry-pérot interferometer based on an air cavity for gas pressure sensing,” *IEEE Photon. J.*, vol. 9, no. 2, pp. 1–9, Apr. 2017.
- [220] D. Zhao, Y. Wu, and J. Wu, “Pressure and temperature sensor based on fiber-optic fabry-perot interferometer by phase demodulation,” *IEEE Access*, vol. 7, pp. 179532–179537, 2019.

- [221] R. Wang, P. Huang, J. He, and X. Qiao, "Gas refractometer based on a side-open fiber optic Fabry–Perot interferometer," *Appl. Opt.*, vol. 56, no. 1, pp. 50–54, Jan. 2017.
- [222] W. Wang, N. Wu, Y. Tian, C. Niezrecki, and X. Wang, "Miniature all-silica optical fiber pressure sensor with an ultrathin uniform diaphragm," *Opt. Express*, vol. 18, no. 9, pp. 9006–9014, Apr. 2010.
- [223] E. Cibula and D. Đonlagić, "Miniature fiber-optic pressure sensor with a polymer diaphragm," *Appl. Opt.*, vol. 44, no. 14, pp. 2736–2744, May 2005.
- [224] H. Gao, Y. Jiang, Y. Cui, L. Zhang, J. Jia, and J. Hu, "Dual-cavity fabry–perot interferometric sensors for the simultaneous measurement of high temperature and high pressure," *IEEE Sens. J.*, vol. 18, no. 24, pp. 10028–10033, Dec. 2018.
- [225] R. Wang and X. Qiao, "Hybrid optical fiber Fabry–Perot interferometer for simultaneous measurement of gas refractive index and temperature," *Appl. Opt.*, vol. 53, no. 32, pp. 7724–7728, Nov. 2014.
- [226] Z. Li, J. Tian, Y. Jiao, Y. Sun, and Y. Yao, "Simultaneous measurement of air pressure and temperature using fiber-optic cascaded Fabry–Perot interferometer," *IEEE Photon. J.*, vol. 11, no. 1, pp. 1–10, Feb. 2019.
- [227] X. Wang, J. Xu, Y. Zhu, K. L. Cooper, and A. Wang, "All-fused-silica miniature optical fiber tip pressure sensor," *Opt. Lett.*, vol. 31, no. 7, pp. 885–887, Apr. 2006.
- [228] D. Duan, Y. Rao, and T. Zhu, "High sensitivity gas refractometer based on all-fiber open-cavity Fabry–Perot interferometer formed by large lateral offset splicing," *J. Opt. Soc. Am. B*, vol. 29, no. 5, pp. 912–915, May 2012.
- [229] P. Jia *et al.*, "Temperature-compensated fiber-optic Fabry–Perot interferometric gas refractive-index sensor based on hollow silica tube for high-temperature application," *Sens. Actuators B Chem.*, vol. 244, pp. 226–232, Jun. 2017.
- [230] "Molar refractivity," *Wikipedia*. [Online]. Available: [https://en.wikipedia.org/w/index.php?title=Molar\\_refractivity&oldid=1015083973](https://en.wikipedia.org/w/index.php?title=Molar_refractivity&oldid=1015083973)

- [231] R. Johnson, “Computational Chemistry Comparison and Benchmark Database, NIST Standard Reference Database 101.” National Institute of Standards and Technology, 2002.
- [232] Z. Wu *et al.*, “Mitigation of Radiation-Induced Fiber Bragg Grating (FBG) Sensor Drifts in Intense Radiation Environments Based on Long-short-Term Memory (LSTM) Network,” *IEEE Access*, pp. 1–1, 2021.

## APPENDIX

**Dopant Composition and Thermal Effects on Optical Fibers**

To quantify the effect of temperature on different dopants that creates fibers was investigated by subjecting different fibers at different temperatures. The dopant concentrations of fibers were quantified by electron microprobe analyzer (EMPA). Temperature effects of dopants were modelled. Fibers for temperature testing were purchased from different companies. A list of commercially purchased fibers is listed in Table A.1. The fibers were chosen due to their better performance in harsh environments based on the literature. The expected radiation response of these fibers based on literature is also shown in the Table A.1.

**Table A.1 Commercially purchased fibers along with the radiation response**

Fiber	Company, Part number	Wavelength [nm]	Dose Rate	Total Dose	Loss at 25°C	Description
Ge-doped	Corning, SM28ULTRA	1310 nm	333 rad/min	13.2 Mrad	47 dB/km	
Ge-doped	Nufern, R1310-HTA	660 nm		13 MGy		Radiation resistant under $\gamma$ -ray irradiation.
Ge-doped	Thorlabs, 1550 BHP	1550 nm		13.2 Mrad		Radiation resistivity.
Ge-doped	Fiberguide, AFS 105/125/225/3 25N	1310 nm		13.2 Mrad		Radiation resistant.
PSC	Nufern, R1550-HTA	660 nm		13 MGy		Radiation resistant under $\gamma$ -ray irradiation.
PSC	Polymicro, FIA200220500	850 nm	11.4 rad/min krad/min	1 Mrad	18 dB/km	
B-Ge-doped	Newport, F-SBG-13/15					Radiation hardness
Er-doped	Thorlabs, M5-980-125	980, 1530 nm		2.4 krad	12 and 7dB/m	Radiation hardness for space applications.
Nd-doped	Newport, F-DF1000					N/A
Yt-doped	Newport, F-YDC-1100-8/230	1000-1600 nm		2.3	8%	

\*PSC=pure silica core, PS=pure silica, Ge=Germanium, B-Ge= Boron-Germanium, Er=Erbium, Yt=Ytterbium, Nd=Neodymium

In this report we submit the test all of those fiber (as shown in Table A.1) for effect of temperature on transmission of light through the fiber.

### **A.1. Experimental Setup for Fibers Composition Measurements**

EPMA was performed to determine the composition of different fibers. The procedure to test a fiber for EPMA is given below and is schematically shown in Fig A.1

- (i) Cut the fibers to 1 inch with a cleaving tool
- (ii) Keep these fibers in epoxy resin for 12 hours
- (iii) Polish the fiber samples mechanically with different grades of silicon carbide (SiC) (starting with the low grade)
- (iv) Check the fiber surface by microscope while polishing with different grades of SiC
- (v) Then polish the samples mechanically with magnetic plate with different diameters
- (vi) Check the fiber surface by microscope while polishing with different magnetic plates
- (vii) Once mechanically polishing is done, make the fiber surface so flat by using diamond lapping
- (viii) Check the fiber surface by microscope while polishing with different diamond lapping
- (ix) Finally mount these samples for EMPA.

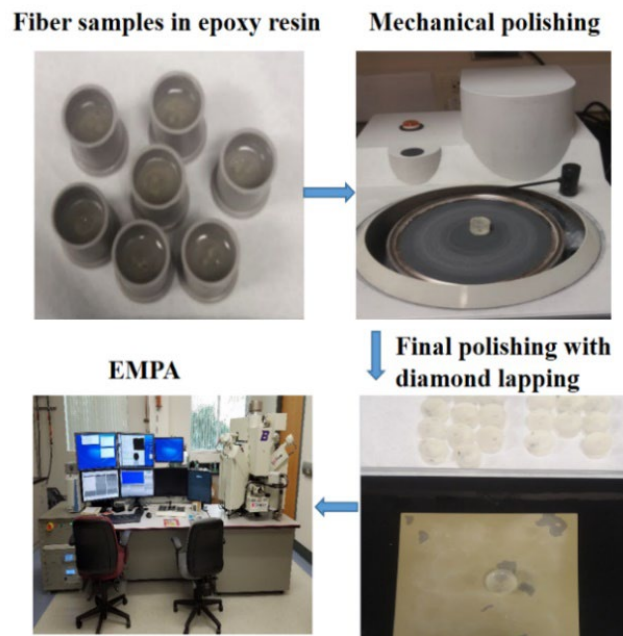


**Figure A.1 EMPA for finding doping concentrations of fibers.**

The corresponding doping concentrations for different commercially available fibers are shown in table A.2.

**Table A.2. Dopant concentration of different fibers at core**

Fiber	Company	Core	Cladding	Core dopants (%mole)
Ge-doped	Corning	Ge-doped	PS	3.08 (GeO <sub>2</sub> )
Ge-doped	Nufern	Ge-doped	PS	0.014(GeO <sub>2</sub> ), 0.21 (F)
Ge-doped	Thorlabs	Ge-doped	PS	0.69 (GeO <sub>2</sub> )
Ge-doped	Fiberguide	Ge-doped	PS	27.75 (GeO <sub>2</sub> )
PSC	Nufern	PSC	F-doped	1.09 (F)
PSC	Polymicro	PSC	F-doped	0.05 (GeO <sub>2</sub> ),0.13 (F)
B-Ge-doped	Newport	B-Ge-doped	PS	N/A
Er-doped	Thorlabs	Er-doped	PS	N/A
Nd-doped	Newport	Nd-doped	PS	0.004 (Nd <sub>2</sub> O <sub>3</sub> )
Yb-doped	Newport	Yb-doped	PS	0.31 (Yb <sub>2</sub> O <sub>3</sub> )

### A.2. Experimental setup for temperature testing

The experimental setup for understanding the effects of temperature on optical fibers is shown in Fig. A.2. Most of the fibers had acrylate/polyamide coating and a chemical etching was performed to remove the coating. The temperature tests were performed using thermolyne furnace (0-1200°C). The uncoated fiber was inserted into the furnace with the help of a quartz glass tube. One end of the fiber was connected to the laser and the other end was connected to Optical spectrum Analyzer to measure the transmission of fiber.

Four types of lasers were used to test the temperature response of different types of fibers at different wavelength.

- (i) ASE 1064 laser (OEQuest)
- (ii) 1310 laser (Thorlabs)
- (iii) Tunable laser C+L bands (Santec)
- (iv) ALS laser C+L bands (Amonics)

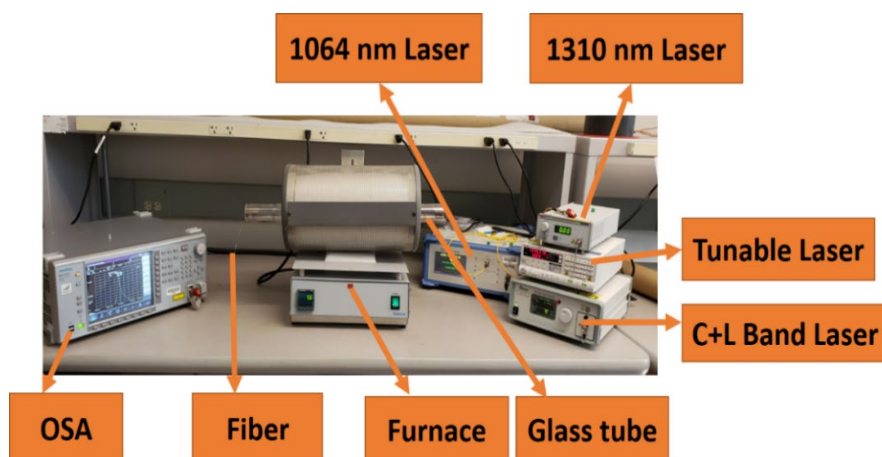


**Figure A.2** Experimental setup for temperature testing of fibers.

The input optical power was kept fixed while testing different fibers. Temperature was increased from room temperature (25°C) to 800°C with a ramp of 3°C/minute and data was recorded every 50°C interval. To understand the annealing effects on fibers, fiber was kept at 800°C for 12 hours.

### **A.3 Experimental Results of Thermal Effects on Fibers**

The effect of temperature on the transmission spectrum will be discussed in the following section.

#### **A.3.1. Ge doped fibers**

Figs. A.3, A.4 and A.5 show the transmission characteristics of Ge doped fibers from four different companies.

*Effect at 1550nm:* The lower germanium dopant fiber (0.014% Nufern and 0.69% Thorlabs) at its transmission wavelength of 1550 nm, worsens with increase in temperature.

Even annealing does not improve the transmissivity. These two fibers work better at low temperature around 200°-300°C. On the other hand, fiber from Corning with moderate GeO<sub>2</sub> (3.08%) shows improved transmissivity at higher temperatures. However, annealing the fiber again worsens its transmission. An excessive GeO<sub>2</sub> (27.75%) concentration containing fiber from Fiberguide offers substantial transmissivity around 300°C. It is

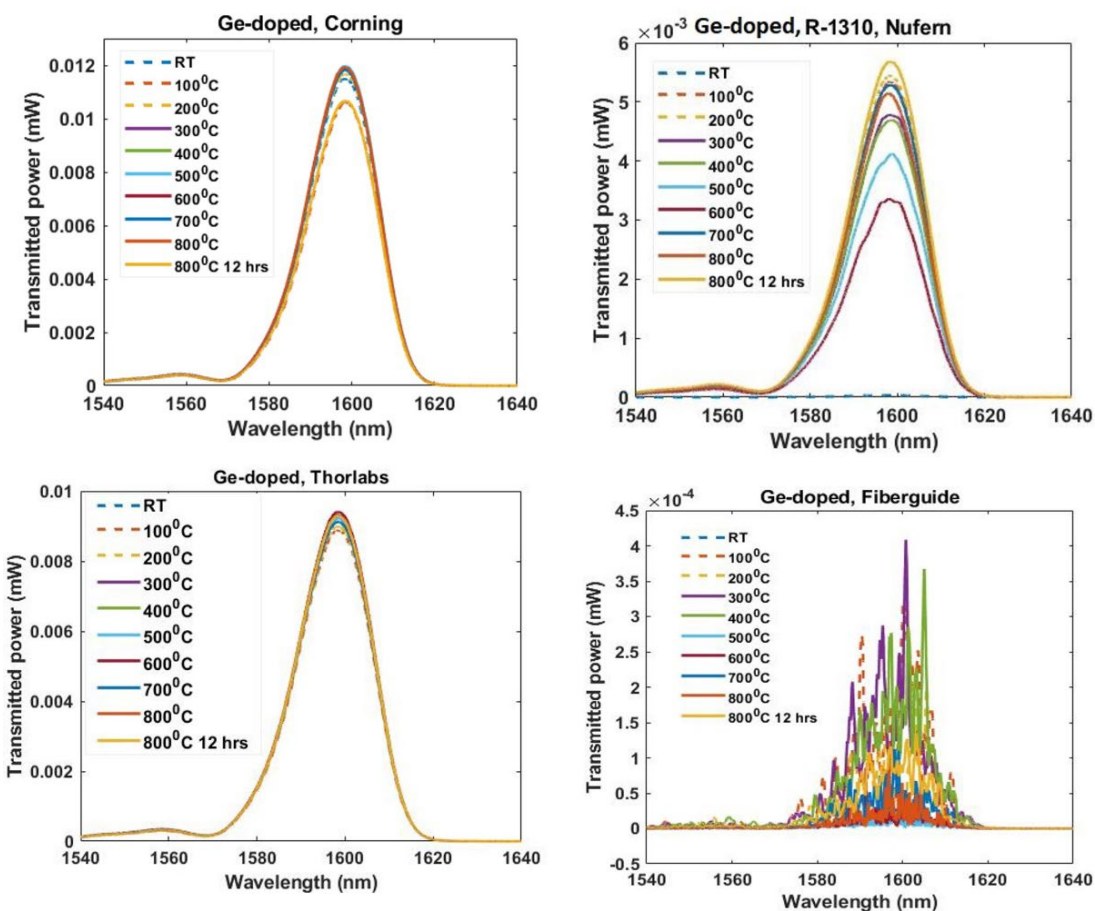


**Figure A.3** Temperature effects on different compositional germanium doped fibers at 1550 nm

assumed that loose connection distorts the transmitted spectrum for this fiber. One can deduce from Fig. A.3 that suitable amount of GeO<sub>2</sub> is highly expected for high transmissivity of fibers. Among the four fibers stated here, moderate GeO<sub>2</sub> (3.08%)

concentration containing fiber from Corning offers better transmittivity for the same input power at 1550 nm.

*Effect at 1310nm:* Among the four fibers, Nufern R-1310 (0.014% GeO<sub>2</sub>) shows comparatively better transmissivity at high temperature at this wavelength because this fiber was specially fabricated for operating wavelength 1310 nm which is shown in Fig.

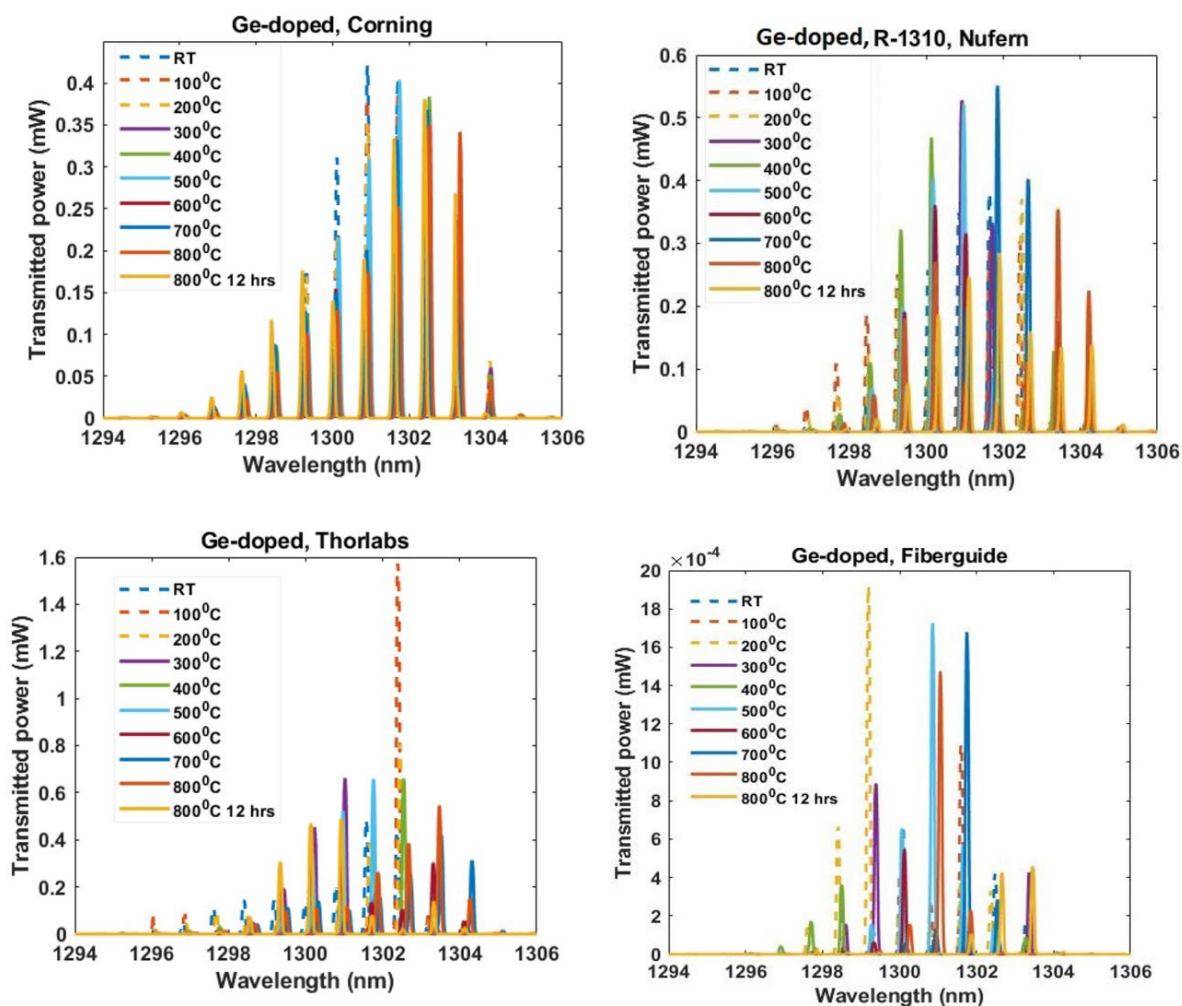


**Figure A.4** Temperature effects on different compositional germanium doped fibers at 1310 nm

A.4. On the other hand, high GeO<sub>2</sub> concentration (27.75%) loses its transparency drastically. Overall, all fibers stated here exhibits lower transmissivity when they were exposed to high temperatures for long time.

*Effect at 1064 nm:* Temperature effects on fibers at 1064 nm wavelength is shown in Fig. A.5. Fibers from Corning (3.08%) and Nufern (0.014%) shows substantial improved transmittivity when thermal treatment was performed at high temperatures for long time. On the other hand, at low temperatures (RT – 300°C), fibers from Thorlabs (0.69%) and

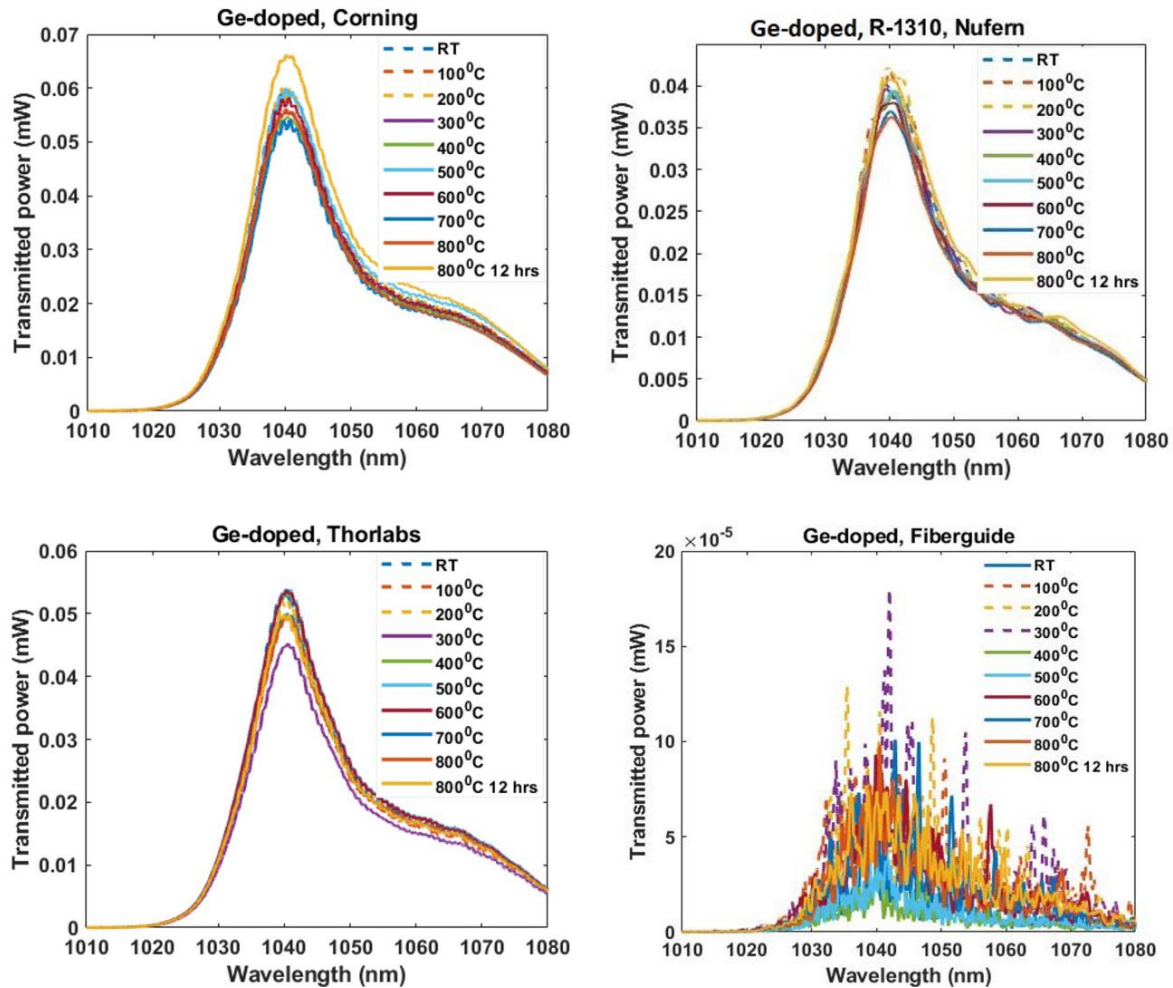


**Figure A.5 Temperature effects on different compositional germanium doped fibers at 1064 nm**

Fiberguide (27.75%) offer better transparency. Again, Corning fiber shows highest transmitted power among these four fibers at 1064 nm.

### A.3.2. Pure silica core (PSC) fibers

In this section we discuss the effects of temperature in these so-called pure silica core. Figs. A.6, A.7, and A.8 show the transmission characteristics of pure silica core fibers from two different companies.

*Effect at 1550nm:* Temperature effects on fibers at 1555 nm wavelength is shown in Fig. A.7. The PSC fiber from Nufern (1.09% F) clearly indicates that high temperatures improve the fiber performance at 1550 nm wavelength. Although the core of this fiber is made of pure silica, EMPA shows 1.09% F in the core. Our assumption is that these dopants might have been in the cladding and leaked into the core during the fabrication. On the other hand, Polymicro fiber (0.05 % GeO<sub>2</sub>, 0.13% F) shows better transmissivity at temperatures 400°C and 700°C. However, annealing drastically reduces its transparency. Please note that loose connections might distort the transmitted spectrum of this fiber. It

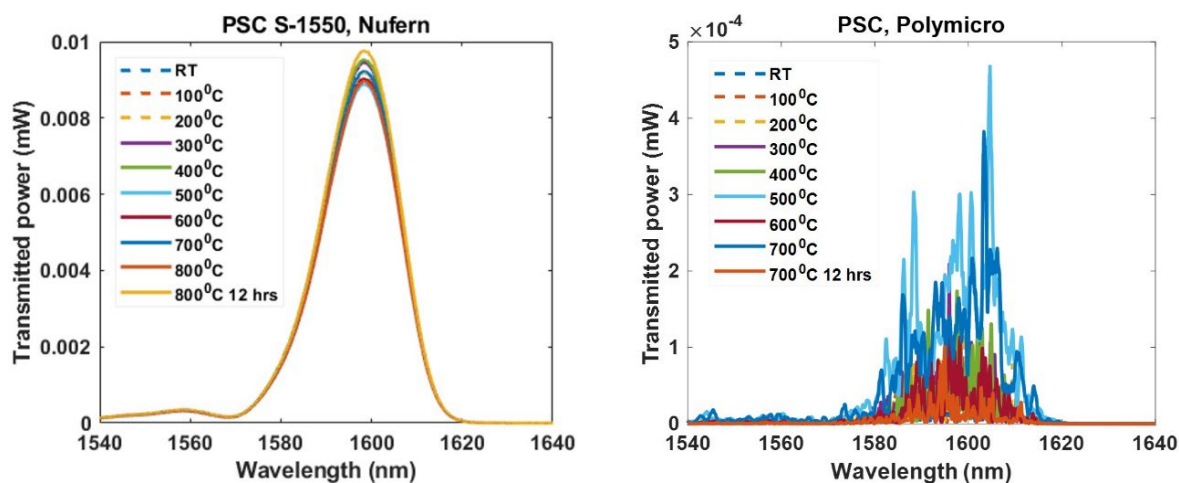


**Figure A.6** Temperature effects on different compositional PSC fibers at 1550 nm.

is our hypothesis that high fluorine rich fiber improves the transmissivity that can be seen from Fig. A.6.

*Effect at 1310 nm:* At this wavelength, Nufern fiber offers good transmissivity around low temperatures which can be seen in Fig. A.7. However, trend reverse whenever temperatures were increased even at annealing. On the contrary, Polymicro fiber improves its transparency when temperatures were increased gradually.

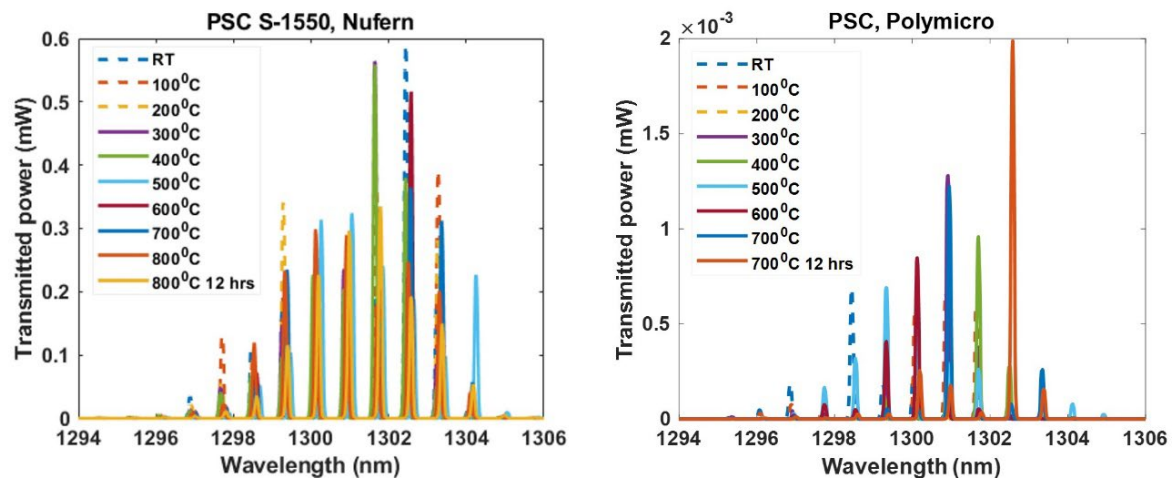


**Figure A.7** Temperature effects on different compositional PSC fibers at 1310 nm.

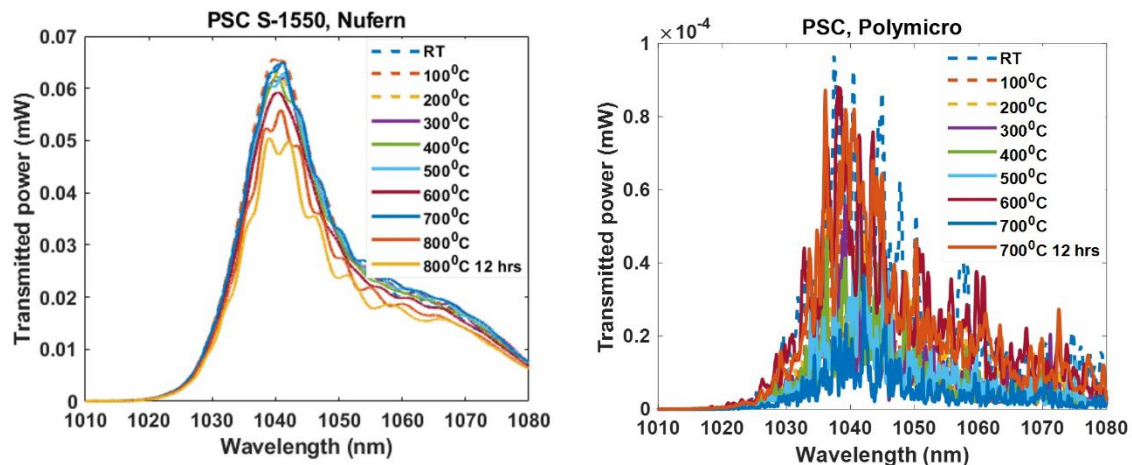


**Figure A.8** Temperature effects on different compositional PSC fibers at 1064 nm.

*Effect at 1064 nm:* It can be seen from Fig. A.8 that both fibers (Nufern and Polymicro) show good transmissivity at low temperatures. High temperatures as well as annealing darkens both the fibers.

### A.3.3 Specialty fibers

We tested four specialty fibers for this work. Their characteristics at different temperatures have been highlighted in the subsequent sections.

#### A.3.3.1. Boron Germanium Co doped fibers

First, we focus on the Boron-Germanium codoped fiber from Newport. This fiber can find applications in neutron detection as Boron has a high neutron cross section. Thermal effects on this fiber are shown in Fig. A.9 at different operating wavelengths.

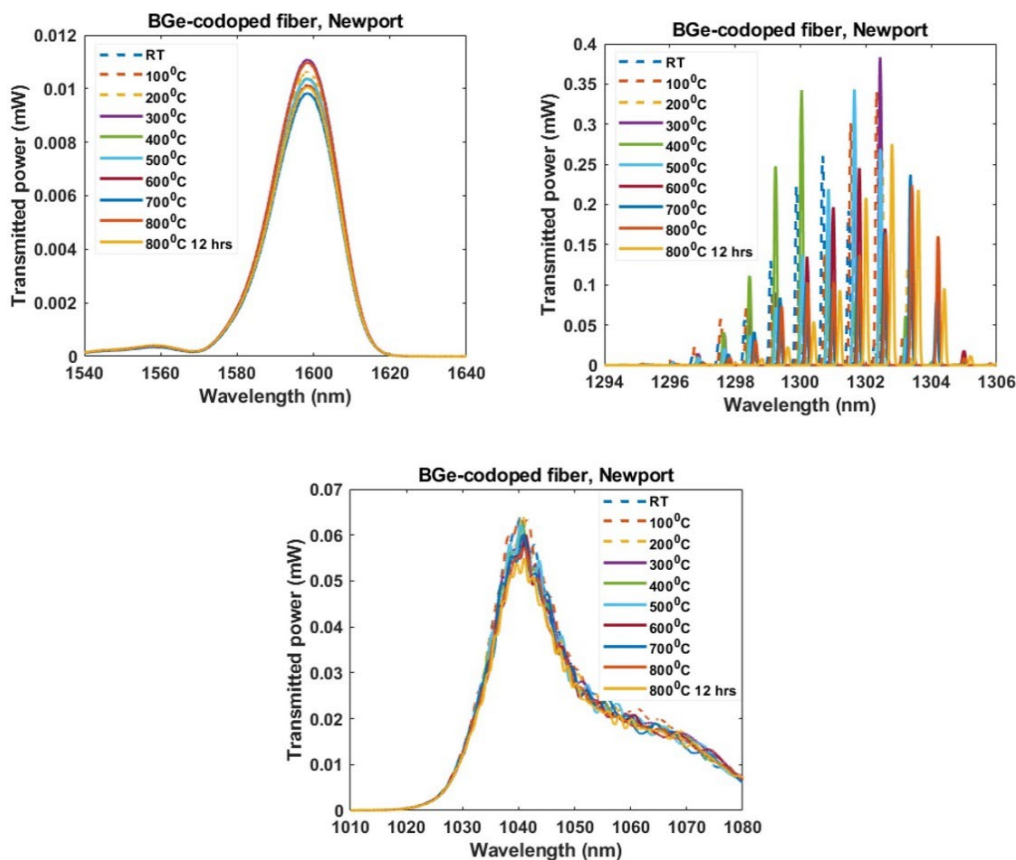


**Figure A.9** Temperature effects on Boron-Germanium codoped fiber at different wavelengths.

*Effect at 1550 nm:* The transmission decreases with increasing temperature however, annealing improves the transmission at 800°C.

*Effect at 1310 nm:* Transmission drops with increasing temperature by a significant magnitude.

*Effect at 1064 nm:* Transmission is fairly stable with a slight decrease with increasing temperatures.

### A.3.3.2. Erbium doped fibers

Erbium doped fibers have yet to be tested inside a reactor. We performed the temperature measurements of one Er-doped fiber from Thorlabs. The effect of temperature at different wavelengths is shown in Fig. A.10.

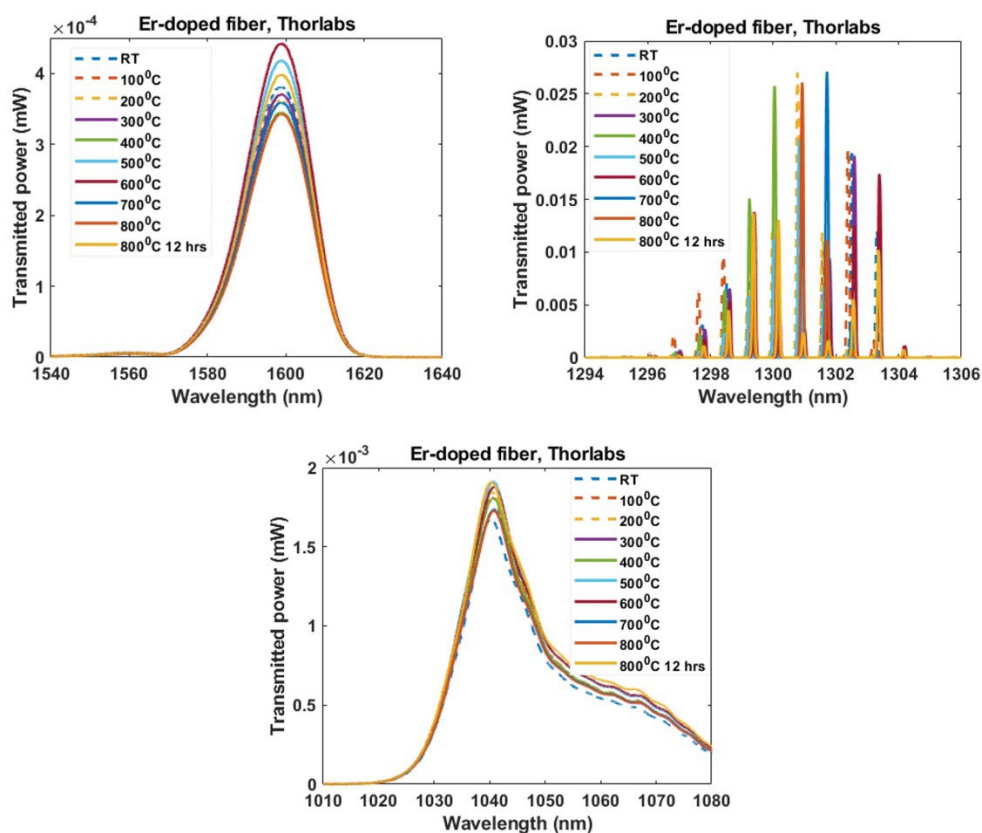


**Figure A.10** Temperature effects on Erbium doped fiber at different wavelengths.

*Effect at 1550 nm:* The transmission decreases with increasing temperature however, annealing improves the transmission at 800°C of the fiber from Thorlabs.

*Effect at 1310 nm:* Transmission drops with increasing temperature by a significant magnitude

*Effect at 1064 nm:* Transmission is fairly stable with a slight decrease with increasing temperatures.

### A.3.3.3. Neodymium doped fibers

Here we focus on the Neodymium doped fiber from Newport. This fiber contains 0.004%  $\text{Nd}_2\text{O}_3$  in the core. We performed the temperature measurements of these fiber (Fig A.11). The effect of temperature at different wavelengths are as follows:

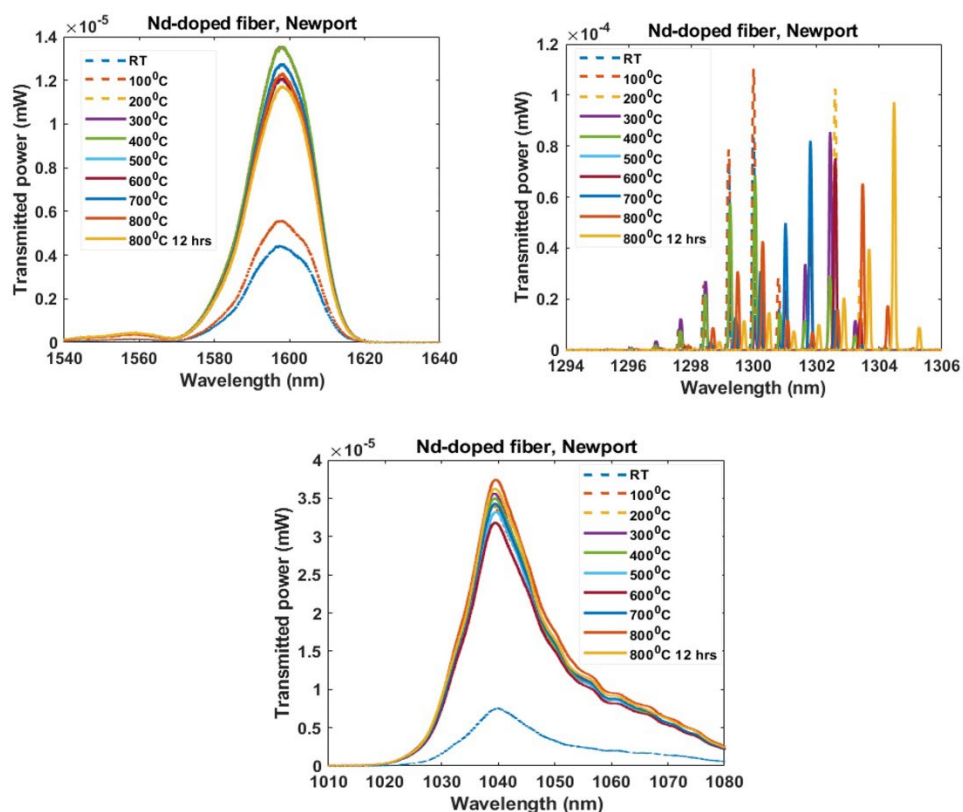


**Figure A.11** Temperature effects on Neodymium doped fiber at different wavelengths.

*Effect at 1550 nm:* Increasing temperature improves signal transmission till 400°C. After 400°C the transmitted power drops slightly with increasing temperature. Annealing at 800°C reduces the transmission power.

*Effect at 1310 nm:* The fiber performance is best at room temperature, it steadily decreases with increasing temperature, with annealing recovering the transmission

*Effect at 1064 nm:* The fiber transmission improves with increasing temperature at 800°C.

#### A.3.3.4. Ytterbium doped fibers

The effects of thermal treatment on ytterbium doped (Yb-doped) fiber is shown in Fig. A.12 at different wavelengths.

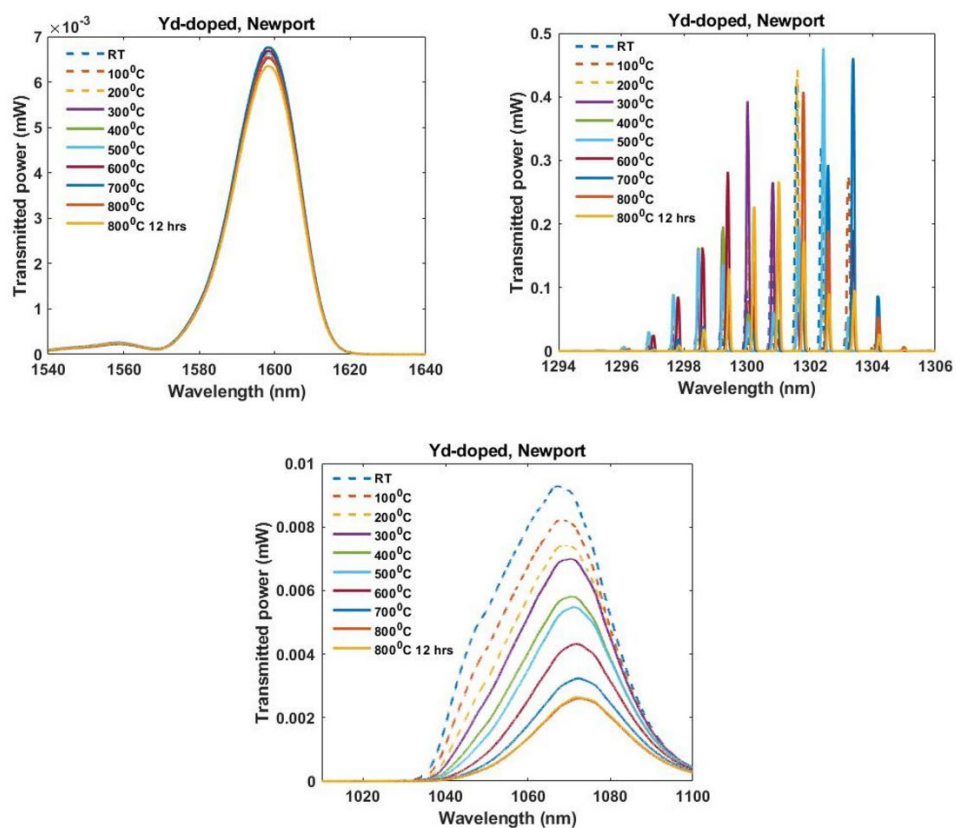


**Figure A.12** Temperature effects on Ytterbium doped fiber at different wavelengths.

*Effect at 1550 nm:* This fiber shows improved transmissivity when temperature was gradually increased from room temperature (RT) to 700°C. However, further increment of temperature reduced its performance.

*Effect at 1310 nm:* As temperature was increased from RT to 700°C, its performance improved. Again, annealing darkened the fiber and caused some losses by creating defects.

*Effect at 1064 nm:* It is clear from Fig. A.13 that at 1064 nm, the fiber performance inversely proportional to the temperature.

In this appendix, the thermal effects on different commercially available fibers have been discussed. It has been shown that different dopants amount also show distinct behavior from each other. While one type of fiber shows better stability at time temperatures at one wavelength, fiber performance reduces at another wavelength. To fully understand the thermal effects on fibers, further studies are required.